A Search for $\nu_\mu \rightsquigarrow \nu_e$ Oscillations in the NOMAD Experiment

Andrew R. Godley

A thesis
submitted for the degree of
Doctor of Philosophy
at the
University of Sydney

August, 2000

Abstract

The NOMAD experiment is a neutrino oscillation experiment, capable of identifying ν_μ, $\overline{\nu}_\mu$, ν_e, $\overline{\nu}_e$ and ν_τ for use in oscillation analyses. A search for $\nu_\mu \rightsquigarrow \nu_e$ oscillations is conducted, emphasising the development of two separate beam simulators, to provide the background, (no oscillation), ν_e signal.

Both beam descriptions include fits to the results of the SPY experiment that measured hadron production from a 450 GeV proton beam on beryllium target. An independent analysis of the raw SPY data to produce the particle yield is reported.

A series of criteria are described for the selection and classification of neutrino events. These produce the data samples necessary for both tuning the beam simulation and determining the oscillation signal.

The development of a GEANT and FLUKA based Monte Carlo beam simulator is presented, providing good agreement to the measured neutrino beam. This simulation method has sizeable variations depending on the beamline geometry, which is not known precisely. This causes large systematic errors.

An empirical parametrisation is proposed and used for the first time in a NOMAD oscillation search. It uses the measured neutrino spectra at NOMAD, except the ν_e, to infer the meson production at the target, and then predict the ν_e spectrum. This method has good agreement with the data and is also insensitive to alterations of the beamline geometry, resulting in much smaller systematic errors.

The reduction of the systematic errors allows the $\nu_\mu \rightsquigarrow \nu_e$ oscillations search to be performed with much greater precision. Comparisons of the ν_e/ν_μ ratio between the empirical parametrisation and data yields no evidence for $\nu_\mu \rightsquigarrow \nu_e$ oscillations, setting a limit on the mixing parameter, $sin^2(2\theta) < 1.9 \times 10^{-3}$(90% CL) at high Δm^2. The present sensitivity of the analysis on the mixing parameter is 0.0017.

Acknowledgements

I would like to say a few words to thank those involved in helping me with this thesis. Firstly there is my supervisor, A/Prof Lawrence Peak who warmly brought me into Falkiner High Energy Physics, and since then has been equally thoughtful and helpful in his supervision of this work and my schedule. Dr Kevin Varvell must also be gratefully thanked as his guidance was invaluable when I started this project and he continued answering my queries endlessly. The other members of Falkiner kept the work place pleasant and amiable, particularly during outings and talks. They are Drs Andy Bakich, Grant Gorfine, Reza Hashemi and Juris Ulrichs, (with whom I shared a flat in St Genis.)

There are many people at CERN who I would also like to thank. Dr Emmanuel Tsesmelis took the role of my supervisor during my first excursion to CERN in 1997. I owe a great deal to him for supporting my work in SPY and the neutrino beam studies, whilst also for presenting my work at CERN when I was in Sydney. When my focus shifted to the empirical parametrisation and the oscillation search I received great help from Dr Antonella de Santo, with whom I worked on the event selection and the empirical fitting programmes. Dr Fred Weber was also involved in these projects. Dr Sanjib Mishra provided deeper insights into the oscillation search, its requirements, goals and pitfalls. I am grateful to him for his help. Of course I was greatly helped by Dr Paul Soler who frequented both CERN and Falkiner in my time. Paul took interest in my projects, presented my work, reliably kept me up to date with the happenings at CERN and provided any extra aid I needed.

I had the pleasure of spending time with many friendly students. At Falkiner there was Bruce Canu, Malcolm Ellis, Aldo Saavedra, Joe Seisdedos, Jaime Varas and Jiangui Wang. Bruce provided all the distractions that one needed. Malcolm and Joe were officemates, available for conversation on all topics. Aldo lightened up my whole time in Sydney, both at work and after, whilst Jaime regaled everyone with stories of his exploits. I would also like to thank the two former students, Drs Steven Boyd and Bruce Yabsley, both of whom helped me a great deal. Amongst many other things, Steve provided expertise when I was studying the FCAL and Bruce advice on LaTeX. At CERN I would like to thankk Jukka Kokkonen and Dr Kai Zuber. From Melbourne University I would like to thank Brendan Dick, for many a relaxing sunday afternoon whilst at CERN. A special hello goes to my fellow Board Members at St Genis Uni.

To everyone mentioned, and those I forgot, thank you very much!

Author's Contribution

This work includes contributions from other members of the NOMAD collaboration. These contributions are acknowledged below on a chapter by chapter basis. Also note that the introduction is merely the author's summary of readily available neutrino theory and experimental results, given to provide a background for the project.

The description of the NOMAD experiment arises from the author's working knowledge of the systems, as well as published papers and internal papers, duly acknowledged. This is also true for the description of the SPY experimental setup.

The study of the SPY data is the author's work. The analysis of G.M. Collazuol and A. Guglielmi was used as a springboard, and was subsequently ratified during the author's investigation.

The neutrino event classification comprises work conducted by the author and A. DeSanto. The Calisto selection programme was written and maintained by the author, whilst Readall was developed by A. DeSanto until December 1999, and then by the author. The selection criteria are based on the studies of the NOMAD Phase II group, further refined by A. DeSanto, S.R. Mishra and the author.

The testing of NUBEAM involved a great deal of the author's time. Whilst most developments where implemented into the NUBEAM code by D. Daniels, F.J.P. Soler, V. Valuev and T. Weiße, tests and comparisons were carried out by the author, amongst others. A. Ferrari was responsible for the development of FLUKA, and G.M. Collazuol and A. Guglielmi for the SPY weighting, and again testing was undertaken by the author. The comparison of simulations to the muon pit data was conducted by the author alone, within NOMAD. The FCAL analysis was entirely the author's work, along with the comparison of NUBEAM to the drift chamber data. The systematic error study reported is that of V. Valuev.

The concept of the empirical parametrisation in NOMAD is S.R. Mishra's. The description given is of the author's implementation of the concept, to obtain a parametrisation independently to S.R. Mishra. The initial fitting programme was set up by F. Weber. The author made the extensions and adaptations necessary to include the simplex fitting mechanism, $\overline{\nu}_\mu$ and $\overline{\nu}_e$ fitting, the fit to SPY data and the production of the ν_e estimate. The independent prediction of the ν_e flux formed a major part of the work for this thesis.

The last chapter is the author's analysis, with the inclusion of S.R. Mishra's beam prediction and small contributions noted therein.

Preface

This thesis is a report on work carried out for the degree of Doctor of Philosophy in the Falkiner High Energy Physics Department at the University of Sydney. The work was undertaken as part of the NOMAD Collaboration at CERN. This thesis describes the NOMAD experiment and the analysis of its data for indications of muon neutrino to electron neutrino oscillations, featuring the prediction of the neutrino beam by the empirical parametrisation, in a blind analysis. Additional studies, relevant to the oscillation search, are also presented.

The first chapter introduces the theory of neutrinos. A history is given as to their importance in particle physics and cosmology. The concept and relevance of a massive neutrino is introduced, and neutrino oscillations are examined as an avenue for determining neutrino mass.

Chapter 2 describes the NOMAD experiment. The neutrino oscillation search technique is summarised, which indicates the necessary requirements of NOMAD. The neutrino beam is briefly discussed, followed by a rundown on the subdectors that comprise NOMAD. The NOMAD triggering, slow control and data taking are detailed, along with a description of event reconstruction and simulation in NOMAD.

The stand-alone experiment, SPY, is described in chapter 3. This experiment measured meson production relevant to the NOMAD neutrino beam. The layout of the SPY experiment is described, and then an analysis of its data is presented, including particle identification and yield computations. The results of this analysis and an indication of the future uses of the SPY data in neutrino beam simulation and parametrisation are given.

The fourth chapter deals with the classification of neutrino interactions within NOMAD. It presents the selection criteria for accepting and classifying neutrino triggers and also tabulates the efficiency of the selection process, which is later used in data to simulation comparisons. The event samples produced by these criteria are used throughout this thesis. The determination of the number of electron and muon neutrinos in this chapter, along with the beam predictions of the two following chapters, form the two parts of the oscillation search.

Chapter 5 summarises the traditional effort to simulate the neutrino beam with the programmes NUBEAM and FLUKA, and with fits to the SPY data. The chapter explains why the neutrino beam is so critical to the oscillation search and the available means for testing its simulation, including the muon pit data and quasielastic-like events in the FCAL. The three beam focusings used are described, and then the results of their simulation are compared with the NOMAD data.

The empirical parametrisation is proposed in chapter 5 as a new and novel beam flux prediction method. The theory, practice and merits of the method are described. A parametrisation is then fully determined from fits to SPY and NOMAD data. This parametrisation is cross checked with the parametrisation of S.R. Mishra in the next chapter.

The work of chapters 4, 5 and 6 are combined in chapter 7 to determine the oscillation signal. A study of systematic errors and a discussion of why the empirical parametrisation is better suited to the oscillation search than NUBEAM alone are included. The principles of a blind analysis are highlighted, before the oscillation signal is searched for by the comparison of the expected ν_e/ν_μ energy spectrum with that from data. The results are then quoted and discussed, before being reiterated in the conclusion.

Contents

Abstract i
Acknowledgements ii
Author's contribution iii
Preface iv
Contents vi
List of Figures xi
List of Tables xvi

1 Introduction and Theory **1**
1.1 Introduction 1
1.2 Neutrinos in Cosmology 3
1.2.1 Relic Neutrinos 3
1.2.2 Dark Matter 3
1.3 Neutrino Physics 5
1.3.1 Dirac and Majorana Neutrinos 5
1.3.2 Neutrino Interactions 6
1.3.3 Neutrino Sources 8
1.4 Neutrino Oscillations 10
1.5 The Neutrino Mass Situation 12
1.5.1 The See-Saw Mechanism 12
1.5.2 Direct Mass Measurements 13
1.5.3 Oscillation Search Results 14
1.5.4 The Ongoing Search 18

2 The NOMAD Experiment **21**
2.1 Introduction 21
2.2 Oscillation Searches 22
2.2.1 Muon Neutrino to Tau Neutrino 22
2.2.2 Muon Neutrino to Electron Neutrino 23
2.3 NOMAD as a check on LSND 23
2.4 The Neutrino Beam 24
2.4.1 Proton Acceleration and Beam Cycle 24

2.4.2 Beam Monitoring 26
2.4.3 Target 27
2.4.4 Neutrino Beam Generation 27
2.4.5 Focusing and Decay Tunnel 28
2.4.6 Muon Pits and Shielding 29
2.4.7 Expected Beam 29
2.5 Detector Description 29
2.5.1 The Magnet 30
2.5.2 Veto Counters 32
2.5.3 Forward Calorimeter 33
2.5.4 Drift Chamber 34
2.5.5 Transition Radiation Detector 36
2.5.6 Trigger Planes 38
2.5.7 Preshower 39
2.5.8 Electromagnetic Calorimeter 40
2.5.9 Hadronic Calorimeter 41
2.5.10 Muon Chambers 42
2.6 NOMAD Control Systems 44
2.6.1 Data Acquisition 44
2.6.2 Trigger Conditions 45
2.6.3 Slow Controls 47
2.7 Simulation and Reconstruction of Events 47
2.7.1 Event Generation 48
2.7.2 Detector Simulation 48
2.7.3 Event Reconstruction 49
2.8 The NOMAD Data Set 49

3 The SPY Experiment 51
3.1 Introduction and Motivation 51
3.2 Experimental Layout 52
3.2.1 Beam and Target 52
3.2.2 The H6 Spectrometer 54
3.2.3 Data Acquisition and Triggering 58
3.3 Particle Identification 59
3.3.1 Electron and Muon Identification 59
3.3.2 Intermediate Momenta 60
3.3.3 High Momenta 62
3.4 Production of Yields 64
3.4.1 Detector and Selection Efficiencies 64
3.4.2 Prescales 64
3.4.3 Acceptance 66

3.4.4 Correction for Particle Decays 67
3.4.5 Strange Particle Decays 68
3.4.6 Normalisation to Protons on Target 69
3.4.7 Empty Target Subtraction 69
3.5 Results and Comparisons 71
3.5.1 Momentum Dependence 72
3.5.2 Angular Dependence 73
3.5.3 Target Length Dependence 73
3.5.4 Other SPY Results 79

4 Neutrino Event Classification 81
4.1 Common Lepton Selection Criteria 82
4.1.1 Quality and Filter Cuts 82
4.1.2 Vetoing Through-Going Muons 85
4.1.3 The LEP Condition 85
4.1.4 Prompt Lepton Selection 86
4.2 Muon Identification 87
4.3 Electron Identification 89
4.3.1 Phase II Selection 89
4.3.2 Prompt Electron Selection 92
4.3.3 Increased Background Rejection 94
4.4 Selection Efficiencies 95
4.4.1 Energy Smearing 103
4.5 Hadronic Energy Scale 105

5 Simulation of the Neutrino Beam 111
5.1 Development of NUBEAM 112
5.1.1 Early Versions and Prehistory 113
5.1.2 Version 4.00 114
5.1.3 Version 5.00 114
5.1.4 Version 6.00 117
5.2 Development of FLUKA 120
5.2.1 FLUKA Versions 121
5.2.2 SPY Weighted FLUKA 123
5.3 Running NUBEAM and FLUKA 125
5.3.1 Interfacing FLUKA to NUBEAM 125
5.3.2 NUBEAM Decay Multiplicity 125
5.3.3 Weighting Event Monte Carlo 126
5.4 Muon Pit Comparisons 127
5.4.1 Layout of the Muon Pits 128
5.4.2 Calibration 129

5.4.3 Comparison with Simulation 130
5.5 Quasielastic Like Events in The FCAL 131
5.5.1 Further Details of the FCAL 133
5.5.2 Low ν Events 134
5.5.3 Event Selection and Efficiency 136
5.5.4 Comparison with Simulations 139
5.6 Drift Chamber Events 140
5.6.1 Positive, Negative and Zero Focusing Beams 140
5.6.2 Data Monte Carlo Comparisons 142
5.6.3 Comparison with CHORUS Data and Simulation . . . 148
5.7 Systematic Errors 152
5.8 Summary of Improvements 155

6 Empirical Parametrisation of the Neutrino Beam 157
6.1 Introduction and Motivation 157
6.2 Theoretical Concept 158
6.3 Implementation 159
6.3.1 Data Sample 159
6.3.2 Target Monte Carlo Sample 160
6.3.3 Meson Production Parametrisation 163
6.3.4 Corrections to the Estimate 165
6.3.5 Normalisation of Pion and Kaon Spectra 169
6.3.6 Mechanism to Produce a Trial Flux Estimate 171
6.3.7 Simplex Minimisation 173
6.3.8 SPY Data Fit 174
6.3.9 Producing the ν_e Estimate 176
6.4 Results 180
6.4.1 ν_μ Fit 180
6.4.2 $\overline{\nu}_\mu$ Fit 185
6.4.3 $\overline{\nu}_e$ Fit 193
6.4.4 ν_e Prediction 193

7 Oscillation Search 199
7.1 Discussion of Beam Simulators 199
7.1.1 Empirical Parametrisations 200
7.1.2 Official Parametrisation Compared to Data 203
7.1.3 Official Parametrisation Compared to NUBEAM 205
7.1.4 Official Parametrisation Systematics 211
7.1.5 Benefits of the Empirical Parametrisation 215
7.2 Theory of Small Signal Searches 215
7.2.1 Blind Analysis and Consequences 215

7.2.2 Double Ratio and Analysis Binning 216
7.2.3 Statistical Approach 217
7.2.4 Oscillation Contribution 218
7.3 Statistical Errors 219
7.4 Systematic Errors 219
7.4.1 Event Classification 219
7.4.2 Background 221
7.4.3 Electron Selection 221
7.4.4 Energy Reconstruction 222
7.4.5 Summary of all Systematic Errors 223
7.5 Results 223
7.5.1 Measured Oscillation Signal 225
7.5.2 Significance 227
7.5.3 Future Work 228
Conclusion 233

Bibliography **235**

List of Figures

1.1 The contribution of neutrino mass to the relative density . . . 5
1.2 Neutrino nucleon interaction Feynman diagrams 7
1.3 $\nu_\mu \rightsquigarrow \nu_e$ phase space 19

2.1 Layout of the WANF optimised for NOMAD 25
2.2 Cycle of the SPS 26
2.3 The effect of the horn and reflector in focusing particles of varying energy 28
2.4 Neutrino spectra at NOMAD 30
2.5 Detector layout (1995-96) 31
2.6 Layout of NOMAD veto planes 32
2.7 Top view of the FCAL 34
2.8 A single drift chamber, with detail of a detection gap 35
2.9 Schematic view of a TRD module 37
2.10 Trigger plane layout 38
2.11 An exploded view of the Preshower 39
2.12 Schematic view of the lead glass blocks that comprise the ECAL 41
2.13 The front view of the HCAL 42
2.14 Muon chamber layout 43
2.15 The standard configuration of the NOMAD data acquisition . 45
2.16 Accumulated BCT on the T9 target 50

3.1 The T4 target station in plan view 54
3.2 The SPY spectrometer, shown in the horizontal and vertical planes 56
3.3 Energy deposited in the first module, as a fraction of the total deposited, plotted against the total deposited 60
3.4 The mass squared fit produced by the time of flight counters at 20 GeV/c 61
3.5 Background from empty target runs 70
3.6 Background yields 72

3.7 Momentum distribution of particle yields from a 100 mm target, at 0 mrad 74
3.8 Momentum distribution of particle ratios from a 100 mm target, at 0 mrad 75
3.9 The angular distribution of particle yields from a 100 mm target at 40 GeV/c (left) and 15 GeV/c (right) 76
3.10 The angular distribution of particle yields from a 100 mm target at 40 GeV/c (left) and 15 GeV/c (right) 77
3.11 Particle yields from 100, 200 and 300 mm target lengths at 15 and 40 GeV/c, in the forward direction 78

4.1 A candidate ν_μ CC event as seen in the yz view of the NOMAD event display 88
4.2 Likelihood distributions for simulated 10 GeV pion and electron tracks crossing all nine TRD modules 90
4.3 Candidate ν_e CC event, as viewed in the NOMAD event display 95
4.4 Reconstruction differences in the z vertex position 96
4.5 The ν_μ DIS selection efficiency as a function of generated neutrino energy. 99
4.6 The $\overline{\nu}_\mu$ DIS selection efficiency as a function of generated neutrino energy. 100
4.7 The ν_e DIS selection efficiency as a function of generated neutrino energy. 102
4.8 The $\overline{\nu}_e$ DIS selection efficiency as a function of generated neutrino energy. 102
4.9 The ν_μ QE selection efficiency as a function of generated neutrino energy. 104
4.10 The ν_μ RES selection efficiency as a function of generated neutrino energy. 105
4.11 Scatter plot of E_{vis} versus E_ν for ν_μ DIS CC Monte Carlo . . . 106
4.12 Determining the hadronic energy scale 107
4.13 Monte Carlo and data ν_μ spectra without the hadronic energy scale 109
4.14 Monte Carlo and data ν_μ spectra with the hadronic energy scale110

5.1 Changes due to version 4.04 in the neutrino energy spectra for the four types 115
5.2 Version 5.00 changes in the neutrino energy spectra for the four types 116
5.3 The distribution of primary proton interaction points in the decay tunnel 118

5.4 The distribution of primary proton interaction points that lead to a ν_μ or $\overline{\nu}_\mu$ at NOMAD 119
5.5 Version 6.12 changes in the neutrino energy spectra for the four types 121
5.6 Positive focusing NUBEAM 6.12 weight functions 127
5.7 Layout of the first three muon pits 129
5.8 Simulation of the angular distribution of muons and electrons in the calibration emulsion of muon pit 3 131
5.9 Comparison of the data to simulated x and y spatial distributions of the muon flux in the pits 132
5.10 Side view of the FCAL 135
5.11 Selection efficiency of quasielastic (QE) neutrino events in the FCAL as a function of reconstructed neutrino energy. 138
5.12 Spatial distributions of low ν events in the FCAL 139
5.13 Energy spectrum of low ν events in the FCAL compared to Monte Carlo flux predictions of NUBEAM 6.12 with FLUKA 98. 140
5.14 Negative focusing NUBEAM 6.12 weight functions 142
5.15 Zero focusing NUBEAM 6.12 weight functions 143
5.16 Positive focusing ν_μ DIS drift chamber data and simulation . . 145
5.17 Positive focusing $\overline{\nu}_\mu$ DIS drift chamber data and simulation . . 146
5.18 Positive focusing $\overline{\nu}_e$ DIS drift chamber data and simulation . . 147
5.19 Negative focusing $\overline{\nu}_\mu$ DIS drift chamber data and simulation . 149
5.20 Negative focusing ν_μ DIS drift chamber data and simulation . 150
5.21 Zero focusing ν_μ DIS drift chamber data and simulation 151
5.22 Zero focusing $\overline{\nu}_\mu$ DIS drift chamber data and simulation . . . 152

6.1 Neutrino spectra separated according to neutrino parent . . . 159
6.2 The five radial bins and the drift chamber. 161
6.3 Selection efficiency for ν_μ as a function of true neutrino energy 166
6.4 ν_μ spectrum showing the approximate energy ranges where pions and kaons dominate 170
6.5 Fits to SPY K^+/π^+ data 177
6.6 Fits to SPY K^-/π^- data 178
6.7 NOMAD ν_μ data versus the empirical parametrisation in the five radial bins, linear 182
6.8 NOMAD ν_μ data versus the empirical parametrisation in the five radial bins, logarithmic 183
6.9 NOMAD ν_μ data versus empirical parametrisation in the combined radial bin 184

6.10 NOMAD ν_μ negative focusing data versus empirical parametrisation in the combined radial bin 186
6.11 NOMAD $\overline{\nu}_\mu$ data versus the empirical parametrisation in the five radial bins, linear 187
6.12 NOMAD $\overline{\nu}_\mu$ data versus the empirical parametrisation in the five radial bins, logarithmic 188
6.13 NOMAD $\overline{\nu}_\mu$ data versus empirical parametrisation in the combined radial bin 189
6.14 NOMAD $\overline{\nu}_\mu$ negative focusing data versus the empirical parametrisation in the five radial bins, linear 190
6.15 NOMAD $\overline{\nu}_\mu$ negative focusing data versus the empirical parametrisation in the five radial bins, logarithmic 191
6.16 NOMAD $\overline{\nu}_\mu$ negative focusing data versus empirical parametrisation in the combined radial bin 192
6.17 NOMAD $\overline{\nu}_e$ data versus empirical parametrisation in the combined radial bin, linear 194
6.18 NOMAD $\overline{\nu}_e$ data versus empirical parametrisation in the combined radial bin, logarithmic 195
6.19 The empirical parametrisation prediction of ν_e, linear 196
6.20 The empirical parametrisation prediction of ν_e, logarithmic . . 197

7.1 Independent and official parametrisation predictions of ν_μ CC low ν events 201
7.2 Ratio of independent over official parametrisation prediction of the ν_e/ν_μ ratio at low ν 202
7.3 The ν_μ energy spectra (high ν) of data and the official parametrisation 204
7.4 The $\overline{\nu}_\mu$ energy spectra (high ν) of data and the official parametrisation 206
7.5 The $\overline{\nu}_e$ energy spectra (high ν) of data and the official parametrisation 207
7.6 Official parametrisation and NUBEAM predictions of ν_μ CC high ν events 208
7.7 Official parametrisation and NUBEAM predictions of $\overline{\nu}_\mu$ CC high ν events 209
7.8 Official parametrisation and NUBEAM predictions of $\overline{\nu}_e$ CC high ν events 210
7.9 Official parametrisation and NUBEAM predictions of ν_e CC high ν events 212
7.10 Comparison of the ν_e/ν_μ ratio as predicted by NUBEAM and the official parametrisation 213

7.11 $R_{e\mu}$ determined with the standard energy scale and a 10% lower scale 223
7.12 $R_{e\mu}$ from the 1995 high ν data (points) and as predicted by the official parametrisation (histogram) 224
7.13 $R_{e\mu}$ from the 1995 low ν data (points) and as predicted by the official parametrisation (histogram) 225
7.14 The 90% confidence limit obtained for $\nu_\mu \rightsquigarrow \nu_e$ oscillations from the 1995 NOMAD data 226
7.15 The exclusion region of the analysis and the original LSND allowed region 227
7.16 The exclusion region of the analysis and the revised LSND allowed region 229
7.17 The 90% confidence level sensitivity expected from this analysis, using the entire NOMAD data set. 230
7.18 The revised allowed region of LSND compared to the sensitivity expected from this analysis, including the entire NOMAD data set. 231

List of Tables

1.1 Ranges of Δm^2 applicable to the four neutrino sources. 12

2.1 Summary of Data taken by NOMAD from 1995 to 1998 50

3.1 Summary of the different SPY running conditions 53
3.2 Particles identified in each of the four timing subgroups for a 20 GeV/c run. 62
3.3 Particles identified in each of the six timing subgroups for a 40 GeV/c run. 64
3.4 Summary of identified particles 65
3.5 Definitions of the trigger scalers used in SPY 66
3.6 The calculated spectrometer acceptances used in this analysis 68
3.7 Summary of identified particles in the empty target runs . . . 71

4.1 Minimum z allowed for the fiducial volume. 84
4.2 Maximum values of hits for the through-going muon veto, according to the number of tracks in the event. 86
4.3 Maximum allowable scattering angles in radians for leptons, according to the number of tracks in the event. 87
4.4 Monte Carlo ν_e DIS events failing the standard selection which then either fail the LEP adjusted selection or are recovered. . 94
4.5 Effect of the Calisto event filter on the data 97
4.6 Selection efficiencies for ν_μ and $\overline{\nu}_\mu$ DIS events 98
4.7 Selection efficiencies for ν_e DIS events 101
4.8 Selection efficiencies for $\overline{\nu}_e$ DIS events 103
4.9 Efficiency for the selection of events from RES and QE Monte Carlo samples 104

5.1 he changes to the neutrino spectra shape and size with NUBEAM version 116
5.2 Effect of FLUKA upgrades on the neutrino beam at NOMAD 123
5.3 Data and simulated muon fluxes 133

5.4 FCAL quasielastic event selection 137
5.5 Expected ratios of charged current neutrino events expected in the beam 144
5.6 The average DIS neutrino energy and number of events for positive focusing data and simulation 148
5.7 The average DIS neutrino energy and number of events for negative focusing data and simulation 148
5.8 The average DIS neutrino energy and number of events for zero focusing data and simulation 148
5.9 The predictions of GBEAM 99 versus NUBEAM 5.00 153
5.10 NOMAD and CHORUS data comparison 153
5.11 Ratios of ν_e/ν_μ in the modified field versions to the standard version 155
5.12 Ratios of ν_e/ν_μ in the modified material versions to the standard version 156
5.13 Ratios of ν_e/ν_μ in the modified alignment versions to the standard version 156

6.1 Results of event selection, with and without the $\nu < 5$ GeV condition. 160
6.2 Normalisation factors for combining the resonance, quasielastic and deep inelastic Monte Carlo samples. 162
6.3 Base parameters entered in NUBEAM for meson production. . 165
6.4 Scales to the backgrounds to the $\overline{\nu}_\mu$, ν_e, and $\overline{\nu}_e$ signals for different ranges of ν. 169
6.5 Pion and kaon normalisation factors, for each of the five radial bins and combined bin (cm). 171
6.6 SPY K/π production, versus those obtained from the fit, displayed according to secondary momentum. 176
6.7 SPY K^+/π^+ production, versus those obtained from the fit, displayed according to p_T at the two given secondary momenta.179
6.8 SPY K^-/π^- production, versus those obtained from the fit, displayed according to p_T at the two given secondary momenta.179
6.9 Final meson production parameters after completion of the fitting process. 181
6.10 χ^2 of the fitted flux to the ν_μ data 181
6.11 χ^2 of the fitted flux to the $\overline{\nu}_\mu$ data 185

7.1 The breakdown of the neutrinos in terms of their parents . . . 203
7.2 Comparison of the number of high ν CC events in data with the predictions of NUBEAM and the official parametrisation. . 211

7.3 Energy binning for $R_{e\mu}$, (GeV). 217
7.4 Percentage statistical errors for the data and Monte Carlo samples used in the oscillation search 219
7.5 Cuts and their variations used in the systematic error studies. 220
7.6 Event numbers and efficiencies used to calculate the unfolded number of ν_μ and ν_e events. 220
7.7 The unfolded number and ratio of ν_μ and ν_e events 221
7.8 The contributions to the systematic error on $R_{e\mu}$. 224

Chapter 1

Introduction and Theory

1.1 Introduction

Since the 1960s, the field of particle physics has been dominated by the standard model. This model is the inclusive quantum theory of the strong interaction and the unified electromagnetic and weak interactions. It involves the ordering of the fermions, quarks and leptons, in three generations of increasing mass, and presents bosons as exchange particles that give rise to the forces. Large numbers of experiments were conducted to explore both the predictions of the model and to uncover flaws. Whilst the standard model has been extensively ratified, (most comprehensively by the LEP experiments at CERN, whose combined results have recently been summarised in Chazelle (1999)) only inconclusive hints have been obtained to imply physics beyond the standard model. One such hint has come from neutrino physics, generating much interest and excitement.

Neutrinos are fundamental particles, proposed by Wolfgang Pauli in 1930 to explain why electrons emitted in beta decay have a continuous energy spectrum, and further, why this spectrum has a total energy less than the Q-value, (change in nuclear energy), of the beta decay transition. Pauli hypothesized that a neutral particle, emitted with the electron, was responsible for the apparent missing energy in the decay. The original theory had a neutral particle with a mass of the order of the electron mass, and a penetrating power an order of magnitude greater than the photon. These properties, close to those accepted today, of a weakly interacting low mass particle, left the neutrino undiscovered experimentally until the cross section of the inverse beta decay, equation 1.1, was measured by Reines et al. (1956).

$$\overline{\nu}_e + p \rightarrow e^+ + n \tag{1.1}$$

Pion and muon decays were also shown to have decay spectra consistent with the emission of one or two neutrinos. This eventually led to the discovery of a second neutrino, the muon neutrino ν_μ, characterized by its tendency to produce muons, rather than electrons, in interactions with nucleons. The number of neutrino flavours with mass less than 45 GeV has since been constrained, by measurements of the Z boson decay width at LEP, to be three, (ALEPH Collaboration, 1999). Previously, the same constraint had been obtained from big bang nucleosynthesis, using the abundance of primordial ^{4}He, see Olive et al. (1999). The three flavours correspond to the three generations of quarks and charged leptons of the standard model. Thus the third, and still undetected neutrino, is the tau neutrino ν_τ.

The neutrino is modeled theoretically in the standard model. The neutrino only interacts through the weak interaction, that is the exchange of W or Z bosons. Moreover, only the left handed neutrino is thought to interact. The absence of right handed neutrinos, both in the theory and observation, implies that the neutrino must be massless. However most extensions to the standard model include massive neutrinos, (such as those of Arason et al. (1990); Kitano and Oda (1999)) and as will be discussed below there already exists experimental indications for them. Thus neutrino mass is one good indication of potential physics beyond the standard model. Conclusive measurements are now required for the masses of the three neutrinos. These measurements will subsequently aid in the selection of the most appropriate of the many standard model extensions theorised today.

In spite of the immense importance of neutrino mass, its measurement is not trivial. This is mainly due to such a small mass being predicted for the neutrino. Direct measurements, as discussed in section 1.5.2, are difficult, whilst garnering few insights into the actual mass. The most likely avenue for mass measurements comes from the quantum mechanical effect of neutrino oscillations, where a neutrino of one flavour can oscillate into another flavour. This phenomenon is only possible if the neutrino masses are non-degenerate.

This chapter will present the theory of neutrino interactions, neutrino models, (including massive neutrinos), and neutrino oscillation physics. The current status of neutrino mass measurements will be reviewed, including the future extensions to these measurements. The cosmological relevance of neutrinos is discussed firstly, providing an additional reason for the importance of determining the neutrino mass.

1.2 Neutrinos in Cosmology

1.2.1 Relic Neutrinos

Big bang cosmology was developed in 1940 by Gamow, (for a modern description see Kolb and Turner (1990)). In this model the universe is extremely hot and has an extremely high density directly after the big bang. All particles with mass much less than kT, (Boltzman constant times temperature), are in equilibrium with radiation, for example electrons:

$$\gamma + \gamma \rightleftarrows e^+ + e^- \tag{1.2}$$

The universe expands and cools, such that at a time around 10^{-2} s after the big bang T is 10^{11} K and the universe contains photons, electrons, neutrinos and a few protons and neutrons, (left over from the matter antimatter annihilations). The density has dropped to around 2.5×10^9 g/cm^3. The neutrinos are also in thermal equilibrium with the electron plasma with respect to the weak interaction processes:

$$\nu + \overline{\nu} \rightleftarrows e^+ + e^- \tag{1.3}$$

The neutrino mean free path λ is proportional to T^{-5} whilst the size of the universe is proportional to T^{-1}. Thus, with the continued cooling of the universe, λ becomes much larger than the universe at t $\sim$ 0.1 s. This means that the neutrinos can no longer "see" the rest of the matter in the universe. This is called neutrino freeze out. The frozen out neutrinos continue to cool, and over the 1.5×10^{10} years till today, their temperature has dropped to 1.9 K. This leaves the number density for each neutrino flavour at $N_{\nu_i} \simeq 113$ cm^{-3}. These neutrinos from the big bang are referred to as relic neutrinos, and still exist everywhere in universe. They form the second most abundant group of known particles, after the photons forming the cosmic microwave background. The cosmological importance of neutrinos arises from this abundance.

1.2.2 Dark Matter

Three potential fates for the universe exist. It could be an open universe, which expands forever, a closed universe, which expands for a while and then starts contracting to a "big crunch", or the universe could be flat where it expands to a stable size. How the universe behaves depends on its density in comparison to the critical density, the density of the flat universe:

$$\rho_c = \frac{3}{8\pi G} H_o^2 \tag{1.4}$$

where G is Newton's gravitational constant and H_o is the Hubble Constant, equal to the Hubble expansion parameter h times 100 km s^{-1} Mpc^{-1}. Current observations put the visible density of the universe near 0.001 ρ_c, for a value of h somewhere between 0.5 and 0.7, (the true value is difficult to determine from current methods and data). Thus if a closed or flat universe is desired, more matter than is seen by conventional astronomy is needed.

This turns out to be the case. Measurements of the rotational curves of spiral galaxies have shown that they are faster than would be expected from their visible mass, reported in White and Fabian (1995). The implied but unseen extra mass is the so-called dark matter. One of the main candidates for dark matter are massive neutrinos, which, as was shown above, are extremely abundant throughout the universe. It is important to note that whilst massive neutrinos play a role in large scale structure and flatness of the universe, they do not help to solve discrepancies in the rotation of spiral galaxies.

The neutrino mass density is written as:

$$\rho_\nu = 113 \text{ cm}^{-3} \sum_{i=1}^{3} m_{\nu_i} \tag{1.5}$$

which allows the preferred neutrino mass to be calculated, depending on the dark matter model used. One model has all the mass required to close the universe as hot dark matter, (hot is interpreted as comprising of relativistic particles, e.g. low mass relic neutrinos). This would require the sum of the three neutrino masses to be around 45 eV for $h = 0.7$. A second model, see Primack et al. (1995), has the universe comprised of 30% hot dark matter and 70% cold dark matter, (heavy particles, perhaps including as yet unknown heavy, possibly sterile, neutrinos with mass greater than 2 GeV). In this case, the neutrino mass sum would be closer to 9 eV. This is shown in figure 1.1, which represents the effect of the neutrino mass on the closure of the universe. $\Omega_o h^2$ represents current knowledge of the ratio of the density of the universe to the critical density, and so a value near unity is desirable. This corresponds to an eV or GeV range neutrino. Further, as can be seen in figure 1.1, neutrinos in the mass range 100 eV to 1 GeV have to be unstable, else they would over close the universe.

Knowledge of the neutrino masses will therefore provide insights into the constituents of the universe and the correct dark matter model. This will lead to an understanding of the destiny and flatness of the universe.

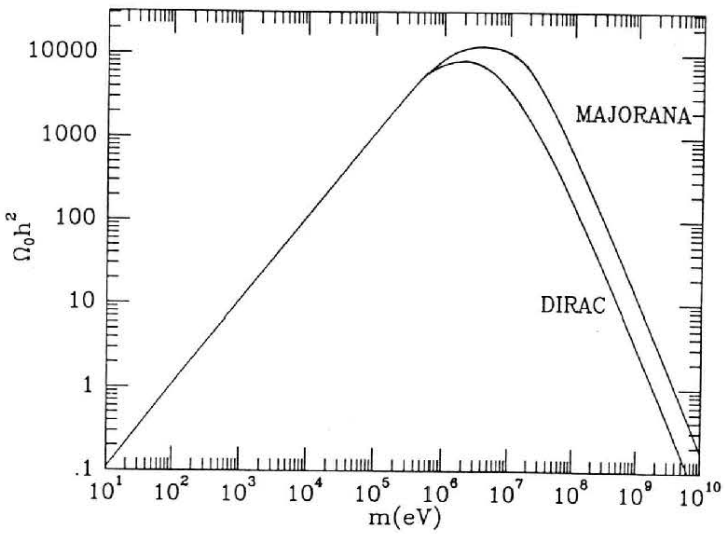

Figure 1.1: The contribution of neutrino mass to the relative density of the universe, where a value of unity is desired for a flat universe. Dirac and Majorana are two neutrino descriptions, outlined in section 1.3.1 (Taken from Kim and Pevsner, 1993, figure 14.1)

1.3 Neutrino Physics

The standard model predicts the neutrino to be a spin 1/2, neutral and massless particle. The (anti)neutrino has a lepton number of (-)1, a quantity which is expected to be conserved in its interactions. The two theoretical descriptions of the neutrino are now outlined, followed by an outline of their interactions with matter and their experimental sources.

1.3.1 Dirac and Majorana Neutrinos

The neutrino can be successfully described by two different models. The first of which is a Dirac neutrino, where the neutrino exists in a negative, or left handed, helicity state and the antineutrino exists in a positive, right handed, helicity state. Right handed neutrinos and left handed antineutrinos are not observed. Dirac neutrinos will conserve lepton number. The quarks and charged leptons are Dirac particles.

The alternative model is the Majorana model, originally postulated for neutrons by Majorana (1937). The Majorana neutrino is its own antiparticle; they are in fact just opposite helicity states. This description leads to

interactions in which lepton number is not conserved, as the number would depend on which helicity state is involved, not whether it is a neutrino or antineutrino.

In order to distinguish between the existence of the Dirac or Majorana neutrino, an experiment needs to utilise an helicity flip, allowing the emitted neutrino to reinteract, which will only occur for Majorana neutrinos. Neutrinoless double beta decay is one possibility, where a nucleus decays to produce two electrons and no neutrinos. Further, the sum of the energy of the two electrons will be fixed, as there are no neutrinos to carry off energy. The two interactions are:

$$n \rightarrow p + e^- + \overline{\nu} \tag{1.6}$$

then the Majorana antineutrino undergoes an helicity flip allowing it to reinteract as a neutrino:

$$\nu + n \rightarrow e^- + p \tag{1.7}$$

The overall reaction violates lepton number conservation by two units. If this reaction is observed it will provide evidence for massive Majorana neutrinos. Further, the probability of the required helicity flip is proportional to the mass of the neutrino, allowing the mass of the neutrino to be directly measured. However, this also implies that Majorana and Dirac neutrinos can not be differentiated if the neutrino mass is zero.

Neutrinoless double beta decay is searched for in $^{76}_{32}$Ge, where the half life for the decay has been determined to be greater than 5.6×10^{25} years. The corresponding limit on the average of the three neutrino masses is then less than 0.2 eV, for Majorana neutrinos. This result is from Bandis et al. (1999).

Majorana neutrinos are preferred by theorists as they provide an explanation, see section 1.5.1, for why the neutrino mass is tiny in comparison to the other leptons, (for example, a ν_e of 5 eV would be five orders of magnitude lighter than the electron.) Dirac theory provides no real insight into this inequality. If neutrinos are massive, they are most likely Majorana neutrinos.

1.3.2 Neutrino Interactions

Neutrinos interact and scatter off matter as described by the electroweak theory of the standard model. There are two varieties of neutrino interactions with nucleons, charged current and neutral current. Their Feynman diagrams

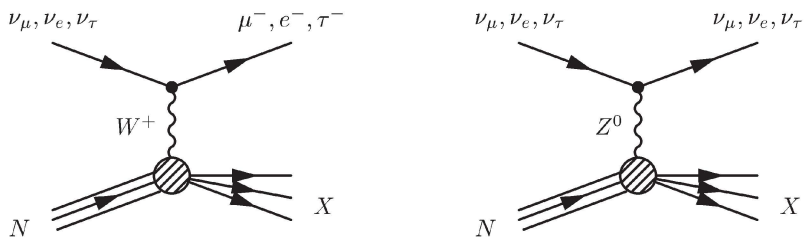

(a) Charged Current (b) Neutral Current

Figure 1.2: Neutrino nucleon interaction Feynman diagrams. Antineutrinos exchange a W^- charged current interactions, and produce positive leptons. X is the hadron shower, which contains the products of the struck nucleus.

are given in figure 1.2. Neutrinos also scatter off electrons and muons, as will be described in section 1.5.3.

The charged current interaction involves the exchange of a W boson between the neutrino and a quark in the target nucleon. Leptons are emitted in accordance with the flavour and lepton number of the incoming neutrino. For example a ν_e will produce an e^-, and $\overline{\nu}_\mu$ a μ^+. These interactions are extremely useful when ascertaining neutrino flux, as the lepton from the top vertex can label each neutrino interaction. This lepton is termed either prompt or leading.

Charged current interactions are divided into three different kinematical regions, deep inelastic scattering (DIS), quasielastic (QE) and resonance (RES). DIS occurs when $|q|^2 \gg m_N^2$, (where q is the four momentum transfered to the nucleon from the lepton), and $E_\nu \gg m_N$. These large exchanges of energy cause the breakup of the nucleon and are characterised by a large hadron shower, X. QE events are so named due to their near elastic nature. The target nucleon remains intact, but charge conservation requires it to change charge by one:

$$\nu_\mu + n \rightarrow p + \mu^- \tag{1.8}$$

The resonance events refer to interactions where a short term resonant state of the target nucleon is created, which later decays. Resonance and quasielas-

tic events are referred to as non-scaling events due to their cross sections not increasing (scaling) with energy, as is the case with DIS events. Further, both tend to have low lepton nucleon exchange energy, defined as:

$$\nu = \frac{q.P}{M} = E - E' \tag{1.9}$$

where P is the momentum of the nucleus of mass M and E and E' are the initial and final lepton energies.

The other category of neutrino interactions is neutral current, where a Z^0 is exchanged, in place of the W. This necessitates the emission of an outgoing neutrino. These events are less useful in neutrino flux measurements, but do however cause a background to the charged current events that must be understood.

The total charged current cross sections for the inclusive reaction of any neutrino of flavour l with nucleon N:

$$\nu_l + N \rightarrow l + X \tag{1.10}$$

producing all possible final hadronic states X are, (Auchincloss et al., 1990):

$$\sigma(\nu) \simeq 0.67 \times 10^{-38}\ (E_\nu/GeV)\ cm^2 \tag{1.11}$$

$$\sigma(\overline{\nu}) \simeq 0.32 \times 10^{-38}\ (E_\nu/GeV)\ cm^2 \tag{1.12}$$

Note that it is very small cross section, and also that there is an energy dependence, such that high energy neutrinos will be easier to detect.

1.3.3 Neutrino Sources

The four main sources of detectable neutrinos are now discussed.

Solar Neutrinos

The central nuclear reaction in the sun is:

$$4p \rightarrow\ {}^4He + 2e^+ + 2\nu_e + 26.7\ MeV \tag{1.13}$$

where the two neutrinos carry away 0.59 MeV. Note the double counting as the energy from the annihilation of the positrons is included in the 26.7 MeV. The number density of neutrinos can be determined from the measured luminosity of the sun, as $N_{\nu_e} = 1.8 \times 10^{38}\ s^{-1}$. This implies a flux of solar neutrinos at Earth of $\phi_{\nu_e} = 6.4 \times 10^{10}\ cm^{-2}s^{-1}$. However, whilst it is reasonably straightforward to predict the flux of neutrinos, their energy spectrum is not yet fully understood. It depends on the internal temperature distribution of the sun, and on the kinematics of the nuclear reactions involved. The best model of this is the standard solar model (SSM), see Bahcall and Ulrich (1988), which has been recently verified by helioseismology, see Ricci et al. (1999).

Atmospheric Neutrinos

Cosmic ray interactions in the atmosphere cause massive showers of particles. Pions produced in these showers can decay to form neutrinos:

$$\pi^{\pm} \rightarrow \mu^{\pm} + \overset{(-)}{\nu}_{\mu} \tag{1.14}$$

and the muon also subsequently decays via:

$$\mu^{\pm} \rightarrow e^{\pm} + \overset{(-)}{\nu}_{\mu} + \overset{(-)}{\nu}_{e} \tag{1.15}$$

The atmosphere represents eleven interaction lengths, and so it is reasonable to assume that the majority of pions and muons decay before reaching the Earth. Thus two is naïvely obtained for the ratio of ν_μ to ν_e hitting the surface of the Earth. Using a ratio is advantageous, as flux model uncertainties are of the order of 30%, whilst common systematics mean the uncertainty on the ratio is just $\sim 5\%$.

Reactor Neutrinos

Nuclear reactors are high intensity isotropic sources of $\overline{\nu}_e$ from the beta decay of fission fragments. The neutrinos produced have energies less than 10 MeV, with an average energy of ~ 3 MeV. The flux of $\overline{\nu}_e$ is known quite well, to an uncertainty of $\sim 2.7\%$ above 2 MeV.

Accelerator Neutrinos

Neutrinos are produced as tertiary particles by accelerators, generally from pion decays. The neutrinos produced have energies from hundreds of MeV to

hundreds of GeV. How neutrino beams are generated for study is expanded on in section 2.4, which describes the CERN neutrino beam.

1.4 Neutrino Oscillations

As mentioned in the Introduction, neutrino oscillations are the most promising method of determining if neutrinos have non zero mass. To derive the (mass dependent) oscillation probability, assume that neutrino mixing exists. This implies that the flavour states of the neutrinos we detect, $|\nu_\alpha\rangle$ where $\alpha = e, \mu, \tau$, only have definite flavour and not definite mass. They are in fact superpositions of the true mass eigenstates $|\nu_i\rangle$. The neutrino flavour state would then be written:

$$|\nu_\alpha\rangle = \sum_i U_{\alpha i} \ |\nu_i\rangle \tag{1.16}$$

where $U_{\alpha i}$ is the 3×3 unitary mixing matrix. Now, time evolve this neutrino state by time t:

$$|\nu_\alpha(t)\rangle = \sum_i e^{i(\vec{p}_i\vec{x} - E_i t)} U_{\alpha i} \, |\nu_i\rangle \tag{1.17}$$

The probability that this neutrino state has oscillated into flavour β at time t is then given by:

$$\begin{aligned} P_{\nu_\alpha \to \nu_\beta} &= |\langle \nu_\beta | \nu_\alpha(t) \rangle|^2 && (1.18) \\ &= |\sum_i e^{i(\vec{p}_i\vec{x} - E_i t)} U_{\alpha i} U^*_{i\beta}|^2 && (1.19) \\ &= \sum_i \sum_j U_{\alpha i} U^*_{\beta i} U^*_{\alpha j} U_{\beta j} \ e^{i(\vec{p}_i - \vec{p}_j)\vec{x}} e^{-i(E_i - E_j)t} && (1.20) \end{aligned}$$

and simplified using $\langle \nu_i | \nu_j \rangle = \delta_{ij}$. E_i can be further simplified, with the assumption that the neutrinos are relativistic, $|\vec{p}| \gg m_i$:

$$E_i = \sqrt{p^2 + m_i^2} \ \approx \ p + \frac{m_i^2}{2p} \ \approx \ p + \frac{m_i^2}{2E} \tag{1.21}$$

where natural units of $c = \hbar = 1$ are being used. Substituting this approximation into equation 1.20, and further assuming that the neutrinos are traveling along the x-axis:

$$P_{\nu_\alpha \to \nu_\beta} = \sum_i \sum_j U_{\alpha i} U^*_{\beta i} U^*_{\alpha j} U_{\beta j} \; e^{-i \frac{\Delta m^2_{ij}}{2E} t} \tag{1.22}$$

where $\Delta m^2_{ij} = m^2_i - m^2_j$ is the difference between the squares of the mass eigenvalues of the two mass eigenstates. Thus oscillations are only possible if non-degenerate mass eigenstates exist. To understand the physical appearance and nature of oscillations, the simplifying assumption of two neutrino mixing, say muon to electron, is insightful. Here the mixing matrix is:

$$U = U^* = \begin{pmatrix} \cos\theta & \sin\theta \\ -\sin\theta & \cos\theta \end{pmatrix} \tag{1.23}$$

where θ is the mixing angle and determines the degree to which the flavour states are mixtures of the mass states. Equation 1.22 then becomes:

$$P_{\nu_\mu \to \nu_e} = \sin^2(2\theta) \; \sin^2\left(\frac{\Delta m^2_{21} t}{4E}\right) \tag{1.24}$$

$$= \sin^2(2\theta) \; \sin^2\left(\frac{\pi L}{L_{osc}}\right) \tag{1.25}$$

Note that $L = ct$ has been used so that the probability is in terms of the distance the neutrino has traveled, and also that the second equation substitutes the oscillation distance L_{osc}, defined below:

$$L_{osc} \equiv \frac{4\pi E}{\Delta m^2_{21}} = \frac{2.48(E/GeV)}{(\Delta m^2_{21}/eV^2)}[km] \tag{1.26}$$

This distance is the length at which the oscillation probability returns to zero. The oscillation is in fact a cycle, $\nu_\mu \rightsquigarrow \nu_e \rightsquigarrow \nu_\mu$. When the length is much larger than L_{osc}, the $sin^2(\pi L/L_{osc})$ term averages to a half and the oscillatory behaviour is absent, leaving the probability to revert to that of a classical transition. At lengths close to L_{osc}, oscillatory behaviour is most prominent.

The search for neutrino oscillations is now defined in a phase space of Δm^2 and $sin^2(2\theta)$. The phase space probed is determined by the energy of the neutrinos in an experiment and the distance from the source to the detector. Observing oscillations for a given energy neutrino at a set distance will produce a contour in $\Delta m^2 - sin^2(2\theta)$ phase space. It is then the task of the mass models, described in section 1.5.1, to further determine the mass of the neutrinos. For the four neutrino sources of section 1.3.3 the typical L and E values are listed along with the ranges of Δm^2 they imply in table 1.1.

Neutrino Source	$L(m)$	$E(MeV)$	$\Delta m^2(eV^2)$
Solar	10^{11}	0.1 - 10	10^{-12} - 10^{-10}
Atmospheric	10^4 - 10^7	10^2 - 10^3	10^{-5} - 0.1
Reactor	10 - 10^3	1 - 10	10^{-3} - 1
Accelerator	10^2 - 10^3	10^3 - 10^5	0.1 - 10^2

Table 1.1: Ranges of Δm^2 applicable to the four neutrino sources.

1.5 The Neutrino Mass Situation

Much theoretical and experimental research has already been undertaken to understand neutrino mass. A brief description of the main theoretical model for neutrino mass will be given, along with limits on the mass of each flavour of neutrinos from direct measurements. Neutrino oscillation experiments, past, current and future, are then outlined including a plot of set and expected limits on the $\Delta m^2 - sin^2(2\theta)$ phase space, as well as currently allowed regions.

1.5.1 The See-Saw Mechanism

The see-saw mechanism, (detailed in M. Gell-Mann and Slansky (1979)) is one model which proposes why the neutrino mass is so tiny. Consider a left handed and right handed neutrino of one generation, the mass matrix $\mathcal{M}$ can be written as:

$$\mathcal{M} = \begin{pmatrix} 0 & m \\ m & M \end{pmatrix} \tag{1.27}$$

where m is the Dirac coupling and M is the Majorana coupling, and there is no left handed Majorana coupling. The mass values of the two neutrinos can be extracted as the eigenvalues of this matrix, giving:

$$m_1 \simeq \frac{m^2}{M} \quad \text{and} \quad m_2 \simeq M \tag{1.28}$$

assuming $M \gg m$. This can be interpreted as the left handed neutrino, which interacts, as predominantly the light m_1 neutrino, partnered by the heavy right handed neutrino, predominantly m_2, which is not known to interact. The two neutrinos scale according to M, (heavy neutrino gets heavier and the light gets lighter), whilst their product remains equal to m^2. This is

the see-saw mechanism. A small neutrino mass is obtained for the known left handed neutrino due to the high mass M of the right handed neutrino. M is suggested to be at the grand unified theory (GUT) scale, as large as 10^{16} GeV. Values of the GUT scale are discussed in Tu and Xue (1984).

To expand this to all three generations, a six by six mass matrix must be solved, giving the eigenvalues:

$$m(\nu_i) \simeq \frac{m_{f,i}^2}{M} \tag{1.29}$$

where $m_{f,i} = (m_u, m_c, m_t)$ or (m_e, m_μ, m_τ). That is to say that the neutrino masses scale with the square of either the lepton or quark masses. This is assuming a constant M for each generation, which may not be the case. Scaling with $m_{f,i}^2$ is referred to as the quadratic see-saw.

1.5.2 Direct Mass Measurements

The mass of the electron neutrino is directly measured in the tritium decay:

$$H^3 \rightarrow He^3 + e^- + \overline{\nu}_e \tag{1.30}$$

The end point of the energy spectrum of emitted electrons, E_e, is compared with the energy gained in the transition from H^3 to He^3, $E_o = 18.6$ keV. This difference is a measure of the neutrino mass. Tritium decay is chosen due to its low E_o as event production at the end of the spectrum depends on $(E_o\text{-}E_e/E_o)^3$. The results of the Mainz experiment, see Weinheimer et al. (1999), give an upper limit on $m(\nu_e)$ at 2.8 eV, however tritium decay experiments have always measured a negative mass for ν_e, (i.e. $E_e > E_o$), due to an excess of events towards the end point.

The electron neutrino mass has also been inferred from the arrival time of neutrinos from supernova 1987a. In a supernova, neutrinos are modeled as being emitted in a 10 ms burst. However, massive neutrinos will have an arrival time proportional to their energy. Depending on the model of supernova neutrino emission used, the ν_e mass limit has been placed between 6 and 30 eV, see Hirata et al. (1987); Bionta et al. (1987).

The muon neutrino mass is determined by measuring the momentum of the emitted muon from a pion decay at rest:

$$\pi^+ \rightarrow \mu^+ + \nu_\mu \tag{1.31}$$

An experiment at the Paul Scherrer Institute set a limit on the ν_μ mass at 0.17 MeV, refer to Assamagan et al. (1996). The measurement is limited by uncertainty in the pion mass.

The tau neutrino mass is measured in the decay of the tau to five pions and a ν_τ. This decay has been measured by ALEPH, and a limit set near 18 MeV, (Cerutti, 1999).

The direct mass measurements arise from the kinematics of weak decays and are in general difficult experimentally. They rely heavily on the resolution of energy measurement and the knowledge of atomic effects on the decay products. With the exception of perhaps the mass of the electron neutrino, their results provide little information, particularly not to Cosmology.

1.5.3 Oscillation Search Results

The major constraint in the detection of neutrinos is their low cross section. Massive detectors are required in order to obtain enough interactions to see oscillation phenomena. A great number of experiments have searched for neutrino oscillations, ranging across all of the sources mentioned in section 1.3.3. The results of these past experiments are now summarised, preceded by a short description of their apparatus and procedure. Further information on the experiments can be found from the Neutrino Oscillation Industry webpage, (Goodman, 2000).

Solar Neutrinos

Experiments investigating solar neutrino fluxes must be certain of the origin of the neutrinos interacting in their detectors. Kamiokande, and its larger replacement SuperKamiokande, are water Čerenkov detectors, featuring a massive tank of water viewed by photomultiplier tubes, see Fukuda et al. (1996, 1998b). They identify solar neutrinos from their scattering off electrons:

$$\nu_e + e^- \rightarrow \nu_e + e^- \tag{1.32}$$

The energy and direction of the scattered electrons is used to ensure only solar neutrinos are counted. These neutrinos are selected on the basis of their angle with respect to the solar direction, whilst a continuous angular background of non solar neutrinos must be subtracted.

Homestake, the first experiment to detect solar neutrinos, used a massive chlorine filled tank to detect solar neutrinos by looking for traces of ^{37}Ar, the product of the interaction:

$$\nu_e + {}^{37}Cl \rightarrow e^- + {}^{37}Ar \tag{1.33}$$

whilst SAGE, see Abdurashitov (1994), and GALLEX, see Hampel et al. (1998), look for neutrino capture in gallium:

$$\nu_e + {}^{71}Ga \rightarrow e^- + {}^{71}Ge \tag{1.34}$$

A ν_e flux lower than the expected flux calculated in section 1.3.3, was observed by SAGE, GALLEX, Kamiokande and other experiments. If the detectors and background events are well understood, and if the neutrino emission models of the sun are correct, then these measurements imply oscillations.

There are a number of ways of interpreting these oscillations. The first is that the oscillations occur in vacuum, (between the Sun and the Earth), implying a $\Delta m^2 \simeq 10^{-10} - 10^{-11}\ eV^2$.

A second interpretation considers matter enhanced oscillations, where neutrinos traveling through matter would experience a refractive index n, analogous to light. This idea was developed by Wolfenstein (1978) and affects the evolution of neutrinos with time, equation 1.17, scaling $i\vec{p}\vec{x}$ by n. The refractive index is the same for all neutrinos except ν_e, which can scatter off electrons in the additional charge exchange channel. Thus the ν_e experiences an extra term in its energy, $\sqrt{2}G_F N_e$, (where N_e is the number density of electrons and G_F is the Fermi coupling constant). This can be reinterpreted as an alteration of its mass squared, which in turn affects the ν_e oscillation probability.

For the case of constant N_e, the equation of neutrino motion is solvable to produce mass eigenvalues, different from the vacuum values derived in section 1.4. The Earth is assumed to have constant N_e. For a variable N_e, like the Sun, these eigenvalues are no longer correct. The adiabatic condition, where N_e is constant over an oscillation length simplifies this case. The altered mass will depend on the N_e that the ν_e is experiencing at any particular location in the sun. Mixing is maximal at a "resonant" value of N_e. This resonant effect, which increases oscillation probability in matter, is called the MSW effect, see Mikheyev and Smirnov (1985).

Under the assumption of matter oscillations, two allowed regions of $\nu_\mu \rightsquigarrow \nu_e$ have been determined using the intersection of the regions from the above mentioned solar neutrino experiments. These two regions are given in figure 1.3. SMA and LMA refer to small and large mixing angle regions.

Atmospheric Neutrinos

The aim of atmospheric neutrino experiments is to measure the ratio of ν_μ to ν_e and compare this to the naïve expectation value of two. Neutrinos are identified via their quasielastic interactions, equation 1.8. The outgoing muons from the interactions are flagged by a single penetrating track in the event, and the electrons by an electromagnetic shower. The measured ratio of muons to electrons can then be compared to expectation.

The Kamiokande experiments are also capable of measuring atmospheric neutrinos, see Fukuda et al. (1994, 1998a). These experiments have shown a decrease in the expected ratio of two, and further, this has been shown to be due to a deficit in the number of ν_μ. This can be interpreted as $\nu_\mu \rightsquigarrow \nu_\tau$ or $\nu_\mu \rightsquigarrow \nu_e$ oscillations. Their allowed region for $\nu_\mu \rightsquigarrow \nu_e$ oscillations is given in figure 1.3. However, further measurements by Super Kamiokande, which measure the zenith angle distribution of ν_e and ν_μ separately show that the ν_μ deficit is not the result of $\nu_\mu \rightsquigarrow \nu_e$ oscillations. It is also ruled out by the reactor experiments listed below.

Other atmospheric neutrino experiments, such as NUSEX, FREJUS and SOUDAN2, which use segmented calorimeters, also obtained ratios less than, or slightly less than expectation, but not as conclusively as Kamiokande.

Reactor Neutrinos

Reactors produce a well understood source of $\overline{\nu}_e$, see section 1.3.3. A neutrino detector placed near a reactor allows a disappearance search, $\overline{\nu}_e \rightsquigarrow \overline{\nu}_x$ to be undertaken. If oscillations are present, fewer $\overline{\nu}_e$ will be seen than expected, hence disappearance.

Two recent experiments are CHOOZ, see Apollonio et al. (1999), and Palo Verde, Wang (1999). These use gadolinium doped scintillator as their detector material, and are placed around a kilometre from the reactors. They record ~30 neutrinos events a day. These events, the inverse beta decay of equation 1.1, are characterised by a prompt electron signal when it annihilates to produce two photons, and a late photon signal from the neutron being captured in the gadolinium:

$$n + p \rightarrow d + \gamma \tag{1.35}$$

These two experiments see no deficit of $\overline{\nu}_e$ consistent with oscillations, and so can rule out the Kamiokande deficit being caused by $\nu_\mu \rightsquigarrow \nu_e$ oscillations, see figure 1.3. An older reactor experiment Bugey, see Declais et al. (1995), is also shown in figure 1.3. It was a liquid scintillator detector placed within

100 m of its three reactors and only partially ruled out the Kamiokande region.

Accelerator Neutrinos

Neutrino experiments have been carried out for almost three decades at accelerators. The main goals of these experiments were measuring neutrino cross sections, electroweak parameters, structure functions and elements of the Cabibbo Kobayashi Maskawa mixing matrix. Experiments such as CDHS, WA66 at BEBC, CHARM II, E776, E531 and CCFR also investigated neutrino oscillations with their data, but saw no evidence. Early neutrino detectors such as BEBC were bubble chambers. These comprise a superheated liquid, usually hydrogen, under pressure. This caused the liquid to be unstable and to produce bubbles around ions where pressure was released, and so could be used to track charged particles. The number of events collected were in the hundreds to tens of thousands. Bubble chambers were complemented with counter experiments, like CDHS, which were able to record a greater number of events, but with less detail. The limits from CCFR and E776 are included in figure 1.3.

LSND is an accelerator experiment at Los Alamos, first run in 1993. This experiment was designed to search for $\overline{\nu}_\mu \rightsquigarrow \overline{\nu}_e$ oscillations. The experiment searches for $\overline{\nu}_e$ in a beam of $\overline{\nu}_\mu$ arising from the decay at rest of muons, in turn generated by a proton beam impinging on a beam stop. $\nu_\mu \rightsquigarrow \nu_e$ oscillations were later searched for from ν_μ arising from pions that decay in flight. The neutrinos travel 30 m from the beam stop to the detector and have a maximum energy of 52.8 MeV. The experiment was designed to detect $\overline{\nu}_e$ with the following interaction:

$$\overline{\nu}_e + p \rightarrow e^+ + n \tag{1.36}$$

followed by the capture of the exiting neutron:

$$n + p \rightarrow d + \gamma(2.2MeV) \tag{1.37}$$

The trigger of a $\overline{\nu}_e$ event is then a positron followed by a 2.2 MeV photon correlating in position and time. The positron detection was achieved with a mineral oil scintillant mixture, in which prompt positrons produced Čerenekov light, measured by arrays of photomultiplier tubes. All sides of the detector except the bottom were covered with a veto shield, to flag incoming charged particles from the beam or cosmic rays. Between the detector

and beam stop there is also the equivalent of 9 m of steel to shield out non neutrino beam particles.

LSND sees more $\overline{\nu}_e$ events than expected from known backgrounds, (additional detail on this is given in section 2.3), and has determined a region in phase space where $\overline{\nu}_\mu \rightsquigarrow \overline{\nu}_e$ are claimed to exist, see Athanassopoulos et al. (1996). The favoured oscillation parameters of LSND are $\Delta m^2 = 19\text{eV}^2$ and $sin^2(2\theta) = 0.006$. The limits of $\nu_\mu \rightsquigarrow \nu_e$ and $\overline{\nu}_\mu \rightsquigarrow \overline{\nu}_e$ are expected to be the same due to unitarity, which implies that processes and rates for particles and antiparticles are equal.

The KARMEN experiment at Rutherford Labs is a very similar design to LSND and hopes to investigate the entire LSND oscillation signal. KARMEN is also a scintillator based detector, looking for $\overline{\nu}_e$ from a $\overline{\nu}_\mu$ beam. KARMEN as yet sees no excess of $\overline{\nu}_e$ events and so partially excludes the LSND allowed region, see KARMEN Collaboration (1999). Both the KARMEN and LSND results can be seen in figure 1.3.

1.5.4 The Ongoing Search

New experiments are being designed, in order to further refine the allowed phase space for oscillations. It is important that precise data is taken and that all positive signals are confirmed, preferably using neutrinos from a manmade, and hence well understood, source.

Two new solar neutrino experiments are the Sudbury Neutrino Observatory(SNO), see Chen (1985), which uses a thousand ton heavy water detector, and BOREXINO, (Maneira, 1999), a hundred ton liquid scintillator detector. The solar neutrino result, for large mixing angles is due to be investigated by KamLAND, a reactor experiment outlined in Suzuki (1994). KamLAND comprises a thousand ton of scintillating isoparaffin oil, which will measure neutrinos from five different reactors in Japan, at distances ranging between 150 and 200 km. An event rate of two per day is expected. KamLAND features a remarkable increase in L from early reactor experiments, which accounts for its ability to search the low mass region of solar neutrino oscillations, see figure 1.3.

The atmospheric neutrino problem will be investigated using long baseline accelerator experiments. K2K, see Nishikawa (1992), uses a beam of neutrinos created at KEK, and sent 250 km to SuperKamiokande, which has the benefit of using the same detector that has already shown the deficit in atmospheric ν_μ. MINOS, proposed in MINOS Collaboration (1998), will have a neutrino beam generated at FermiLab traversing 730 km to a purpose built detector. The phase space expected to be covered is shown by the labeled dashed lines in figure 1.3. CERN has a long baseline experiment, sending a

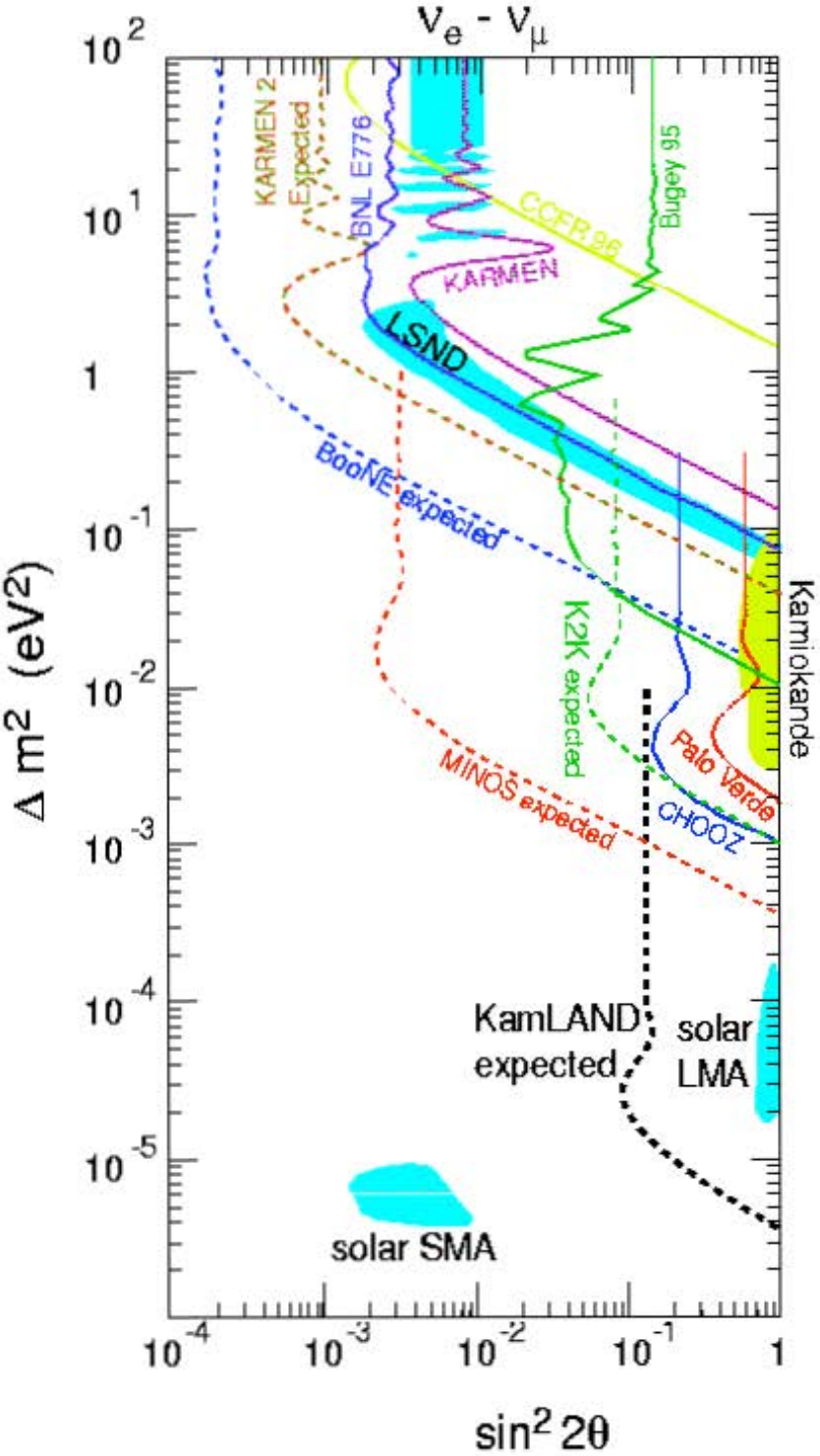

Figure 1.3: $\nu_\mu \leftrightarrow \nu_e$ phase space. Allowed regions are shaded, excluded regions are to the right of solid lines and expected search regions to the right of dotted lines. (Taken from DiLella, 1999)

beam to Gran Sasso, see Acquistapace et al. (1998). This experiment will have a similar sensitivity to MINOS.

The LSND region must also be ratified. This is the task of the continuing KARMEN experiment and the new BOONE experiment. BOONE, proposed in Church et al. (1997), features a ν_μ beam created by 8 GeV protons at FermiLab. The beam travels 500 m before reaching the detector, a sphere of mineral oil, surrounded by photomultiplier tubes. Based on the oscillation parameters of LSND, BOONE should see almost twice the number of ν_e than if no oscillations were present.

However, this is not the end of the story. CERN has a short baseline accelerator experiments of its own, NOMAD, which can check the high δm^2 region of the LSND result. This search at NOMAD is now presented.

Chapter 2

The NOMAD Experiment

2.1 Introduction

The NOMAD (Neutrino Oscillation MAgnetic Detector) experiment is situated at CERN (the European Laboratory for Particle Physics) in Geneva, Switzerland. It was proposed by Astier et al. (1991), with construction being completed in 1995, and data collected from 1995 to the end of 1998. The primary purpose of the experiment is to search for muon neutrino to tau neutrino oscillations.

NOMAD combines the benefits of counter experiments, high statistics, and bubble chambers, high spatial resolution. As such, it is capable of measuring and identifying interaction products, to classify the neutrinos interacting. Further, the large sample of interactions recorded allows a range of measurements to be made, additional to the muon neutrino to tau neutrino oscillation search. In particular, a second oscillation search, from muon neutrino to electron neutrino, has been undertaken.

NOMAD has a sister experiment, situated just upstream in the same beamline, named CHORUS (CERN Hybrid Oscillation Research apparatUS), see Eskut et al. (1997). The experiments were commissioned together to allow confirmation of potential oscillation signals. The two experiments undertake the oscillation search in different ways. CHORUS utilises its high spatial resolution to label tau neutrino interactions, whilst the NOMAD search is based on kinematic criteria.

The sensitivity of NOMAD in oscillation searches is in the cosmologically relevant mass range, $\delta m^2 > 1$ (eV/c^2)^2. The mixing angle reached is expected to be over an order of magnitude smaller than $\sin^2 2\theta < 5 \times 10^{-3}$ at high δm^2, the best limit when NOMAD was proposed, set by the E531 Collaboration (1986).

Numerous requirements are made on any detector undertaking an oscillation search, depending on the type of search involved. To understand the requirements of the detector design, a brief outline of the NOMAD analysis procedure that dictates it, will be given. The detector description will ensue, outlining where and how these requirements are implemented.

2.2 Oscillation Searches

In general there are two types of neutrino oscillation experiments, appearance and disappearance. These feature a beam of neutrinos, be it from the sun, the atmosphere, a reactor or an accelerator, and one or more detectors, to measure the constituents of the beam after traversing a certain distance. An appearance search involves detecting a discernible increase in neutrinos of a given species from the number expected in the beam, which may well be zero. A disappearance search implies looking for a deficit of neutrinos in the beam compared to expectation. The searches in NOMAD are appearance searches, and are briefly detailed below.

2.2.1 Muon Neutrino to Tau Neutrino

As there is no appreciable source of tau neutrinos in the neutrino beam, any detected can be assumed to have arisen from oscillations. Thus the design of NOMAD must accommodate the detection of ν_τ charged current interactions. These produce τ^-, which subsequently decay. It is these decays that are searched for, as indications of neutrino oscillations. NOMAD can search all the main tau decay channels, including $\tau^- \to \nu_\tau \overline{\nu}_e e^-$, $\tau^- \to \nu_\tau \overline{\nu}_\mu \mu^-$, $\tau^- \to \nu_\tau \pi^- \pi^0$ and $\tau^- \to \nu_\tau \pi^- \pi^+ \pi^-$, however the main channel is the electronic decay.

The decays are identified with kinematic criteria. All the channels involve the production of a new tau neutrino, that will not be detected. A tau decay will therefore leave an event with a momentum imbalance, most easily discernible in the plane transverse to the beam. A quantity p_T^{miss} is defined as the momentum missing in the transverse plane. Its value is determined for each neutrino interaction, and then selections can be made based on its direction and magnitude, to group tau decay candidate events.

Difficulties arise when p_T^{miss} is faked by other (reducible) sources. Firstly, neutral hadrons can also go undetected, creating missing momentum. Secondly, poor resolution, leading to bad track reconstruction and erroneous energy sum, can cause spurious missing momentum. These factors must be taken into account in both detector design and afterwards in the analysis

procedure.

A further requirement of the search is that of electron and muon identification, which is necessary for separating true $\tau \rightarrow e$ or $\tau \rightarrow \mu$ decays from neutral current interactions, (this requirement reappears in the search for electron neutrino oscillations).

For details of the $\nu_\mu \rightsquigarrow \nu_\tau$ analysis and its results refer to Altegoer et al. (1998b) and Astier et al. (1999). Also NOMAD can reinterpret its tau results as electron neutrino to tau neutrino oscillations, due to the appreciable component of ν_e in the beam. This analysis appears in Astier et al. (2000).

2.2.2 Muon Neutrino to Electron Neutrino

The electron neutrino oscillation search, whilst still an appearance search, is different from the tau neutrino search as there is an appreciable background of electron neutrinos in the beam, above which those from oscillations must be searched for. The process involves two bodies of work, a beam prediction and a beam measurement. The prediction and measurement are then compared for discrepancies in their spectra that might be attributed to oscillations. Thus the main requirement for the search is good event classification, in particular electron and muon identification, coinciding with some of the needs of the primary tau analysis. This search is the subject of this thesis.

2.3 NOMAD as a check on LSND

As stated in chapter 1, NOMAD is capable of exploring the high δm^2 region where LSND claims to see evidence for originally $\overline{\nu}_\mu \rightsquigarrow \overline{\nu}_e$ and then also $\nu_\mu \rightsquigarrow \nu_e$ oscillations. The LSND beam is around 40 MeV, much lower than the 24 GeV beam of NOMAD, allowing LSND to search much lower mass ranges, (as explained in section 1.4 and particularly table 1.1, which compares beam distances and energies with δm^2 ranges). The strength of NOMAD is its higher statistics due to a far greater beam flux than LSND. However the percentage of electron neutrinos in the beam is over ten times higher in NOMAD and so must be well understood before subtracting to give the oscillation signal. NOMAD also has backgrounds from misidentified ν_μ events. LSND has substantial backgrounds from cosmic rays as well as beam events and coincidental events that fool the neutrino trigger. NOMAD should do as well as LSND at retrieving the true number of signal ν_e events from the data, the higher statistics of NOMAD then allowing it to reach smaller mixing angles.

2.4 The Neutrino Beam

The West Area Neutrino Facility (WANF) was the focal point of the CERN neutrino physics programme. The WANF has been operational since 1976, shortly after the opening of the Super Proton Synchrotron (SPS). Since then, the WANF has been supplying neutrino beams to west area experiments continuously. NOMAD and CHORUS are the latest experiments to be served by the WANF. Originally, the WANF operated in two modes, wide and narrow band beams, referring to the neutrino energy spread. The WANF was refurbished in 1992-3 for NOMAD and CHORUS, in order to provide a higher beam intensity and a harder spectrum, that was hoped to be more conducive to a ν_τ appearance search. A complete realignment of the beamline was also undertaken, which improved the ν_μ yield per proton by 8%, (Casagrande et al., 1996). Further details on the beamline and its upgrade are found in Acquistapace et al. (1995).

Future, long baseline, neutrino beams at CERN, see for example Acquistapace et al. (1998), will require a considerably downward sloping beam, not possible in the WANF. So, as no further short baseline experiments are foreseen, NOMAD and CHORUS are the last experiments to use the WANF.

The layout of the WANF, after optimisation for NOMAD, is shown in figure 2.1. The individual beamline components, along with the primary proton beam, will be described in the following sections. Descriptions of the beam cycle, neutrino production, expected fluxes and beam simulations are also given.

2.4.1 Proton Acceleration and Beam Cycle

The neutrino beam is a tertiary beam, the first step in its production is the acceleration of the primary proton beam. This beam begins in the duoplasmatron, a 100 keV proton source, (hydrogen ions). Acceleration is then provided by the Linac2, an Alvarez 50 MeV linear accelerator. These two systems produce 1 Hz pulses of durations from 20 to 150 μs. The protons are then accelerated to 1 GeV by the proton synchrotron booster, and passed to the Proton Synchrotron (PS). The PS and the SPS both have a coincident 14.4 s cycle. The SPS is 6.9 km in circumference with the protons cycling every 23 μs. The SPS accelerates protons up to 450 GeV, to feed experiments in the west and north areas of CERN.

The SPS provides two extractions (spills) of protons to the WANF per 14.4 s cycle. Each spill is 6 ms, separated by 2.7 s. The typical spill contains 10^{13} protons. In the short, 2 s gap between the two spills, (the so-called "flat top", due to the proton energy in the SPS plataeuing at 450 GeV), a

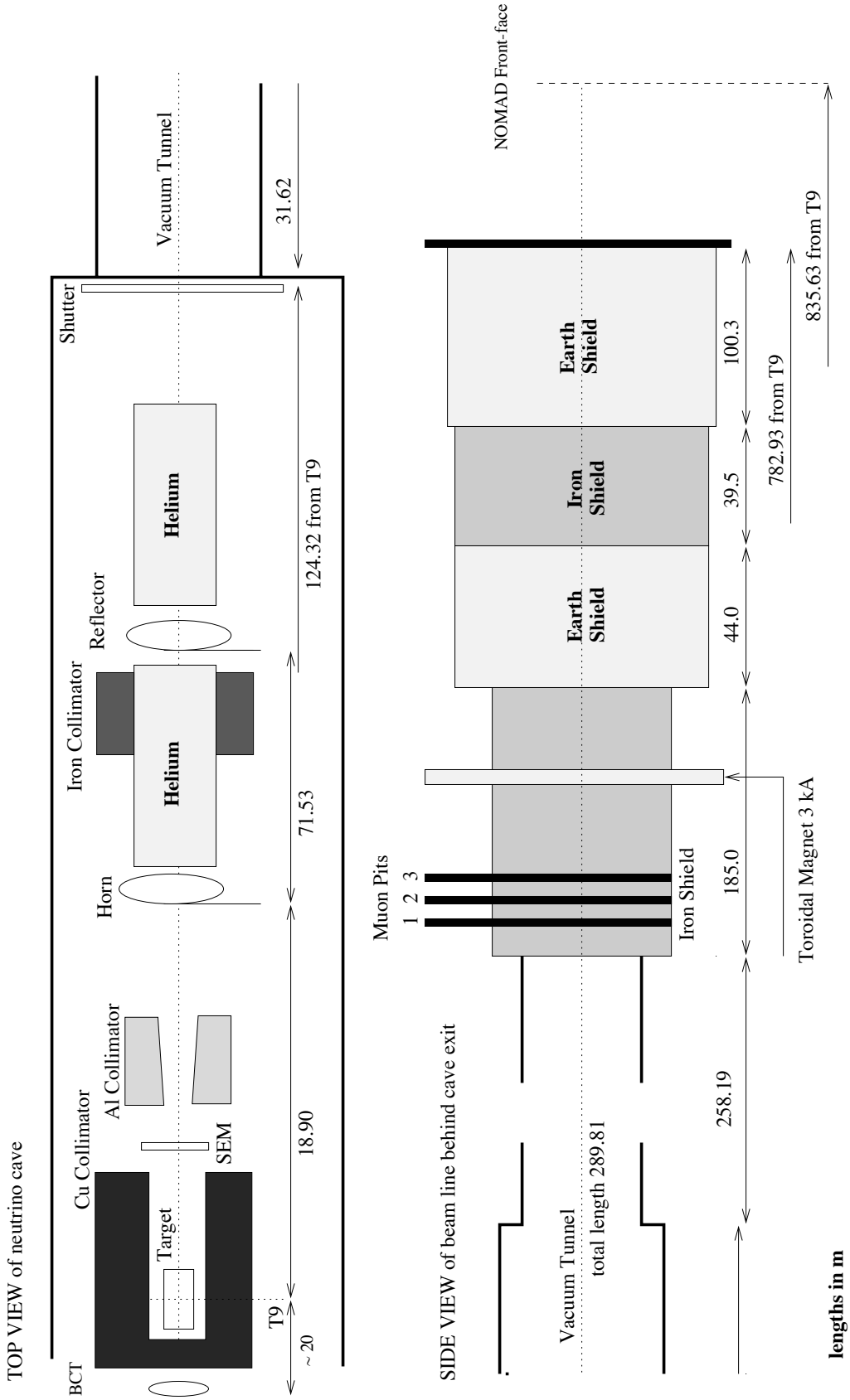

Figure 2.1: Layout of the WANF optimised for NOMAD. Not drawn to scale. (Taken from Altegoer et al., 1998a)

muon beam is sent into the west area. These muons are used by NOMAD for calibration purposes as explained later in this chapter. The SPS cycle is shown schematically in figure 2.2.

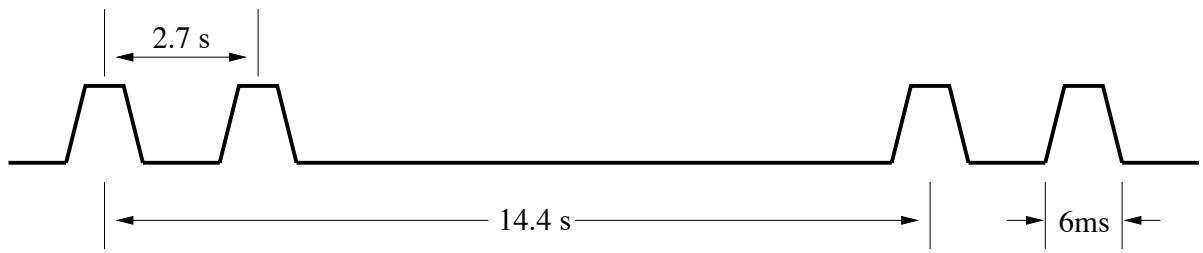

Figure 2.2: Cycle of the SPS showing the two neutrino spills separated by the muon flat top. Not drawn to scale.

2.4.2 Beam Monitoring

Monitoring of the beam provides important feedback for steering, focusing and safety. The WANF beam monitors include:

- **Beam Current Transformers** BCTs are used to measure the proton flux incident on the T9 target. One is placed just after the protons are extracted from the SPS, the other is placed just before the target. They are used to generate the POT (protons on target), which is used as a global normalisation.

- **Miniscans** To aid in steering and focusing of the primary proton beam, horizontal and vertical miniscans are placed in front of the T9 target. These consist of a wire stepping across a range, covering the target, from 4 to -4 mm. These scans are essential for determining the fraction of protons that miss the target.

- **Secondary Emission Monitors** The primary beam is also measured by SEMs grouped into before, TBIU, and after, TBID, the target. The TBIU contains SEMs as split foils to measure the horizontal and vertical asymmetry, without a centre, to measure beam halo, and finally two to measure intensity. The TBID measures halo and intensity.

- **Beam Split foil Grid monitors** Two detectors, BSGH and BSGV, have been placed in front of the entrance to the decay tunnel. Additionally ionisation chambers were added at this position in 1996 and

1998. Both measure meson flux and profiles, and aid in the alignment of the beam.

The entire beam monitoring system, along with status readouts from the beamline elements, (like magnet currents and coolant flow), have been compiled with FactoryLink to produce a simple control programme. This control programme is available to both CHORUS and NOMAD as well as the SPS control room, and also allows for the recording of beam data, in particular POT and beam quality. This data is later used for normalising results to POT and to exclude data taking runs where there were unsuitable beam conditions.

2.4.3 Target

The current WANF uses the T9 target station. Previous incarnations had used both the T9 and T11 target stations. The target itself comprises 11 beryllium rods, 100 mm long and 3 mm in diameter. The rods are spaced by 9 cm air gaps and are cooled by two helium blowers each. The rods are held in place by thin beryllium holders. The target is immediately followed by a copper collimator. An aluminium collimator resides further downstream, beginning 3.55 m from the centre of the target. It allows an average opening angle of 8 mrad.

2.4.4 Neutrino Beam Generation

The collision of the SPS proton beam with the T9 target produces secondary mesons, which then decay to form the neutrino beam. Pions are predominantly produced, an order of magnitude greater than kaon production. The actual ratios of secondaries was measured by the SPY experiment, which is reviewed in chapter 3. The main decays producing muon neutrinos are listed below:

$$\pi^+ \rightarrow \quad \mu^+\nu_\mu \quad \sim 100\% \tag{2.1}$$
$$K^+ \rightarrow \quad \mu^+\nu_\mu \quad \sim 64\% \tag{2.2}$$
$$K^+ \rightarrow \quad \pi^o\pi^+(\rightarrow \mu^+\nu_\mu) \quad \sim 21\% \tag{2.3}$$
$$K_L^0 \rightarrow \quad \pi^\pm\mu^\mp\nu_\mu \quad \sim 27\% \tag{2.4}$$

Also, the decays producing electron neutrinos are:

$$K^+ \rightarrow \quad e^+\nu_e \quad \sim 5\% \tag{2.5}$$
$$K_L^0 \rightarrow \quad \pi^\pm e^\mp \nu_e \quad \sim 39\% \tag{2.6}$$

Electron and muon neutrinos are also produced by muons in the beam, which may in turn have come from earlier pion and kaon decays:

$$\mu^+ \rightarrow e^+\nu_e\overline{\nu}_\mu \quad \sim 100\% \tag{2.7}$$

Only the positive decays are shown. The number following the decay equation is its approximate branching ratio.

2.4.5 Focusing and Decay Tunnel

The neutrino beam is focused by converging the secondary mesons before they decay. This is achieved with the horn and reflector. These are toroidal lenses, pulsed with 100 and 120 kA currents respectively, synchronous with the SPS cycle. The horn and reflector are constructed from an inner conductor, the shape of a truncated cone, joined at both ends to the cylindrical outer conductor. The end of the horn, where the inner radius is smallest, is called the neck. In normal running, the current flows with the beam in the inner conductor, and back in the outer conductor, to create a toroidal field around the beam, focusing positive particles and deflecting negatives. The focusing produces a parallel beam with a spread of energies as shown in figure 2.3. It was estimated that the focusing provides an enhancement of ten to the neutrino flux, five by the horn alone.

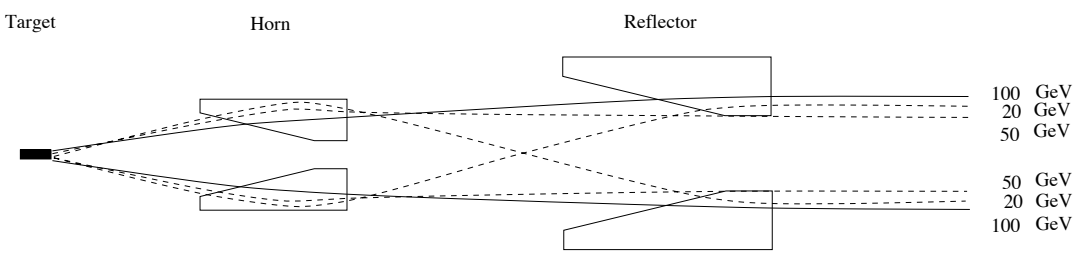

Figure 2.3: The effect of the horn and reflector in focusing particles of varying energy. (Taken from Boyd, 1998)

Tubes filled with helium were added to the beamline, in order to reduced meson interactions, (compared to the number in air). After the focusing, the mesons are allowed to decay in the vacuum tunnel, which has a pressure of 0.5 Torr. This 290 m tunnel is where the majority of the neutrinos are born.

2.4.6 Muon Pits and Shielding

Shielding is placed after the decay tunnel in order to absorb all undecayed mesons and muons, to ensure that only neutrinos reach the detector. Additionally, there is a 3 kA toroidal magnet designed to deflect the muons away from the beam axis. The shielding is both iron and earth. Despite the shielding and magnet, a veto is still required in front of NOMAD to remove the remaining non neutrino particles, see section 2.5.2.

At the beginning of the shielding, there are eight muon pits, the first three of which were used during NOMAD running. These pits contain arrays of silicon detectors for measurement of the muon flux. As the majority of muons traversing the pits arise from the same meson decays that produce the neutrinos, the pits provide an excellent, independent monitoring of the neutrino beam, and aid with its steering and flux measurement. The pits are placed behind increasing amounts of iron, providing a rudimentary energy distribution of the beam, as only the high energy muons will reach the second and third pits. Data from the muon pits is used in comparison with Monte Carlo simulations of the beam in section 5.4.

2.4.7 Expected Beam

The expected flux of ν_μ along with the contamination of $\overline{\nu}_\mu$, ν_e and $\overline{\nu}_e$ in the beam is graphed in figure 2.4. This prediction of the beam was based on NUBEAM 4.00, the first stable beam simulation programme for NOMAD. Many calculations pertaining to the beam were made from version 4.00, as well as forming the basis of the Monte Carlo event generator, described in section 2.7. The development of NUBEAM is detailed in chapter 5. Other, more quantitative descriptions of the expected beam are also left for chapter 5.

2.5 Detector Description

The design of NOMAD was focused on the tau neutrino oscillation search outlined in section 2.2.1. The detector is shown schematically in figure 2.5 along with the co-ordinate system. The axes are centred in the middle of the first drift chamber. The beam is at an angle of ~ 42 mrad to the z axis, and intercepts the y axis zero in the electromagnetic calorimeter, from below.

The following sections will describe the individual sections of NOMAD, the subdetectors and the magnet, in more detail.

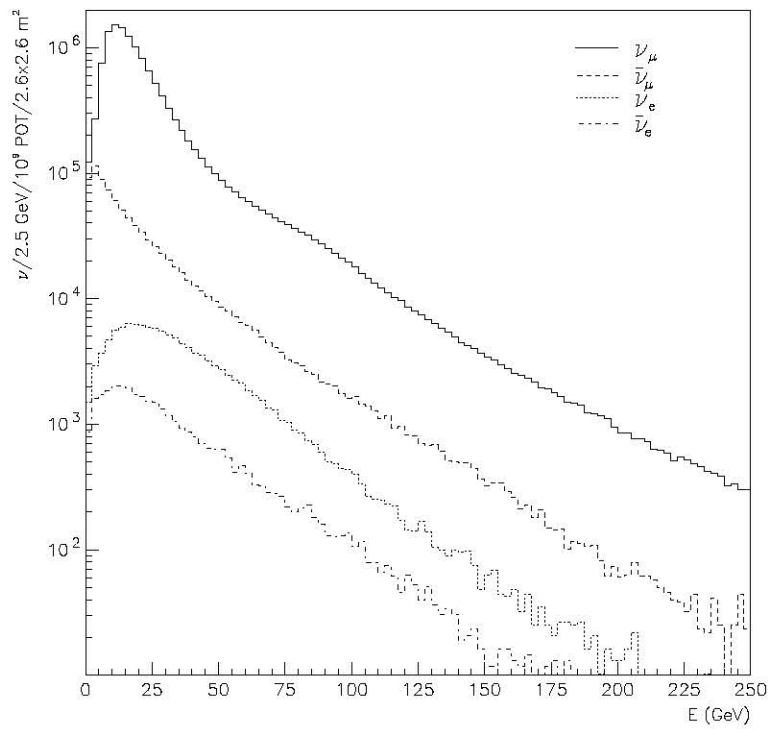

Figure 2.4: Neutrino spectra at NOMAD, showing the degree of contamination in the predominantly ν_μ beam, as predicted by NUBEAM 4.00.

2.5.1 The Magnet

The dipole magnet from the former UA1 experiment, described in Barranco Luque et al. (1980), is reused in NOMAD. The magnet coil is constructed from aluminium, with two supports, called I's, and the casing, C's, made from iron. The magnetic field is 0.4 T, requiring a current of 5713 kA. The field is horizontal, perpendicular to the neutrino beam direction, that is to say along the x axis. The field volume of the magnet is $7.5 \times 3.5 \times 3.5$ m^3. Inside this is the "basket" which supports the drift chamber and other subdetectors. The two supports, which acted as the return yoke in UA1, have been instrumented here as calorimeters.

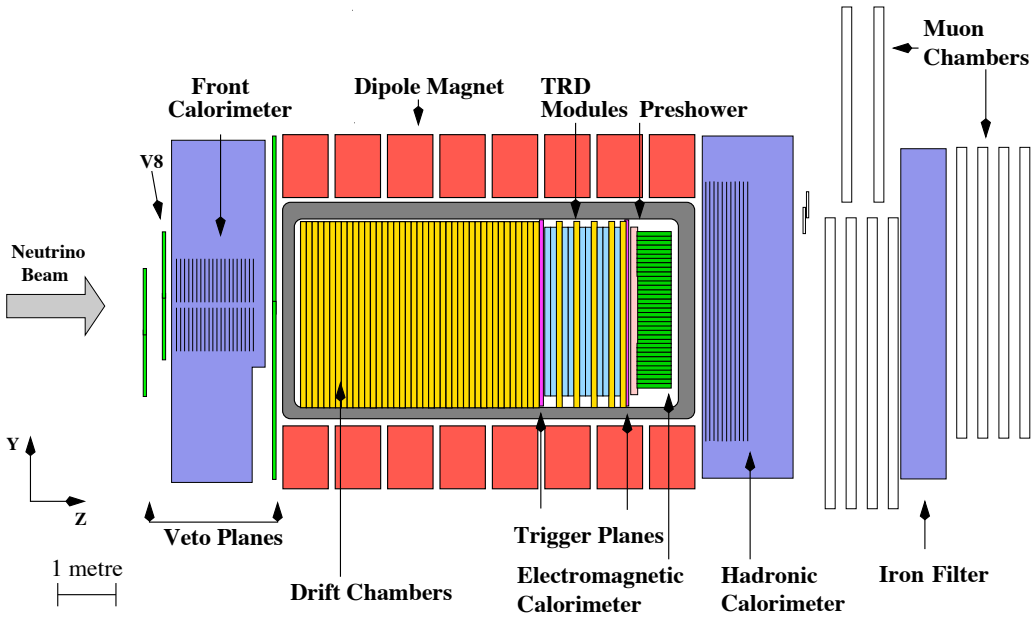

(a) Side view

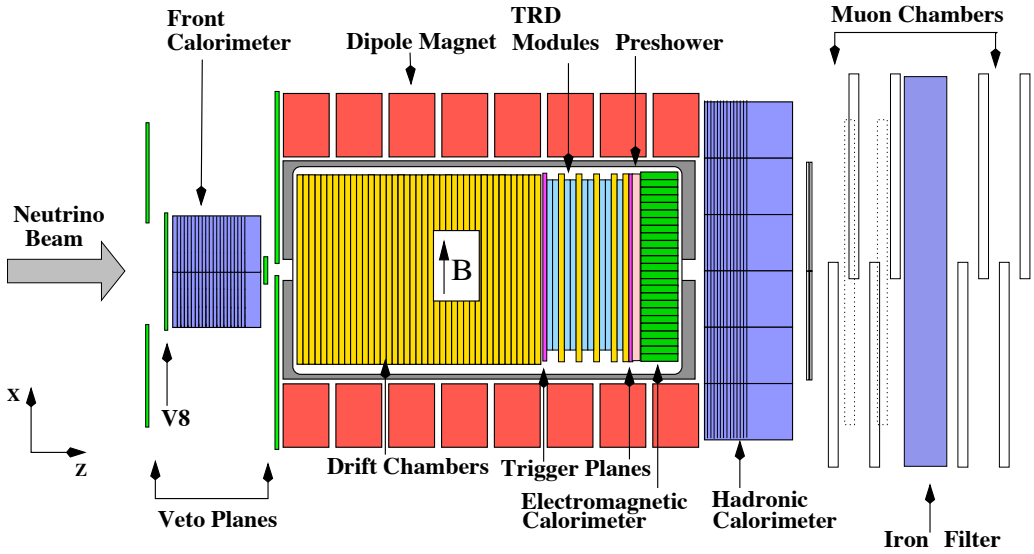

(b) Top view

Figure 2.5: Detector layout (1995-96). (Adapted from Altegoer et al., 1998a)

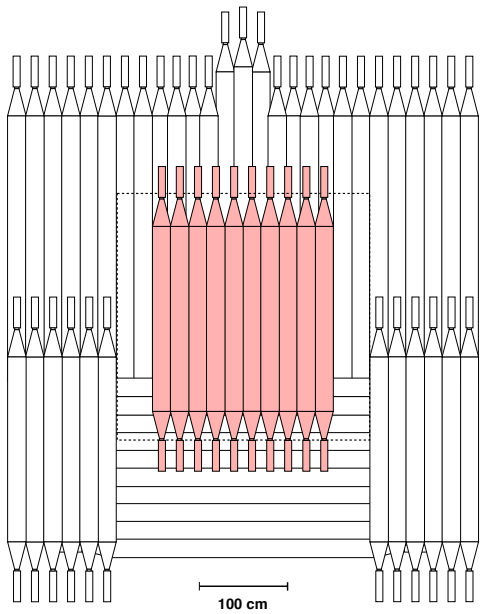

Figure 2.6: Layout of NOMAD veto planes, in banks, as seen by the beam. (Taken from Altegoer et al., 1999)

2.5.2 Veto Counters

The NOMAD veto comprises 59 scintillator counters, covering an area of $5.4 \times 5\,\mathrm{m}^2$. It is the most upstream subdetector and is used to prevent muons traveling in the beam or its halo from causing valid triggers. The veto also rejects other charged particles from interactions upstream of the detector. Nine groups, known as banks, cover the front of NOMAD, including behind the front calorimeter, see figure 2.5. The front view of the system is given in figure 2.6. The dotted square represents the effective drift chamber target area. There are still spurious interactions that occur downstream of the veto, such as those in the magnet coil and the basket support structure of the drift chamber. These are removed during analysis with vertex position selections.

The scintillators used are Nuclear Enterprise NE-110 with dimensions of $2 \times 21 \times (210 \text{ or } 300)\ \mathrm{cm}^3$. The scintillators are read out, at both ends, by Phillips XR-2020 photomultiplier tubes, except for three single ended counters. Stray fields of up to 200 gauss require mu metal shields to be added to the tubes.

Mean timers, further described in Cavestro et al. (1991), are used to ensure that even in the 3 m scintillators, where the transit time difference between different particles causes timing jitter, the output signal is indepen-

dent in time of the position that the particle traversed the counter. The mean timers are fed from LeCroy 4413 discriminators, with thresholds typically set at 25 mV. Each mean timer receives 16 inputs, eight pairs from each of the counters in a bank, and has an output for each of the pairs plus a logical OR of all eight. These outputs are handled by a LeCroy 1876 96 channel FASTBUS TDC module.

To form the veto trigger, the logical OR of all the counters is taken, excluding the three upper right and three upper left counters, that are deemed unnecessary compared to the dead time their inclusion would cause. Triggers in the front calorimeter use only veto bank 8, which is directly in front of it, see figure 2.5 and figure 2.6 where bank 8 is shaded.

The efficiency of the veto in rejecting charged particles has remained stable throughout running at 96-97%. The contribution to the overall dead time of the experiment from the veto, averaged over the two neutrino spills, is around 4%. More details of the veto system are available from Altegoer et al. (1999).

2.5.3 Forward Calorimeter

The front support of the magnet, the I, has been instrumented to form the forward calorimeter (FCAL) creating a massive active target. This subdetector was designed with the aim of investigating multi muon neutrino events and neutral heavy particles.

The front I has 23 4.9 cm iron plates, separated by 1.8 cm air gaps. The first 20 of these gaps have been instrumented with scintillator counters, read out at both ends with photomultiplier tubes. Each scintillator is $175 \times 18.5 \times 0.6$ cm^3 in dimension. Five consecutive counters are bunched together with light guides to form a module, see figure 2.7. Ten modules are then combined vertically, to create an FCAL "stack" of 50 counters. The beam is incident upon an effective instrumented area of 175×190 cm^2. The FCAL is equivalent to five nucleon interaction lengths in depth, the active area alone weighing 17.7 tons.

Calibration of the FCAL proceeded *in situ*. Module to module calibration was achieved using highly relativistic muons traversing the FCAL, as approximations to minimum ionising particles (mip). This produced a mip to ADC count scale. The absolute energy scale, the hadronic energy equivalent of a mip, was found by exploiting the Bjorken y distribution, y_{Bj}, which is well known. As the exiting muon momentum is accurately measured, any mismeasurement of the hadronic energy by the FCAL will appear as distortions in the y_{Bj} distribution. An example of the use of this technique is given in Sakumoto et al. (1990). With these methods, the absolute energy scale

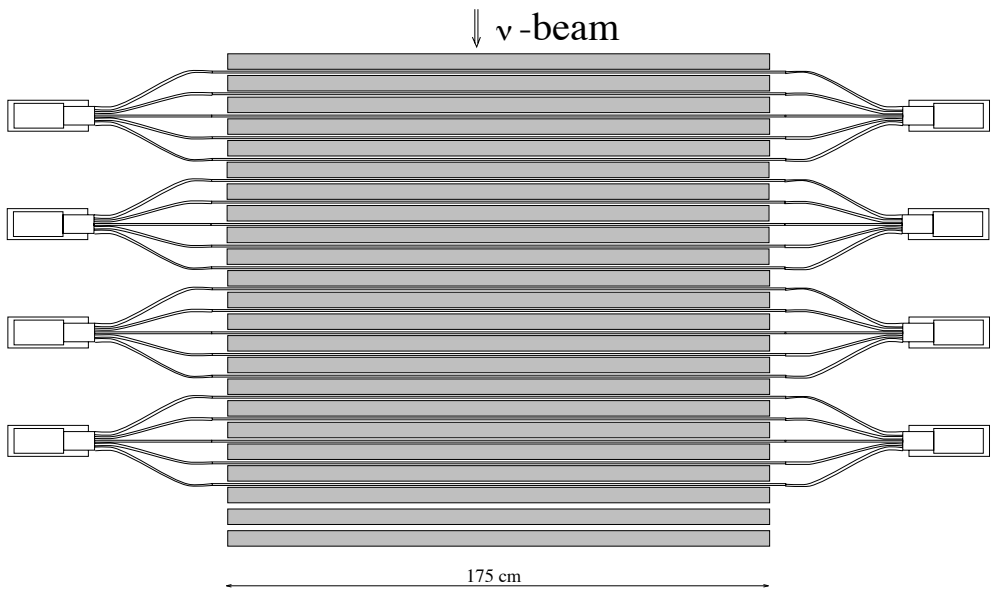

Figure 2.7: Top view of the FCAL, showing the combination of individual counters to form modules. (Taken from Altegoer et al., 1998a)

of the FCAL has been determined to be 2.95 mip/GeV. More information pertaining to the FCAL, and in particular its calibration, can be obtained from Boyd (1998).

2.5.4 Drift Chamber

The drift chamber is the main component of NOMAD. It forms both the target and the central tracker. This caused some conflicts in design as the target must be as heavy as possible to maximise the number of interactions but the tracker must be light to reduce multiple scattering and other degrading effects. The drift chamber used low density low atomic number materials in its construction, thus limiting the distance between consecutive measurements to less than 1% of a radiation length.

The basic design of an individual chamber starts with an aramid fibre panel, utilising a honeycomb structure, covered on both sides with a kevlar epoxy resin skin. Each panel is 1.2 cm thick and has an area of 3×3 m^2. Four such panels make up a chamber, with 0.8 cm gaps between them. These gaps are filled with an argon(40%) ethane(60%) mixture at atmospheric pressure, which must be circulated with a purifier, to remove oxygen and water vapour, as the chambers are not airtight. The three gaps also contain the sense wires,

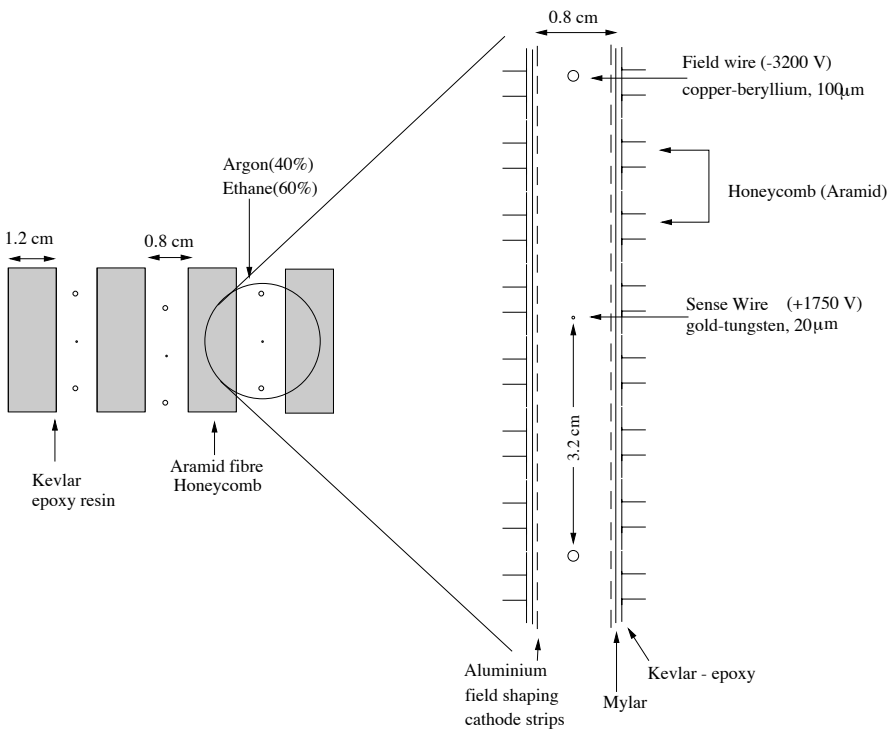

Figure 2.8: A single drift chamber, with detail of a detection gap. (Adapted from Boyd, 1998)

in the following order: +5, 0 and -5 degrees to the magnetic field. These wires are gold plated tungsten, 20 μm in diameter, which are interspersed with copper beryllium field wires, of 100 μm diameter, separated by a distance of $\pm$3.2 cm. The sense wires, 3 m long, are glued in three places to support rods to prevent movement from gravitational and electrostatic forces. The potential wires are at -3200 V, and the sense wires at +1750 V, creating a field of 1 kV/cm, which induces a drift velocity of 50 mm/μs for ionisation electrons.

Aluminium cathode strips are added to provide field shaping. They are run at potentials stepped by 400 V from -3200 V opposite the field wires, to 0 V opposite the sense wire. Further, to compensate for the Lorentz force, the set of strips on one cell wall, is offset by 100 V from the facing set. Each strip is 2.8 mm wide and 12 μm thick. The strips are printed on mylar, at 1.2 mm spacings, which is then glued to the panel. The panels are held apart with spacers opposite melamine inserts in the honeycomb. The layout and construction is summarised in figure 2.8.

There are 49 individual chambers, 11 modules of four, with a further five

in the transition radiation detector, section 2.5.5. During 1995, NOMAD was running whilst under construction, creating periods where there were only four and then eight modules. Further, from 1997 onwards, the first drift chamber module was removed to make space for STAR (Silicon TARget), a prototype silicon neutrino detector. STAR is reported separately in Barichello et al. (1998).

The chambers represent a fiducial mass of 2.7 tons, covering 2.6×2.6 m^2. Each chamber is 0.02 radiation lengths. The individual wires are 97% efficient.

Sense wire signals are sent to preamplifiers, then discriminators and then LeCroy 1876 TDCs. Track separation of 1 mm can be achieved, and the stereo angle of 5° allows 1.5 mm resolution along the wires. The spatial resolution was studied using muons, and for normal incidence was determined to be 150 μm. The resolution of the momentum p is parametrised by:

$$\frac{\sigma_p}{p} \approx \frac{0.05}{\sqrt{L}} \oplus \frac{0.008p}{\sqrt{L^5}} \tag{2.8}$$

where L is the track length and $\oplus$ indicates addition in quadrature. The first term corresponds to multiple scattering effects, and the second to single hit resolution. For a more detailed drift chamber description, see Anfreville et al. (1997).

2.5.5 Transition Radiation Detector

The TRD of NOMAD was designed for electron pion separation. It achieved its goal of a pion rejection factor above a thousand, whilst retaining a 90% efficiency for electrons, in the momentum range 1 to 50 GeV/c. The design of the TRD also had to contend with the constraints of limited longitudinal space and a retainment of less than 2% of a radiation length between the individual drift chambers it separates.

The TRD comprises nine modules, four pairs plus one. Each pair, as well as the single module, is followed by an individual drift chamber, section 2.5.4. The ordering of the chambers and modules can be seen in figure 2.5. A TRD module is composed of two components, the radiator and the detection plane.

The radiator is 315 polypropylene foils, 15 μm thick, and 2.85×2.85 m^2 in area, separated by a 250 μm air gap. The foils are held in an aluminium frame in order to preserve their shape.

The detector plane is 176 vertical straw tubes, 3 m long and 16 mm in diameter, with 0.2 mm spacing for convenience of design. The tubes are filled with a xenon(80%) methane(20%) mixture, and are constructed from wound

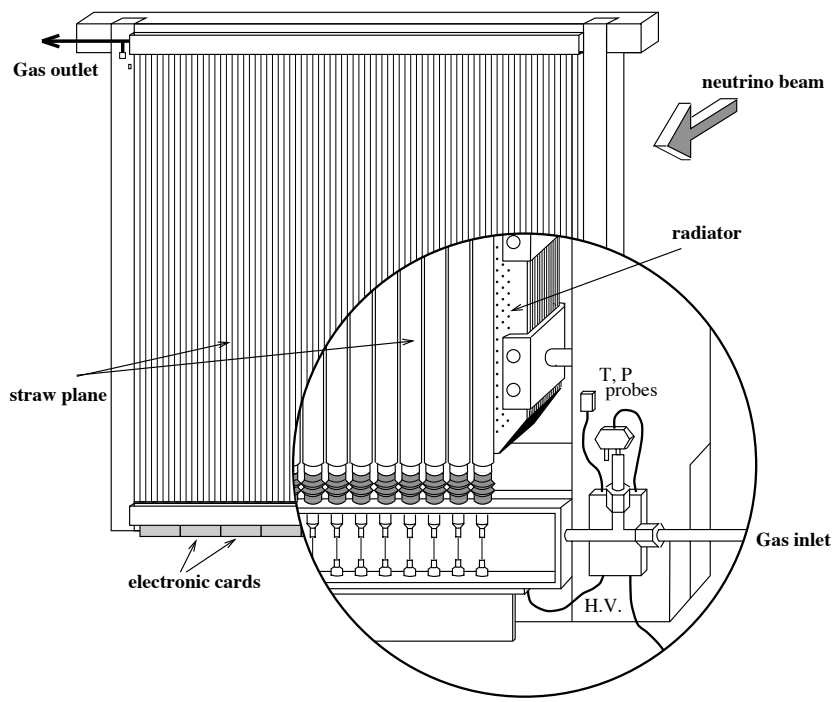

Figure 2.9: Schematic view of a TRD module. (Taken from Altegoer et al., 1998a)

mylar strips, 12.5 μm thick, coated with 115 nm of aluminium. Down the centre of the tubes are the sense wires, gold plated tungsten with a 50 μm diameter. The setup of a module is shown in figure 2.9. The radiator can be seen in the zoomed region along with the high voltage and gas monitors.

The calibration is carried out continuously, using a permanent strip of ^{55}Fe radioactive sources, placed horizontally across the middle of the straw tubes. The ^{55}Fe signals are read out between neutrino spills, and can be used to indicate variations in the high voltages, as well as the temperature, pressure and mixture of the gas.

Transition radiation occurs when a charged particle, above a threshold speed, crosses an interface between two media of different dielectric constants, (Garibian, 1958, 1959, 1960a,b; Garibian et al., 1975), which is the situation in the radiator of the TRD, between the foils and gas. Only electrons in NOMAD have sufficiently high Lorentz factors, $\gamma > 500$, to cause transition radiation. This allows differentiation of electrons and pions in the TRD. Charged particles of low γ will only deposit energy in the tubes from ionisation losses, whereas electrons will also deposit energy from the transition radiation X-rays. A detailed description of the TRD is given in Bassompierre

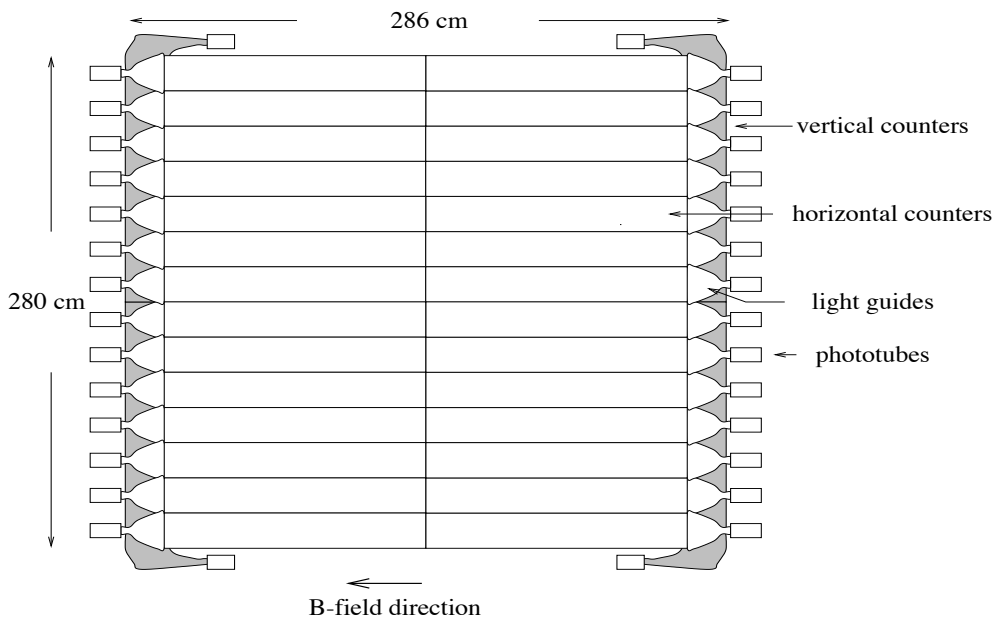

Figure 2.10: Trigger plane layout. (Taken from Altegoer et al., 1999)

et al. (1998a) and its performance is described in Bassompierre et al. (1998b).

2.5.6 Trigger Planes

NOMAD has two trigger planes, one after the drift chamber, and the other behind the TRD. They cover an area of 280×286 cm^2. To achieve this coverage, they each include 32 single ended scintillators, 28 horizontal, with a 124 cm length, and 4 vertical, with a 130 cm length, as shown in figure 2.10. The scintillators are read out by photomultiplier tubes, where the 4 tubes for the vertical planes are placed at 90° to the scintillator, in order to remain parallel to the magnetic field, and thus limit its detrimental effects.

The scintillator used is Bicron Corporation BC 408 and the photomultiplier tubes are Hamamatsu R-2490-05, which use transmission mesh dynodes in order to reduce the effects of the magnetic field. The reduction of the response of the tubes due to the 0.4 T field is only 30%. The mesh dynodes are described fully in Takasaki et al. (1985); Suzuki et al. (1987).

The individual trigger signals are sent to LeCroy 4416 discriminators, which are in turn passed to LeCroy 1876 TDCs to record the individual counter times for offline analysis and a LeCroy 4564 to take the logical OR of each plane to form the $\mathbf{T}_1$ and $\mathbf{T}_2$ trigger conditions.

The single track efficiency of the planes is $97.5 \pm 0.1\%$. Detailed descrip-

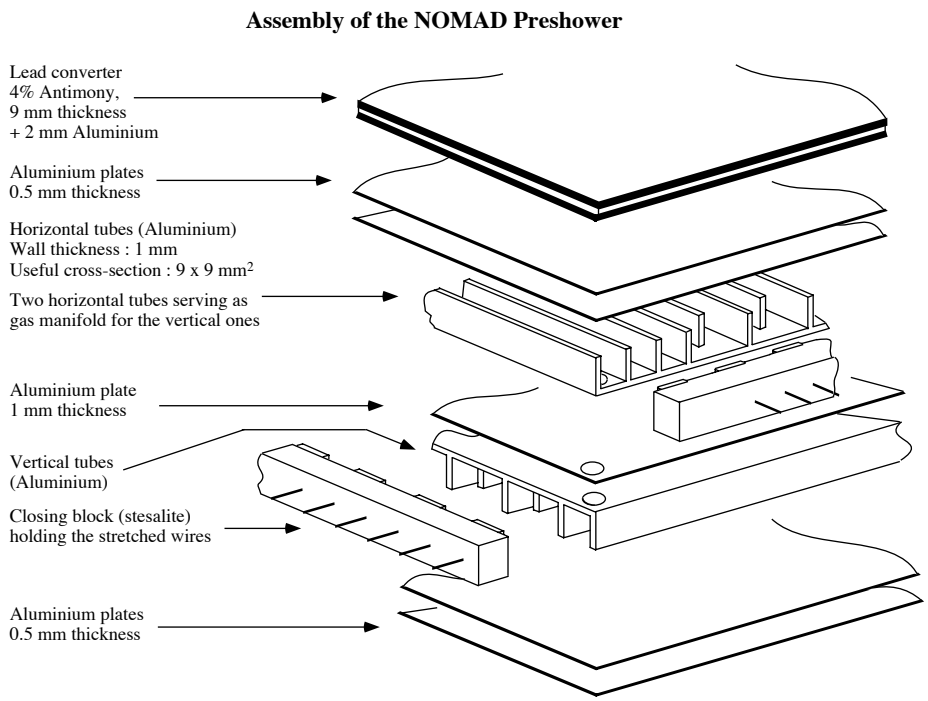

Figure 2.11: An exploded view of the Preshower. (Taken from Altegoer et al., 1998a)

tions of the trigger planes, associated electronics and efficiencies can be found in Altegoer et al. (1999).

2.5.7 Preshower

Photon conversion and electron showering is deliberately initiated in the preshower, PRS, by its high atomic number converter. The PRS consists of 2 planes of proportional tubes, 286 horizontal, 288 vertical, (the two "missing" tubes act as a gas manifold for the vertical plane), placed behind a 9 mm lead(96%) antimony(4%) converter. The tubes are square, with a 81 mm^2 cross section, and are constructed from aluminium, 1 mm thick. Each tube contains a gold plated tungsten sense wire, 30 μm in diameter. These wires are held at the ends by stesalite closing blocks and glued to supports in the middle. They carry a potential of $\pm$1500 V. The gas in the tubes is argon(80%) CO_2(20%). The individual components and construction of the PRS are shown in figure 2.11.

Muons from the flat top are used to monitor the PRS, in particular variations in gain due to temperature and pressure changes in the gas. The

individual tube gains show a dispersion of around 6% for the 574 tubes, mainly due to inhomogeneities in the gas flow.

High precision position measurement is facilitated by the PRS due to its 1 cm grid, compared to the much larger block size of the electromagnetic calorimeter that follows it. This then aids separation of overlapping clusters in the electromagnetic calorimeter. The PRS is also used in combination with the TRD and electromagnetic calorimeter to separate pions and electrons.

2.5.8 Electromagnetic Calorimeter

The electromagnetic calorimeter, ECAL, is crucial for electron and photon energy measurement, covering an energy range of 100 MeV to 100 GeV. Measurement of photons allows the ECAL to determine the neutral component, largely from π°, of the transverse momentum sum of an event. Lastly, the ECAL, along with the PRS, aids the TRD in electron identification.

In order to meet the large dynamic energy range requested, lead glass was chosen for its high resolution and uniformity. There are 875 lead glass blocks, stacked in a grid 35 by 25. A single block is 19 radiation lengths deep, with a cross sectional area of 79×112 mm^2. The blocks are read out by two-stage photomultiplier tubes, tetrodes. The face of the blocks is cut at 45° so the tetrode is at 45° to the field direction, see figure 2.12. This limits the effects of the magnetic field on the tetrode, so the response is reduced by only 20%, leaving a gain of 40.

The tetrode signals are passed to a charge preamplifier, then a shaper and finally a peak sensing ADC to produce the energy deposited in the block, now called a cell. A second signal is passed through a shaper, discriminator and then logical OR with the 16 surrounding cells to produce a time measurement, which can be used to reject those cells which are not part of the event. The timing resolution is a few nanoseconds for a greater than 1 GeV deposit. The timing signals can also be summed to produce the ECAL trigger information, section 2.6.2. The ECAL performance is monitored using two blue LEDs placed alongside each tetrode, where the response to their signal is compared to the reference response for variations over time. This monitoring method is described in Autiero et al. (1996b).

Before construction, the ECAL cells were calibrated in a 10 GeV/c electron beam. The LEDs are used to enable the transfer of measurements taken in the testbeam with no field, to actual running conditions at 0.4 T. The linearity of the response to electrons from 1.5 to 80 GeV is corrected logarithmically, to keep deviations below 1.0%. The resolution was determined to be $\Delta E/E = 1.04 \pm 0.01 + 3.22 \pm 0.007/\sqrt{E}$, where the first term represents detector losses and the second, shower fluctuations. Details of the testbeam

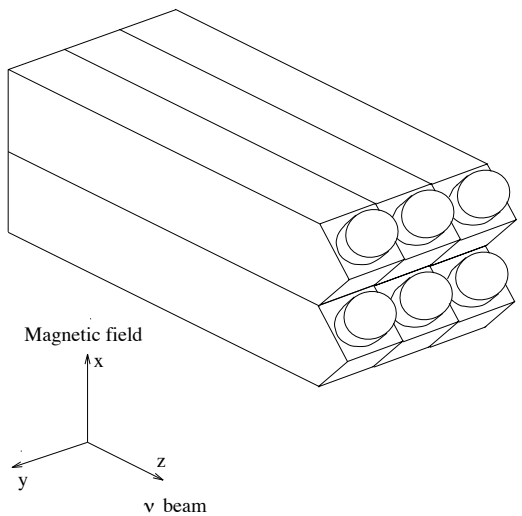

Figure 2.12: Schematic view of the lead glass blocks that comprise the ECAL. (Taken from Altegoer et al., 1998a)

and calibration are given in Autiero et al. (1997, 1999a). The response to photons is measured by reconstructing the π° mass, both in test beams and in NOMAD running, see Autiero et al. (1998b). More details of the ECAL development are located in Autiero et al. (1996a).

2.5.9 Hadronic Calorimeter

The rear magnet support I is also instrumented, and forms the hadron calorimeter or HCAL. The HCAL is useful in tau decay searches as it detects neutral hadrons that might otherwise add to the missing momentum signal. Also, the HCAL is used to measure the energy of charged hadrons, complementary to the momentum measurement of the drift chamber.

The geometry of the HCAL is similar to the FCAL. The support I is constructed from six sets of 23 4.9 cm plates separated by 1.8 cm air gaps. The sets are placed side by side as illustrated in figure 2.5b. The support I then creates a wall $5.4 \times 5.8 \times 1.5$ m^3 in volume, that is a filter of hadrons for the following muon chambers as well as a support for the basket.

The instrumentation of the HCAL is by way of scintillator paddles, with dimensions of $360 \times 18.3 \times 1$ cm^3. Light pipes are added at each end to stretch to the edges of the wall. The scintillators are placed 11 rows deep and 18 high. The active area facing the beam is 3.6×3.5 m^2 and is 3.1 interaction lengths deep. This is summarised diagrammatically in figure 2.13.

The scintillators are connected to photomultiplier tubes whose signals are

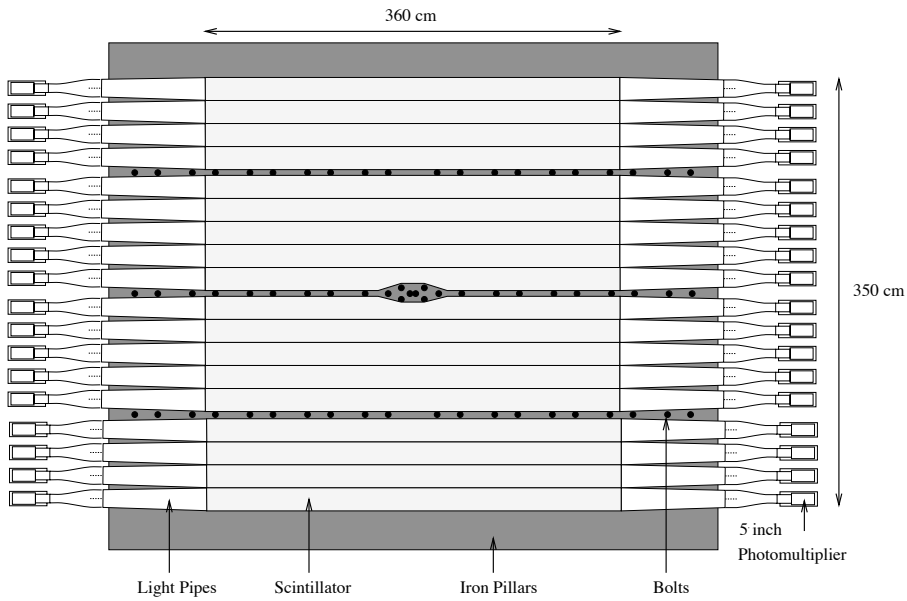

Figure 2.13: The front view of the HCAL. (Taken from Altegoer et al., 1998a)

split, one being charge integrated and sent to an ADC for energy and position information, the other being discriminated and passed to a TDC for event timing. This timing signal can also be used for triggering, section 2.6.2. The horizontal position is determined from the ratio of signals at each end of the paddle, giving a resolution of approximately 20 cm. The vertical position is obtained using the pattern of energy distribution between the modules. Finally, the energy is taken from the mean of the two photomultiplier tube signals.

2.5.10 Muon Chambers

Ten drift chambers from the UA1 experiment, (Eggert et al., 1980), are used in NOMAD as muon chambers. Only muons are expected to reach these chambers due to the absorption of hadrons in the HCAL. The individual chambers are grouped into five modules, and these modules are further grouped into two stations. The two stations are separated by an 80 cm iron absorber which provides additional hadron filtering. The three modules upstream of the absorber, 1, 2, and 5, form station 1, and the two after, 3 and 4, form station 2. In 1996 a gap in the coverage of the chambers was closed with the addition of several small scintillators. This layout can be seen in figure 2.14. Each chamber is 3.75×5.55 m^2 in area and contains

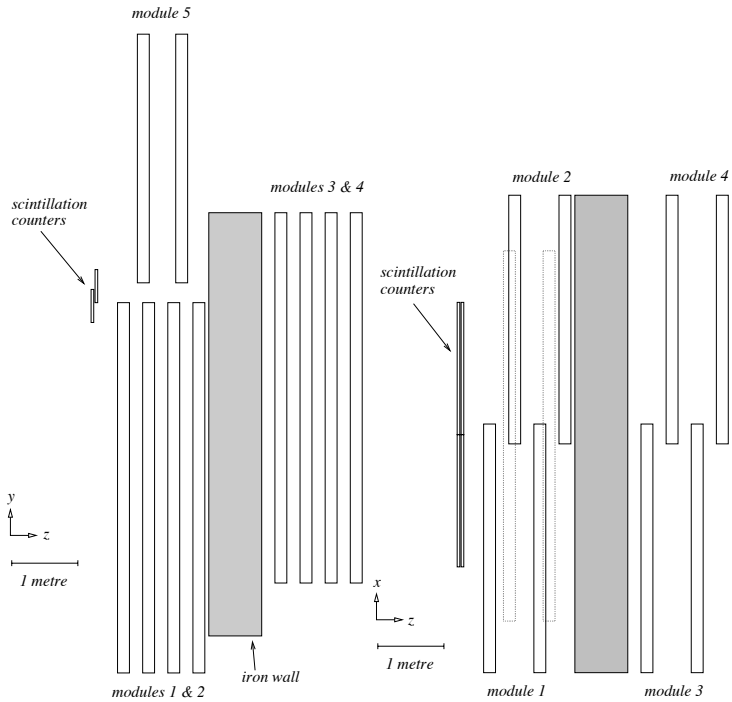

(a) Side view (b) Top view

Figure 2.14: Muon chamber layout showing modules, iron absorber and additional scintillators. (Taken from Yabsley, 1999)

two sets of horizontal and two sets of vertical drift tubes, for a total of 1210 tubes, each with a drift distance of 7cm. The gas mixture used is argon(40%) ethane(60%).

The tracks in each station are first reconstructed in the xz and yz projections, usually from three or four hits, and then combined to form a list of possible tracks in xyz space. The track reconstruction efficiency is about 97%. The xyz tracks are then compared with tracks extrapolated from the drift chamber, in order to find a match. When a match is made, the associated drift chamber track is then identified as a muon.

High energy muons passing through the chambers are used to assess its performance. The typical position resolution is between 350 and 600 μm. This is affected by the gas quality. The hit efficiency of the tubes is 92.5%, with the dead areas between tubes causing an inefficiency of 6.5%.

2.6 NOMAD Control Systems

Modern accelerator driven experiments have large data transfer and recording requirements. To handle this NOMAD adopted a modular approach, which allowed reduction in development time and cost. Both the hardware and software are expanded on in this section.

2.6.1 Data Acquisition

Coinciding with the beam spills, NOMAD triggers arrive in short intervals, separated by long periods of relative inactivity. To minimise dead time, digitised information is first buffered with FASTBUS electronics, to be read out at the end of each spill. There are three types of FASTBUS modules, twelve-bit charge-integrating ADCs, twelve-bit peak-sensing ADCs and sixteen-bit TDCs with one nanosecond resolution. The two types of ADC were designed at CERN, and have 64 channels and a 256 event memory. The TDCs are LeCroy 1876, with 96 input channels with a 64 kilobyte buffer. A maximum of 11 648 channels are read out per event.

The readout of the front-end electronics is controlled by five VME based boards (FIC 8234) with Motorola 68040 processors, using a VME Subsystem Bus, connected to slave controllers (F68b7) in the 12 FASTBUS crates. Four megabytes of additional buffering is available from each FASTBUS controller card. Block transfers, assembly of subevents and integrity (consistency) checks are performed by the VME controllers. The subevents are then passed through a VME interconnect bus to a sixth VME processor, the event builder, to assemble all the pieces into events, together with beam information. The final product is written temporarily to disk before, twice a day, they are transferred to a tape vault for storage on DLTs.

The software running the data acquisition is comprised of elements known as *stages*. This framework is based on the CERN designed CASCADE software, described in Perrin et al. (1993). It provides buffer management, event access facilities and scheduling. Data arrival drives the stages, thus stages must have at least one input source with any number of output sources. The scheme implemented is summarised diagrammatically in figure 2.15. This shows the information flowing to the event builder, including beam information and calibration, as well as detector monitor and status summaries, described in section 2.6.3.

The run control is a C^{++} implemented finite state machine for X-windows that uses a database to record current states of the monitoring programmes and predetermined rules for moving between the various states. This database, in summary form, is used later in reconstruction and analysis of events.

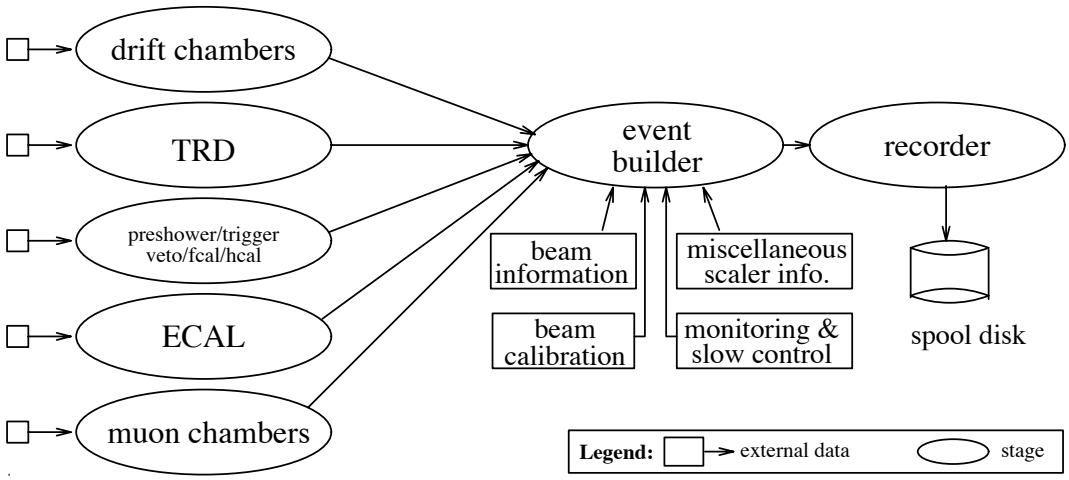

Figure 2.15: The standard configuration of the NOMAD data acquisition. (Taken from Altegoer et al., 1998a)

In summary, over 1.5 megabytes of data are recorded per minute. A typical neutrino event contains around 2000 32 bit words before reconstruction. Further, six times this amount flows through the acquisition system as calibration events, which are not recorded. The data taking time lost due to downtime and inter run transitions is less than 3%.

2.6.2 Trigger Conditions

The trigger logic for NOMAD is handled by a specially designed VME based module, MOTRINO (MOdular TRIgger for NOMAD), described in Schmidt (1997). Its purpose is to take the signals from the subdetectors to form triggers for events of interest. The module operates in two modes, six modules function in a trigger receiver (slave) mode and two others are in trigger formation (master) mode. MOTRINO has many features, including the generation of time signals synchronised with the SPS cycle, combination of up to eight subdetector signals, recording the status of the trigger bits, moderation of the trigger rates and determination of the live time. The NOMAD triggers are explained below, starting with the neutrino gate triggers. $\mathbf{T}_1$ and $\mathbf{T}_2$ are signals of hits in the first and second trigger planes respectively, and $\mathbf{V}_{(8)}$ is a hit in the veto (bank 8). **FCAL**, **FCAL′** and **ECAL** are threshold levels from the FCAL and ECAL. Trigger rates are given in terms of triggers per 10^{13} POT (protons on target), that is to say the order of the number of protons impinging on the T9 target in a neutrino spill.

- $\overline{\mathbf{V}} \times \mathbf{T}_1 \times \mathbf{T}_2$ is the main NOMAD trigger for the study of neutrino interactions in the drift chamber. The rate for this trigger is $\sim 5.0/10^{13}$ POT. The background in this trigger comes from cosmic rays, beam muons that are not vetoed and neutrino interactions in the magnet coil and basket.

- $\overline{\mathbf{V}}_8 \times \mathbf{FCAL}$ is the trigger for deep inelastic neutrino interactions in the FCAL, with a threshold of 4 mip ($\sim$ 2.0 GeV). The rate is $\sim 6.5/10^{13}$ POT, with a negligible background from cosmic rays.

- $\overline{\mathbf{V}}_8 \times \mathbf{FCAL}' \times \mathbf{T}_1 \times \mathbf{T}_2$ is the second FCAL trigger designed for the study of quasielastic-like events. The $\mathbf{FCAL}'$ threshold is between 1.2 mip and 4.0 mip, where the trigger planes coincidence is included to reduce triggering from noise. The rate is $\sim 1.0/10^{13}$ POT.

- $\overline{\mathbf{V}} \times \mathbf{ECAL}$ is the trigger for neutrino events in the ECAL. The trigger rate is $\sim 2.0/10^{13}$ POT, due to the large mass of the ECAL, around 20 tons. This was the original trigger setting in 1995, but the livetime was too low due to $\overline{\mathbf{V}}$.

- $\overline{\mathbf{T}_1 \times \mathbf{T}_2} \times \mathbf{ECAL}$ was used from 1996 to 1998 instead of the above trigger, and had a higher livetime, but similar rate.

- **CHORUS-NOMAD** is used in neutral heavy particle searches, where the particle is produced in CHORUS and decays in NOMAD. The trigger forms a subset of the main NOMAD trigger, with the addition of a valid CHORUS trigger.

- **RANDOM** is used to study detector occupancy, particularly out-of-time muons from the neutrino beam. The trigger records detector activity 22 μs after an SPS spill.

As explained in section 2.4.1 the SPS cycle provides neutrinos to NOMAD in two burst separated by a 2.7 s flat top. During this time, muons are incident on NOMAD from a separate beam line. Triggers have been set up in NOMAD to take advantage of these muons to further study the detector response. The muon gate triggers are now described.

- $\mathbf{V} \times \mathbf{T}_1 \times \mathbf{T}_2$ selects through going tracks which are used for drift chamber alignment and calibration of subdetectors.

- $\mathbf{V}_8 \times \mathbf{T}_1 \times \mathbf{T}_2 \times \mathbf{FCAL}'$ is similar to the above trigger, however it enhances muons crossing the FCAL and other areas of the detector, that are less likely to occur in the previous trigger, as the muon beam crosses NOMAD at an angle.

- $\mathbf{V}_8 \times \mathbf{T}_1$ and $\mathbf{V}_8 \times \mathbf{T}_2$ are used to measure the efficiency of the trigger planes

- $\mathbf{V}_8 \times \mathbf{T}_1 \times \mathbf{T}_2 \times \mathbf{ECAL} \times (\overline{\mathbf{HCAL}})$ is used in the study of electrons from muon decays or delta rays. The HCAL is added, in anti-coincidence, when looking for muon decays.

In each neutrino spill, approximately 15 neutrino candidate triggers are taken, and during the flat top, a further 60 muon triggers are signaled, only around 20 of which are recorded. More details of the entire trigger system are found in Altegoer et al. (1999).

2.6.3 Slow Controls

The NOMAD slow control is handled by a Sun workstation and several Apple Macintosh computers running LabVIEW, (NIC, 1994). All voltages, gas systems and temperature probes in the experiment are monitored by the Macintoshes, passing summary information to the Sun workstation. In the event of detector problems, with one or more of the above variables being out of range, an alarm is sounded. Further, periodic samples of slow control data are saved for later inspection for detector faults. Each of the nine subdetectors plus the beam, scaler and trigger information have monitoring programmes that connect to the data acquisition stages and create summary histograms, for inspection.

2.7 Simulation and Reconstruction of Events

To understand how well the detector will function, or to estimate the efficiency of the event selection procedure, it is necessary to simulate events, in which the exact details are known, to be compared with what is determined by the detector and selection algorithms. This is achieved with a Monte Carlo generation, where events are created randomly within a set of given physics criteria. When completed, such events are in the same form as actual data, signals from the various subdetectors. Both data and Monte Carlo events then need to be reconstructed from this rudimentary detector output to produce more usable information about the event, such as tracks and vertices. The programmes used by NOMAD are outlined below.

2.7.1 Event Generation

Simulated events in NOMAD are generated using the NEGLIB (NOMAD Event Generator LIBrary, Meyer and Rubbia, 1994). The programme uses LEPTO 6.1, described in Ingelman (1992), to simulate deep inelastic lepton-nucleon scattering. It determines an input neutrino energy and position by sampling from NUBEAM 4.00 energy versus radius squared beam tables. Datacards allow the choice of incoming neutrino type, beam energy window, decay channels as well which part of the detector the initial interaction will take place, e.g. FCAL. The geometry of NOMAD is used to generate the vertex position according to the material density distribution along the beam axis. The fragmentation of produced partons into hadrons is performed with the JETSET version 7.4 package, (Sjöstrand, 1994).

Recall that the neutrino beam is ~ 42 mrad below the NOMAD z axis, and that it intersects the y zero in the ECAL. When the beam first enters the drift chamber, it is at $y \sim -20$ cm. This offset is reproduced by NEGLIB, but not the slope. Events must therefore be rotated from the NEGLIB to the NOMAD reference frame:

$$y' = y\cos\theta - z\sin\theta \quad z' = z\cos\theta + y\sin\theta \tag{2.9}$$

where a study of NEGLIB and data events determined $\theta = -35.3$ mrad, (Weber et al., 1998).

NEGLIB also includes quasielastic and resonance type lepton-nucleon interactions, which can be handled separately. The output of NEGLIB is directly available for analysis, as well as being the input to the next stage of the simulation.

2.7.2 Detector Simulation

After events have been generated, the response of the detector in tracking and recording must be taken into account. For this, NOMAD uses a GEANT based description of the detector called GENOM (GEant NOMad library). GEANT is a general package for simulating the passage of particles through matter, more information can be obtained from Goossens et al. (1994). GENOM is described in detail in Altegoer et al. (1996). This is the final stage for the simulated events, as they can now be reconstructed along with real data events.

2.7.3 Event Reconstruction

The reconstruction is performed in two stages. The first stage, Phase I, reconstructs raw data from each subdetector with RECON, a general reconstruction package. The RECON package is described in Bird (1993). At the completion of this stage, tracks and vertices in the drift and muon chambers, as well as clusters of hits (energy deposits) in the calorimeters, have been assembled. The second stage, Phase II, identifies the individual particles of an event, by matching tracks in the drift chambers with tracks and clusters in the other subdetectors. The Phase II output is then stored in a DST (Data Summary Tape, Varvell, 1997), format for use in analyses. From here, event selection and identification is performed as detailed in chapter 4.

2.8 The NOMAD Data Set

The NOMAD experiment collected its main data from 1995 to 1998 inclusively. The CERN SPS beam runs during the European summer, from April through September. A measure of the amount of beam given to NOMAD is the accumulated POT (Protons on Target). This is measured by the BCTs (Beam Current Transformers), located just upstream of the neutrino beam target, T9. A plot of accumulated POT is given in figure 2.16. The plot also shows 1994, where NOMAD was scheduled to run, but only had at most two drift chamber modules in place, due to a problem with their original method of manufacture. However, the other subdetectors, except FCAL, were in place, and data was taken. This data was used for calibration and optimisation. A period of approximately two months in the middle of 1997 can also be seen where there was no beam due to a fire at the SPS.

A numerical summary of NOMAD data taking is given in table 2.1, which indicates the number of triggers taken, the number of ν_μ charged current events in the official NOMAD fiducial area of 2.6×2.6 m^2, as well as selected beam information. Good POT refers to protons on target when NOMAD was taking data. The 1995 run is divided into the three drift chamber configurations that were run that year, as explained in section 2.5.4. Also note that the 1998 run is split into three types of neutrino beam, positive focusing, negative focusing and zero focusing. These will be explained later in chapter 5.

In conclusion, NOMAD has collected over a million neutrino charged current interactions, for use in its oscillation searches. The NOMAD data set is hence the largest collection of its kind, enabling a detailed search, plus accurate evaluation of other standard neutrino physics quantities.

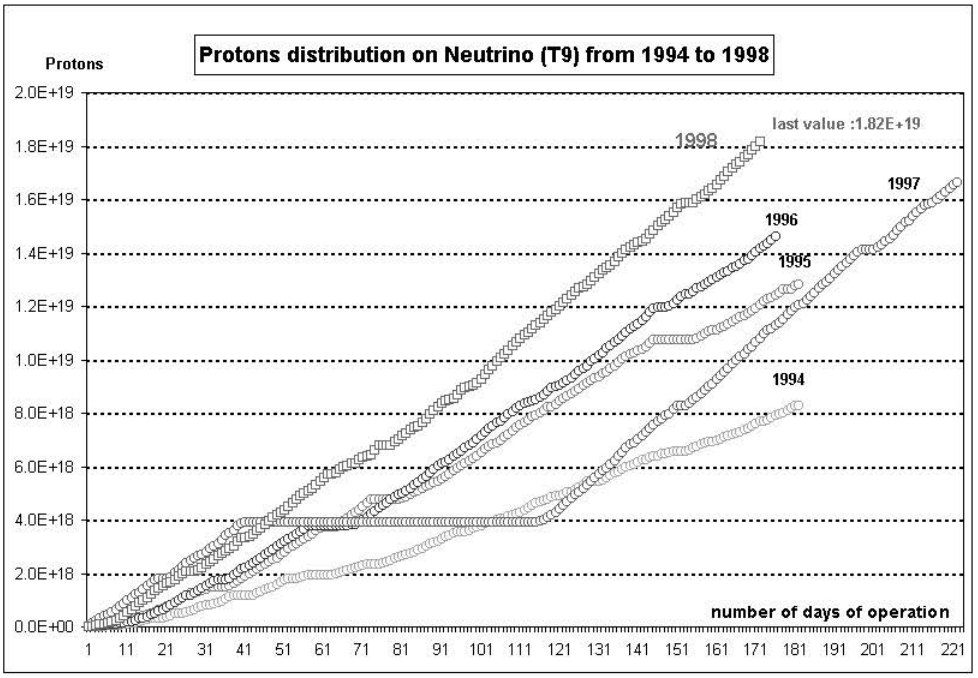

Figure 2.16: Accumulated BCT on the T9 target. Taken from the CERN-SPS web page.

Year	Period	POT	Good POT	Triggers	ν_μCC
1995	4 Mod	1.26×10^{19}	0.27×10^{19}	16.7×10^6	0.3×10^5
	8 Mod		0.33×10^{19}		0.7×10^5
	11 Mod		0.28×10^{19}		0.8×10^5
1996		1.46×10^{19}	1.41×10^{19}	25.5×10^6	3.8×10^5
1997		1.66×10^{19}	1.57×10^{19}	24.6×10^6	3.28×10^5
1998	Pos	1.82×10^{19}	1.20×10^{19}	25.4×10^6	3.26×10^5
	Neg		0.43×10^{19}	3.9×10^6	0.14×10^5
	Zero		0.04×10^{19}	0.2×10^6	0.03×10^5

Table 2.1: Summary of Data taken by NOMAD from 1995 to 1998. (Adapted from Soler, 1998)

Chapter 3

The SPY Experiment

3.1 Introduction and Motivation

The Secondary Particle Yields (SPY/NA56) experiment was proposed, (Ambrosini et al., 1996), in order to measure particle production rates from a beryllium target, hit by a 450 GeV/c proton beam, mirroring the initial collision producing the neutrino beam of the West Area Neutrino Facility (WANF). SPY concentrated on measuring low momentum secondaries, below 60 GeV/c, an area not previously investigated. This lower momentum range is of particular importance to the WANF, and hence NOMAD, as up to 50% of the neutrino flux is produced from meson decays in this range.

Secondary production models currently in use, such as multi parameter fits like FLUKA 92, or parametrisations like those in Malensek (1981), are based on extrapolations of old experimental data, which had poor if any coverage of the momentum ranges of importance to neutrino production in the WANF. Precise measurement of the production rates of pions and kaons, as well as their relative rates of production, obtained by SPY, can greatly improve current simulations of neutrino beam production. In particular, SPY concentrated on determining as accurately as possible the pion to kaon ratio, the ratio that directly affects the contamination of ν_e, (predominantly from kaon decays), in the ν_μ beam. This quantity is one of the main concerns in the $\nu_\mu \rightsquigarrow \nu_e$ oscillation search, and currently has a high error.

Other applications for the SPY data include enhancing the fitting procedure of the empirical parametrisation developed in chapter 6, (a second method of predicting the neutrino beam). This method uses measured neutrino spectra at NOMAD to derive the meson production at the target. However, when determining pions and kaons contributing to the ν_μ spectra, the relative contribution of kaons, in the approximate neutrino energy range 10

to 70 GeV/c, can not be fixed from the neutrino data. Instead the SPY results help to fix the kaon contribution.

The most recent experiment relevant to SPY was Atherton et al. (1980). The Atherton experiment used 400 GeV/c primary protons, and measured secondaries from their collision with a beryllium target, down to a momentum of 60 GeV/c. SPY aimed to have a higher accuracy than the Atherton experiment, as well as measuring momenta below 60 GeV/c. To provide an overlap for comparison with the Atherton results, SPY would take data at 67.5 and 135 GeV/c as well.

SPY aimed to have an exhaustive coverage of the angle and momentum ranges for secondary production, not just in the current WANF beam, but also for future neutrino beams such as that now approved for the CERN to Gran Sasso long base line neutrino oscillation search, (Acquistapace et al., 1998). To facilitate the transfer the SPY results to experiments with alternative target configurations, a range of plate targets with varying thicknesses was used, as well as the cylindrical T9-like target, (see section 3.2.1). The various running conditions for SPY are listed in table 3.1. Note the two Atherton overlap points, the low momentum coverage, down to 7 GeV/c and the two angular scans at 15 and 40 GeV/c.

This chapter summarises the activities of the SPY experiment as well as detailing an independent analysis of the SPY data set. This separate analysis was undertaken as a check to the main SPY analysis.

3.2 Experimental Layout

The SPY experiment undertook its measurements using the particle spectrometer of the NA52 heavy ion experiment, (NA52 is described in Arsenescu et al. (1999)). This spectrometer resides in the H6 beamline of the north area at CERN. Secondaries were generated from collisions in the T4 target station which, along with the WANF, is served by a 450 GeV/c proton beam from the SPS. A short review of the beam, target area, spectrometer and data acquisition follows.

3.2.1 Beam and Target

The secondaries that SPY measured were created from the collisions of the proton beam with the beryllium target, in a setup very similar to the WANF. For SPY, this collision occurred in the T4 target station, which is shown schematically in figure 3.1. SPY had a beam intensity of 10^{12} protons per

p/z (GeV/c)	Target Length	Angle to the z-axis (mrad)
+135	100,200,300 mm,T9	0
+67.5	100 mm	0
+40	100 mm	-15,±11.25,±5.625,+3.75,+1.875,0
	T9	-15,+5.625,0
	200,300 mm	0
+30	100 mm,T9	0
+20	100,T9	0
+15	100	+30,+22.5,±15,±10,+5,0
	T9	-15,+5,0
	200,300 mm	0
+10	100,200,300 mm,T9	0
+7	100 mm,T9	0
-67.5	100 mm,T9	0
-40	100 mm	-15,-11.25,-5.625,±3.75,±1.875,0
	200,300 mm,T9	0
-15	100 mm	-15,-5,0
-10	100 mm	0
-7	100 mm,T9	0

Table 3.1: Summary of the different SPY running conditions, p/z is rigidity, a combination of the charge and momentum of the secondary. Target length refers to the plate targets, T9 is three cylindrical targets each 100 mm.

burst, considerably reduced from that of the WANF. T4 also provides secondary beams for the H8 and P0 beamlines.

The T4 target station includes four main magnets. The magnets B1T and B2T are used to select the incident protons, and B3T and BEND1 select the momentum and angle of the secondaries. Possible particle trajectories through the target station to H6 are shown in figure 3.1. Both positive and negative emission angle particles can be collected, using B3T and BEND1. Secondary angles of up to 15 mrad can be selected with these two magnets. To increase the selection up to 30 mrad a process called "wobbling" is used, which entails varying the angle of incidence of the primary beam on the target with B1T and B2T.

A scan varying the field strength of B1T and B2T was performed to check the zero value of the production angle. It was determined to be within 0.1 mrad of the nominal value.

The main targets used by SPY were beryllium plates, of varying lengths

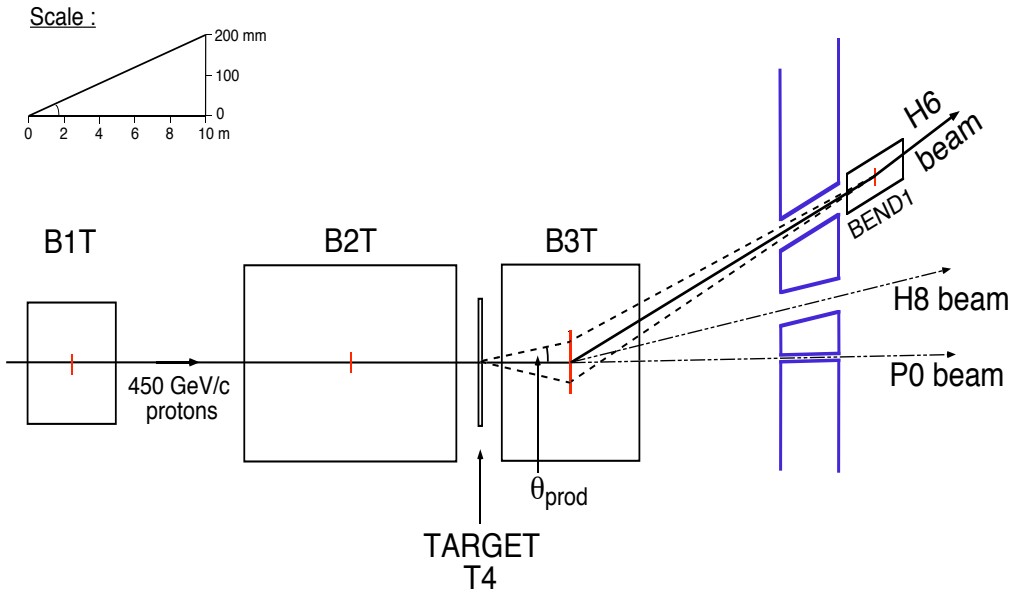

Figure 3.1: The T4 target station in plan view. (Taken from Ambrosini et al., 1999)

in accordance with table 3.1. The plates are 160 mm wide and 2 mm high, and are easily interchanged at the target station. The large width allows the study of angular dependencies, without introducing new uncertainties. A T9-like target is also used which comprises three 100 mm beryllium rods, 3 mm in diameter, and spaced with 90 mm of air. This is identical to the WANF target, T9, except that the actual T9 target has 11 such rods and spacing.

Proton beam monitoring is achieved with Secondary Emission Monitors (SEMs) located upstream and downstream of T4. These measure the beam intensity, spot size and position, and also aid in the steering of the beam. The two types of SEMs are constructed from aluminium or titanium foil. Further details, including the calibration, are left for section 3.4.6.

3.2.2 The H6 Spectrometer

The H6 spectrometer, in the SPY configuration, is shown in figure 3.2 with views of the horizontal and vertical bending planes. The horizontal plane selects the angle of the particles, and the vertical is for momentum analysis, covering a range from 5 to 200 GeV/c. The solid line is the trajectory of a particle offset by 1 mrad at T4, the dotted line shows that of a particle

on axis. The spectrometer is 524 m in length. Below is a description of the individual components of the spectrometer. In this description, all distances are relative to the T4 target.

Collimators

There are three collimators in the spectrometer, one for each of horizontal (x), vertical (y) and momentum bite ($\Delta p/p$). These are used to maintain the trigger rate at a feasible level, and can operate up to an acceptance of $\Delta p/p \times \Delta\Omega = \pm 1.5\% \times 2.1$ μsr, where $\Delta\Omega$ is the solid angle acceptance. To reduce uncertainties in the acceptance arising from unknown field effects in the spectrometer magnets, the collimators must be placed as far upstream as possible. The two spatial collimators are at 41 and 48 m, following just two quadrupoles, with the momentum collimator at 128 m, after six quadrupoles, only three of which could effect the momentum selection of the collimator. This is a substantially better setup than the Atherton experiment. The collimators were tested and calibrated prior to being placed in the spectrometer and in addition an *in situ* test was performed at the beginning of SPY data taking, measuring proton fluxes. These tests showed a linear response in the flux to the size of the opening in the collimators, however the zero opening was not consistent with zero flux for the spatial collimators. Actual zeros were measured as C-hor = -0.44 ± 0.18 mm and C-vert = -1.34 ± 0.16 mm. These measurements are presented in Lehmann (1997).

Time of Flight (TOF) Counters

There are five TOF counters, used to time particles along the beamline. The timing is the used to calculate a particle mass estimate for particle identification purposes. They are made from 8 vertical strips of scintillator, two mirrored sets of strips with widths 20, 12, 10, 8 mm. TOFs 1, 3 and 5 have 1 cm deep strips, giving a timing resolution of 74±1 ps, whilst 2 and 4 are 0.5 cm, with a resolution of 100±1 ps. The area covered is a maximum 10×10 cm^2. They are constructed from CRON 404 scintillator, and read out by Hamamatsu R 1828-1 photomultipliers. To produce mass information, the time t_o for a massless particle to travel between the the counters and the extra time Δt that a massive particle requires, are combined with the selected secondary momentum p of the run. Thus $m \simeq p\sqrt{2\Delta t/t_o}$, assuming natural units of $c = 1$. The ability to use mass information to identify particles is limited to low momentum runs, where the timing resolution is considerably smaller than Δt. The TOFs are placed at 144, 226, 367, 445 and 524 m. The efficiency to record a hit in at least one TOF is 0.986±0.001.

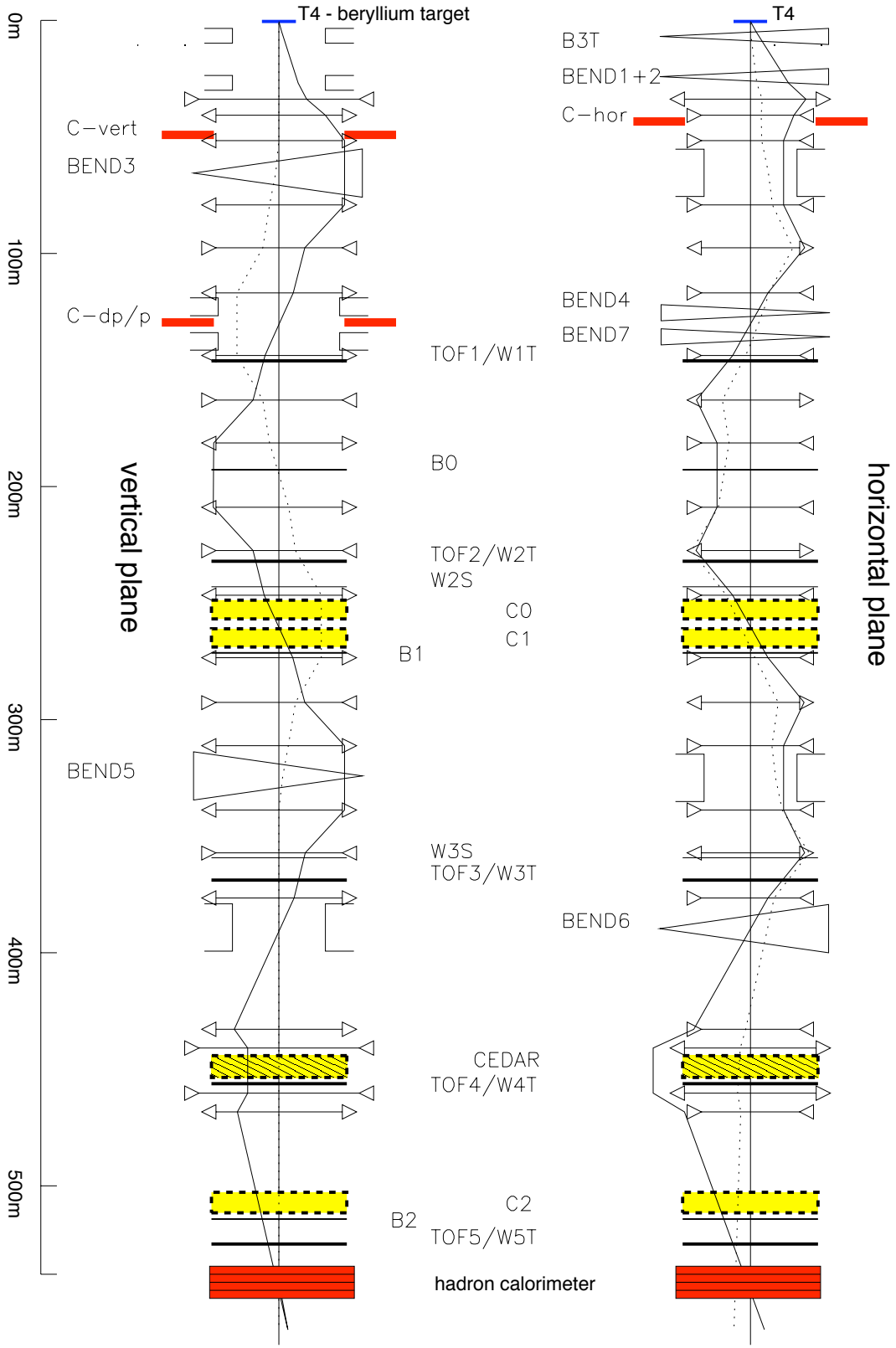

Figure 3.2: The SPY spectrometer, shown in the horizontal and vertical planes. Not to scale perpendicular to the beam line. (Taken from Ambrosini et al., 1999)

Multiwire Proportional Chambers

Each TOF counter is followed by a multiwire proportional chamber. There are two additional chambers before TOFs 2 and 3. They cover 10×10 cm^2 and have wires of 3 mm spacing with an argon(75%) isobutane(25%) gas mixture. The chambers can either have two wire orientations, x and y, or three, x, y and u (45° to x and y). The wire chambers are used for the comparison of beam dispersions between data and predictions for the acceptance calculations, see section 3.4.3.

Threshold Čerenkov Detectors

The spectrometer includes three Čerenkov detectors, C0, C1, and C2. The detectors are placed at 258, 268 and 505 m respectively. C0 and C1 have a common nitrogen supply, whilst C2 is supplied with helium. The two gases provide different ranges of particle identification. All have separate electronic readouts. Each supply can be adjusted over the pressure range from 50 mbar to 3 bar, with an uncertainty of ± 5 mbar. The pressure is adjusted to allow differentiation between particles above and below a velocity threshold, to select low mass particles. In particular, CO and C1 provide pion and kaon separation at low momentum, and kaon proton separation at higher momentum, whilst C2 is set to flag leptons.

CEDAR

The CEDAR (ČErenkov Differential counter with Achromatic Ring) is used to aid in pion selection at high momentum. Čerenkov radiation is emitted in a cone, the angle of which is dependent on the velocity of the particle producing it. This increases the particle selection ability of a normal Čerenkov detector, which only relies on the emission of Čerenkov radiation. The CEDAR uses helium at pressures between 10 and 13 bar, varying with the pion selection threshold at each secondary momentum. It is situated at 440 m.

Hadron Calorimeter

The calorimeter comprises five modules, built from 3 mm thick scintillator plates separated with 3.2 mm depleted uranium plates and 0.2 mm steel foils. The first four modules have 45 layers, whilst the last has just 30. The scintillator is further separated into 12 vertical strips each 5 cm wide, where three adjacent strips are viewed by the same photomultiplier. The calorimeter is placed at 539 m and has an active area of 60×60 cm^2 with a depth of approximately seven nuclear interaction lengths. It has an electromagnetic

energy resolution of $\sigma_E^{em}/E = 0.174E^{-1/2} \oplus 0.009$ and hadronic energy resolution $\sigma_E^{had}/E = 0.356E^{-1/2} \oplus 0.028$. The purpose of the calorimeter was to provide lepton identification, especially in the high momentum runs. The efficiency of the calorimeter in detecting an energy deposit is 0.995±0.001.

Trigger Planes

The three trigger scintillator planes, B0, B1 and B2, provide particle triggers and timing information. They are placed at 191, 268 and 505 m. The actual trigger logic used will be described in the following section.

3.2.3 Data Acquisition and Triggering

There are two central triggers for SPY, from which more complex triggers are derived. These are trigger **A** (**TOF2** × **B1**) and **B** (**TOF4** × **B2**). The spectrometer is split for analysis purposes into upstream and downstream of TOF3, and so triggers **A** and **B** represent these two sections. In low momenta running, 7 or 10 GeV/c, only the upstream section is used due to particle decays reducing the efficiency of detection if the downstream section was included. Thus for those runs, only trigger **A** is required. In all other runs, **A** × **B** forms the trigger.

The efficiency of **A** is determined from the ratio of (**TOF2** × **B1**) × (**TOF4** × **B2**) to **TOF4** × **B2**. The efficiency of **B** is determined in section 3.4.3 in combination with the so-called transmission coefficient.

The **A** × **B** trigger can be combined with a veto from the Čerenkov detectors. In intermediate and high momentum runs, this combination is used to downscale the number of pions recorded in favour of kaons, which have a considerably lower production rate. However, this additional veto is switched, from being included or not, after each event readout. Thus half the data recorded will still resemble the true beam composition. This prescaling is removed in the analysis, as described in section 3.4.2.

The data acquisition livetime is obtained from the ratio of the acquired to total triggers. The livetime is different between the particle species due to downscaling, as only heavy particles, kaons and protons, will always cause a valid trigger. Protons, which are abundant in both the true and enriched kaon data sets, are used to test for systematic effects between the livetimes of the two samples.

3.3 Particle Identification

The bulk of the SPY analysis was the determination of the raw numbers of pions, kaons and protons in each of the runs listed in table 3.1. Separate to the main SPY analysis, presented in Ambrosini et al. (1999), a second, independent analysis was carried out, which will be described below. This second analysis was conducted to ensure the reproducibility of the initial (particle selection) stage of the SPY analysis.

The runs are grouped by momentum, where the same detector and trigger settings are used to identify the particles. The low momentum runs, 7 and 10 GeV/c, were not included in this independent analysis, which instead focused on the intermediate, 15 and 20 GeV/c, and high, 30 GeV/c and above, momentum ranges.

All particles were required to deposit at least 1.5 GeV/c in the calorimeter to ensure the quality of the trigger.

3.3.1 Electron and Muon Identification

All momentum ranges utilised the hadron calorimeter to label electrons and muons. The readout of the calorimeter gives the energy deposited by a particle in each of the five modules. Electrons characteristically deposit all their energy in the first module, whilst muons deposit an amount equivalent to a minimum ionising particle (mip) in each module, ($\sim$ 0.5 GeV). These traits can be seen in figure 3.3, which shows the ratio of energy deposited in the first module of the calorimeter, E_i over the total energy deposited, E_{cal}, as a function of the energy deposited, for a 40 GeV/c run. Thus, electrons are at the top of the plot, losing all their energy in the first module. The muon mip can also be seen, with about a fifth of its energy deposited in this first module.

The electron selection required 98% of the energy of the candidate to be deposited in the first module, and less than 0.8% in the second, with a further cut on total energy deposited, depending on the selected momentum of the run.

Muon selection was based on the proximity to the average (Gaussian) mip peak position in all five modules:

$$\sum_{i=1}^{5} \left(\frac{E_i}{E_{cal}} - \overline{\left(\frac{E_i}{E_{cal}} \right)} \right) \leq 0.15 \tag{3.1}$$

where the mip peak positions were determined for each secondary momentum.

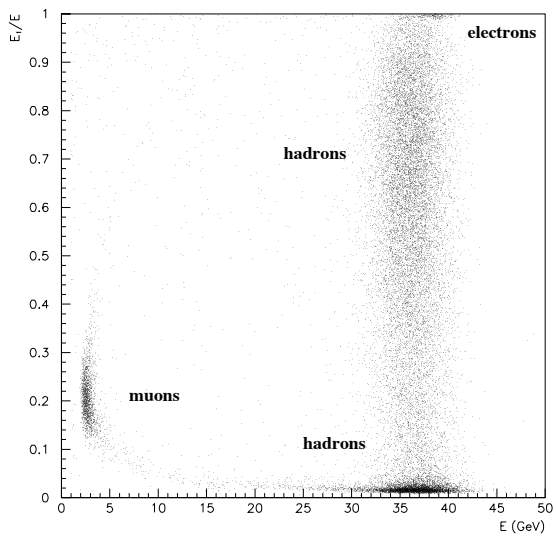

Figure 3.3: Energy deposited in the first module, as a fraction of the total deposited, plotted against the total deposited, clearly showing the muon, electron, and hadron separation available. From a 40 GeV/c run.

This selection process was always in place as a lepton veto, (leptons are not included in this measurement of secondary products.) Most leptons that are collected are due to meson decays, either after the second trigger, in which case they will be identified as their parent meson by the Čerenkov counters, see below, or from earlier decays, which are accounted for by scaling up by the decay probability, described in section 3.4.4.

3.3.2 Intermediate Momenta

The trigger for the 15 and 20 GeV/c runs was the coincidence of **A** and **B**, and also included pion downscaling, using C0 + C1 (pion detection) in anticoincidence with **A**. C2 was used in anticoincidence with **B** in order to veto electrons and muons, by setting its threshold just above the pion threshold. Those leptons remaining were removed using the calorimeter as previously described.

The five TOFs combine to give a mass hypothesis for each particle. The mass squared peaks are shown in figure 3.4. As can be seen, although the pion and kaon peaks are overlapping, the proton peak is well separated, allowing

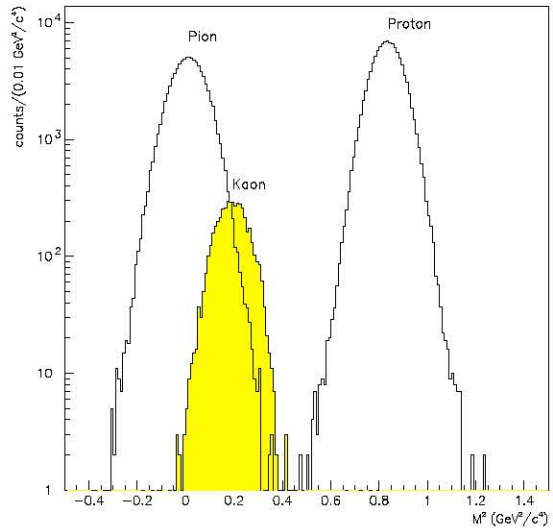

Figure 3.4: The mass squared fit produced by the time of flight counters at 20 GeV/c. The pions and kaons were separated using the timing criteria of the Čerenkov counters.

for the identification of the protons.

Separation of pions and kaons is achieved with the timing information from the Čerenkov counters. C0 and C1, as well as the CEDAR, had their gas pressure set to only flag pions. Each counter would register either an in time hit (ith), an out of time hit (oth) or no hit (noth). These time signals from C0 and C1 were used to form logical subgroups from which pions and kaons could be more easily tagged. The CEDAR remained as redundancy, either removing the remaining overlap of pions and kaons when necessary, or being used for detector efficiency studies. The groupings were taken from Collazuol and Guglielmi (1996a), and used in the analysis as follows.

i) C0ith + C1ith This is the main pion sample, as only pions can produce a signal in C0 or C1. Contamination is only due to leptons, which are rejected with the calorimeter. Occasionally protons can appear in this sample due to a proton trigger overlapping with a light particle which causes a signal in C0 or C1. These are rejected with the mass squared criteria from the TOFs.

ii) C0oth × C1oth Particle overlap between pions and protons with light particles triggering C0 and C1 comprise this subgroup. There is no

difficulty separating the pions and protons in this sample with the reconstructed TOF mass.

iii) C0noth × C1noth This sample contains predominantly kaons and protons, which are separated with the TOF information. As this sample is much smaller than the total, the pion and kaon mass peaks do not overlap. This allows the pion contamination to be removed using the TOFs.

iv) (C0oth × C1noth) + (C0noth × C1oth) A second timing group is caused by light particle overlap with kaon and protons. Particles are resolved with the TOFs. Pion contamination is also present due to losses in C0 and C1. The CEDAR provides pion identification in these cases.

An example of the number of particles identified in each timing subgroup is given in table 3.2 for a 20 GeV/c run. Note that the electrons are assumed to be from pion and kaon decays, and so should not necessarily be included when comparing the triggers to total particles identified. This is also true, but to a lesser extent, for the muons.

Group	Triggers	Pions	Kaons	Protons	Electrons	Muons
i	100004	91676	0	0	8328	3166
ii	69	55	0	10	4	3
iii	116303	71	4823	110898	507	1096
iv	453	13	22	415	2	5

Table 3.2: Particles identified in each of the four timing subgroups for a 20 GeV/c run.

These identification methods are applied to all the 15 and 20 GeV/c runs in table 3.1, including different angles, target thicknesses and charge.

3.3.3 High Momenta

In the high momentum range, the resolution of the TOFs produce mass squared peaks too broad to allow separation of the particles. Thus, particle identification was based solely on the Čerenkov detectors and timing information from the trigger and TOF planes. C0 and C1 were set below the proton threshold, so as to signal leptons, pions and kaons but not protons, whilst C2 has been set to flag only pions and leptons, (as such, C2 is also used

for downscaling purposes). The CEDAR was again set at the pion threshold. As in the intermediate momenta analysis, timing subgroups are constructed, following the guidelines of Collazuol and Guglielmi (1996b). There are now six groups, due to the inclusion of C2.

i) (C0ith + C1ith) × (C2ith) This is the main pion group, where a hit in a Čerenkov detector is required in both up and downstream sections of the spectrometer. Lepton contamination is removed with the calorimeter.

ii) (C0ith + C1ith) × (C2noth) All of the kaons fall into this sample, where a signal is expected from C0 or C1, but not from C2. Contamination from pions and protons exists due to inaccuracies in the Čerenkov counters. Pion flagging was achieved using the trigger timing difference between planes A and B, where the pion trigger arrives approximately 60 ns earlier. Further rejection was achieved by considering the pulse height distribution from C2. This showed a spread of counts, separate from the main concentration at zero, associated to the pions. Proton identification was also achieved using the pulse heights of C0 and C1.

iii) ((C0noth × C1noth) + (C0noth × C1oth + C0oth × C1noth)) × (C2noth) This criteria was used to identify protons, which are not expected to produce any hits in counters. Although a small percent of triggers in this sample could also fit the lepton calorimeter requirements, the combination of no time hit signals could really only be due to protons.

iv) $\overline{(\mathbf{C0ith} + \mathbf{C1ith})}$ × (C2noth) Pions giving out of time signals in the Čerenkovs are grouped here. Only those with self consistent times in C0 and C1 are then accepted. The CEDAR also provides some pion identification for this subgroup.

v) C0oth × C1oth × C2noth Unresolvable pulse heights and timing in C0 and C1 prevented proton and kaon separation in this group, leaving these triggers unidentified.

vi) C2oth A second sample with a large number of unidentified triggers, allowing only proton identification in the subset **C0noth × C1noth × C2oth**.

An example of the particles identified in each of the six timing subgroups, for a 40 GeV/c run, is given in table 3.3.

Group	Triggers	Pions	Kaons	Protons	Electrons	Muons
i	93597	79537	0	0	5668	8572
ii	19037	1127	16732	83	934	62
iii	100109	0	0	100109	199	35
iv	164	108	0	0	6	8
v	143	0	0	0	2	0
vi	863	0	0	720	31	64

Table 3.3: Particles identified in each of the six timing subgroups for a 40 GeV/c run.

3.4 Production of Yields

The runs are analysed to identify the triggers as either protons, pions or kaons as outlined in section 3.3. The raw number of particles identified, are presented in table 3.4. These initial results then have to be adjusted in order to produce the true particle yield at the target. The individual corrections required to produce the true yields are now reviewed.

3.4.1 Detector and Selection Efficiencies

The main efficiencies that need to be included are those of the TOFs, calorimeter, Čerenkovs, trigger and selection procedure. The selection efficiency and Čerenkov detector efficiencies have not been recalculated for this independent analysis, as the results are for comparative purposes, and the efficiencies are very close to unity. The misidentification rates between the pions, kaons and protons are also neglected, as again these are low. Misidentification as an electron is included, a correction that is largest at low momenta, around 2.5% for pions and kaons at 15 GeV/c, described in Bonesini (1996).

3.4.2 Prescales

To restore the downscaled pion component to that of the true beam, the prescaling factors must be removed. The prescales are calculated from the various trigger rates in a given run. There are two prescales. *ScaleH* is for the heavy particles (protons and kaons) which appear regardless of the Čerenkov pion veto. *ScaleL* is for the light particles (pions) which are only present in the sample without the veto. The prescales are simply the number of triggers on tape divided by the total number of triggers. The unscaled number of particles is produced by dividing by the relevant prescale. The

p/z (GeV/c)	Target (mm)	Angle (mrad)	π	K	p	ScaleH	ScaleL	POT (10^{13})
15.0	100	0.000	86500	1504	103598	0.927	0.0765	25.03
20.0	100	0.000	91802	4858	111323	0.844	0.0732	12.98
30.0	100	0.000	81665	12141	104975	0.530	0.0488	8.183
40.0	100	0.000	81277	17352	103724	0.289	0.0331	7.698
67.5	100	0.000	82834	19690	109279	0.326	0.0593	10.83
135.0	100	0.000	71227	8372	105786	0.054	0.0203	10.45
-15.0	100	0.000	86349	2273	84479	0.960	0.0439	51.91
-40.0	100	0.000	90270	33256	75480	0.730	0.0356	9.493
-67.5	100	0.000	106943	45503	47943	0.883	0.0672	17.22
40.0	300	0.000	79650	17815	107460	0.115	0.0128	8.357
40.0	200	0.000	83497	17821	107824	0.168	0.0191	7.605
40.0	T9	0.000	76069	16606	101943	0.114	0.0124	8.441
15.0	200	0.000	81244	1486	101341	0.868	0.0751	14.06
15.0	300	0.000	88982	1619	112477	0.825	0.0741	12.12
40.0	100	15.000	71414	15186	101906	0.854	0.1696	38.33
40.0	100	11.250	84390	15412	116290	0.535	0.0850	8.584
40.0	100	5.625	90432	16498	106633	0.325	0.0355	8.230
40.0	100	3.750	88929	17058	104174	0.300	0.0319	7.938
40.0	100	1.875	83321	16987	102502	0.293	0.0333	7.528
40.0	100	-5.625	90414	16684	106682	0.328	0.0364	8.321
40.0	100	-11.250	83945	15743	115884	0.573	0.0923	8.489
40.0	100	-15.000	76400	15403	120819	0.847	0.1667	10.13
15.0	100	30.000	72082	1010	103689	0.989	0.1567	49.61
15.0	100	22.500	79086	1262	104512	0.972	0.1199	38.60
15.0	100	15.000	84521	1341	103758	0.955	0.0896	31.81
15.0	100	10.000	87257	1507	104613	0.930	0.0755	26.65
15.0	100	5.000	86982	1542	103691	0.927	0.0734	24.89
15.0	100	-10.000	88292	1560	105639	0.927	0.0756	27.38
15.0	100	-15.000	84804	1380	104587	0.946	0.0888	29.32
-40.0	100	3.750	94815	32043	74890	0.853	0.0431	8.490
-40.0	100	1.875	92114	32608	74983	0.840	0.0422	8.162
-40.0	100	-1.875	93420	32158	72892	0.846	0.0423	8.191
-40.0	100	-3.750	93902	31356	74102	0.853	0.0428	8.443
-40.0	100	-5.625	95734	30885	75892	0.871	0.0466	9.355
-40.0	100	-11.250	91877	27583	79691	0.939	0.0735	14.77
-40.0	100	-15.000	85859	24850	78912	0.965	0.0974	22.53

Table 3.4: Summary of identified particles tabulated with the corresponding momentum, charge, angle of emission and target thickness. Also listed are the prescale factors and POT for the respective runs.

scalers $sspya1 - 2$ and $sspyb1 - 5$, hold the number of triggers for the conditions as defined in table 3.5. Recall that the trigger logic differs between runs. The corresponding prescale factors for the two momentum conditions are given in equations 3.2 and 3.3.

Scaler	Definition
$sspya1$	total triggers on tape
$sspya2$	$(\mathrm{B1} \times \mathrm{TOF2} \times \overline{(C0 + C1)}) \times (\mathrm{B2} \times \mathrm{TOF4} \times \overline{C2}) \times \mathrm{GATE}$
$sspyb1$	total triggers on tape ($= sspya1$)
$sspyb2$	$(\mathrm{B1} \times \mathrm{TOF2}) \times (\mathrm{B2} \times \mathrm{TOF4} \times \overline{C2}) \times \mathrm{GATE}$
$sspyb3$	$(\mathrm{B1} \times \mathrm{TOF2}) \times (\mathrm{B2} \times \mathrm{TOF4} \times \overline{C2})$
$sspyb4$	$(\mathrm{B1} \times \mathrm{TOF2} \times \overline{(C0 + C1)}) \times (\mathrm{B2} \times \mathrm{TOF4} \times \overline{C2})$
$sspyb5$	$(\mathrm{B1} \times \mathrm{TOF2}) \times (\mathrm{B2} \times \mathrm{TOF4})$

Table 3.5: Definitions of the trigger scalers used in SPY. The condition GATE refers to a trigger being recorded.

15-20 GeV/c

$$ScaleH = \frac{sspya2}{sspyb4} \quad ScaleL = \frac{sspya1 - sspya2}{sspyb3 - sspyb4} \tag{3.2}$$

30-135 GeV/c

$$ScaleH = \frac{sspyb2}{sspyb3} \quad ScaleL = \frac{sspya1 - sspyb2}{sspyb5 - sspyb3} \tag{3.3}$$

The calculated prescales for each run are included in table 3.4.

3.4.3 Acceptance

The acceptance $\mathcal{A}$ of the spectrometer is a combination of the geometrical acceptance, (solid angle acceptance $\Delta\Omega$ and transmitted momentum bite $\Delta p/p$), with the particle transmission coefficient $\mathcal{T}$:

$$\mathcal{A} = \Delta\Omega \frac{\Delta p}{p} \mathcal{T} \tag{3.4}$$

The collimators are responsible for the fixing the geometrical acceptance and have separate settings for above 40 GeV/c momenta, and for 40 GeV/c

and below, to allow for the increased rate of particle production at higher momenta. The study estimated the geometrical acceptance as $(16.53 \pm 0.54) \times 10^{-3}$ μsr%$\Delta p/p$ for $p \leqslant 40$ GeV/c and $(3.22 \pm 0.19) \times 10^{-3}$ μsr%$\Delta p/p$ for $p > 40$ GeV/c, see Ambrosini et al. (1999).

The transmission coefficient accounts for particle losses along the beamline and was calculated with the TURTLE beam transport simulation package, (Brown and Iselin, 1974). To allow testing of the simulation package, special runs were undertaken where only protons were recorded. Beam profile comparisons between these proton runs and simulations at TOF2 , where the beam is widest, agreed well. In the downstream half of the beamline, the transmission rates where 8% higher in the simulation than data.

The transmission coefficient was broken down into $\mathcal{T}_A^{\pi,K,p}$, the transmission in the first half of the beamline that agreed well with data, and $\mathcal{T}_B^{\pi,K,p}$ which was corrected by the ratio between the transmission of the protons in TURTLE and data. Due to differing nuclear cross-sections, predicted transmissions for pions, kaons and protons will be different. There is no variation attributed to charge.

The original TURTLE simulation is reported in Moffitt (1997), and the corrections are outlined in Tabarelli de Fatis (1997a). Values of the spectrometer acceptance for each momentum and particle type, including transmission coefficient, as used in this analysis, are given in table 3.6. These values were later updated for the final SPY results after additional refinements of $\mathcal{T}_B$.

3.4.4 Correction for Particle Decays

Recall that the particle identification process required at least 1.5 GeV/c of energy to be deposited in the calorimeter, implying that the candidates must reach the calorimeter to be accepted. To account for pion and kaon decays before the calorimeter, the yields need to be scaled back up by the decay probability:

$$P(L) = e^{-m_x L/|p|\tau_x c} \tag{3.5}$$

where x is the particle type, c the speed of light, τ_x the proper mean lifetime, and m_x the mass. The length L is 539 m. This correction is most important at low momenta where, for example at 15 GeV/c, the beamline represents 4.8 decay lengths to a kaon.

It has been noted that the assumption of the loss of all particles decaying before the calorimeter is invalid, as a fraction of these have decay products which can fake a meson signal in the calorimeter, and earlier in the beamline.

p (GeV/c)	Particle	$\mathcal{A}$ μsr%$\Delta p/p$
135	Pion	2.55×10^{-3}
	Kaon	2.62×10^{-3}
	Proton	2.43×10^{-3}
67.5	Pion	2.53×10^{-3}
	Kaon	2.61×10^{-3}
	Proton	2.40×10^{-3}
40	Pion	12.84×10^{-3}
	Kaon	13.17×10^{-3}
	Proton	12.14×10^{-3}
30	Pion	12.26×10^{-3}
	Kaon	12.69×10^{-3}
	Proton	11.57×10^{-3}
20	Pion	11.74×10^{-3}
	Kaon	11.98×10^{-3}
	Proton	11.14×10^{-3}
15	Pion	9.33×10^{-3}
	Kaon	9.61×10^{-3}
	Proton	8.87×10^{-3}

Table 3.6: The calculated spectrometer acceptances used in this analysis. (Adapted from Bonesini, 1997a, table 4)

This effect is most important at intermediate momenta, changing the yields by as much as 4%. The correction is fully described in Tabarelli de Fatis (1997b).

3.4.5 Strange Particle Decays

Strange particles decaying shortly after their production in the target can increase the pion and proton yields, especially at low momenta. The decays $K_s^0 \rightarrow \pi^+\pi^-, \Lambda \rightarrow \pi^- p, \Sigma \rightarrow n\pi^+$ were studied in the H6 beamline, with both a GEANT simulation and a fast, purpose built generator. The study reported in Bonesini (1997b) revealed 4.8% at 7 GeV/c, down to 1.2% at 135 GeV/c, of the pion yield was from strange particle decays. The contamination decreases with emission angle. The report also cited a proton yield from strange particles of 14.4% and 2.1% in 7 and 135 GeV/c runs respectively. By comparing the two simulation methods, an error estimate of 25% was derived for the correction. Whether or not the correction should be

applied depends on the use of the SPY results. Including the reduction will give the true pion and proton productions at the target, neglecting it would be preferred when considering the secondary beam at distances greater than the strange particle decay lengths.

3.4.6 Normalisation to Protons on Target

To determine the relative yields between runs, each run is normalised to the number of protons on target (POT) which is measured with the secondary emission monitors (SEMs). Calibration measurements were made on the SEMs before and during the SPY run, against the beam current transformers (BCTs) of the WANF. These measurements showed the titanium SEM with an accuracy of 1.3% and ±1% stability level to be better than the aluminium SEM. This allowed the overall proton intensity delivered to be determined to within an uncertainty of 1.7%. The calibration provides an absolute scale from the recorded count to true POT as $(1.07 \pm 0.01) \times 10^4$. The complete calibration of the SEMs in the SPS is reported in Marchionni (1996). Absolute POT for each run is noted in column nine of table 3.4.

The profile scanning SEMs gave the fraction of the beam protons hitting the plate targets as 0.988±0.007, (protons miss the target in the vertical plane). No protons missed the T9-like target.

3.4.7 Empty Target Subtraction

At each momentum and charge, plus selected angles, runs were taken without a target (empty target runs) to measure the number of interactions between the protons and objects in the target area such as the SEMs, air and the vacuum windows. These runs were analysed in the same manner as outlined in section 3.3, and the raw number of particles identified is summarised in table 3.7. Yields are then produced from these numbers and subtracted from those of the target runs, to give the true production from the target alone.

To investigate how the background subtraction should be undertaken, the backgrounds as a percent of total yield of the 100 mm target was plotted against momentum. This was repeated for each particle type. The only corrections from the above sections that do not cancel are the prescales and POT normalisation, both of which were included. The individual plots were fitted with constant functions of momentum, shown in figure 3.5. These plots show only small variations with momentum and no systematic trends. Moreover, the constant values between the particle types are fairly consistent.

Plots were then constructed with combinations of positive, negative and all particles, see figure 3.6. Again, no large fluctuations or trends with mo-

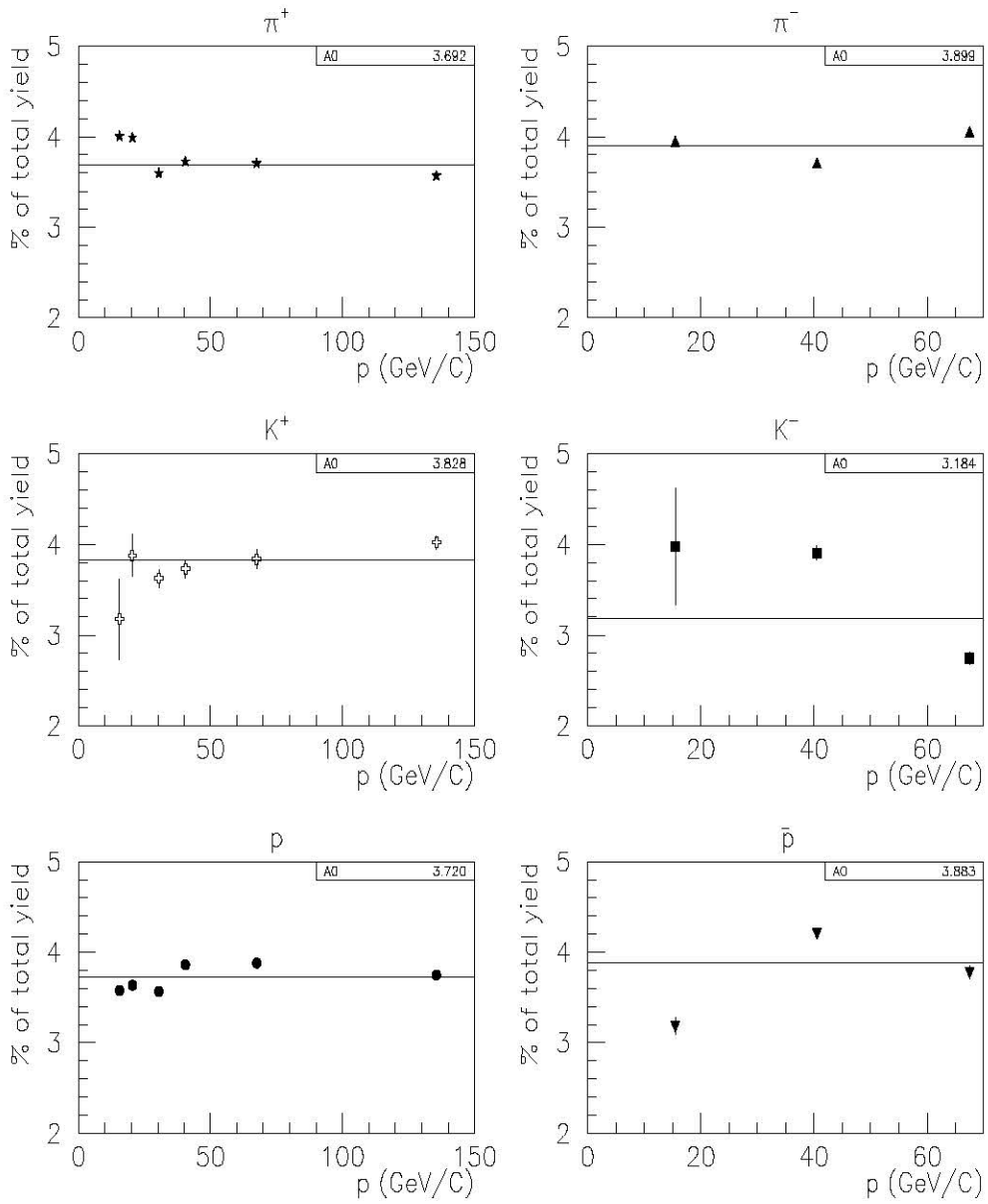

Figure 3.5: Background from empty target runs, as a percent of total yields, versus momentum. A constant function has been fitted for each particle type, of value A0. The error bars represent statistical errors only.

p/z (GeV/c)	π	K	p	ScaleH	ScaleL	POT (10^{13})
15	7631	53	4015	1.07314	0.175757	23.99
20	7754	295	6339	1.03720	0.121445	16.54
30	14207	1535	13081	0.78524	0.100057	19.29
40	8427	1525	9427	0.97761	0.132294	5.357
40	12393	1972	14427	0.98733	0.188436	17.40
67.5	6316	1360	7636	0.98230	0.203893	6.473
135	31248	4028	47432	0.40012	0.152442	17.12
-15	6752	38	1129	1.24264	0.267861	16.86
-40	10392	2350	5746	1.00433	0.084070	12.49
-67.5	12610	1894	2807	0.99770	0.142328	23.63

Table 3.7: Summary of identified particles in the empty target runs. The second 40 GeV/c entry is for the 11.25 mrad angle run.

mentum could be inferred from these plots, and so the distributions were fitted with constant functions.

The main SPY analysis uses a constant background for all momenta and particle types of 3.5%. This is consistent with the constant value independently obtained herein of 3.7%. A background of 3.5% corresponds to a target length of approximately 2.8 mm or 0.68% of an interaction length. Adding together all the materials in the target area equates to 0.6% of an interaction length, in fair agreement with the measured length. A global constant background is preferred, rather than a multi variable background function, due to the low coverage of the empty target runs taken. The analysis of the 11.5 mrad run showed a decrease in background with angle, as might be expected.

3.5 Results and Comparisons

The independent analysis, described in section 3.3, was primarily to be used as a comparison of the raw number of particles identified. However, to also allow the comparison of trends with secondary angle and momentum, as well as to check normalisation procedures, prescale and POT values, yields have been produced. Data from table 3.4 was adjusted using the corrections described in section 3.4 except for strange particle decays, and small effects previously noted as negligible, to produce the secondary particle yields. All SPY results shown in this section are from this independent analysis, except

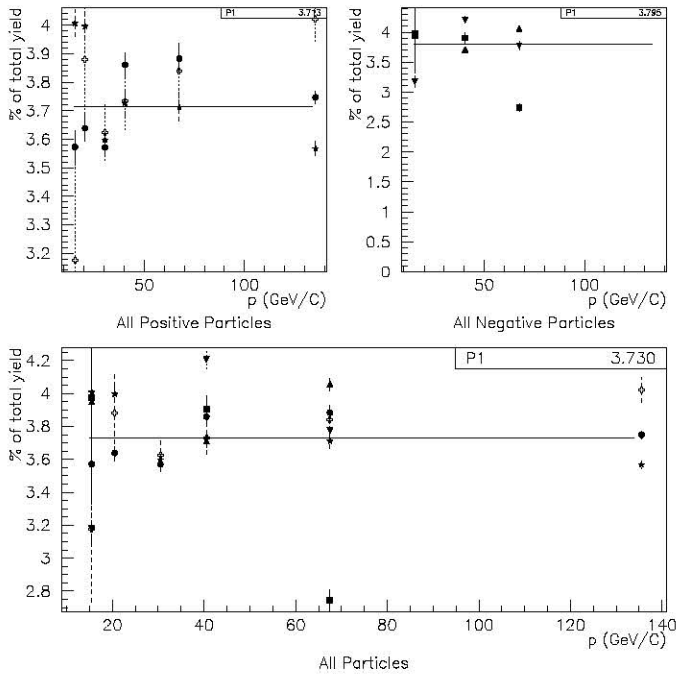

Figure 3.6: Background yields, combined positive, negative and all particles, fitted with constant functions. The symbols represent the same particles as in the individual plots of figure 3.5.

those of section 3.5.4. Only statistical errors were considered when producing the plots of the yields. In general, these errors are smaller than the symbol size of the plots.

The main SPY analysis was more detailed and comprehensive than this independent analysis, achieving the goals of a 3% error on particle ratios and a 5% error on particle fluxes. However the importance of this analysis was as a check of analysis procedure. Good agreement was obtained at the particle identification stage. All values in table 3.4, including prescales and POT, agreed with those obtained at the same stage in the main SPY analysis. The shapes of the yields, with respect to angle and momentum, also agreed.

3.5.1 Momentum Dependence

The secondary particle yields as a function of secondary momentum are shown in figure 3.7 for the 100 mm target in the forward angle. These

distributions compare well with those of a preliminary SPY analysis, Collazuol (1997), and also the final SPY result, Ambrosini et al. (1999), with the main differences arising from the yield corrections that were not included. Also shown are two points from the Atherton experiment. As the Atherton experiment used 400 GeV/c primary protons, its two lowest points, 60 and 120 GeV/c, correspond, in $x_{Feynman}$, (secondary momentum over beam momentum), to the 67.5 and 135 GeV/c points of SPY, and are accordingly plotted in figure 3.7. However the invariant cross section formula, equation 3.9, requires the points to first be scaled by $(450/400)^2$. The agreement between this analysis and the Atherton results represents a confirmation of the SPY data taking and analysis procedure.

The particle ratios were also calculated, and are plotted in figure 3.8. These results compare well with the preliminary and final SPY studies, as well as being reasonably close to the Atherton values.

3.5.2 Angular Dependence

The angular scans at 15 and 40 GeV/c were also analysed and the yields are given in figure 3.9. Both the negative and positive scans were analysed at 40 GeV/c, but only the positive for 15 GeV/c. Positive and negative angles were taken, but as can be seen in table 3.4, the results are quite symmetric, and so only the positive angles are plotted. Again, comparisons between this and the main SPY analysis showed acceptable agreement.

The particle ratios were calculated, see figure 3.10, and comparisons with other analyses again proved satisfactory.

3.5.3 Target Length Dependence

The dependence of the particle yields on target thickness was studied, with target lengths of 100, 200 and 300 mm used during the 15 and 40 GeV/c runs. Early predictions of secondary production were based on naïve absorption models where secondaries re-absorbed into the target did not produce tertiary particles. Using such a model, see Malensek (1981), the length dependence for the production of secondaries is:

$$f(L) = \frac{e^{-L/\lambda_s} - e^{-L/\lambda_p}}{1 - \lambda_p/\lambda_s} \tag{3.6}$$

where λ_s is the absorption length for the produced secondaries, in particular $\lambda_\pi = 57.83$ cm and $\lambda_K = 65.24$ cm, and $\lambda_p = 43.26$ cm represents the absorption length for the incoming protons, (values quoted are for beryllium

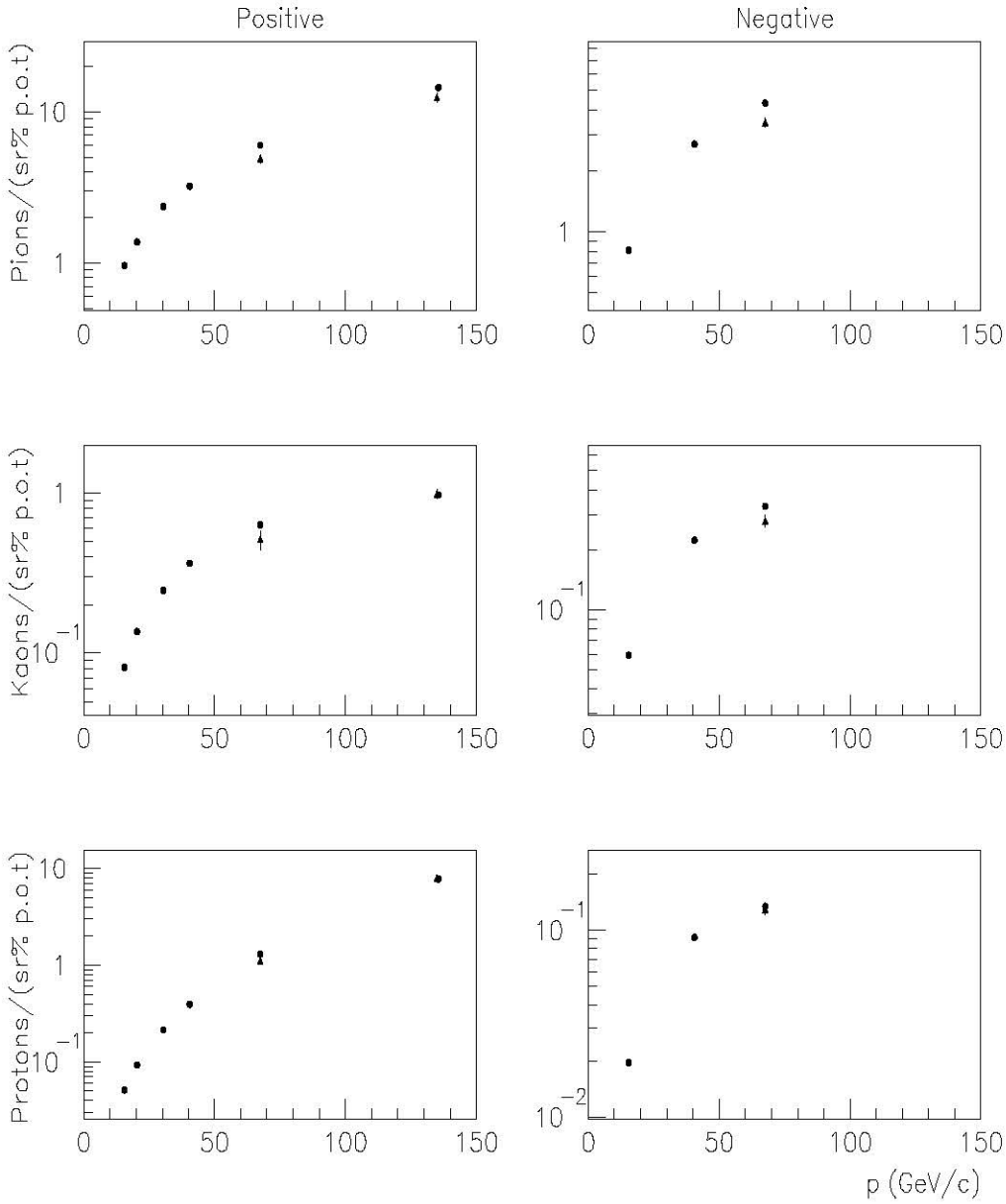

Figure 3.7: Momentum distribution of particle yields from a 100 mm target, at 0 mrad, with positively and negatively charged particles on the left and right respectively. The Atherton results are shown as triangles.

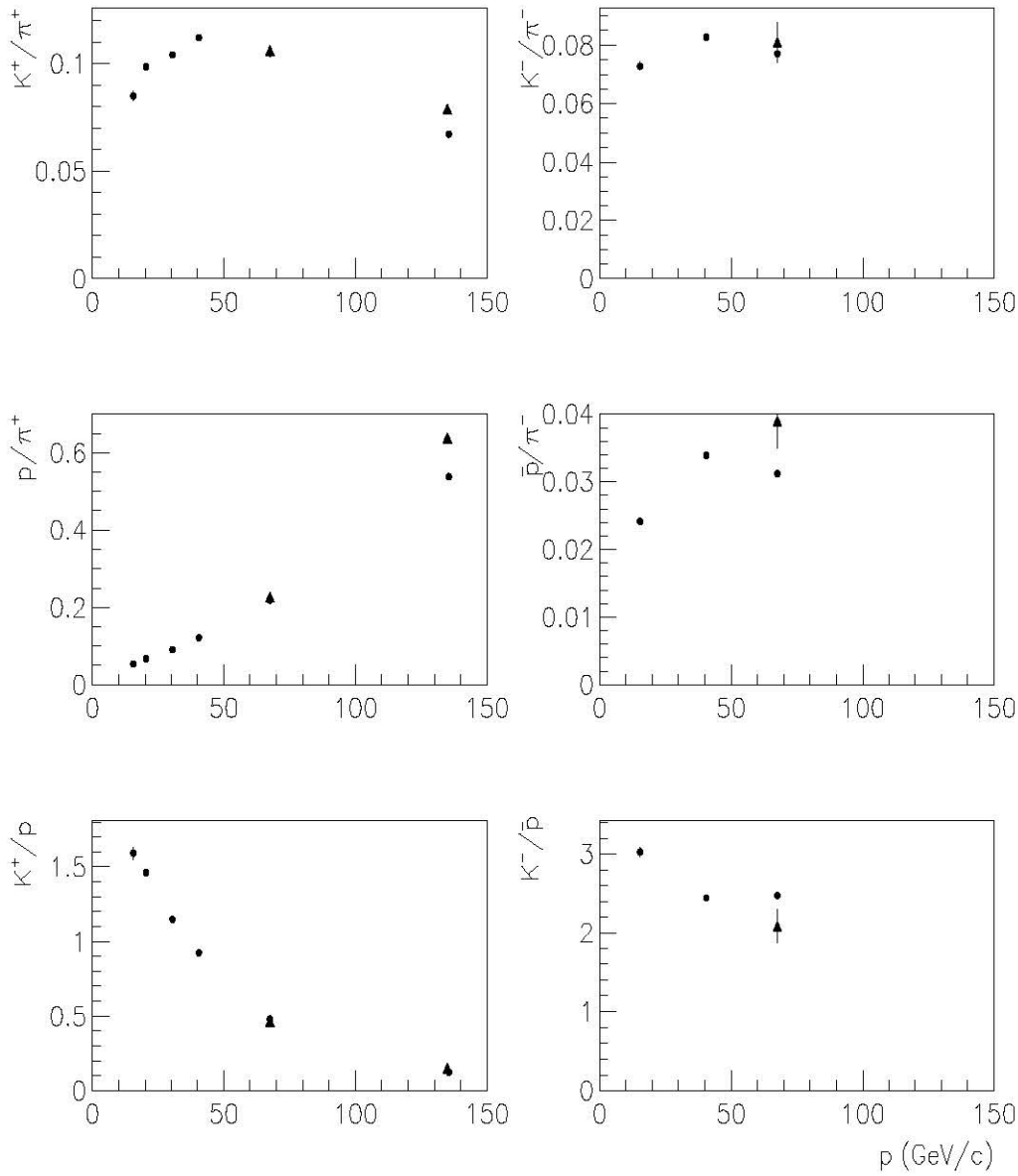

Figure 3.8: Momentum distribution of particle ratios from a 100 mm target, at 0 mrad, with positively and negatively charged particles on the left and right respectively. The Atherton results are shown as triangles.

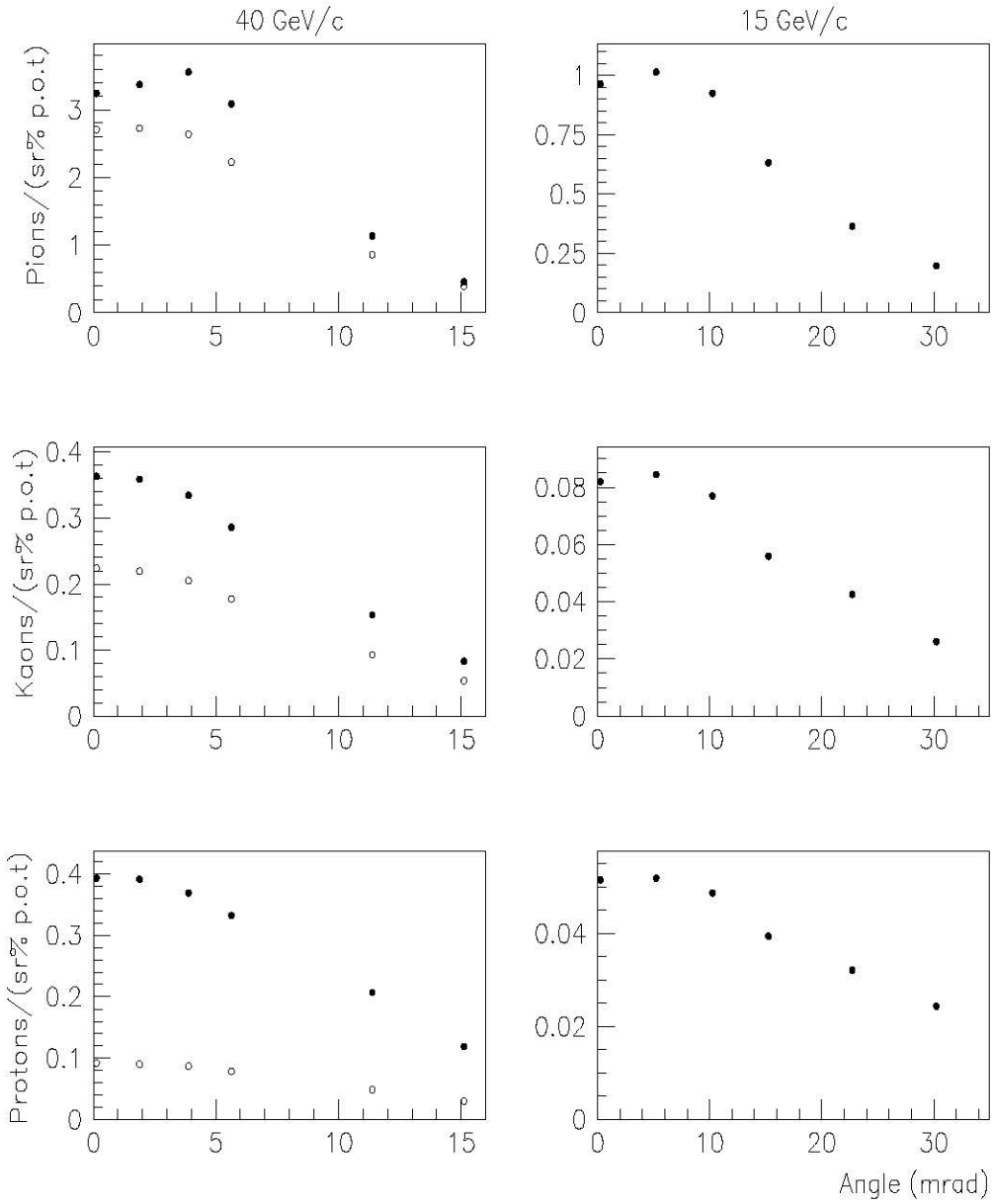

Figure 3.9: The angular distribution of particle yields from a 100 mm target at 40 GeV/c (left) and 15 GeV/c (right). In the 40 GeV/c plots, the empty circles represent negatively charged particles.

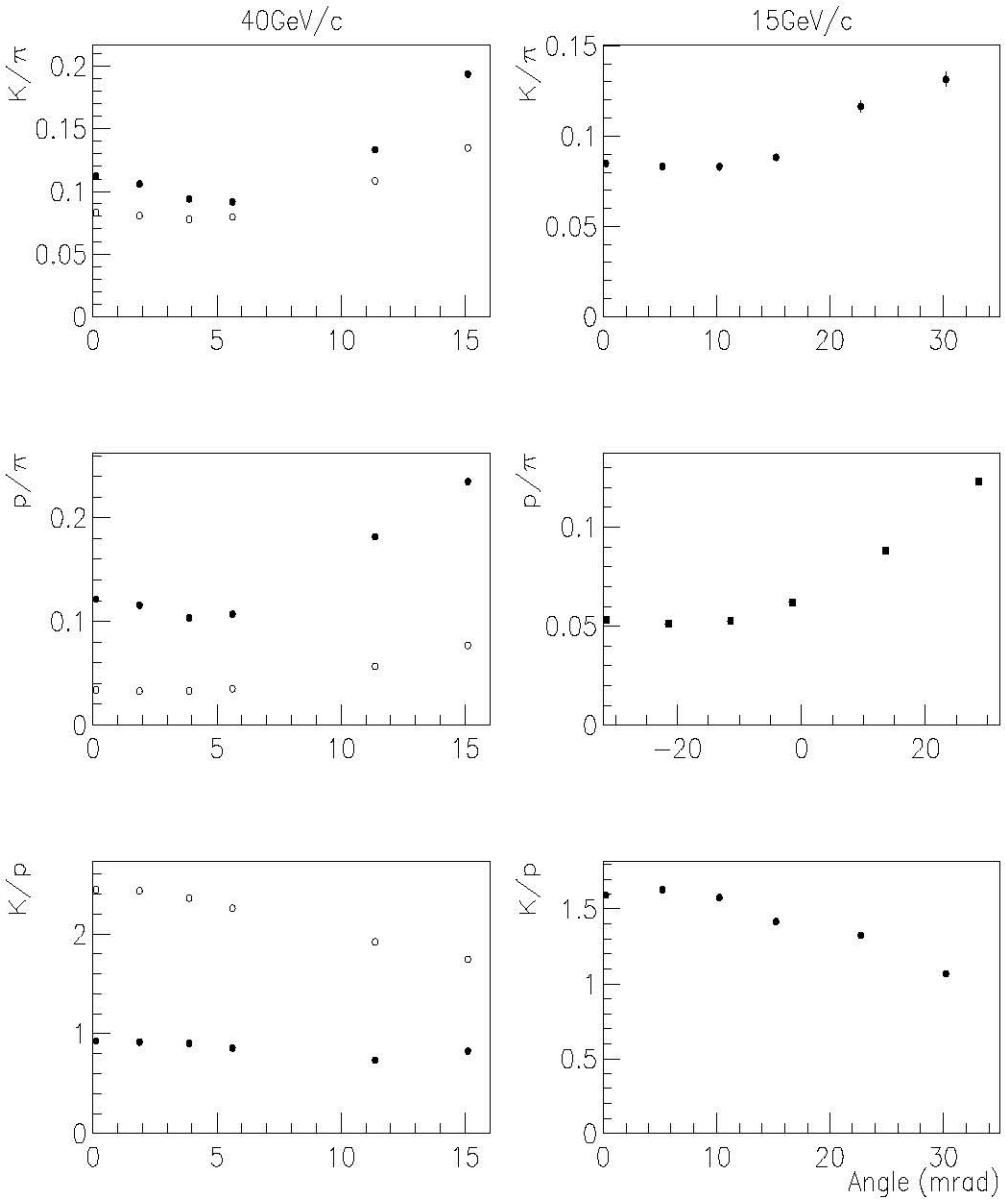

Figure 3.10: The angular distribution of particle yields from a 100 mm target at 40 GeV/c (left) and 15 GeV/c (right). In the 40 GeV/c plots, the empty circles represent negatively charged particles.

targets). The dependence on λ implies that the kaon to pion ratio varies slowly with target length. Secondary protons are described by:

$$f(L) = \frac{L}{\lambda_p} e^{-L/\lambda_p} \tag{3.7}$$

The measured yields as a function of target length were compared with these models. Figure 3.11 shows the comparison, where the yields have been normalised to that of the 100 mm target. Further, the data points have been offset around their nominal target length to keep the plot clear. Also included is the T9-like target, which includes a length of 300 mm of beryllium.

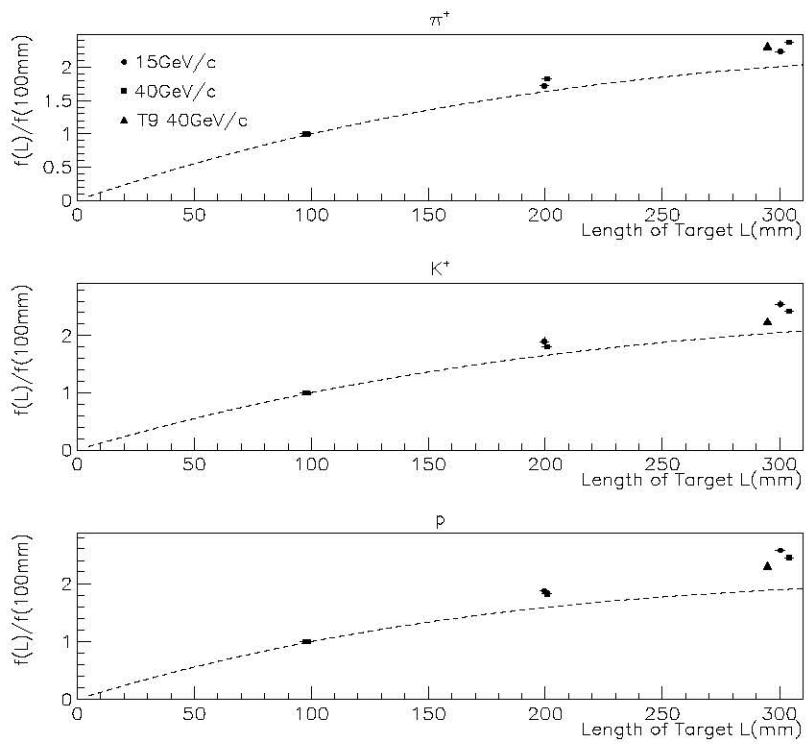

Figure 3.11: Particle yields from 100, 200 and 300 mm target lengths at 15 and 40 GeV/c, in the forward direction. The yields are normalised to those of a 100 mm target. The dotted line shows the prediction of the naïve absorption model

There is a clear discrepancy in figure 3.11 at longer target lengths, where the measured yield is underestimated by the theory. The naïve absorption

model is shown not to be sufficient in describing the data, implying that tertiary production from re-absorbed secondaries occurs, an effect that would become more relevant with increasing target length.

The study also shows good agreement between the T9-like target and the 300 mm plate target in the forward direction. Angular emission with respect to target length is expanded on in section 3.5.4.

3.5.4 Other SPY Results

The other findings drawn from the SPY data set, not considered in this independent analysis, are briefly outlined here for completeness.

Target Shape Dependence

Two types of target were used, the flat plate and the cylindrical T9-like target. The T9-like target had 300 mm of beryllium, and as expected produced the same secondary yield in the forward direction as the 300 mm plate target, within errors. Due to less absorption in the T9-like target than in the plate in the lateral direction, a higher yield is expected for angles above 3 mrad. This increase was observed in the data, and is well modeled by:

$$f(\theta, L) = \int_0^L exp\left(\frac{-t(x)}{\lambda_p}\right) \; exp\left(\frac{-t_{res}(x,\theta)}{\lambda_s}\right) \; \frac{dx}{\lambda_p} \tag{3.8}$$

where, θ is the production angle, L is the target length, x is the longitudinal position, t is the target thickness, t_{res} is the thickness a secondary particle must cross to escape the target and $\lambda_{p,s}$ are the interaction lengths of the proton and secondary, (taken from Bonesini et al., 1996). To account for tertiary production, equation 3.8 is scaled by the ratio of the yield from the 300 mm target in data to that from the naïve absorption model, of section 3.5.3. Steps are seen in the angular distribution of the yields, which are caused by the discrete structure of the target. Further details can be obtained from Ambrosini et al. (1999).

Inclusive Invariant Cross Sections

The inclusive invariant cross section is obtained from:

$$E\frac{d^3\sigma}{dp^3} = 100Y\frac{E}{p^3}\frac{A}{N_0\rho\lambda_p f(L)} \tag{3.9}$$

where Y is the yield, A, ρ, L are the atomic weight, density and length of the target respectively, N_0 is Avogadro's number, E is the energy and p is the momentum. Equation 3.6 or 3.7 is used for the target production efficiency $f(L)$. To remove the lack of tertiary production in the modeled equations, the cross section is calculated at each target thickness, for a given momentum, and then extrapolated to zero target thickness. The results of this are given in (Ambrosini et al., 1999, table 15 and figure 21), and extends previous p-A interaction studies, most recently Barton et al. (1983), to higher energies, where data was previously unavailable.

SPY with a Carbon Target

Proposed new neutrino beam experiments are also considering the use of graphite targets, whose mechanical properties could allow up to twice the incident beam intensities of beryllium targets. Whilst thought has been given to a second SPY experiment, studying protons on carbon with a similar momentum range, see Elsener and Tabarelli de Fatis (1997), it should be noted that the SPY results can already be translated to targets of different materials. The invariant cross sections scales with the atomic weight of the target like:

$$E\frac{d^3\sigma^{A_1}}{dp^3} = \left(\frac{A_1}{A_2}\right)^{\alpha} \cdot E\frac{d^3\sigma^{A_2}}{dp^3} \tag{3.10}$$

where α is a function of incident hadron type and momentum, as well as p_T, x_F of the outgoing particle. Current values of α would mean that scaled SPY results would have a 7-12% total error. See Bonesini (1998) for more details.

Chapter 4

Neutrino Event Classification

NOMAD was designed as a high statistics neutrino detector, tagging a neutrino event when there was a signal from the two trigger planes that bracket the transition radiation detector, without a signal from the veto. Over four years of running, NOMAD has collected a large number of such triggers. The $\nu_\mu \rightsquigarrow \nu_e$ oscillation search requires true neutrino events to be extracted from these triggers, and subsequently have them classified according to the type of neutrino interacting. Only then can the events be used to produce a ν_e energy spectrum, relative to the ν_μ, which might show inconsistencies, when compared to expectation, indicative of oscillations.

Neutrino charged current (CC) events are classified by the outgoing (leading or prompt) lepton, here either a muon or an electron. Event classification must therefore identify muons and electrons in the data, and then determine if they are from the primary vertex. In NOMAD, this primary vertex is defined as the first drift chamber vertex in terms of its z position, (with the exclusion of vertices from tracks heading backwards using timing information).

Neutral current (NC) events have a neutrino as the outgoing lepton and so cannot be classified according to leptonic flavour by NOMAD. This renders them unusable in the oscillation search. However NC events can still initiate a neutrino trigger. Electrons and muons are created by photon conversions or hadron decays within the hadronic shower of the struck nucleus. These *non prompt* leptons can be misinterpreted as the leading lepton, and hence wrongly classify the event as CC, creating a background to the true CC event spectrum. Further, there exist some muons, unfiltered by the earth shield, traveling with the neutrino beam. If not vetoed, (as they have either geometrically missed the veto plane, or the veto did not activate due to inefficiency), they can interact in the target to fake ν_μ CC events, (with delta electron production causing fake ν_e CC events). These muons are called

through-going. The rejection of these backgrounds is prioritised when developing the selection algorithms.

Rigorous event selection is not only of interest to the direct $\nu_\mu \rightsquigarrow \nu_e$ oscillation search, but also to the empirical parametrisation of chapter 6. It requires clean samples of ν_μ, $\overline{\nu}_\mu$ and $\overline{\nu}_e$ to predict the ν_e flux, which is later required by the oscillation search itself.

The selection criteria used will be described in the following section. The implementation of the criteria is in two stages. The initial loose selection of events is achieved in routines written with the Calisto package, (Cervera et al., 1998), which runs off the standard NOMAD data summary tapes (DSTs), (Varvell, 1997). The Calisto package is based on Camel, (Bird, 1994), and allows the user to work with the data in terms of tracks, vertices and clusters within each event. HBOOK, (Bunn et al., 1995), "ntuples" are produced with Calisto containing an array of variables, relevant to event selection and presentation, for each event with a candidate leading lepton. More stringent requirements are then imposed on the events in the ntuples via a purpose coded FORTRAN programme named Readall. This programme produces a wide variety of distributions of the ultimately selected and classified neutrino events.

Note that throughout this chapter, unless specifically mentioned, muons shall refer to both charges, and electrons to both electrons and positrons.

4.1 Common Lepton Selection Criteria

Many of the requirements for the selection of a neutrino event are common to both ν_μ and ν_e. These include conditions, or cuts, relating to the quality of the event or the removal of through-going muons. Also common is the recovery of obvious leptons and the identification of prompt leptons. These cuts will now be discussed, in the approximate order that they are applied.

4.1.1 Quality and Filter Cuts

Recon Filter

As mentioned earlier, events with high track and hit density are difficult to reconstruct, they also require long times and may be reconstructed with errors or not at all. It is therefore desirable to remove these events before the main reconstruction. The removal of contamination to the neutrino data from through-going muons, cosmic ray muons and neutrino interactions in the magnet, is also useful. Thus a filter is applied during the initial reconstruction of events. This filter must reject most of the background whilst

also preserving all the neutrino events that are suitable for analysis. The four main conditions of this filter are:

- To reject large multiplicity events from the front I of the magnet, the number of hits in the first drift chamber plane, called the veto plane, must be less than 30.
- The number of wires hit in a plane is limited to eight.
- The total number of hits in the transition radiation detector must be less than 200.
- The total number of in time drift chamber hits must be less than 5000.
- For single track events, a fiducial volume check is applied, to rule out events from the magnet or through-going tracks. Further, these single tracks must have momentum greater than 0.5 GeV/c.

Calisto Filter

Calisto has a number of inherent selection conditions, designed to filter out badly formed, unworkable or erroneous data:

- DST Info: Data actually exists for this event.
- Online Error: No error flags stored from runtime errors.
- Muon Chambers: No muon chamber error flags.
- Reconstructed Vertex Summary Bank: Bank must exist in DST.
- Vertex: A vertex was reconstructed for this event.
- Primary Tracks: Number of primary tracks is between 1 and 1000.

An event failing any of these is rejected.

Monte Carlo Event Filter

The selection efficiency, see section 4.4, will be determined from simulated events. Before this process can take place "truncated" Monte Carlo events must be removed. These are events that are dumped before reconstruction for being too complicated and time consuming. Also, the empirical parametrisation only uses low exchange energy events, so a mix of quasielastic, resonance and deep inelastic scattering Monte Carlo is required. To avoid double

counting of quasielastic and resonance events present in the deep inelastic Monte Carlo, it must be limited to $W^2 > 1.4$ GeV^2, (see section 6.3.2 for an in depth explanation). A further cut to all three Monte Carlo samples is against the modulus of the generated Fermi momentum of the struck nucleus, $p_F < 1$ GeV. This cut removes the unphysically long tail, (up to 4 GeV), in the Fermi momentum distribution of the generated events. The W^2 cut reduces the Monte Carlo sample by 6.1%, and the p_F cut reduces the sample by a further 4.1%.

Fiducial Volume

The drift chamber target presents an x, y area of 3×3 m^2, roughly perpendicular to the neutrino beam direction, over a z distance of 400 cm. A reduced volume is used in this analysis, as interactions in the magnet can create vertices in the outer edges of the drift chamber that are not of interest in this study. The fiducial volume chosen is $|x| < 130$ cm, -125 cm$< y < 135$ cm, and $z < 405$ cm with minimum z varying depending on experimental setup, as detailed in table 4.1. The different setups are due to the partwise installation of drift chamber modules in 1995, and the removal of the first drift chamber module to allow for the STAR detector in 1997 and 1998, see section 2.5.4. The 5 cm offset in fiducial y is due to the slope and offset of the beam, which means the beam crosses more of the magnet at the bottom of the detector than the top, so a larger drift chamber region needs to be excluded. The fiducial volume cut is first implemented in Calisto, and later tightened by Readall for events with only one track. These one track restrictions reduce the $|x|$ and $|y|$ maxima by 10 cm, and use z as defined in the second row of table 4.1. Calisto allows Monte Carlo events in a 320×320 cm^2 area. In Readall, this is reduced to the standard fiducial area after rotation of the events to the NOMAD frame, see section 2.7.1.

	95 4 mod	95 8 mod	95 11 mod	1996	1997	1998
min z (cm)	265.0	115.0	5.0	5.0	40.0	40.0
1 track (cm)	270.0	120.0	15.0	15.0	45.0	45.0

Table 4.1: Minimum z allowed for the fiducial volume.

Quality Cuts

Imperfections in the reconstruction of events, see section 2.7.3, manifest themselves as unreasonable momenta or energies, and poor track fitting.

Events with large numbers of drift chamber hits, corresponding to large numbers of tracks, are the hardest to reconstruct correctly. The following cuts on event quality are designed to remove potentially ill reconstructed events:

- Unused Hits: The fraction of drift chamber hits unused in track reconstruction must be less than 0.75.
- Charged Tracks: The number of charged tracks associated to the primary vertex must be less than 50.
- Visible Energy: The total reconstructed energy of the event must satisfy E_{vis} less than 300 GeV.

4.1.2 Vetoing Through-Going Muons

As mentioned earlier, muons generating signals in the drift chamber that were not rejected by the veto counters are termed through-going muons. The empirical parametrisation analysis will need to include one track neutrino events, as these comprise $\sim 17\%$ of the low ν events used. Therefore, care must be taken to avoid selecting through-going muons, which are easily confused with one track neutrino events. The drift chamber veto plane, (the first plane), is used for further rejection of through-going muons. As muons are likely to cause a hit in the chambers immediately upon entering, they can be distinguished from neutrino events by the number of hits in the veto plane, and by the number of hits before the primary vertex if it exists.

In the following, Veto Hits refers to the number of hits in the drift chamber veto plane within a 2.5 cm radius of the backwards extrapolation of the lepton track in question. Tube Hits refers to the number of hits in the drift chamber in a 3 cm diameter tube, 50 cm long in the direction of the backwards extrapolation of the track. The backwards extrapolation occurs from where the primary vertex has been reconstructed.

Table 4.2 shows the upper limits on Veto Hits and Tube Hits for a muon track to be accepted as not being a through-going muon. Events with four or more tracks are not subject to the through-going muon veto. Note that there is no limit on Tube Hits for three track events. These limits were determined from a scan performed by DeSanto and Mishra (1999), of actual muon events from the muon gate trigger, (see section 2.6.2 for a definition of this trigger).

4.1.3 The LEP Condition

To recover true CC events, that might otherwise be removed by the cuts of this section and the next, the LEP condition was introduced. This variable

Tracks	Veto Hits	Tube Hits
1	0	10
2	1	10
3	3	-

Table 4.2: Maximum values of hits for the through-going muon veto, according to the number of tracks in the event.

indicates when a lepton is truly prompt, despite its failing other selection criteria, whilst maintaining a strong rejection of NC events. LEP is defined as the logical OR of the following conditions, (where p_T^{miss} is the missing transverse momentum of the event, usually attributed to neutrino production):

- p_T of the lepton with respect to the hadron shower direction must be greater than 3 GeV. This minimises the probability of the selection of a lepton from within the hadron shower.
- Minimum angle between the lepton and any charged hadron must be greater than 0.3 rad. This vetoes hadron shower leptons.
- The ratio of p_T^{lep}, (the lepton transverse momentum), to p_T^{miss} must be greater than 1.5.
- $\hat{\nu}$, defined below, is a combination of all the p_T variables, (hadron, lepton and missing), and must be greater than 0.5.

The $\hat{\nu}$ variable is the ratio of the difference between p_T^{lep} and p_T^{miss} over the p_T of the hadron:

$$\hat{\nu} = \frac{p_T^{lep} - p_T^{miss}}{p_T^{had}} \tag{4.1}$$

In a CC event, the electron or muon will give a high p_T^{LEP}, balanced by the hadronic shower, so $\hat{\nu}$ will approach 1. An NC event will have a large p_T^{miss}, and so $\hat{\nu}$ will tend to -1.

4.1.4 Prompt Lepton Selection

There are two main criteria for selecting prompt leptons. The data events are scanned three times, once searching for muons, then electrons and then

positrons. Only one candidate prompt lepton is recorded for an event in the ntuple in each search. When more than one candidate exists within an event, the highest momentum candidate is taken. This is enforced after the so-called Phase II lepton identification, (see sections 4.2 and 4.3.1 for a review of the muon and electron Phase II identification respectively, and section 2.7.3 for details of the event reconstruction of which Phase II is a part). For prompt muon searches, the highest momentum candidate from the combined μ^- and μ^+ sample is selected. For electrons and positrons, charge selection is enforced, before the highest momentum candidate is chosen. This is because there are far fewer ν_e than ν_μ and they require a much closer study. Therefore as many candidate positrons and electrons as possible must be placed in the ntuples.

Prompt lepton candidates must also obey a maximum scattering angle limit. The scattering angle is defined as the angle between the lepton and beam directions. The maximum angle is dependent on the number of tracks, as set out in table 4.3.

Cutting against the scattering angle and momentum relies on the fact that the prompt lepton will have most of the momentum of the incoming neutrino, and so should be the highest momentum track, with little divergence from the beam direction. A lepton with a high scattering angle is more likely to belong to the hadron shower. These traits are present even more so in the low exchange energy events of interest to the empirical parametrisation. An event with a large number of tracks will on average have had more momentum imparted to the struck nucleon, so the lepton would be less forward. To reflect this, the maximum scattering angle increases with the number of tracks in the event.

	1 track	2-3 tracks	tracks $\geqslant 4$
Scattering Angle	0.15	0.40	0.99

Table 4.3: Maximum allowable scattering angles in radians for leptons, according to the number of tracks in the event.

4.2 Muon Identification

In this analysis, muons are exclusively identified by the muon chambers. The loose identification of Phase II is that a DC track can be matched to a hit in the muon chambers within 40 cm in the first station, or within 50 cm in the second station. This identification is stored in the DSTs. The selection can

be tightened by considering the goodness of fit between the track and the hit in the muon chamber, and accepting only those combinations with a total χ^2 less than 20, over the four degrees of freedom of the fit, (see section 2.5.10 for a description of the fit). Passing this criteria in either station is sufficient. A quality cut of muon momentum greater than 2.5 GeV is also used to rule out potentially anomalous or coincidental track to hit matching. This is called tight Phase II muon identification.

Prompt muons are accepted according to the criteria of section 4.1.4. The charge of the events is obtained from the direction of curvature in the magnetic field. The charge selection is imposed after all other cuts, to increase the consistency between the acceptances of the two charges.

Cuts against gamma conversions, described in the next section, are the only other constraints placed on the ν_μ and $\overline{\nu}_\mu$ CC candidates. An example of a ν_μ CC candidate is displayed in figure 4.1. It clearly shows the muon, passing through the hadron calorimeter and producing a matched hit in each muon chamber. The muon track is balanced by the hadron shower tracks above it.

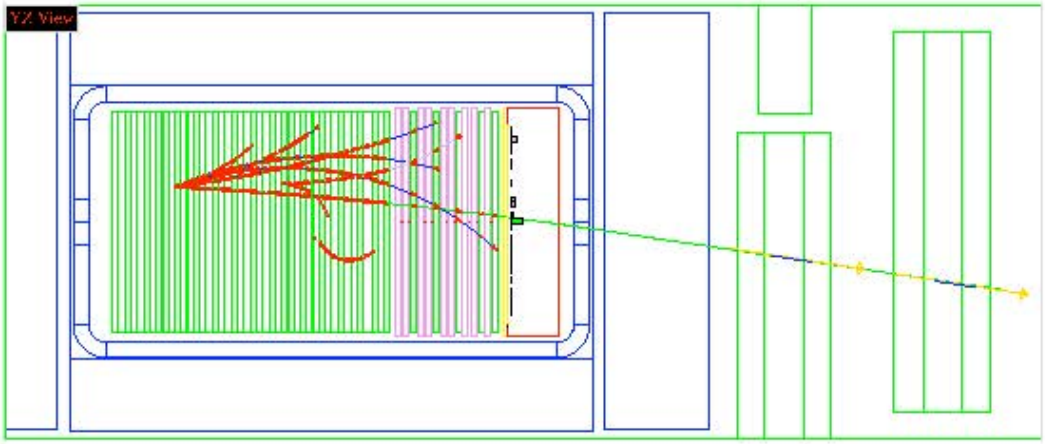

Figure 4.1: A candidate ν_μ CC event as seen in the yz view of the NOMAD event display. The display shows the drift chamber hits and the tracks reconstructed from them, as well as hits in the muon chambers, far right. Energy deposits in the electromagnetic calorimeter are represented by its histogram.

4.3 Electron Identification

4.3.1 Phase II Selection

Electron selection is part of the Phase II reconstruction. Phase II uses information from the transition radiation detector, the preshower, the electromagnetic calorimeter and the drift chamber, (see relevant areas of section 2.5), to ascertain a probability for a particle to be an electron. Of these, the transition radiation detector is the primary source of electron identification.

Transition Radiation Detector (TRD)

The TRD identifies electrons by the transition radiation they produce when traversing the interfaces within the detector. Only particles with a Lorentz factor, γ, above a certain limit, produce this radiation, and for most energies in NOMAD, this is exclusively electrons. This allows for differentiation between electrons and pions, the main contamination to the electron signal.

Electrons are selected using the likelihood function:

$$L = \sum_{i=1}^{N} \log \frac{P(\varepsilon_i|e)}{P(\varepsilon_i|\pi)} \tag{4.2}$$

where $\vec{\varepsilon} = (\varepsilon_1, \varepsilon_2, \ldots, \varepsilon_N)$, with ε_i the energy deposited in the *ith* TRD module ($N \leqslant 9$). $P(\varepsilon_i|e)$ is the probability of an electron producing $\vec{\varepsilon}$, and $P(\varepsilon_i|\pi)$ the probability for a pion, where every charged particle except an electron is assumed to be a pion. The likelihood can only be expressed as in equation 4.2, if the ε_i are independent. This is true for pions, and an acceptable approximation for electrons.

One difficulty with the TRD is that it registers energy deposits in vertical straw tubes. Thus events can occur where two or more tracks deposit energy in the same tube. Here, the identification process requires the generation of four likelihoods, $(\pi, \pi), (e, e), (\pi(p_1), e(p_2))$ and $(e(p_1), \pi(p_2))$ where p_1 and p_2 are the momenta of the two tracks being examined. The hypothesis with the maximum likelihood is chosen.

The probability distributions are determined from simulations of the TRD and are also compared to test beam data. The likelihood ratios for simulated 10 GeV pion and electron tracks crossing all nine TRD modules is given in figure 4.2. The electron acceptance required sets a threshold on the likelihood. Conversely, a tolerable pion contamination can also enforce a threshold. The electron acceptance has been set at 90% in Phase II. Tracks with likelihoods greater than the threshold are identified as electrons by the TRD.

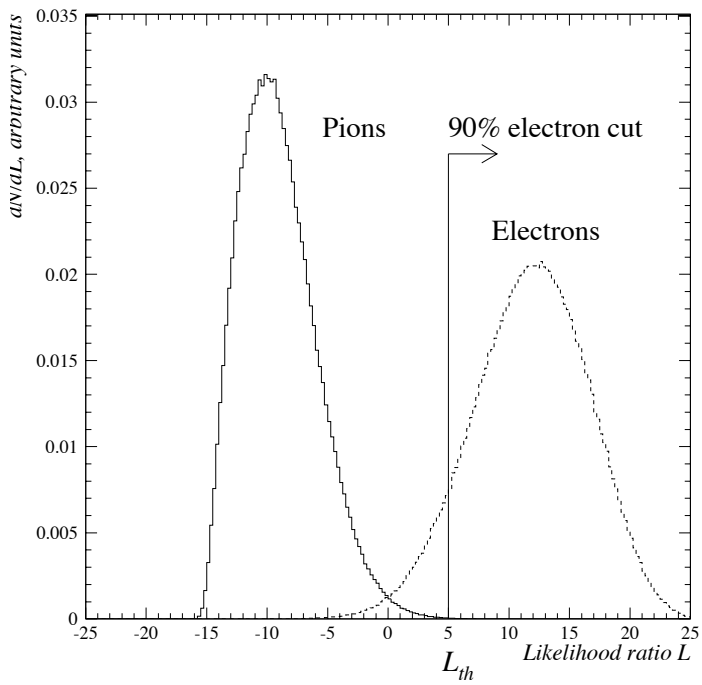

Figure 4.2: Likelihood distributions for simulated 10 GeV pion and electron tracks crossing all nine TRD modules. The likelihood threshold is set to 90% electron acceptance. (Taken from Altegoer et al., 1998a)

The TRD has reliable electron identification abilities for electrons with energies between 0.5 and 50 GeV, when 4 to 9 modules are hit. Higher energies see pions starting to produce transition radiation. At lower energies, electrons no longer emit transition radiation. Phase II defines each TRD track as either an electron, pion or no identification possible.

Muons from the flat top, see section 2.4.1, were used to test the TRD *in situ*. The TRD provided a 1.1 $\times 10^{-3}$ rejection factor of muons. Further, delta electrons from these muons were correctly identified. More details of the performance of the TRD are found in Bassompierre et al. (1998b).

Preshower (PRS)

The PRS has limited electron identification capacity, especially if used alone. The pulse heights from the PRS can be used to differentiate pions and elec-

trons. After analysis of pion test beam data, a pulse height threshold for electron identification with energy E was determined:

$$0.836 + 6.86 \ln(E/\mathrm{GeV}) - 0.22(\ln(E/\mathrm{GeV}))^2 \tag{4.3}$$

in units of minimum ionising potentials. The analysis is presented in Autiero et al. (1997). At energies above 4 GeV, this identification yields a 90% efficiency, but can leave a pion contamination of up to 10%.

Electromagnetic Calorimeter (ECAL)

The ECAL can provide electron identification from its pulse heights, and also in combination with those from the PRS. However, Phase II selects on the following variable:

$$EoP = \frac{E_{clu}}{P_{end} - \Delta P_{end}} \tag{4.4}$$

where E_{clu} is the energy in the associated cluster, (defined in section 4.3.2), of the track, P_{end} is the momentum at the end of the track in the DC, and ΔP_{end} is the error on this momentum. Electrons will dump all their energy in the ecal, and so this ratio will be close to unity, whereas pions will act as a minimum ionising particle, causing the ratio to be closer to zero. To remove pions, the ECAL vetoes particles with $EoP < 0.85$.

Drift Chamber (DC)

The DC is used to help identify electrons from photon conversions. Candidates for this exist when the vertex of a particle track in the DC is a neutral charge vertex (V0) with invariant mass below 0.1 GeV. Here, if the particle has not been vetoed by the above detectors, and if the other track from the V0 is identified as an electron by the TRD or $EoP < 0.85$, then this particle is also called an electron. Conversely, if the other track is vetoed by the TRD or ECAL, the first particle is also rejected.

Phase II Algorithm

Selection of electrons by Phase II then follows the algorithm:

- TRD Accept if an electron is identified, veto if a pion is identified.

- PRS Accept if an electron is identified with a pion contamination less than 0.1, veto if a pion is identified. This is only used if the TRD could not identify the particle.

- ECAL Vetoes if EoP is less than 0.85, and can override the previous selection of the TRD and PRS.

- DC The V0 condition is used only when none of the above have classified the particle.

Further information on Phase II electron identification can be obtained from Autiero et al. (1999b).

4.3.2 Prompt Electron Selection

Electrons in an event are identified by Phase II. From these a prompt electron can be selected. The criteria, common to prompt muon and electron selection, section 4.1.4, are applied. Briefly these conditions select the highest momentum electron, with a low scattering angle. However, there are a higher number of electrons than muons produced in the hadronic shower, particularly from gammas converting to electron-positron pairs, and so additional, stronger criteria are required to reject these. Moreover, as ν_e CC events represent only 1% of the events in NOMAD, there is a large sample of ν_μ CC events to produce these background electrons. Therefore the first additional requirement is a muon veto such that there are no identified muons in the event.

To ensure that the electron is not from a gamma conversion, the minimum reconstructed mass from the pairing of the candidate with every other charged track must be greater than 0.1 GeV. Gamma conversions are also guarded against with a condition requiring Δz, the distance between the first hit included in the reconstructed fit of the track and the primary vertex, to be less than 15 cm. If the electron is from a gamma conversion, its track is unlikely to start at the primary vertex, and will therefore have a sizeable Δz. This cut will also work against Dalitz decays, where a π^0 decays to a photon and an electron positron pair. To enhance the consistency between ν_μ and ν_e selection, these two conditions are also imposed on the prompt muon candidates. The gamma conversion cut has almost no effect on muon candidates, whilst the Δz can appreciably reduce the sample size, see section 4.4.

To tighten the Phase II electron selection, the pion contamination provided by the TRD likelihood functions must be less than 0.005. Further, a new variable is constructed to exploit the ECAL energy measurement:

$$E_{cut} = \frac{E_{clu} - P_{end}}{E_{clu} + P_{end}} \tag{4.5}$$

Like EoP, this variable shows the consistency of the particle momentum and energy measured in the ECAL, which should approach zero for electrons, (dumping all their energy in the ECAL), and be significantly negative for pions, (acting as minimum ionising particles, and not dumping all their energy). The cut imposed is then $-0.1 < E_{cut} < 0.075$.

Beyond the energy momentum consistency and the pulse height thresholds, (not used here except that a cluster must have 20 MeV to appear in the DST), the ECAL can flag electrons according to the shape of the cluster formed in the ECAL. An ECAL cluster represents the collection of cells with energy deposits, that have been associated together. The cells are also associated to a DC track with the clusterisation of Feldman (1995). The extrapolated intercept of the track in the ECAL forms the seed for the clustering algorithm. Cells are gathered around the seed within a predetermined distance, and cells that overlap clusters have their energy shared, according to the relative energy of the competing clusters. A neutral cluster can be formed additionally, if the cluster energy greatly exceeds the track momentum. The radii of the elliptical clusters are determined from the energy weighted distribution of the cells. The two radii must both be less than 6 cm, in order for the cluster to be consistent with an electron.

Kinematic cuts are also implemented to help reduce the background of electrons from the hadronic shower. These cuts are itemised below and have been chosen so as to retain a high signal efficiency. Further, the choice of variables to cut against was motivated by the fact that they are dimensionless. Thus selection does not depend heavily on the energy resolution, which otherwise could cause the event to be misidentified.

- $y_{Bj} < 0.85$
- $\hat{\nu} > -0.75$
- $\frac{p_T^{miss}}{E_{vis}} < 0.150$

Note that y_{Bj} is defined in the data and reconstructed Monte Carlo as the ratio of ν over E_{vis}, where $\nu = E_{vis} - p_l$ and p_l is the momentum of the lepton candidate, ($\hat{\nu}$ is a separate variable, defined in section 4.1.3).

The LEP condition of section 4.1.3 is used to allow leptons that fail some of the above criteria, to still be accepted as prompt leptons. The following cuts are adjusted by the LEP condition:

- $\Delta z < 15$ cm OR (LEP AND $\Delta z < 50$ cm)
- Minimum reconstructed mass > 0.1 GeV/c^2 OR LEP
- $-0.1 < E_{cut} < 0.075$ OR LEP
- $\frac{p_T^{miss}}{E_{vis}} < 0.150$ OR LEP

Note that the LEP exceptions apply to muon selection as well. To see the effect of the adjustments, table 4.4 lists the number of electrons failing the standard cut, and the number that then fail and pass the LEP adjustment. The table shows that most of these true ν_e DIS events that otherwise would have been rejected, are recovered by the inclusion of LEP.

Cut	Standard	LEP Adjusted	Recovered
E_{cut}	184474	6221	178253
$\frac{p_T^{miss}}{E_{vis}}$	2752	37	2715
Min Mass	8757	168	8589
Δz	63844	29383	34461

Table 4.4: Monte Carlo ν_e DIS events failing the standard selection which then either fail the LEP adjusted selection or are recovered.

A candidate ν_e CC event is displayed in figure 4.3. The electron track produces a large energy in the ECAL, seen in the ECAL histogram on the event display. The electron was identified by the Phase II algorithm. Note that the track is also from the primary vertex and is well isolated. There is no identified muon.

4.3.3 Increased Background Rejection

After observing the size of the initial background contamination, it was decided to add a further cut to the electron selection. This "isolation" cut is:

$$Q_{lep} > (2 - \frac{\phi_{lh}}{\pi}) GeV/c \tag{4.6}$$

where ϕ_{lh} is the angle between the lepton and hadron shower vector, and Q_{lep} is the transverse momentum of the lepton with respect to the hadron shower, both of which will be large for prompt events. The cut was determined in

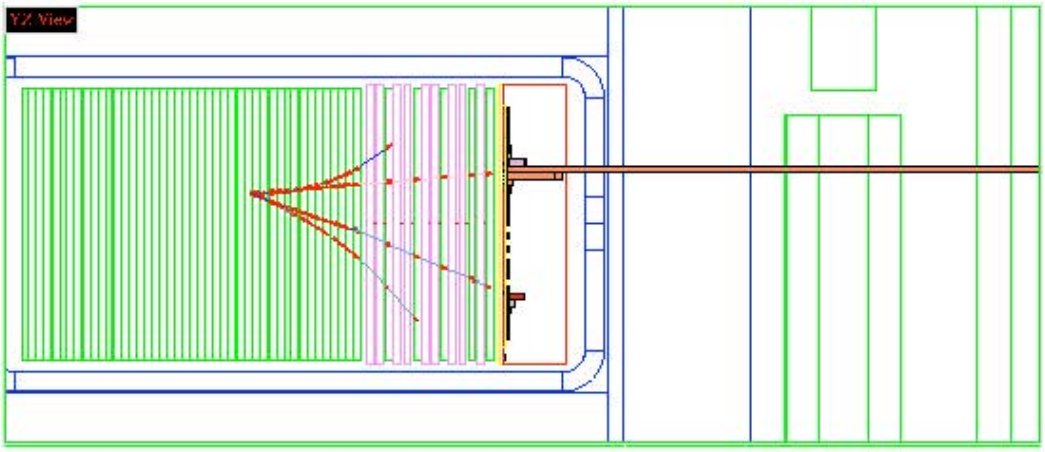

Figure 4.3: Candidate ν_e CC event, as viewed in the NOMAD event display. See the text for a description of the event.

a study of background Monte Carlo, DeSanto (1998). Although this cut is not applied to $\overline{\nu}_\mu$ classification, it is used in determining the $\overline{\nu}_\mu$ background scale, sectioncorrections-background.

4.4 Selection Efficiencies

The neutrino data is subjected to the above criteria to produce the four neutrino samples: ν_μ, $\overline{\nu}_\mu$, ν_e, $\overline{\nu}_e$. These data samples are used in the beam flux studies and the oscillation search of the following chapters. To understand how the selection process distorts the true energy spectra of the neutrinos, and also to allow the approximation of the true number of neutrino events, the selection efficiency must be determined.

This efficiency is produced using Monte Carlo neutrino events. The efficiency is simply the number of true neutrino events selected over the number generated. In practice, this is achieved with two samples of events, the total Monte Carlo sample generated, which is described in terms of the true (generated) values of its variables, (energy, position etc) and a selected sample which is described in terms of both the generated and reconstructed values. The two samples are normalised within a set fiducial volume, that of section 4.1.1. Furthermore, the fiducial volume is defined in both samples using the generated vertex position. The Monte Carlo filter cuts, section 4.1.1, are also applied to both samples, before any efficiency is determined.

Enforcing the fiducial volume on the generated vertex position ignores the

possibility of events having their position smeared into or out of the fiducial volume. To test whether it is reasonable to do so, the degree to which the position was smeared is investigated. Figure 4.4 shows the difference between the reconstructed and generated z position. The position smearing is worst in z due to the spacing of the wires. In y it is tiny, the root mean square (RMS) of the equivalent graph of figure 4.4 for y is 0.05 cm. In x, it is slightly worse at 0.08 cm as the x position must be determined from the stereo angle calculations. However, even in z the RMS is only 0.16 cm, and so the number of vertices inside the fiducial volume is unlikely to be greatly effected by the position smearing. Note also that there is no systematic bias of the reconstructed vertex in z; this is the same in x and y.

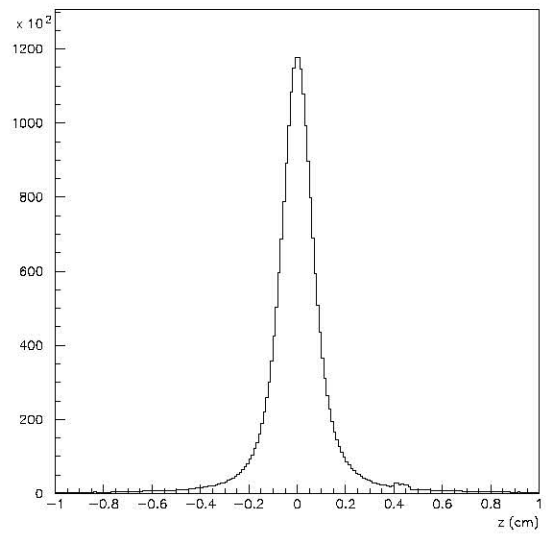

Figure 4.4: Reconstruction differences in the z vertex position. The step at 0.4 cm arises from the increase in events 0.4 cm before the sense wires in the aramid honeycomb.

The Monte Carlo has also been reweighted, in order to use a more recent description of the neutrino beam. This reweighting procedure is described in section 5.3.3. The beam description used is a preliminary empirical parametrisation, Mishra (1999). However this weight was only applied to ν_μ and $\overline{\nu}_\mu$ spectra, as there was no new parametrisation available for ν_e or $\overline{\nu}_e$at the time.

The Calisto filter is applied first, and is common to both data and Monte Carlo, and all neutrino types. The effect of each cut, as an efficiency is

tabulated individually in table 4.5. The "Total" in the first row refers to the number of events in the DST. The number of data events passing each cut is also shown. This includes the combined 1995 to 1998 data. The filter is fairly efficient and is later included in the overall selection efficiency. Throughout this section, the efficiency tables only include the deep inelastic scattering (DIS) Monte Carlo. This is because DIS represents the vast majority of events in NOMAD, and as such, has been the most prolifically produced. A summary for quasielastic (QE) and resonance (RES) Monte Carlo will be presented at the end of this section.

	Data	ν_μ DIS MC		$\overline{\nu}_\mu$ DIS MC		ν_e DIS MC		$\overline{\nu}_e$ DIS MC		ν_μ NC MC	
Total	3329999	3623579		588925		2371203		297223		1308392	
		ε_{abs}	ε_{rel}	ε_{abs}	ε_{rel}	ε_{abs}	ε_{rel}	ε_{abs}	ε_{rel}	ε_{abs}	ε_{rel}
DST Info	3324723	1.00	1.00	1.00	1.00	0.999	0.999	0.999	0.999	1.00	1.00
Online Err	3286521	1.00	1.00	1.00	1.00	0.999	1.00	0.999	1.00	1.00	1.00
Mu Cham.	3087891	0.968	0.968	0.977	0.977	0.931	0.931	0.949	0.949	0.978	0.978
RVXS Bank	3087891	0.968	1.00	0.977	1.00	0.930	0.999	0.947	0.999	0.978	1.00
Vertex	3079931	0.964	0.996	0.968	0.991	0.927	0.997	0.943	0.995	0.901	0.921
Primary Trk	3079931	0.964	1.00	0.968	1.00	0.927	1.00	0.943	1.00	0.901	1.00

Table 4.5: Effect of the Calisto event filter on the data. Also tabulated are the corresponding efficiencies calculated with the ν_μ, $\overline{\nu}_\mu$, ν_e and $\overline{\nu}_e$ Monte Carlo (MC), as well as the background sample, ν_μ NC. ε_{abs} is the cumulative efficiency, whilst ε_{rel} is just the efficiency of the given cut.

The acceptance of only Phase II identified muons is the task of the first stage selection. The results of the loose and tight Phase II muon identification are given in table 4.6. The first row gives the number of events inside the fiducial volume. For data, the Calisto filter has also been applied, whilst for Monte Carlo, only the Monte Carlo filter has been applied. The Calisto filter is applied in conjunction with the loose muon identification to the Monte Carlo, so the efficiency quoted for the identification includes the filter efficiency of table 4.5. This is due to the Calisto filter and lepton selection being applied in Calisto, whilst the Monte Carlo filter, which helps produce the base event samples to calculate the efficiency from, is implemented in Readall. All subsequent efficiency tables feature this as well.

The remainder of the table contains the selection cuts of Readall. After the muon identification, which is around 85% efficient, the additional quality cuts, prompt selection and electron consistency cuts have only a minor effect on the number of events. After all the other selections are made, the samples are split according to the charge of the muon to give the $\overline{\nu}_\mu$ (positive) and ν_μ (negative). This leaves the final number of events selected and the combined

efficiency of the process.

Included in table 4.6 is the background rejection. The major background to the ν_μ CC sample comes from the ν_μ NC sample. Less than 0.5% of ν_μ NC is shown to be misidentified as ν_μ CC. When this rejection is combined with the fact that there is only one third the number of NC events present in data compared to CC, this background can safely be neglected. Whilst there exists a small possibility that another neutrino type could fake a ν_μ CC signal, there is such a low contamination of these other neutrinos that this possibility can also be ignored. However, it is the opposite for the $\overline{\nu}_\mu$ signal and the percentage of ν_μ CC and NC events being misidentified, 0.4% and 0.5% respectively, must be accounted for.

		ν_μ DIS CC MC			$\overline{\nu}_\mu$ DIS CC MC			ν_μ NC MC		
Cut	Data	Events	ε_{abs}	ε_{rel}	Events	ε_{abs}	ε_{rel}	Events	ε_{abs}	ε_{rel}
Available	2150881	2977416	1.00	1.00	440064	1.00	1.00	1072987	1.00	1.00
Loose Muon	1190915	2443282	0.821	0.821	394835	0.897	0.897	13528	0.013	0.013
Tight Muon	1180085	2408281	0.809	0.986	389179	0.884	0.986	11215	0.0105	0.829
$p_z > 0$	1180085	2408281	0.809	1.00	389179	0.884	1.00	11215	0.0105	1.00
$E_{vis} < 300$	1175622	2402165	0.807	0.997	388079	0.882	0.997	11157	0.0104	0.995
$N_{ChTrk} < 50$	1175622	2402165	0.807	1.00	388079	0.882	1.00	11157	0.0104	1.00
Unused Hits	1168514	2401616	0.807	1.00	387892	0.881	1.00	11155	0.0104	1.00
Scattering	1141715	2386591	0.802	0.994	384583	0.874	0.991	11014	0.0103	0.987
1 Trk Fid Vol	1113622	2363956	0.794	0.991	371974	0.845	0.967	10952	0.0102	0.994
Min Mass	1111154	2361134	0.793	0.999	371612	0.844	0.999	10459	0.0097	0.955
ΔZ	1100009	2355363	0.791	0.998	370510	0.842	0.997	10058	0.0094	0.962
Thru μ Veto	1076529	2352337	0.790	0.999	369884	0.841	0.998	10043	0.0094	0.999
Positive	34579	10652	0.0036	0.005	368404	0.837	0.996	5137	0.0048	0.511
$\nu < 5$	14073	682	0.0002	0.064	130335	0.296	0.354	830	0.0008	0.162
Negative	1041950	2341685	0.786	0.995	1480	0.003	0.004	4906	0.0046	0.488
$\nu < 5$	357508	670976	0.225	0.287	-	-	-	785	0.0007	0.160

Table 4.6: Selection efficiencies for ν_μ and $\overline{\nu}_\mu$ DIS events, listed for each cut in the selection process, ε_{rel}, and cumulatively, ε_{abs}. Also listed are the number of events remaining in the data and Monte Carlo. The background rejection power is illustrated in the NC column and opposite charge rows of the CC.

The effect on the energy spectrum of the neutrinos due to the selection process is seen in figures 4.5 and 4.6, which show the selection efficiency for ν_μ and $\overline{\nu}_\mu$ DIS respectively, as a function of the generated neutrino energy. The errors only reflect the statistics of the generated samples. There is a low energy cut off to the selection process, due to the 2.5 GeV minimum for muon identification. Moreover, the muon in low energy events will often not reach the muon chambers due to scattering, interaction or being too strongly deflected by the magnetic field, whilst cuts such as that on the lepton

scattering angle tend to remove low energy events. This leads to what is called the low energy "turn on", (of the selection process), and is present here between 2.5 and 15 GeV. Outside this range, few cuts are energy dependent. The efficiency starts to decrease with energy as the events become more crowded leading to misreconstruction and failure of the filter cuts. These efficiency curves can be used to either "unfold" the data for comparisons with flux predictions, or conversely, can be applied to flux predictions for direct comparison to the data.

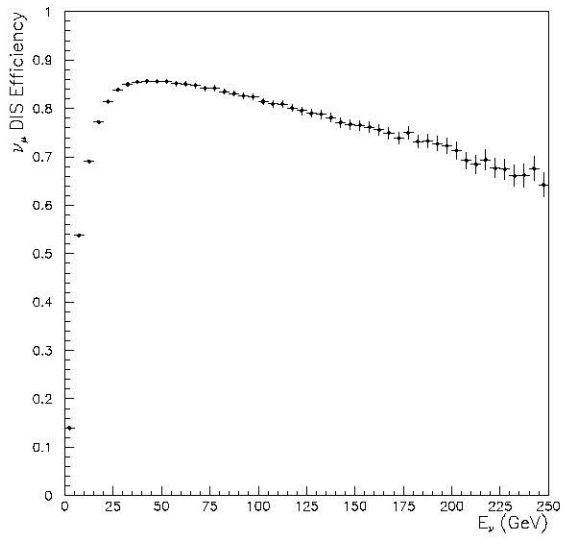

Figure 4.5: The ν_μ DIS selection efficiency as a function of generated neutrino energy.

The efficiency for ν_e selection is presented in table 4.7. The starting data sample is identical to that used for the muon selection above. The Phase II electron identification is shown to be around 68% efficient, after isolating it from the Calisto filter efficiency. However the additional cuts required for prompt electron selection reduce the sample by a further 15%. The final number selected and the total efficiency are listed at the bottom of the table. Again the table also includes the background samples. ν_μ CC and NC are the overwhelming source of background to the ν_e sample. The most effective variables used to reject non prompt electrons are y_{Bj}, $\hat{\nu}$ and Δz, as shown by their relative efficiencies. Additionally, the muon veto drastically reduces the contamination from ν_μ CC. Furthermore, these cuts are also able to preserve a high signal (ν_e) efficiency.

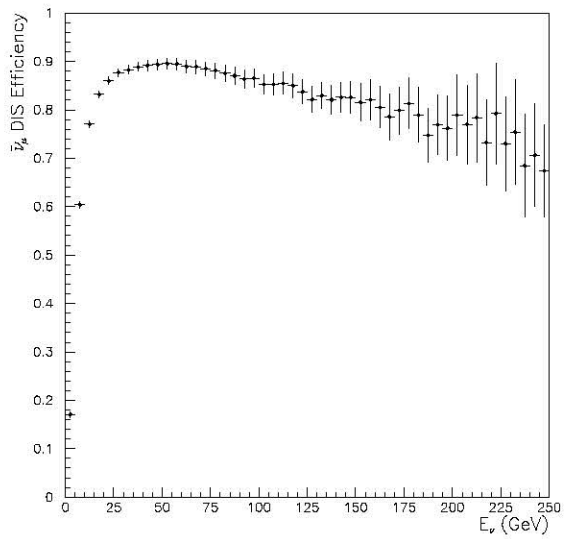

Figure 4.6: The $\overline{\nu}_\mu$ DIS selection efficiency as a function of generated neutrino energy.

The selection efficiency of ν_e DIS as a function of generated neutrino energy is plotted in figure 4.7. Again, the low energy turn on is present, but there is also a considerable reduction in efficiency at high energies, above 75 GeV. As mentioned in section 4.3.1 the TRD is most effective in the 0.5 to 50 GeV range, thus the electron identification itself partly creates the shape seen. Also, the y_{Bj}, $\hat{\nu}$ and Δz cuts remove more high than low energy events.

Consideration must be made when generating the ν_e (and also $\overline{\nu}_e$) selection efficiencies for the 1995 data. In this year, the drift chamber modules were introduced in three stages, starting with the most upstream modules. An electron generated by a neutrino interaction in the upstream modules has less distance to travel to the transition radiation detector and so is more likely to be detected than scattered or lost. Thus the efficiency of the 4 and 8 module data is greater than the 11 module data. To account for this Monte Carlo is also generated with the 4 and 8 module fiducial volume of table 4.1. The 4, 8 and 11 module samples are then combined in accordance with the approximate number of CC events recorded in data in the respective period, as given by table 2.1. Repeating this for the ν_μ and $\overline{\nu}_\mu$ is not necessary as the muon detection is not as strongly dependent on the position of the neutrino interaction. Also, it is not overly necessary to generate 10 module data to adjust the efficiency of the 1997 and 1998 data.

Cut	Data	ν_e DIS CC MC			ν_μ DIS CC MC			ν_μ NC MC		
		Events	ε_{abs}	ε_{rel}	Events	ε_{abs}	ε_{rel}	Events	ε_{abs}	ε_{rel}
Available	2150881	1923028	1.00	1.00	2977416	1.00	1.00	1072987	1.00	1.00
Phase II	49220	1225668	0.637	0.637	55078	0.0185	0.0185	21496	0.0200	0.0200
$p_z > 0$	49220	1225668	0.637	1.00	55078	0.0185	1.00	21496	0.0200	1.00
$E_{vis} < 300$	48766	1220454	0.635	0.996	54508	0.0183	0.990	21361	0.0199	0.994
$N_{ChTrk} < 50$	48766	1220454	0.635	1.00	54508	0.0183	1.00	21361	0.0199	1.00
Unused Hits	48204	1219842	0.634	0.999	54493	0.0183	1.00	21336	0.0199	0.999
Scattering	46738	1212541	0.0631	0.994	54063	0.0182	0.992	20827	0.0194	0.976
1 Trk Fid Vol	46116	1200182	0.624	0.990	53936	0.0181	0.998	20484	0.0191	0.984
E_{cut}	44967	1193961	0.621	0.995	52619	0.0177	0.976	19840	0.0185	0.969
$RadX, RadY$	39656	1167829	0.607	0.978	45590	0.0153	0.866	17092	0.0159	0.861
TRDPiCon	39635	1167802	0.607	1.00	45550	0.0153	0.999	17071	0.0159	0.999
$y_{Bj} < 0.85$	27596	1087578	0.566	0.931	27997	0.0094	0.615	13653	0.0127	0.800
$\hat{\nu} > -0.75$	21749	1037225	0.539	0.954	25137	0.0084	0.898	4826	0.0045	0.353
$\frac{p_T^{miss}}{E_{vis}} < 0.150$	21746	1037188	0.539	1.00	25136	0.0084	1.00	4824	0.0045	1.00
No Muon	14785	1018428	0.530	0.982	4525	0.0015	0.180	4763	0.0044	0.987
Min Mass	14765	1018260	0.530	1.00	4511	0.0015	0.997	4755	0.0044	0.998
ΔZ	12427	988877	0.514	0.971	2477	0.0008	0.549	2917	0.0027	0.613
Thru μ Veto	12277	987341	0.513	0.998	2460	0.0008	0.993	2886	0.0027	0.989
Isolation	10778	929843	0.484	0.942	1255	0.0004	0.510	1564	0.00145	0.542
$\nu < 5$	2745	183278	0.095	0.198	203	0.00007	0.162	527	0.0005	0.337

Table 4.7: Selection efficiencies for ν_e DIS events, listed for each cut in the selection process, ε_{rel}, and cumulatively, ε_{abs}. Also listed are the number of events remaining in the data and Monte Carlo. The background rejection power is illustrated in the ν_μ CC and NC columns.

Much the same situation applies in the case of $\overline{\nu}_e$ selection. The samples are separate as charge selection is carried out as part of the lepton selection in Calisto. This allows a greater number of positrons to be recorded in the analysis ntuples, even to the extent that an event may be recorded twice, once as a ν_e candidate and once as a $\overline{\nu}_e$ candidate, where it is expected that only one will survive the further requirements of Readall, (an event can be recorded even a third time as a muon event, but overlaps here are removed in Readall by the muon veto). The cuts are itemised in table 4.8. Also presented is the efficiency spectrum in figure 4.8.

Quasielastic (QE) and resonance (RES) Monte Carlo samples were also studied, as these are of particular interest to the empirical parametrisation. The sample sizes generated are considerably smaller than the DIS, reflecting their proportion in the data. The size of the sample and the selection efficiency for each neutrino type is listed in table 4.9. As an example of the energy dependence of QE and RES selection efficiencies, those of the ν_μ samples are plotted in figures 4.9 and 4.10 respectively. The small sample size accounts for the fluctuations at high energies, despite the increased bin size.

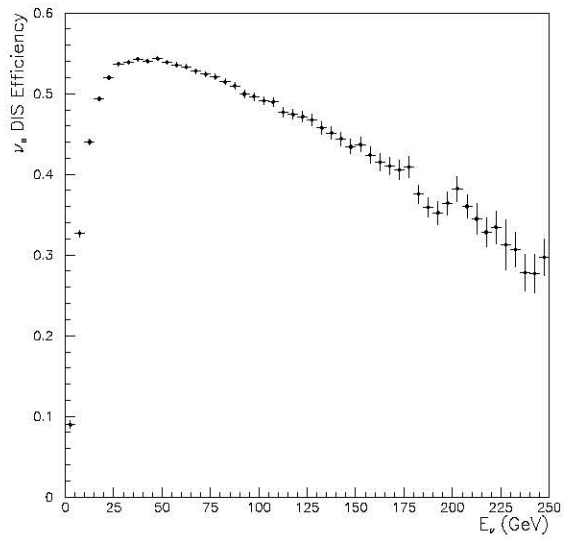

Figure 4.7: The ν_e DIS selection efficiency as a function of generated neutrino energy.

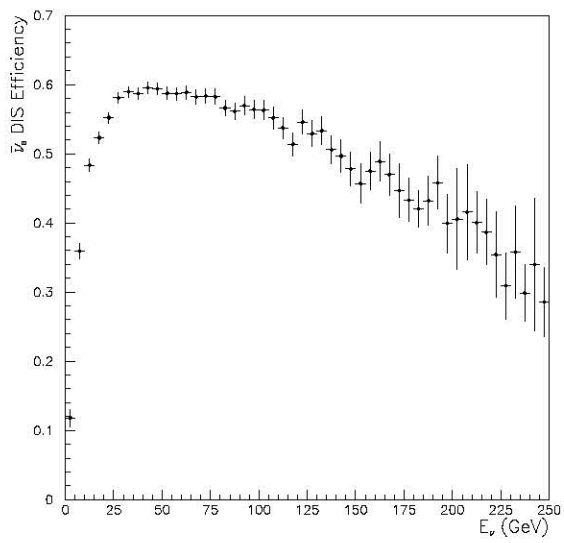

Figure 4.8: The $\overline{\nu}_e$ DIS selection efficiency as a function of generated neutrino energy.

Cut	Data	$\overline{\nu}_e$ DIS CC MC			ν_μ DIS CC MC			ν_μ NC MC		
		Events	ε_{abs}	ε_{rel}	Events	ε_{abs}	ε_{rel}	Events	ε_{abs}	ε_{rel}
Available	2150881	225848	1.00	1.00	2977416	1.00	1.00	1072987	1.00	1.00
Phase II	45181	157269	0.696	0.696	68024	0.0228	1.00	21743	0.0203	0.0203
$p_z > 0$	45181	157269	0.696	1.00	68024	0.0228	1.00	21743	0.0203	1.00
$E_{vis} < 300$	44737	156541	0.693	0.995	67366	0.0226	0.990	21625	0.0202	0.995
$N_{ChTrk} < 50$	44737	156541	0.693	1.00	67366	0.0226	1.00	21625	0.0202	1.00
Unused Hits	44212	156367	0.692	0.999	67348	0.0226	1.00	21605	0.0201	0.999
Scattering	42769	155410	0.688	0.994	66798	0.0224	0.992	21092	0.0197	0.976
1 Trk Fid Vol	42323	150144	0.665	0.966	66692	0.0224	0.998	20762	0.0193	0.984
E_{cut}	40368	149121	0.660	0.993	64181	0.0216	0.962	19791	0.0184	0.953
$RadX, RadY$	33968	146271	0.648	0.981	55010	0.0185	0.857	17097	0.0159	0.864
TRDPiCon	33942	146269	0.648	1.00	54965	0.0185	0.999	17078	0.0159	0.999
$y_{Bj} < 0.85$	20497	141295	0.626	0.966	33564	0.0113	0.611	13769	0.0128	0.806
$\hat{\nu} > -0.75$	15004	132130	0.585	0.935	30089	0.0101	0.896	4995	0.0047	0.363
$\frac{p_T^{miss}}{E_{vis}} < 0.150$	15003	132128	0.585	1.00	30087	0.00896	1.00	4994	0.0047	1.00
No Muon	6319	129925	0.575	0.983	5307	0.0018	0.040	4919	0.0046	0.985
Min Mass	6309	129909	0.575	1.00	5288	0.0018	0.996	4911	0.0046	0.999
ΔZ	3981	126128	0.558	0.971	3328	0.0011	0.629	3096	0.0029	0.630
Thru μ Veto	3880	125820	0.557	0.998	3308	0.0011	0.994	3063	0.0029	0.989
Isolation	2578	118105	0.523	0.939	1489	0.0005	0.450	1636	0.0015	0.534
$\nu < 5$	843	36955	0.164	0.313	263	0.00009	0.177	619	0.0006	0.378

Table 4.8: Selection efficiencies for $\overline{\nu}_e$ DIS events, listed for each cut in the selection process, ε_{rel}, and cumulatively, ε_{abs}. Also listed are the number of events remaining in the data and Monte Carlo. The background rejection power is illustrated in the ν_μ CC and NC columns.

Again a turn on effect is seen, but the QE and RES efficiencies have far less of a decrease with increasing energy.

Appended to each of the efficiency tables is a row for the $\nu < 5$ GeV selection, (recall that in data and reconstructed Monte Carlo, $\nu = E_{vis} - p_l$, where p_l is the momentum of the candidate lepton). This represents the low ν sample to be used in the empirical parametrisation of chapter 6. This cut causes a dramatic reduction in the efficiency for the DIS, but the QE and RES samples are hardly affected by it, as expected of low hadronic energy events. The purpose and use of the low ν events is given in chapter 6.

The estimation of the size of any systematic errors affecting the selection process and subsequent classified samples is found in section 7.4.1.

4.4.1 Energy Smearing

When the NEGLIB Monte Carlo is reconstructed, see section 2.7, the detector effects are simulated by GEANT, transforming the true neutrino energy E_ν into the reconstructed or visible energy, E_{vis}. Previously this detector

	ν_μ		$\overline{\nu}_\mu$		ν_e		$\overline{\nu}_e$	
	RES	QE	RES	QE	RES	QE	RES	QE
Generated	90045	86043	60030	30015	88039	90043	58027	42019
Efficiency	0.878	0.775	0.766	0.575	0.554	0.493	0.477	0.359
$\nu < 5$	0.867	0.768	0.758	0.572	0.532	0.471	0.462	0.354

Table 4.9: Efficiency for the selection of events from RES and QE Monte Carlo samples. The number of events generated to calculate the efficiency is also given.

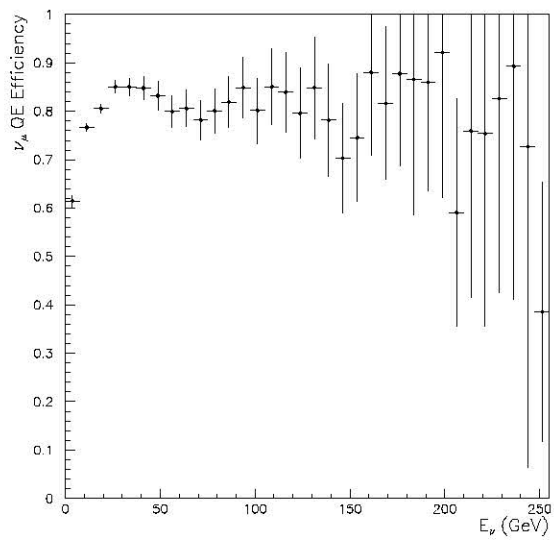

Figure 4.9: The ν_μ QE selection efficiency as a function of generated neutrino energy.

smearing was included within the efficiency, where the efficiency was generated from the ratio of the selected events as a function of E_{vis} to the generated events as a function of E_ν. This method was not rigorous enough as it integrated out the structure in the E_{vis} dependence of the resolution function. Put another way, the method assumes that the E_ν spectrum is the same for data and simulation, which may not be true.

Instead, a smearing function is used, $S(E_{gen}, E_{vis})$. It is a square matrix with dimensions given by the number of energy bins. Each S_{ij} element represents the percentage of events generated by the Monte Carlo with $E_{gen} = E_i$ reconstructed with $E_{vis} = E_j$. An example smearing function is plotted in

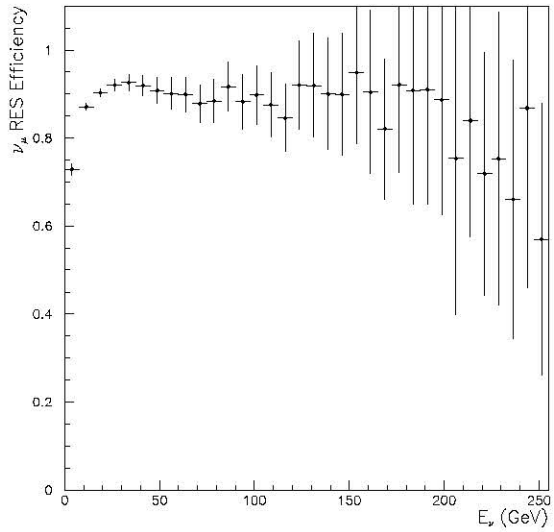

Figure 4.10: The ν_μ RES selection efficiency as a function of generated neutrino energy.

figure 4.11. An E_{vis} distribution is obtained for each bin of E_ν by column normalising the plot (matrix). Thus a generated neutrino, of given E_ν, is shared according to the distribution, amongst the E_{vis} bins. This produces a smeared spectrum in E_{vis} for comparison to data.

4.5 Hadronic Energy Scale

It is suspected that the hadronic energy deposited in neutrino interactions is not equivalent in Monte Carlo and data. It is further speculated that this is due to missing tracks and other reconstruction effects in the data. These kind of effects could be removed if NOMAD, (particularly the drift chamber), could be calibrated in terms of energy deposited. As this would be very difficult, an alternate solution is to apply a hadronic energy scale, to place the Monte Carlo and data are in better agreement.

A scale is determined by considering the average visible energy $\langle E_{vis} \rangle$ as a function of y_{Bj}. These distributions should be identical in data and Monte Carlo if the energy reconstruction is the same. Plots of $\langle E_{vis} \rangle$ versus y_{Bj} for data and Monte Carlo are at the top of figure 4.12. Only events with $\nu > 5$ GeV are used, as low ν events have very little hadronic energy

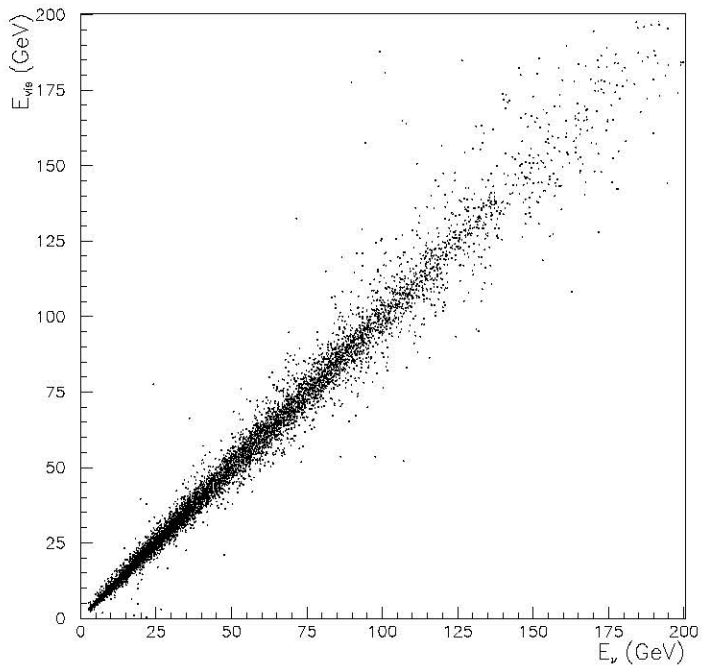

Figure 4.11: Scatter plot of E_{vis} versus E_ν for ν_μ DIS CC Monte Carlo. The plot is column normalised to create a distribution in E_{vis} for each E_ν.

by definition, and so are not effected by any scale or difference. The two distributions have the same general shape, but the ratio plot, bottom of figure 4.12, shows they are significantly skewed.

A linear fit is made to the ratio of the data and Monte Carlo distributions, with only $y_{Bj} < 0.75$ included in the fit. The results are included in figure 4.12, which shows that the ratio is well represented by the linear fit in the given range. This fit then gives the hadronic energy scale between data and Monte Carlo in terms of $y_{Bj} < 0.75$. Thus, the momentum of particles in the hadronic shower are divided by:

$$1.045 - 0.1567 y_{Bj} \tag{4.7}$$

This correction is applied to data events with $\nu > 5$ GeV. The effect of the correction can be seen with the aid of figures 4.13 and 4.14, which show the comparison of ν_μ data to Monte Carlo without and with the hadronic

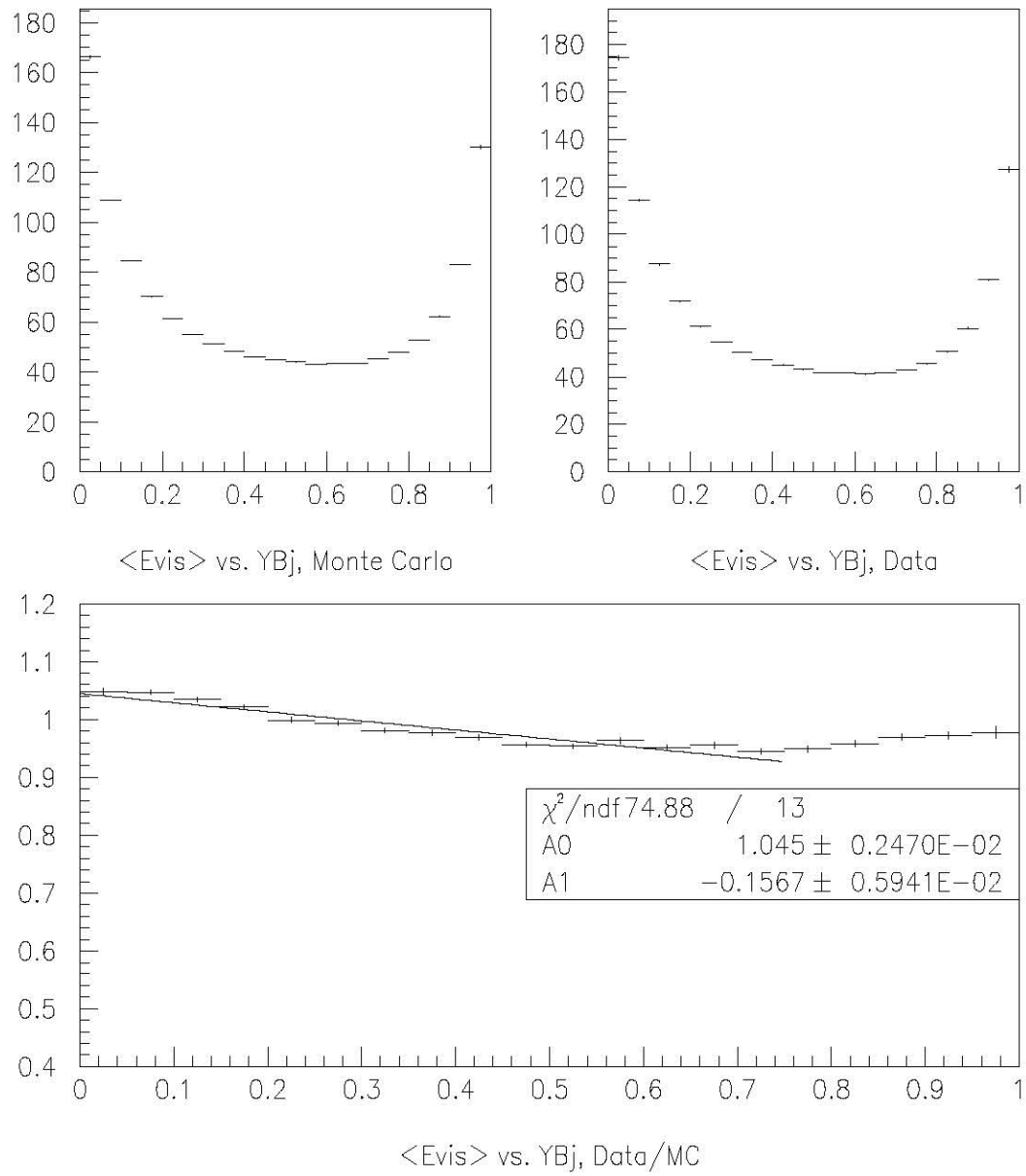

Figure 4.12: How the hadronic energy scale is determined, showing the Monte Carlo and data distributions of $\langle E_{vis} \rangle$ versus y_{Bj}, and then the ratio of data to Monte Carlo and the fit to this ratio.

energy scale respectively. They show a dramatic improvement in the tail of the comparison with the inclusion of the hadronic scale. Other scales were developed with polynomial fits covering the entire y_{Bj} range, with no greater improvement to the comparisons. The scale is used in estimating the systematic error of the energy reconstruction, see section 7.4.4.

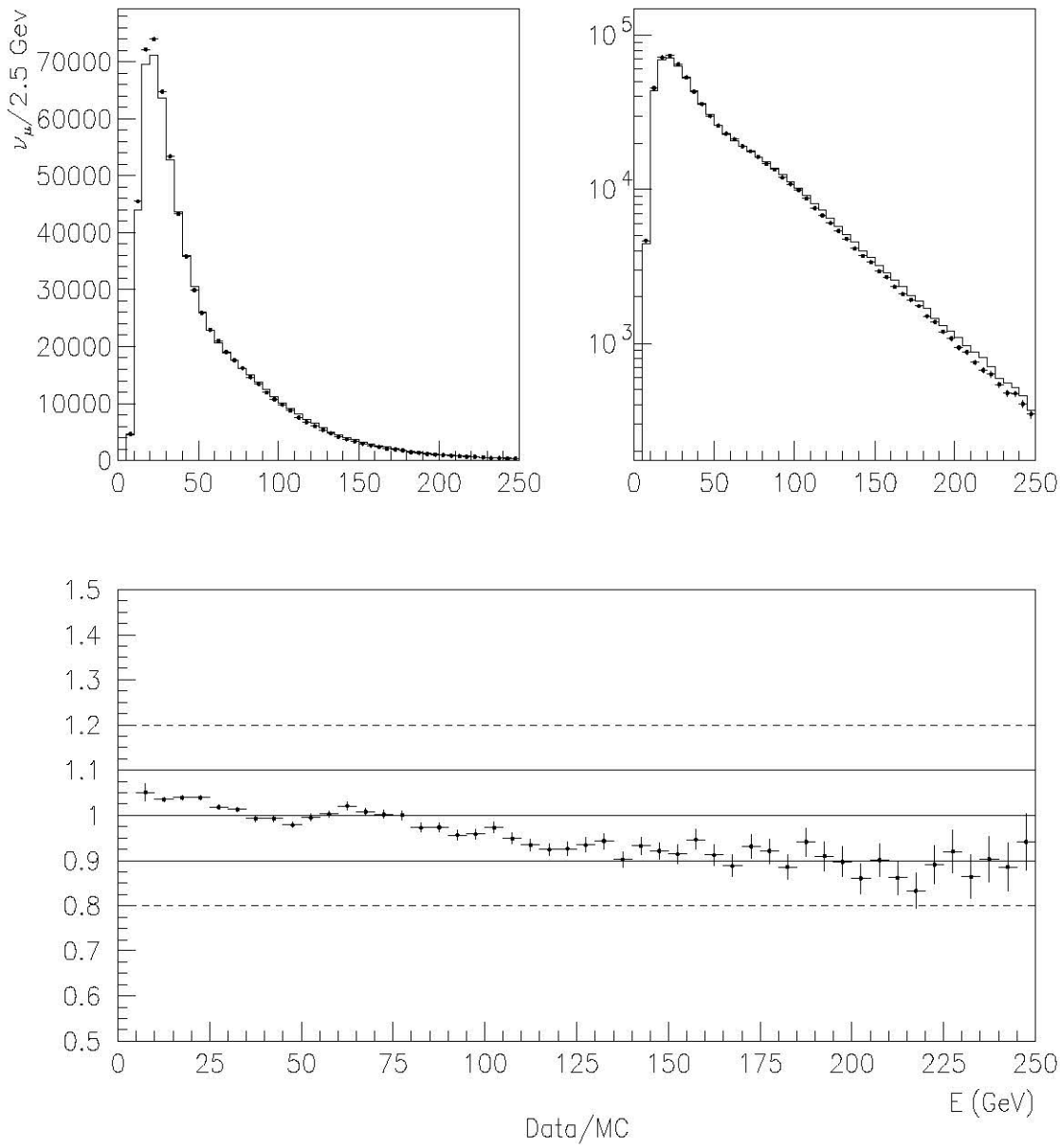

Figure 4.13: Monte Carlo and data (points) ν_μ spectra without the hadronic energy scale, a linear and logarithmic view are given, and the ratio of data to Monte Carlo.

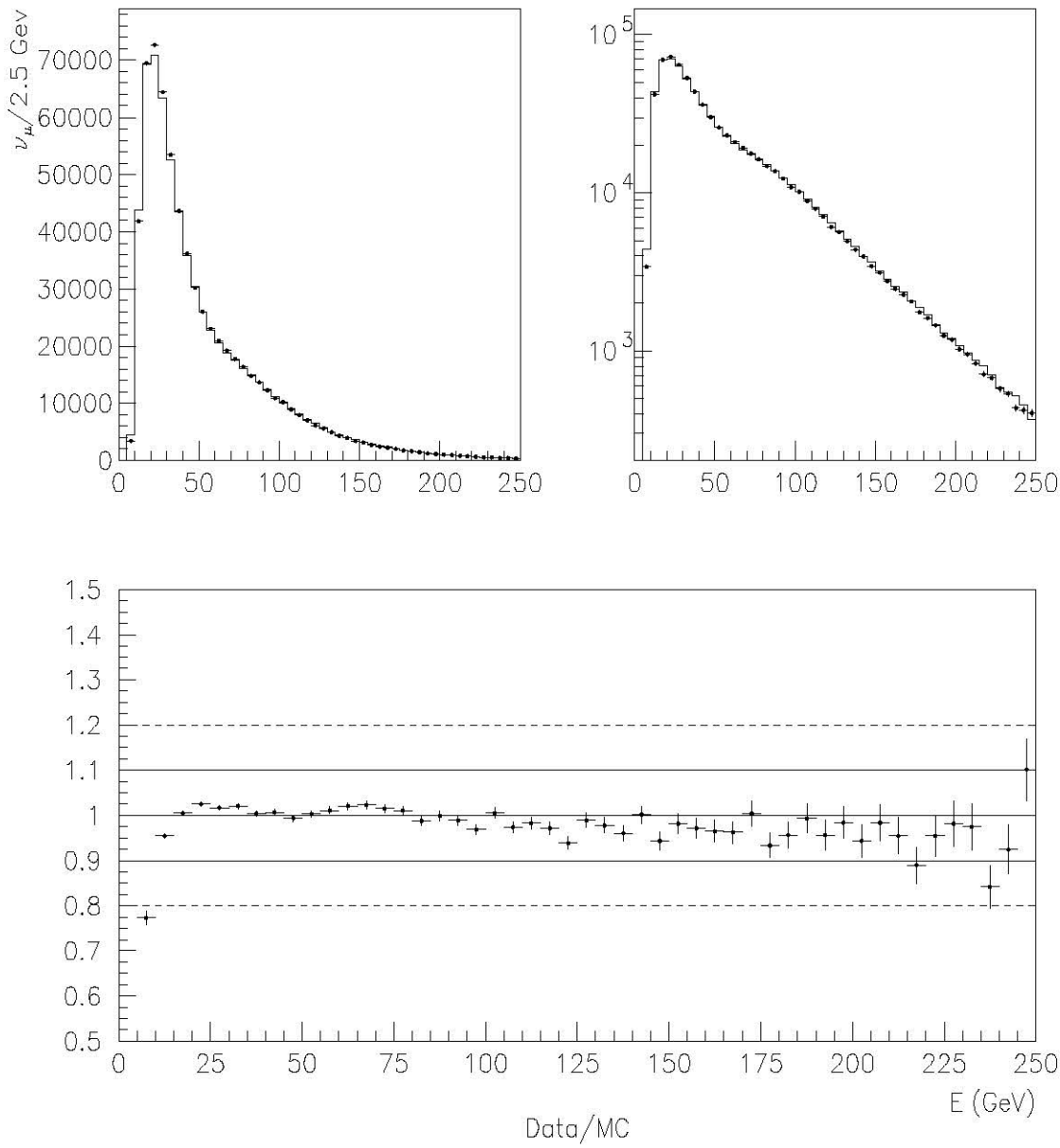

Figure 4.14: Monte Carlo and data (points) ν_μ spectra with the hadronic energy scale, a linear and logarithmic view are given, and the ratio of data to Monte Carlo.

Chapter 5

Simulation of the Neutrino Beam

Neutrino beams are far more complex to describe and simulate than accelerated proton or electron beams, yet neutrino experiments still require a precise knowledge of their beam. Whilst the tau neutrino search in NOMAD only requires a reasonable estimate of the muon neutrino flux to produce an oscillation probability or limit, the $\nu_\mu \rightsquigarrow \nu_e$ search depends heavily on knowing the contamination of ν_e in the ν_μ beam.

The neutrinos are tertiary particles, arising from decays of particles produced in the proton beam on beryllium target collision. A successful simulation will therefore include two main stages: the modeling of the initial collision and the transport, with decays, of the secondaries. The programmes that undertake these tasks are NUBEAM, which is responsible for the particle transport, and FLUKA, which simulates the proton collision. They are described below, followed by comparisons with beam data from three independent sources and a study of systematic errors. These allow a decision to be made as to the reliability of NUBEAM and FLUKA for the $\nu_\mu \rightsquigarrow \nu_e$ oscillation search in chapter 7.

The development of NUBEAM also has applications beyond the oscillation search in NOMAD. The next generation of neutrino experiments, such as the Neutrino Beam to Gran Sasso, (Acquistapace et al., 1998), also have an interest in a high quality beam simulator.

Special note regarding NUBEAM versions

Advancement of the beam simulation programmes was concurrent with the work of this project. Due to the time required to repeat analyses and comparisons with updated beam simulations it is difficult to use the same "lat-

est" version of NUBEAM throughout. Thus the comparisons to the forward calorimeter and muon pit data, and the systematic error study are done with "older" versions of NUBEAM. The comparisons to earlier versions of NUBEAM are still informative, and provide a good grasp of how well the latest NUBEAM will reproduce the data. NUBEAM was further developed, even since writing this chapter. An error was found in the precision of numbers within NUBEAM, depending on which GEANT functions were being called. Also, the step size and maximum deflection used by the simulation for particles traversing the magnetic field of the horn were adjusted to provide more realistic responses to the field. The SPY fit then had to be performed again. The latest simulation is currently NUBEAM 6.21 with FLUKA 98 and SPY C5.1. The comparison to the drift chamber data, (the most important comparison), is made with this simulation. It is also used throughout chapter 7. The systematic study performed with the older version is not expected to be greatly altered, in particular the magnitude of the errors quoted, by redoing it with NUBEAM 6.21. Lastly, as will be revealed in chapter 7, NUBEAM with FLUKA and SPY will not be used in the oscillation search as its systematic errors are much larger than those of the empirical parametrisation. Therefore, using the latest version is no longer vital. However the work done in this chapter is still highly relevant as the empirical parametrisation depends on NUBEAM, and it also provides a point of comparison for the predictions of the parametrisation.

5.1 Development of NUBEAM

NUBEAM is a GEANT, (Goossens et al., 1994), based description of the WANF beamline. It tracks secondaries produced in the primary collision through the focusing elements, (collimators, horn and reflector), and into the decay tunnel, whilst also allowing decays and tracking any subsequent decay products. Neutrinos and any other remaining particles are then propagated through the iron and earth shielding to NOMAD. Refer to figure 2.1 for a schematic of the beamline NUBEAM reproduces. "Recording planes" are inserted in order to ascertain the beam composition along the beamline, particularly in the target and focusing regions, the muon pits and of course at NOMAD. Originally, the primary collision was also modeled by GEANT within NUBEAM, however this task can now also be handled by a standalone FLUKA programme, interfaced to NUBEAM.

It is important to recognise that the NOMAD recording plane within NUBEAM is orthogonal to the beam. In reality, the beam is at a small incline to the NOMAD x, y plane, and is centred in the ECAL, not the NO-

MAD origin, (the first drift chamber module). To account for this, neutrinos from NUBEAM should have their y position rotated and translated to the NOMAD reference frame:

$$y' = y - 20.52 + 0.03531 z_{ran} \quad \text{(cm)} \tag{5.1}$$

where -20.52 cm is the y' intercept at the NOMAD origin, and 0.03531 is the sine of the beam angle. z_{ran} is a randomly generated z position, drawn from a constant distribution from 5 to 405 cm, the extent of the drift chamber. A constant distribution is only an approximation, as whilst the target is uniform, the acceptance of events increases with z. The slope and intercept were ascertained in a study of the average y position versus z of real data events, (Weber et al., 1998).

5.1.1 Early Versions and Prehistory

As some incarnation of the WANF has been running for over two decades, NUBEAM is the result of many iterations and improvements to the simulation programmes over this time. Further, the operation of the WANF has provided a stockpile of neutrino flux data as well as a great understanding of the beam operation, problems, causes and solutions, on which to base NUBEAM. NUBEAM is a direct adaptation of the simulation programme from one of the more recent WANF experiments, CHARM II, (CHARM II Collaboration, 1993). The main change from this programme, called GBEAM, was the inclusion of the alterations to the beamline, to enhance and harden the neutrino flux for CHORUS and NOMAD, see section 2.4. The other change is that NUBEAM utilises FLUKA for simulating hadronic showers, whilst GBEAM was based on GHEISHA (Fesefeldt, 1985). A comparison of NUBEAM with GHEISHA and FLUKA is presented in Weiße (1997). Briefly, GHEISHA is a parametrisation of experimental data and was shown in the above report to produce an unphysical substructure in the kaon distribution. FLUKA is a physical model, fitted to experimental data. GHEISHA produced a ν_μ flux 20% lower than FLUKA and too low a contribution from antineutrinos.

GBEAM was tuned to CHARM II neutrino data, thus the applicability of GBEAM to NOMAD suffered from not only the different beamline, but also the acceptances of CHARM II. Early versions of NUBEAM had implementations of both NOMAD and CHARM II beamlines, in order that comparisons could be made between the two, and to CHARM II data, as no NOMAD neutrino data was yet available. In 1994 NUBEAM 2.02 was released, but provided poor comparisons with CHARM II results. Later,

NUBEAM 3.05 was released, with minor variations 3.06 and 3.07, and became a stable beam simulation, on which many predictions were based. These included the beam alignment, by way of scanning the target, horn and reflector positions, (Casagrande et al., 1996), and estimates on the expected flux and number of neutrino interactions at NOMAD, (Tovey et al., 1995).

Further details on the initial development of NUBEAM are found in the Neutrino Beam Study Group's minutes and transparencies, (Tsesmelis, 1994-96).

5.1.2 Version 4.00

NUBEAM 4.00 was released in 1996 and featured significant alterations from previous versions. These alterations included the addition of flanges, nuts, bolts and other missing materials to the beamline, discovered in a systematic comparison of the GEANT geometry to the actual technical drawings of the beamline. Also muon and kaon decay matrix elements were corrected.

Extensive comparisons were made between NUBEAM and GBEAM+, (the beam simulation programme maintained by CHORUS), studying meson distributions at various distances along the beamline. Discrepancies between them highlighted the presence of faults in both programmes. These corrections were released as version 4.04 and included the correct positioning of decay products, (at the decay point rather than at a default position), redefining some of the GEANT volumes and corrected the implementation of the $K_{\mu 3}$ decay.

The changes to the neutrino energy spectra for the four types, brought about by the modifications in version 4.04 are shown in figure 5.1. The denominator is the NUBEAM 4.00 files used to create the NEGLIB beam table, see sections 2.7.1 and 5.3.3. These plots show appreciable increases to the low energy peak of the three minor components, whilst the main ν_μ component increases uniformly. Table 5.1 shows quantitatively the effects of the changes. The increase in ν_μ flux can be seen, along with the decrease in mean energy for the minor components. Version 4.04 was a transitional version, and was quickly superseded by version 5.00.

5.1.3 Version 5.00

The main modifications to NUBEAM 5.00 were the result of additional comparisons, to GBEAM+, further along the beamline. These indicated more missing material in the GEANT descriptions. Additionally, the K_L^0 decay was debugged.

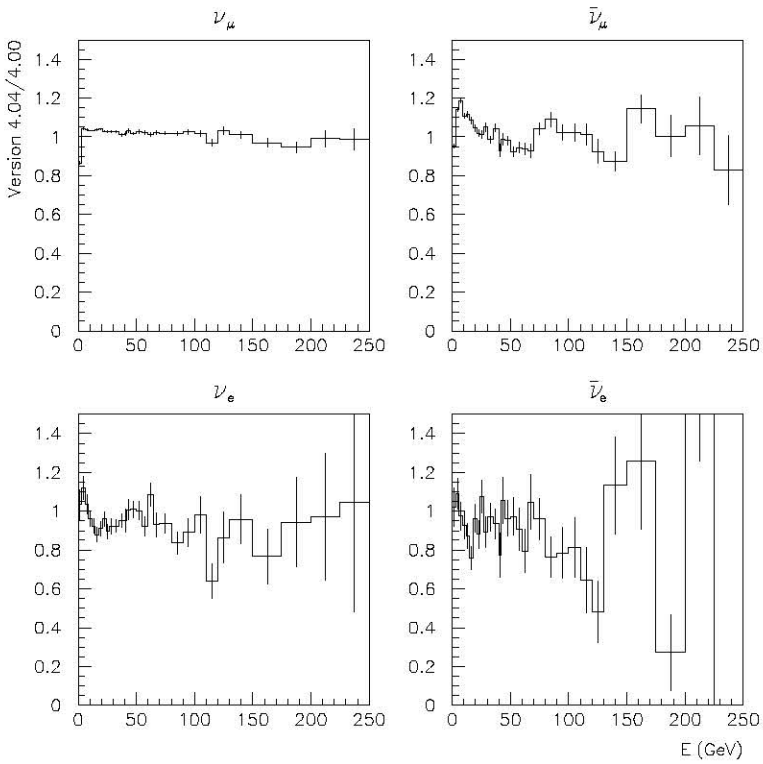

Figure 5.1: Changes due to version 4.04 in the neutrino energy spectra for the four types. Figure 2.4 is used as the NUBEAM 4.00 denominator. Variable binning is used due to lower statistics at high energies.

Figure 5.2 displays the effect of these changes on the neutrino spectra, again using version 4.00, as the denominator. Table 5.1 also outlines the effects on the spectra. NUBEAM 5.00 is shown to keep the ν_μ flux close to version 4.00, whilst increasing the $\overline{\nu}_\mu$.

Minor alterations were introduced with versions 5.01, 5.02 and 5.03, without any real reflection in the neutrino spectra. Further details on the development from version 4.00 to 5.00 are contained within the Neutrino Beam Study Group's minutes and transparencies, (Tsesmelis, 1994-96).

	Version 4.00		Version 4.04		Version 5.00		Version 6.12	
	$\langle E_\nu \rangle$	Flux	$\langle E_\nu \rangle$	Flux	$\langle E_\nu \rangle$	Flux	$\langle E_\nu \rangle$	Flux
ν_μ	23.5	1.27	23.5	1.31	23.4	1.29	23.8	1.15
$\overline{\nu}_\mu$	22.6	0.0891	21.8	0.0946	22.0	0.0944	22.2	0.0922
ν_e	37.0	0.0122	36.5	0.0116	36.5	0.0123	36.8	0.0112
$\overline{\nu}_e$	33.2	0.00336	32.3	0.00312	32.5	0.00329	32.4	0.00305

Table 5.1: The changes to the neutrino spectra shape and size with NUBEAM version. Fluxes are in neutrinos per 100 POT across the NOMAD 2.6 × 2.6 m^2 fiducial volume, average energies are in GeV. The statistical errors on the fluxes are less than 0.1%, 0.5%, 1.3% and 2.6% for ν_μ, $\overline{\nu}_\mu$, ν_e and $\overline{\nu}_e$ respectively.

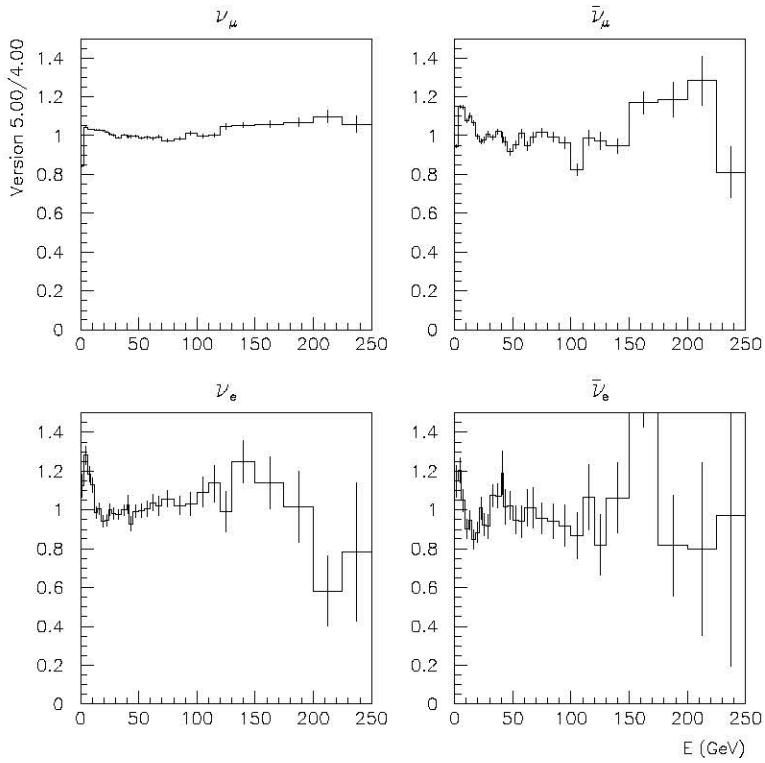

Figure 5.2: Version 5.00 changes in the neutrino energy spectra for the four types. Figure 2.4 is used as the NUBEAM 400 denominator. Variable binning is used due to low statistics at high energies.

5.1.4 Version 6.00

NUBEAM 6.00 is the result of greater accuracy in the details of the recreation of the exact WANF geometry. When previous approximations in implementing the beamline geometry, estimated to have a negligible effect on the ν_μ flux, were combined, the resultant effect on the $\overline{\nu}_\mu$ flux was shown to be much greater than in the ν_μ flux. The following aspects of the GEANT description were subsequently corrected:

- Beryllium holders for the target rods were added.
- The horn and reflector, section 2.4.5, underwent substantial alterations to remove discrepancies with the original technical drawing. The main alterations were the addition of support flanges between the inner and outer conductors and increasing the opening in the neck of the horn. Material was also added surrounding the neck of the horn. Details of these changes are found in Valuev (1999).
- The material definitions of the horn and reflector were changed to allow the magnetic field to penetrate the inner conductor, according to the frequency of the current pulse, (Soler, 1999b).
- The TBID beam monitor was included between the collimators, along with two ionisation chambers placed in front of the vacuum decay tunnel, (see figure 2.1 for these positions). The first ionisation chamber was in fact present only from 1996, and the second for 1998 only.
- The entrance and exit windows of the two helium tubes and 1996 ionisation chamber had been ignored as their 0.3 mm and 0.1 mm depths respectively were too thin for GEANT to take into account. Instead a titanium plate of a combined 1.4 mm was included just before the 1996 ionisation chamber position.
- The decay tunnel was surrounded by a tubular wall, so that particles leaving the tunnel were not lost but had an opportunity to interact.
- Movable iron blocks, remnants from beamdump experiments, were added inside the decay tunnel, after being discovered during a physical inspection of the WANF. These blocks were positioned on a movable rail cart, controlled by two "butoirs", placed at either end of the decay tunnel. The cart remained at the downstream end of the tunnel throughout NOMAD running. The presence of these additional items is illustrated in figure 5.3, where there is an excess of primary proton interactions at

the start of the decay tunnel in the first butoir, and again at the end of the tunnel in the iron blocks and second butoir.

- Particles were allowed to interact in the beamdump at the end of the decay tunnel, rather than being immediately terminated. Figure 5.3 shows the presence of interactions in the beamdump.

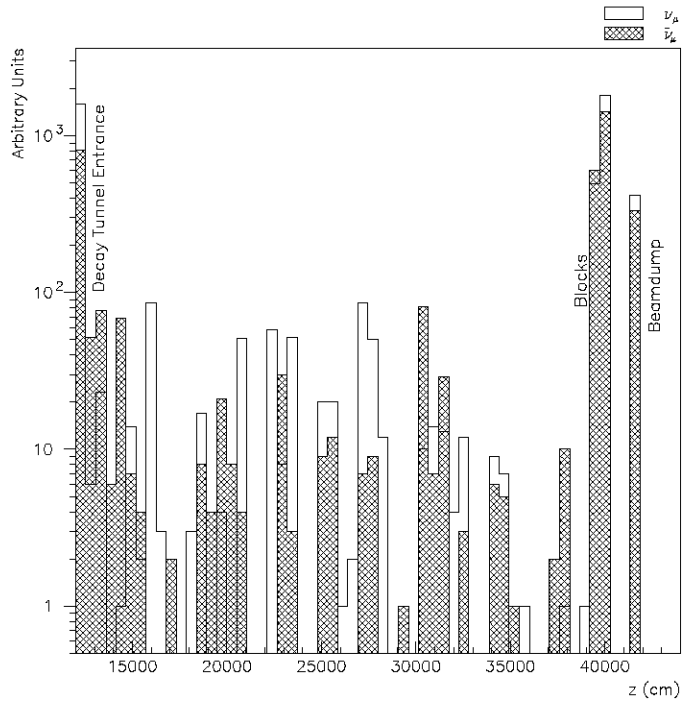

Figure 5.3: The distribution of primary proton interaction points in the decay tunnel, that eventually produce a ν_μ or $\overline{\nu}_\mu$ at NOMAD, showing the presence of the additional simulated material of NUBEAM 6.12.

All of the above additions, except for the inclusion of a magnetic field in the inner conductor, tend to increase the contamination of $\overline{\nu}_\mu$ in the beam. The additional field brings the focusing even closer to center of the beam, further enhancing the ν_μ domination over the $\overline{\nu}_\mu$. The natural composition of the neutrino beam, (without focusing), would be determined by the π^+ to π^- ratio, the majority parents of ν_μ and $\overline{\nu}_\mu$ respectively. This ratio was measured by SPY, and is $\sim 80\%$ averaged over the energies relevant to NOMAD. This composition is roughly confirmed in the ratio of $\overline{\nu}_\mu$ to ν_μ events in NOMAD

during the short period of running with zero focusing, see section 5.6.2. In the focused beam, the ratio of antineutrinos is less than 10%. This implies that interactions downstream of the horn, especially those of primary protons that missed the target, are more likely to produce a $\overline{\nu}_\mu$ that reaches NOMAD, than an interaction before the horn. Thus, any material added downstream of the horn has the effect of increasing the $\overline{\nu}_\mu$ contamination. Material added before the horn also increases the contamination, as this reduces the number of π^+ available for focusing and ν_μ production. This is seen in figure 5.4, and also figure 5.3, which show the interaction point of primary protons, divided into whether a neutrino or antineutrino was eventually produced that would reach NOMAD. They show, as expected, that protons interacting in the target are ten times more likely to give rise to a neutrino than an antineutrino. However, after the horn, the rate of antineutrino production increases to just below that of neutrinos.

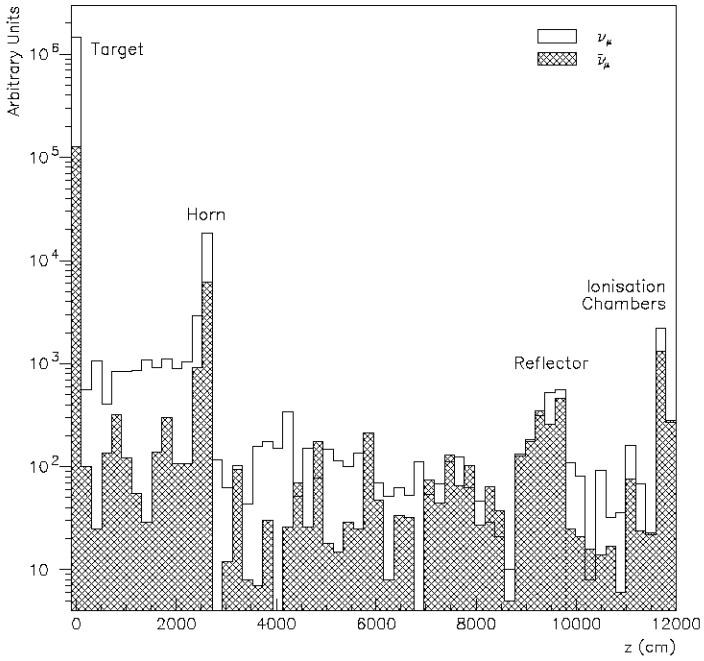

Figure 5.4: The distribution of primary proton interaction points that lead to a ν_μ or $\overline{\nu}_\mu$ at NOMAD, in terms of z, the distance along the beamline. Interactions in the main elements of the beamline are labeled. Produced with NUBEAM 6.12.

Concurrent with the redefining of the GEANT description, was the discovery that the spatial profiles that NUBEAM samples in generating primary protons had x and y widths smaller than the actual beam spot measured by the miniscans, (section 2.4.2). Further the actual distributions were not Gaussian as approximated in NUBEAM. The miniscan profiles were therefore used to create an average histogram in x and y of the proton beam, after relevant pedestal subtraction. Average histograms were determined for each year, and then combined, weighted by the number of protons delivered each year. NUBEAM was then adjusted to sample from these combined histograms. The result of this correction was again an increase in the $\overline{\nu}_\mu$ contamination as there were more protons missing the target. These were likely to interact downstream of the horn, which would increase the $\overline{\nu}_\mu$ flux as explained above. Further information on determining the average histograms from the miniscans can be found in Soler (1999a).

The inclusion of realistic proton beam profiles and the GEANT changes, resulted in the final version of NUBEAM, 6.12. The results of the combined improvements to NUBEAM, from version 4.00 to the present 6.12 are presented in figure 5.5, which displays the ratio of the neutrino energy spectra for the two versions. All the spectra show an increase at low energy, due mainly to the addition of low energy neutrinos from mesons interacting in the decay tunnel walls. The dip after this low energy peak, most clearly seen in the ν_μ spectrum, is due to the alterations in the material and magnetic field of the horn. The $\overline{\nu}_\mu$ spectrum experiences an almost constant increase at low energy. Finally, the ν_e spectrum shows far less of a variation than the $\overline{\nu}_\mu$, the sample used to ascertain how well the simulation is reproducing the data. This implies that the ν_e are less sensitive to changes in the beam line, and that the error assigned to the ν_e spectrum, the signal spectrum for the $\nu_\mu \rightsquigarrow \nu_e$ oscillation search, should be small, see section 5.7. The results are also shown numerically in table 5.1. The most notable change is again the increase in the $\overline{\nu}_\mu$ flux.

5.2 Development of FLUKA

The hadronic production in NUBEAM, both in the beryllium target and the beamline, is handled by the FLUKA simulation package. This programme is maintained by its authors at CERN, and is wholly independent of NUBEAM and NOMAD. A few details of recent improvements to FLUKA, relevant to NUBEAM, will be given.

The original reports on the effects of these developments on the simulation of the neutrino beam to NOMAD can be found in Guglielmi and Collazuol

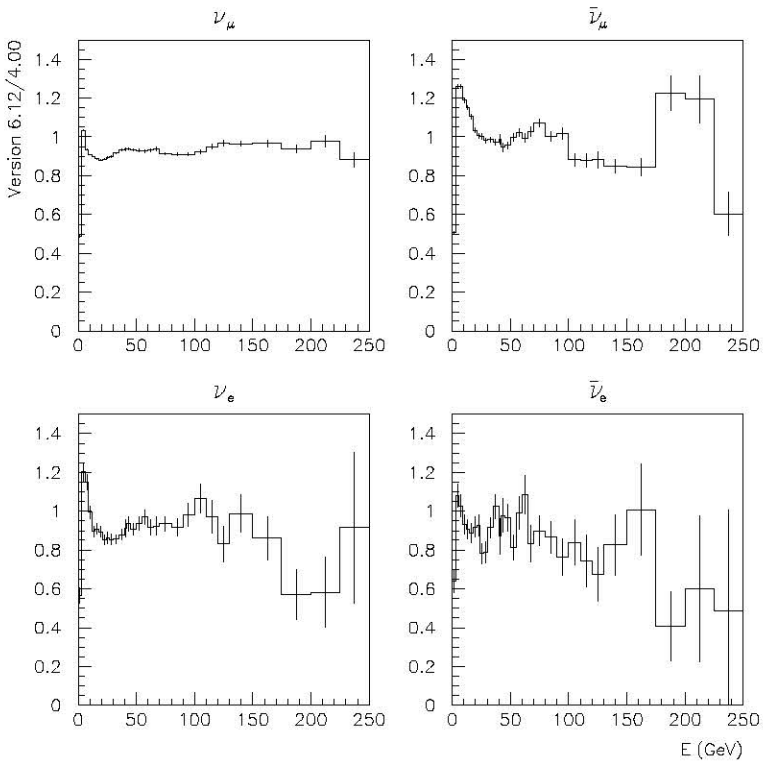

Figure 5.5: Version 6.12 changes in the neutrino energy spectra for the four types. Figure 2.4 is used as the NUBEAM 400 denominator. Variable binning is used due to low statistics at high energies.

(1997-2000), in particular, details of the comparisons of FLUKA to the SPY data. Details of the physical models and their upgrades can be obtained from Ferrari et al. (1992); Ferrari and Sala (1993, 1996).

5.2.1 FLUKA Versions

FLUKA is a generic hadronic shower package, its centre being a Monte Carlo implementation of the Dual Parton Model code, (Capella et al., 1994), for primary hadron-nucleon interactions. This model is extended to hadron nucleus interactions, by using the Glauber Gribov approach, (Gribov, 1969, 1970). The parameters of these models are tuned in FLUKA to fit a wide range of experimental hadron nucleon/nucleus collision data. GEANT, and hence NUBEAM, uses selected FLUKA functions. The functions installed

are from FLUKA 92, (Fasso et al., 1993). Subsequent versions of FLUKA were developed only as a stand-alone programme, and were not implemented in GEANT.

FLUKA 95 was the first stand-alone version interfaced to NUBEAM, see section 5.3.1, to replace the GEANT-FLUKA description of the proton beryllium collision. FLUKA 95 also corrected the transverse development of the hadronic shower, that had not been properly described in FLUKA 92. Pion and kaon production levels generated by FLUKA 95 were compared to those measured by the SPY experiment, and of the earlier Atherton experiment, see chapter 3, (future references to SPY data refer to the combined Atherton and SPY data sets). Good agreement was found up to energies of 100 GeV, after which, FLUKA 95 began to underestimate the measured pion, kaon and proton production in SPY. Further, comparisons to muon pit data, see section 5.4, showed that FLUKA 95 was producing too soft a muon spectrum, and also that the spatial distribution was not sharply peaked enough in the centre.

Both these issues were addressed by the release of FLUKA 97.5 where an error in the implementation of the Dual Parton Model was corrected. This error caused doubling of the transverse momentum in produced mesons that carried one of the quarks from the projectile. Correcting this produced a more forward peaked angular distribution and hardened the energy spectrum. This correction was only required for positive particles. However, negative particles were effected by adaptations made to the fragmentation functions. FLUKA 97.5 was shown to agree with SPY measurements from 5 to 300 GeV, in the forward direction, and have reasonable agreement with the transverse momentum scan data.

The effect of the development of FLUKA on the neutrino beam at NOMAD is summarised in table 5.2. This table illustrates the changes to the neutrino flux, antineutrino contamination, and average energy of the beam. It shows a significant decrease in neutrino flux after FLUKA 92, and a repeated decrease in contamination. The average energy is shown to have slight, but observable, variations.

Close analysis of the FLUKA 95 and 97.5 output showed that neutrinos produced in the target, (e.g. from charm or K_S^0 decays), were being dumped before they could be interfaced to NUBEAM. This reduced the antineutrino contamination at NOMAD. When these target neutrinos where included, the contamination rose by around 2.5%. The inclusion of the target holders and the new proton profiles, found in the development of NUBEAM 6.00, section 5.1.4, also had to be ported to the FLUKA implementation of the target area. These changes, and the recovery of the target neutrinos were introduced as FLUKA 98, the ultimate version to be used with NUBEAM.

	FLUKA 92		FLUKA 95		FLUKA 97.5		SPY C3.0	
	$\langle E_\nu \rangle$	Flux	$\langle E_\nu \rangle$	Flux	$\langle E_\nu \rangle$	Flux	$\langle E_\nu \rangle$	Flux
ν_μ	23.5	1.27	23.6	0.978	23.5	1.05	24.4	0.966
$\overline{\nu}_\mu$	22.6	0.0891	21.8	0.0447	20.5	0.0458	15.6	0.0784
ν_e	37.0	0.0122	37.8	0.00874	39.8	0.00973	36.2	0.00998
$\overline{\nu}_e$	33.2	0.00336	34.1	0.00260	31.0	0.00261	27.5	0.00173

Table 5.2: Effect of FLUKA upgrades on the neutrino beam at NOMAD. The values were obtained from NUBEAM 4.00 interfaced to the listed FLUKA version, (except SPY which used NUBEAM 6.12). The fluxes are in terms of neutrinos per 100 POT across the NOMAD 2.6×2.6 m^2 fiducial volume, average energies are in GeV. The statistical errors on the fluxes are less than 0.1%, 0.5%, 1.3% and 2.6% for ν_μ, $\overline{\nu}_\mu$, ν_e and $\overline{\nu}_e$ respectively.

The original reports on the effects of these developments on the simulation of the neutrino beam to NOMAD can be found in Guglielmi and Collazuol (1997-2000), in particular, details of the comparisons of FLUKA to the SPY data. Details of the physical models and their upgrades can be obtained from Ferrari et al. (1992); Ferrari and Sala (1993, 1996).

5.2.2 SPY Weighted FLUKA

Whilst FLUKA 97.5 and FLUKA 98 provided good agreement with SPY in both the forward direction and angular scans, better results could be obtained by tuning the FLUKA output to the SPY data alone. The versatility of FLUKA in simulating a wide range of collisions and energies is detrimental when a precise value over a small range is required. FLUKA is tuned to collision data from many different experiments, often at high energies, (above 100 GeV), further inhibiting the ability of FLUKA to reproduce the lower energy production rates of SPY and NOMAD. Refitting FLUKA to just the SPY data should produce a better simulation of the NOMAD neutrino beam.

The first step in this process is making a fit to the SPY data, giving a functional form parametrising the SPY results. Then comparisons can be made to FLUKA at all angles from the target up to 10 mrad, (above this, particles do not produce neutrinos that enter NOMAD). This is achieved with a simplified Malensek parametrisation, which has all momentum dependence removed when compared to the full parametrisation of equation 6.8:

$$\frac{d^2N}{dpd\Omega} = \frac{A}{(1+(\frac{p_T}{B})^2)^4} \tag{5.2}$$

where A and B are the parameters of the fit and p_T is the transverse momentum. The fit is performed on angular data from mesons with secondary momentum $p = 15$, 40, 67.5 and 135 GeV. A weight, S, is then determined at each of these momenta according to the ratio of the fitted SPY and FLUKA yields, Y:

$$S(p_{\pi^\pm,K^\pm,p,\overline{p},K_L^0}) = \frac{(\sum_i Y_{\pi^\pm,K^\pm,p,\overline{p},K_L^0}(p,\theta_i))_{\text{SPY Fit}}}{(\sum_i Y_{\pi^\pm,K^\pm,p,\overline{p},K_L^0}(p,\theta_i))_{\text{FLUKA}}} \tag{5.3}$$

This is performed for pions, kaons and protons. K_L^0 production was not measured by SPY, but can be included in the weighting process using the parametrisation:

$$K_L^0 = \frac{1}{4}(K^+ + 3K^-) \tag{5.4}$$

determined from NA31, (Auge, 1989), and NA48, (Barr et al., 1990) data. This parametrisation has an error of 15%. The S ratios are subsequently fitted with a polynomial as a function of forward momentum, to provide the final weight functions, for each hadron. This weight is applied to hadrons at the end of the target rod they were created in, (recall that the T9 neutrino target comprises 11 100 mm beryllium rods, separated by 100 mm air gaps). The handling of subsequent reinteractions is returned to FLUKA. Hadrons are then recorded at a plane 15 cm after the last target rod. The ultimate weight is determined from the ratio of distributions of hadrons at the target plane with and without the fitted S weighting function. Neutrinos at NOMAD are then adjusted by this weight according their parent at this recording plane. Further details of the implementation of this process are left for section 5.3.1.

The effect of the latest SPY weighting, called C3.0, is seen in table 5.2. This shows quite a strong change in the $\overline{\nu}_\mu$ spectrum and flux.

There are three main sources of error from the SPY weighting that must be included if it is used in the beam simulation. The first is from the SPY points themselves, which are between 5 and 10% on the particle yields used. The two remaining sources are from the two fits, first to the angular distributions of SPY points, and then fitting S as a function of momentum. These contribute errors of 2 and 3% at 40 GeV respectively. More details of the SPY weighting can be found in Guglielmi and Collazuol (1997).

5.3 Running NUBEAM and FLUKA

The best beam simulation requires the combination of NUBEAM with the latest FLUKA version and SPY weights. How they are combined, and the other intricacies of running the simulation are now described.

5.3.1 Interfacing FLUKA to NUBEAM

As previously mentioned, FLUKA is now maintained as a stand-alone hadronic interaction package. Using this package, the T9 target has been simulated, including the target rods and holders, and a 450 GeV proton beam, sampled from the new average spatial histograms determined from the miniscans. The outgoing particles are recorded upon reaching an infinite x and y plane, (i.e. perpendicular to the beam), 15 cm downstream of the last target rod. For every particle reaching the plane the x, y, z co-ordinates, the p_x, p_y, p_z momentum components and the particle type are recorded. This would be sufficient information for NUBEAM, however to allow for SPY weighting the type of the particle first produced by the proton interaction and its energy leaving the target rod are also recorded. This is because it is the particle arising from the proton target collision, not those from any subsequent reinteraction, that determines the SPY weight. Of course this weight is then propagated to its daughter particles.

Information on the particles at the target plane is recorded in an ASCII file which can then be read in by NUBEAM. These particles are then transported through the beamline and allowed to decay as in the case when GEANT-FLUKA is used to simulate the target. A HBOOK, (Bunn et al., 1995), ntuple is created storing information on neutrinos that reach NOMAD, in particular their energy, spatial and angular information and ancestral information. Included in the ancestry of a neutrino is the chain of parent particle types, right back to the parent coming from the target rod, which will give the neutrino its weight, according to the SPY measurements.

Note that it was in this interfacing process that the target neutrinos were previously being lost, section 5.2.1, but are now retained. More information on the interfacing process can be obtained from Collazuol and Guglielmi (1998).

5.3.2 NUBEAM Decay Multiplicity

To increase the statistics of a simulation, whilst keeping the time required to a minimum, NUBEAM allows multiple decays. This means that particles produced in the primary proton collision can be repeatedly transported

through the beamline to increase the number of neutrinos reaching NOMAD. There are two factors, one for mesons, and one for muons, which set the number of times a particle is decayed. Throughout this chapter, 100 has been used for meson decays and 1 for muon decays, (except in section 5.4 where the muon pits are investigated and so 10 is used for both meson and muon decay multiplicities to increase the muon statistics). Time is economised by not having to rerun the primary proton collision to generate a new pion. A pion decayed with a multiplicity of 100 produces on average less than two neutrinos reaching NOMAD.

Whilst multiple decays increase the neutrino statistics, the error is no longer Poisson, as the number of neutrinos is artificially high. Neutrinos now arise more often from the same parent, so there is a degree of dependence in the spectrum. Although this is reduced to a minimum, by keeping the number of mesons generated well above the multiplicity factor, (10^4 times greater), the errors must still be inflated. To estimate the degree of inflation, the entire sample of neutrinos is divided into a number of subsamples, roughly the size of the NOMAD data sample. The Poisson errors on the spectral histograms from these subsamples are increased until the average Kolmogorov-Smirnov probability, (Eadie et al., 1971), between the histograms is 50%. The Kolmogorov-Smirnov probability gives the probability that two histograms are drawn from the same parent distribution. For compatible sets of histograms, the probability is uniformly distributed between zero and one, assuming reasonable histogram binning. This produces a statistical error scale factor of around 1.7.

5.3.3 Weighting Event Monte Carlo

Neutrino events in NOMAD are simulated with NEGLIB, section 2.7. This programme samples from beam tables that describe the distribution of neutrinos incident on NOMAD as a function of energy and radius squared. These tables were produced with NUBEAM 4.00. As there have been many iterations of the NUBEAM and FLUKA codes, and as reprocessing the million plus number of neutrino events in NEGLIB is extremely time-consuming, the NEGLIB events are simply weighted. A weight table is created from the ratio of the old version 4.00 beam tables to the new ones, so each NEGLIB event becomes weighted according to its initial energy and radius squared.

A beam table, and hence weight, exist for the four neutrino types, ν_μ, $\overline{\nu}_\mu$, ν_e, and $\overline{\nu}_e$. These individual tables have no universal normalisation, for example to protons on target. Rather, when comparing spectra from two different neutrino types, as will be necessary in the $\nu_\mu \rightsquigarrow \nu_e$ search, a relative normalisation is applied between the two, reflecting the ratio of neutrino

types in the NUBEAM output ntuple. These ratios are given in table 5.5. The weights of NUBEAM 4.00 to NUBEAM 6.12 with FLUKA 98 and SPY C5.1 are plotted in figure 5.6 for ν_μ and $\overline{\nu}_\mu$. For simplicity, these have been projected onto the energy axis, removing the radius squared dependence.

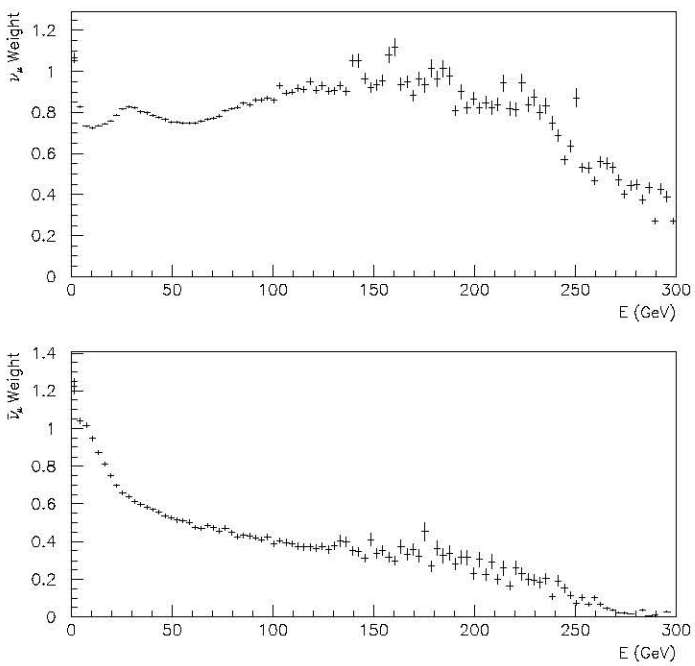

Figure 5.6: The weight functions used, without radial dependence, to bring ν_μ and $\overline{\nu}_\mu$ event Monte Carlo to NUBEAM 6.12 with FLUKA 98 and SPY C5.1. The fluctuations in the ν_μ graph are from the erratic and large weights at high radius.

5.4 Muon Pit Comparisons

The muon pits in the WANF measure the flux of muons traveling with the beam. As most muons are produced with ν_μ in pion decays, measurement of the muon flux, its spatial and energy distribution, provides an insight into the neutrino beam itself. In this regard, the muons pits have three main uses. Firstly, they aid in the steering and tuning of the neutrino beam by insuring that the muons are correctly centred. This also provides a cross check on

whether the currents in the horn and reflector are correct. Secondly, the muon flux determined by the pits can provide an independent measure of the absolute neutrino flux, after normalisation. Whilst feasible, this option has not yet been developed. The third function of the muon pits is as an additional location for comparisons between data and Monte Carlo. If the simulation well represents the neutrino beam generation and transport, it should not only agree with the neutrino data measured at NOMAD, but also with the muon data recorded in the pits. The muon pit comparison will now be reported.

5.4.1 Layout of the Muon Pits

In the WANF there are eight muon pits, with only the three most upstream in operation during NOMAD running. Collectively they are known as the Neutrino Flux Monitoring (NFM) system. The pits are spaced within the first iron shield, directly after the decay tunnel, see figure 2.1. The purpose of the iron shield is to filter out muons in the beam before it reaches NOMAD. Pit 1 follows 4.42 m of iron, there is an additional 20.52 m of iron between pits 1 and 2 and 20.15 m between pits 2 and 3. The increasing amount of iron before the pits allows for a rudimentary energy distribution measurement, as only the higher energy muons will reach pit 3, whilst most reach pit 1.

Each muon pit comprises an array of solid state detectors (SSDs). These are silicon diodes, placed in watertight boxes and mounted on an octagonal support plate. The arrays are illustrated in figure 5.7. The detectors themselves are not to scale; the actual SSD size ranges from 1 to 200 mm^2. The centres of the SSDs are placed 15 cm apart, along radial arms. There are three SSDs in the central position of pit 1, and two in pits 2 and 3.

The pits themselves are small rooms in line with the beam, with the support plate attached to the downstream wall. The plates are movable horizontally and vertically to an accuracy of 2 mm, allowing alignment with the expected beam centre.

For calibration purposes five additional detectors are placed in a calibration box. This is a movable box, which can be positioned in front of every fixed detector in the array. The calibration box also produces a beam scan every eight hours. There is a calibration box in each pit, and also a reference box of five detectors, that is shuffled between the three pits to allow consistent calibration between them.

Muons crossing the SSDs generate a current which is integrated over the length of a beam pulse (spill), the order of a millisecond. The SSDs are unable to distinguish between μ^+ and μ^-, nor electrons that may also be present in the beam, (most likely from muon interactions).

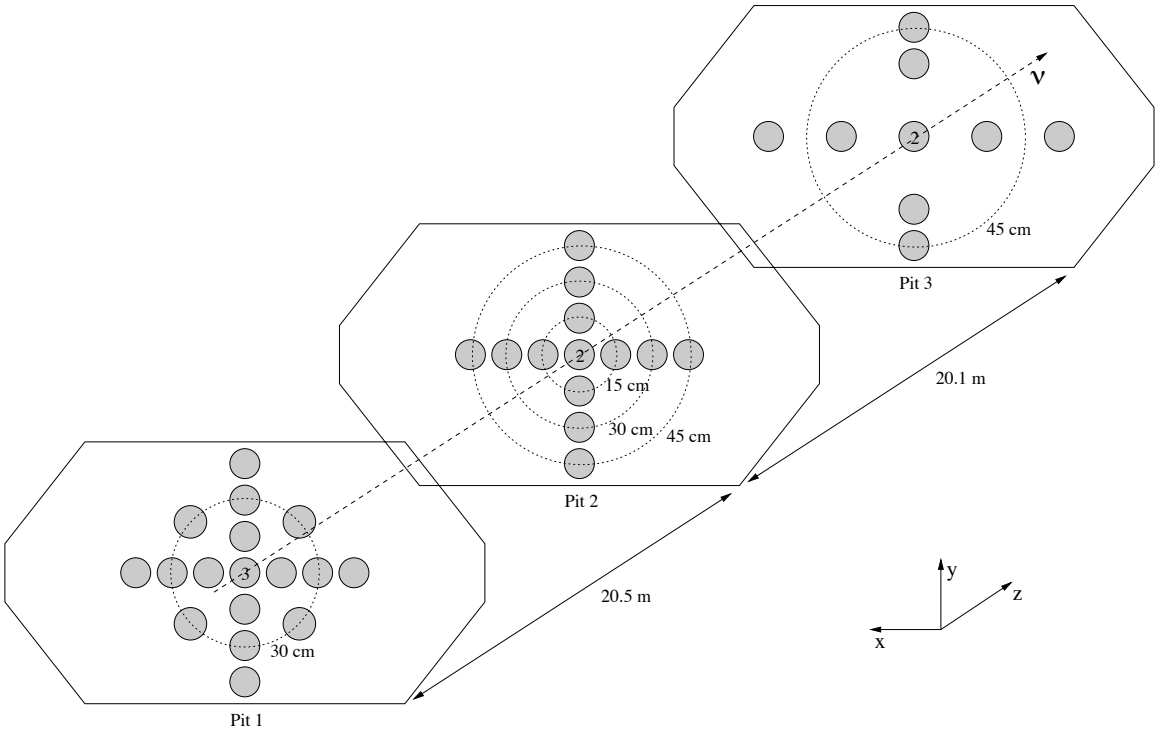

Figure 5.7: Layout of the first three muon pits showing position of SSDs on octagonal mounting plates during NOMAD running. SSDs are on radii, with their centres 15 cm apart. The direction of the neutrino beam is also shown.

For high energy muons, it is safe to assume the response of the detector is independent of their energy. A pedestal subtraction is necessary, where the pedestal is determined from the average of the current in the detector before and after the beam pulse. Degradation of the detector from irradiation requires the detectors to be frequently recalibrated. The maximum flux rate that can be measured is 10^{12} cm^{-2} s^{-1}.

5.4.2 Calibration

The reference and calibration boxes allow relative calibration amongst all the fixed detectors, however to set them to the absolute muon flux, a reference scale must be obtained from the muon flux measured in emulsion plates. Plates of 300 μm thick plastic, 3×4 cm^2 in area, coated on both sides with 100 μm of emulsion are used. Pit 3 is used for the emulsion calibration as it has the lowest flux, lest the emulsion be overpopulated with tracks. The

emulsion is placed in four positions, on the upstream wall of the pit, in front of the ref/cal box, in front of the two central detectors and in front of the fixed detector 30 cm above the centre.

The emulsion calibration is performed three to four times a year in dedicated runs with $\sim 10^{12}$ protons on target. After development, the tracks in the emulsion are counted. An analysis of the angular distribution of the tracks is also performed. This is because knock on electrons are produced in the pits from muon interactions, and can also create tracks in the emulsion. Electrons can be distinguished as on average they have a lower energy than muons and higher track angles. The angular distribution of the electron and muon tracks, for combined charges, was simulated, as part of the work of this thesis, to allow the correct subtraction of the electron low angle background before determining the muon flux. The simulated angular distributions in pit 3 are presented in figure 5.8. The simulated leptons have a low energy cut off at 10 MeV. The ratio of electrons to muons was determined to be 5.5%.

Further details of the calibration process and the setup of the muon pits can be obtained from early reports on their calibration, Heijne (1983) and Abt and Jongejans (1985). Calibrations during the period of NOMAD running are found in Falaleev et al. (1997) and then Bozza et al. (1998).

5.4.3 Comparison with Simulation

The comparison between the measured and calibrated muon data, (Papadopoulos, 1997), and the most recent simulation from NUBEAM 6.11 with FLUKA 98, are given in figure 5.9. These spatial distributions are normalised at their peaks, and allow the comparison between the shapes of the data and simulation. The pit 1 simulation is seen to have an x distribution that is too peaked, despite the changes to FLUKA. Pit 1 y and both x and y in pit 2 agree well however. Although there is a lack of statistics in the pit 3 simulation, differences are still observable, most notably in x. The difference appears as an offset in the peak of the simulation, and has yet to be explained. To understand how the absolute flux and energy dependence compare, the muon flux is listed for the three pits in table 5.3 for data and several NUBEAM (N) and FLUKA (F) combinations, (note SPY weights have not been determined for muons). The integrated flux in pit 1 is difficult to determine due to the non Gaussian distribution of the muons and the high degree of electron contamination, and so is not tabulated. The predictions of NUBEAM 6.11 with FLUKA 98 are shown to be in excellent agreement with the data.

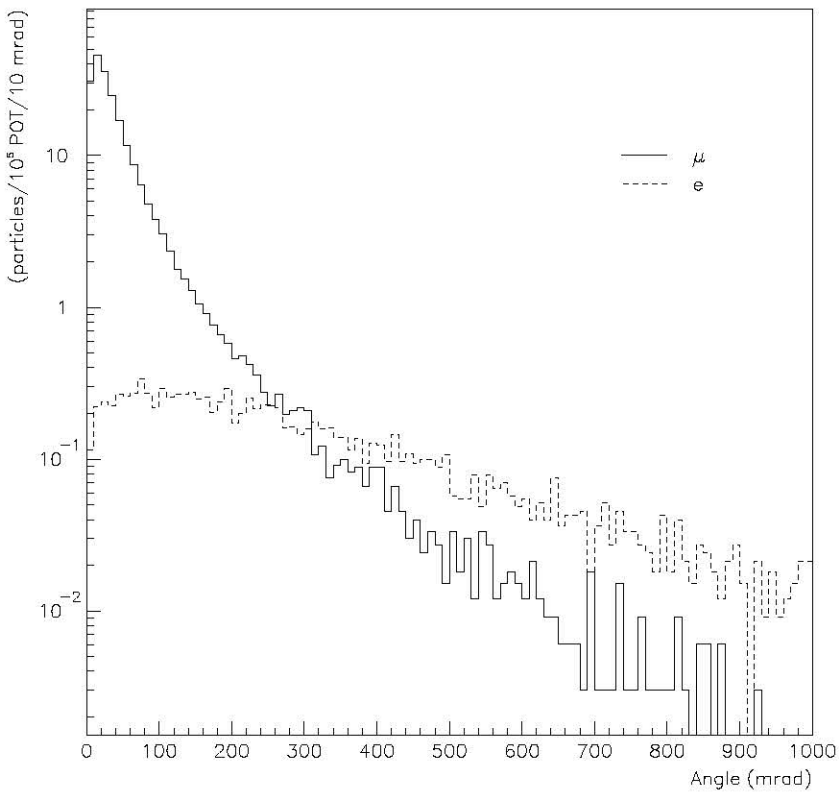

Figure 5.8: Simulation of the angular distribution of muons and electrons in the calibration emulsion of muon pit 3, performed with NUBEAM 4.04 and FLUKA 95.

5.5 Quasielastic Like Events in The FCAL

The Forward CALorimeter(FCAL) presents the neutrino beam with a target six and a half times more massive than the drift chamber. The neutrino data from the FCAL thus provides excellent statistics for studying the ν_μ flux. Low exchange energy, ν as defined in equation 1.9, events are most apt for flux studies, as will be explained in section 5.5.2. Quasielastic-like events, comprising quasielastics, resonances and low ν deep inelastic scattering events, were therefore chosen.

Comparisons of the simulated beam flux to that measured by the FCAL provide another independent cross check of the Monte Carlo. An early study

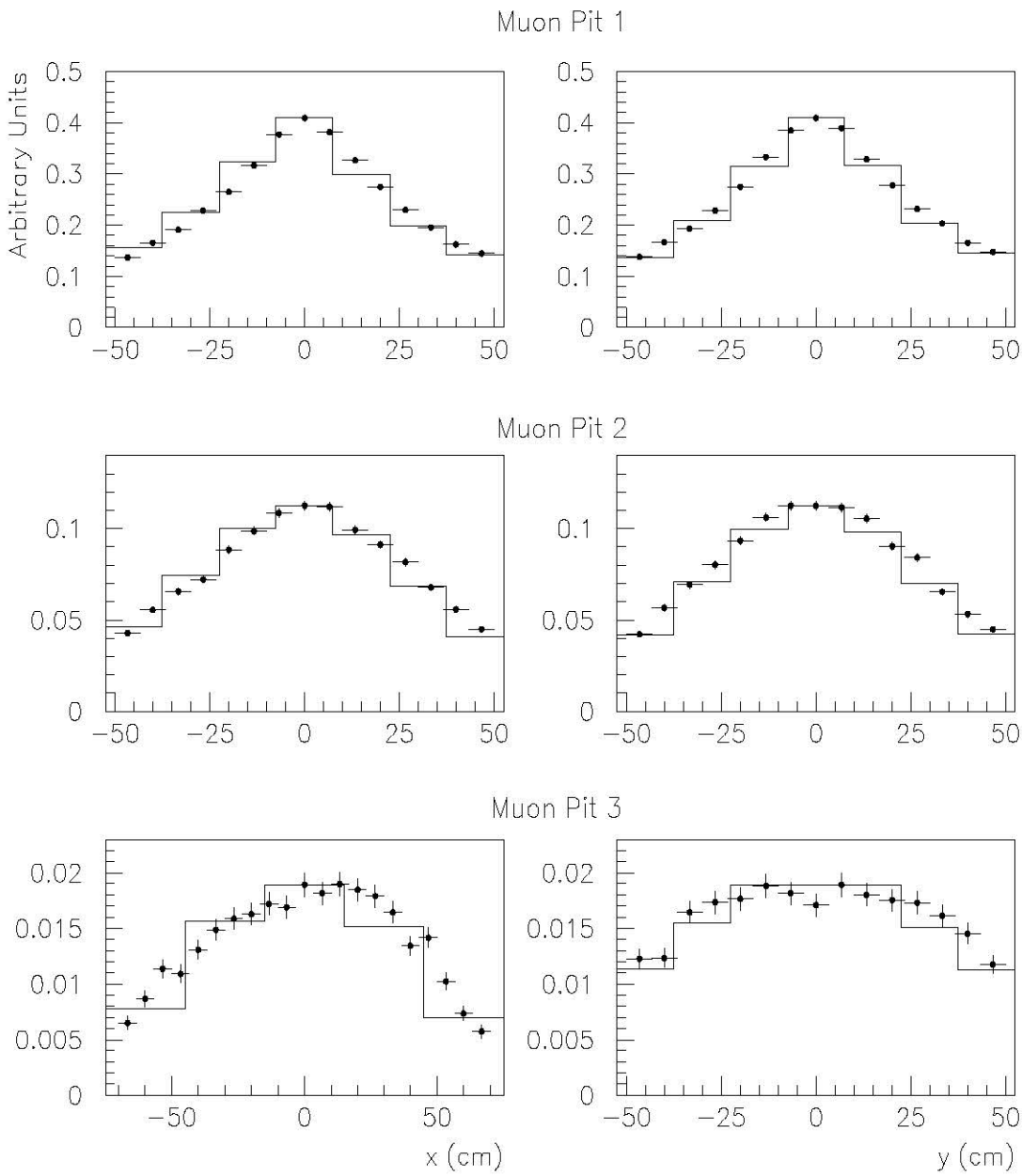

Figure 5.9: Comparison of the data to simulated x and y spatial distributions of the muon flux in the pits. The histograms represent the measured muon flux in the SSDs placed at the central positions of its bins. The simulation, points, is normalised to the data peaks.

	Pit 1	Pit 2	Pit 3
Data	-	564	128(153)
N4.00 F92	1401	471	130(154)
N5.00 F92	2336	647	146(177)
N5.00 F95	1856	523	106(129)
N5.00 F97.5	2030	568	117(141)
N6.11 F98	2107	551	120(145)

Table 5.3: Muon fluxes in units of 10^{-5} muons per proton on target, integrated over 100×100 cm^2, the approximate area of the muon pit arrays. For pit 3, in parentheses, the flux is also integrated over 140×100 cm^2, to include the detectors at 60 cm. The values for data and several simulations are shown.

with just the 1995 eight module FCAL data is presented in Weiße (1997).

The FCAL has already been described in section 2.5.3, outlining its construction, materials, geometry and the energy calibration process. A greater understanding of the FCAL and its event reconstruction are required for this analysis, and so more a detailed description is now presented.

5.5.1 Further Details of the FCAL

The determination of the position of neutrino interactions in the FCAL is considerably less precise than in the drift chamber. Energy produced in a scintillator panel is an indication of an interaction. The horizontal position of this energy deposition can be obtained from the difference in the signal counts, R, at the left and right end photomultipliers tubes (PMT), via:

$$x = \frac{\lambda}{2} \exp\left(\frac{R}{\beta}\right) \tag{5.5}$$

where β is the gain asymmetry between the left and right PMTs, and λ is the attenuation length, ~ 150 cm. The vertical position, y, of the energy deposit, can only be taken as the central position of the scintillator that is hit. In z, as five scintillators are bundled together to form a module, (which are then placed vertically to create the FCAL stacks), the central position of the module with the energy deposit must be used.

The position of the interaction vertex in the xy plane can now be estimated from the mean position of the energy deposits. This is primarily calculated for the first FCAL stack that is hit, (a stack is said to be hit when

more than 0.5 mip, minimum ionising particle, has been deposited). These are referred to as the centre of gravity co-ordinates:

$$x_{FCAL} = \frac{\sum_{i=1}^{10} E_i x_i}{\sum_{i=1}^{10} E_i}, \quad y_{FCAL} = \frac{\sum_{i=1}^{10} E_i y_i}{\sum_{i=1}^{10} E_i} \tag{5.6}$$

where the sum is over the ten modules of the first stack to be hit, and E_i, x_i and y_i are the energy and position in the given module.

A separate method for determining the interaction vertex is to extrapolate the muon track back from the drift chamber to the FCAL stack that was first hit. This method of course relies on the existence of a muon in the event.

An energy scale is required as it was shown that the energy deposition distributions between data and Monte Carlo did not agree. This disagreement is due to saturation in the simulation of the ADCs occurring earlier than in data, and also the poor modeling of hadronic interactions, causing responses to be too small. By minimising the χ^2 between the two distributions whilst varying the energy scale of the Monte Carlo, a value of:

$$\frac{MCEnergy}{DataEnergy} = 0.800 \pm 0.005 \tag{5.7}$$

was obtained. This study is reported in Boyd (1998).

An additional schematic of the FCAL is depicted in figure 5.10. This figure shows the four stacks, as well as the individual scintillator planes. Also illustrated is the support structure of the magnet I.

5.5.2 Low ν Events

There are several reasons why events with low ν are most appropriate for flux studies. The major reason is that the neutrino interaction cross sections of low ν events are largely energy independent, (non scaling processes). Quasielastic and resonance events are non scaling, and it can also be shown that deep inelastic scattering events with ν below some given ν^0 also have an energy independent cross section, up to a correction of the order ν^0/E. This is shown by integrating the energy dependent cross section up to ν^0. In order that the correction is as small as possible, the lowest ν^0 allowed by the statistics of the data is applied. As all three categories of interactions with ν below ν^0 then have energy independent cross sections, the flux is directly proportional to the number of charged current events.

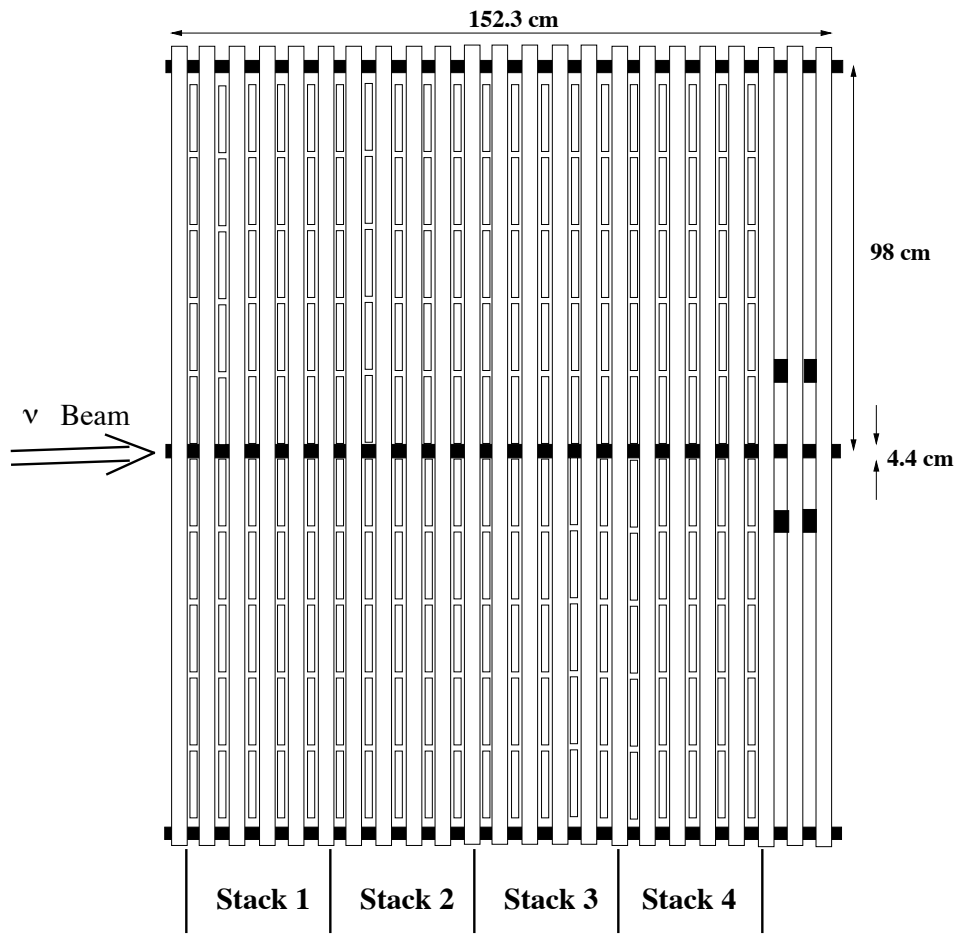

Figure 5.10: Side view of the FCAL showing the positions of the stacks and the (black) support rods. (Taken from Boyd, 1998)

Implementation of a finite ν cut, however, requires a correction function to be applied before the comparison of the Monte Carlo flux spectrum with the data:

$$V(E_\nu, \nu^0) = A - \frac{1}{2}B\frac{\nu^0}{E_\nu} + \frac{1}{6}C\left(\frac{\nu^0}{E_\nu}\right)^2 \tag{5.8}$$

where for ν_μ and ν_e, $A = 1.175$ and $B = C = 0.550$, and for $\overline{\nu}_\mu$ and $\overline{\nu}_e$, $A = 1.175$ and $B = C = 2.040$. This correction function, and the above mentioned cross section integration are presented in Das and Mishra (1997). The values of the parameters were obtained from a fit to the CCFR neutrino data. The effects on the flux of changing them by 10 to 20% were not

noticeable.

Other reasons for desiring low ν events relate to the simplicity of the event. In simulation, there is no necessity to consider nucleon structure, quantum chromodynamic corrections, sea quarks or charm production. In data, identification of the neutrino interaction is easier as the flagging lepton receives nearly all the energy of the neutrino and is simple to detect. Further, there is little concern over inconsistencies between simulated and actual energy scales, or the calibration of energy scales in the Monte Carlo. Rather, the energy spectrum depends on the well measured muon momentum, see section 2.5.4.

Due to the large statistics of the FCAL data to be used, 3.5 million triggers during 1995 11 module running and 12.6 million in 1996, ν^0 could be set at 1 GeV, whilst still leaving enough events for a reliable study.

5.5.3 Event Selection and Efficiency

As explained in section 2.6.2, there are two FCAL triggers, the difference being the threshold on the energy deposited. The **FCAL′** trigger was chosen for this study as it has the lowest threshold, implying that it consists mainly of low ν events. To further enhance this proportion, only pure **FCAL′** triggers were taken, that is to say triggers in anti coincidence with the **FCAL** trigger. The actual threshold of **FCAL′** is unknown, but has been estimated at between 0.5 and 1.5 mip. The selection criteria for neutrino event extraction from these triggers are now described.

Events with only one muon are selected, that is to say only one track reconstructed in the drift chambers, matched to a hit in the muon chambers. As the study aims to produce a ν_μ spectrum, only μ^- are required. The $\sim 4\%$ of μ^+ events are removed with charge selection, provided by the bending of the NOMAD magnet.

In the data, the hadronic energy is used to approximate ν. A study of the hadronic energy resolution was conducted in Boyd (1998). It showed a resolution of $\sigma(E)/E = 104\%/\sqrt{E}$, and further stated that events are fully contained if initiated in stacks 2 or 3. Although there is little leakage of energy in stacks 1 and 4, due to the high statistics available, it was decided to restrict the analysis to stack 2 and 3 events. As the FCAL presents a uniform target to the neutrinos, this approximately halved the number of events.

The fiducial volume is then defined on the muon track, extrapolated back into the FCAL. The track was required to be within $|x, y| < 90$ cm at either the interface between the first and second stack, or the third and fourth stack. This allowed a greater number of tracks to be accepted than applying

the cut a the centres of stack 2 or 3. An additional cut, $y > -85$ cm, was later required to remove through going muons in the bottom of the FCAL, thought to be the result of interactions in CHORUS.

Stack 1 was used as a veto, additional to the veto plane itself. It was required to have $E_{Stack1} < 0.5$ mip. The use of stack 1 as a veto was a further reason to remove it from the analysis.

To ensure the association of the muon with an event in the FCAL, there is a vertex proximity cut. The extrapolated track must match the reconstructed position of the hit, given by equation 5.6, to within 30 cm in x and 18.5 cm in y, (the height of a scintillator paddle). This check was performed at the centre of the first stack hit.

The efficiency of these selection criteria was obtained by applying them to simulated quasielastic events, the main source of low ν events. These events were generated with NEGLIB 5.09, adjusted to include beam tables from NUBEAM 500 with FLUKA 95, and alternative muon acceptance functions for the FCAL, developed by Boyd (1998). The effect of each cut is exhibited in table 5.4. Energy values unfeasible in data are produced by the simulation. Thus, cut 1 was imposed on the Monte Carlo, before considering the efficiency. Cut 2 was used to simulate the acceptance of the trigger planes, $\mathbf{T}_1$ and $\mathbf{T}_2$, and also the efficiency of the veto plane in front of the FCAL, $\mathbf{V}_8$. The selection of low ν events, cut 8, is shown to have the largest effect.

Number	Selection Cut	Events	Efficiency	Relative Efficiency
-	Total Stacks 2 & 3	16391	-	-
1	$0.5 < \text{mip} < 12$	15518	1.00	1.00
2	Trigger $\overline{\mathbf{V}}_8\mathbf{T}_1\mathbf{T}_2$	15030	0.968	0.968
3	Fiducial Volume	14595	0.941	0.971
4	1 Track in DC	13482	0.869	0.924
5	$E_{Stack1} < 0.5$ mip	13481	0.869	1.00
6	Vertex Proximity	13372	0.862	0.992
7	No through muons	12758	0.822	0.954
8	$E_{had} < 1$ GeV	9158	0.590	0.718

Table 5.4: FCAL quasielastic event selection. Column five refers to the effect of the imposed cut alone, whereas column four is cumulative.

The incoming neutrino energy is approximated using:

$$E_\nu = \sqrt{p_\mu^2 + m_\mu^2} + E_{FCAL} \tag{5.9}$$

where E_{FCAL} is the total energy deposited in the FCAL by both the hadron shower and the muon. As the hadronic energy is limited to 1 GeV, most of E_ν is determined by the well measured muon momentum, p_μ. However, due to misalignment of the drift chambers in 1995, the latter half of the year's events require the following momentum correction:

$$\frac{1}{P} \rightarrow \frac{1}{500 \text{ GeV}} + \frac{1}{P} \tag{5.10}$$

The efficiency, as a function of E_ν, is plotted in figure 5.11. Due to only a small number of NEGLIB events being reconstructed, the efficiency was produced with bin sizes increasing with energy. After the initial peak in efficiency, due to the low energy events not being affected by the harshness of cut 8, the selection process is shown to be fairly uniform with energy. The limits used in cuts 1, 6, 7 and 8, were varied by $\pm 10\%$ to obtain errors on the efficiency. This method produced a total selection efficiency of 0.590 ± 0.03.

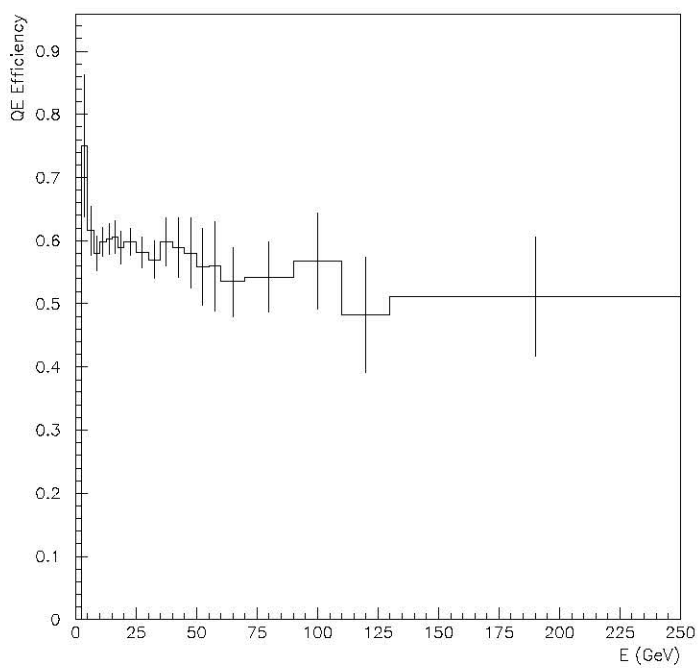

Figure 5.11: Selection efficiency of quasielastic (QE) neutrino events in the FCAL as a function of reconstructed neutrino energy.

5.5.4 Comparison with Simulations

The above selection criteria were applied to the FCAL data from 1995 11 module and 1996 running. To garner some insights into the shape of the neutrino beam, the x and y spatial distributions have been plotted, figure 5.12. The distribution in x should be Gaussian, but there are too few events in the centre. These extra central events were removed as a consequence of the tightening of fiducial y to remove the through going muons. Without the $y > -85$ cm cut, the extra *neutrino* events would make the x distribution more Gaussian. The y distribution is distorted due to the slope and offset of the beam. The beam axis intercepts the FCAL at $y \sim -27$ cm at an angle of ~ 42 mrad. A peak appears in the centre due to the support structure of the FCAL inducing additional neutrino interactions.

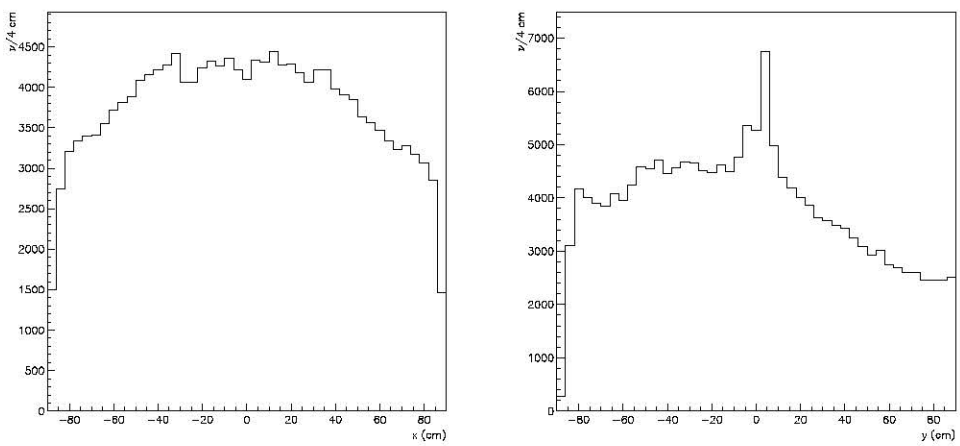

(a) x view (b) y view

Figure 5.12: Spatial distributions of low ν events in the FCAL. See the text for details on the shapes.

The final result of the FCAL quasielastic-like analysis is the comparison of the energy spectrum to the Monte Carlo flux. The flux generated with NUBEAM version 6.12 is used, with FLUKA 98 but no SPY corrections. The NUBEAM flux is first corrected using equation 5.8, then by the selection efficiency of figure 5.11. Finally, it is normalised to the number of events in the data. The results are presented in figure 5.13. The small discontinuities visible in the tail of the Monte Carlo histogram are due to the fluctuations

in the variable binned efficiency. This comparison shows good agreement between the Monte Carlo and the data, implying that the ν_μ flux is well reproduced in simulation. The Monte Carlo fits the peak, the turning point at $\sim$ 55 GeV and the tail of the data spectrum well.

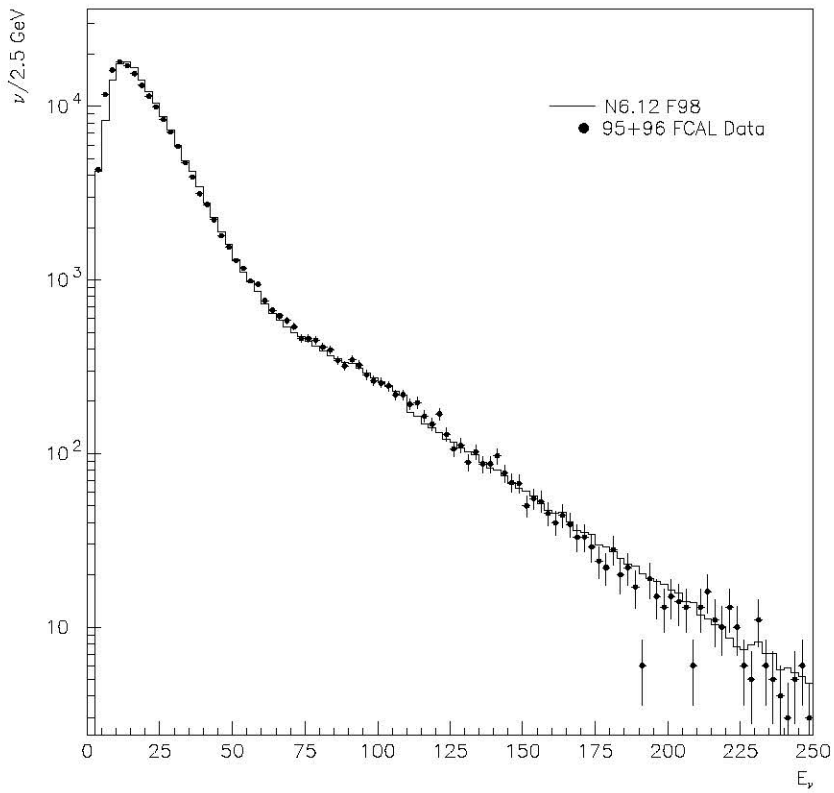

Figure 5.13: Energy spectrum of low ν events in the FCAL compared to Monte Carlo flux predictions of NUBEAM 6.12 with FLUKA 98.

5.6 Drift Chamber Events

5.6.1 Positive, Negative and Zero Focusing Beams

The neutrino beam to NOMAD is predominantly ν_μ, with a small contamination of $\overline{\nu}_\mu$ and also electron neutrinos. The dominance of neutrinos

rather than antineutrinos is due to the focusing of the horn and reflector, section 2.4.5, which selects positive mesons, and the bias towards positive secondaries due to the net +1 charge of the proton on beryllium collision. An antineutrino beam can be produced by reversing the currents in the horn and reflector. Also the natural composition of neutrinos and antineutrinos can be ascertained by producing a beam with zero focusing, that is to say no current in the horn or reflector.

NOMAD recorded additional samples of data with negative and zero focusing beams. These can be used for studying beam systematics. In particular any observed difference between the $\overline{\nu}_\mu$ over ν_μ ratio in data and Monte Carlo could be shown to be either an error in the $\overline{\nu}_\mu$ or the ν_μ estimate by comparing with samples from the negative focusing beam. Zero focusing data provides information as to whether it is the simulation of the focusing elements or the rest of the beamline that is incorrect.

The negative focusing beam is also of interest to charm quark studies performed with NOMAD. A neutrino interacting with d and s quarks, which are present as both valence and sea quarks, can produce charm quarks. Antineutrinos produce charm quarks from interactions with $\overline{d}$ and $\overline{s}$ quarks, which are only present in the quark sea. Therefore, in order to separate the effects of sea and valence quarks, both neutrino and antineutrino interactions are needed.

As earlier mentioned, the negative focusing beam is not an exact opposite of the positive beam, as many other elements of the beamline are optimised for the positive beam and production of negative mesons is lower than that of positives. To allow for the comparison of event Monte Carlo to negative beam data, weight tables must be produced to account for the change in polarity from the NEGLIB beam tables produced for a positive beam by NUBEAM 4.00. Checks were undertaken to ensure that weighting across polarity, as well as to NUBEAM 6.12 with FLUKA 98 and SPY C5.1, would be reliable. Whilst no event Monte Carlo was generated directly from negative beam tables, no difference in the result of three different weighting techniques could be determined. These techniques involved weighting for the polarity, then the updated NUBEAM, weighting for the update in NUBEAM first, then the change in polarity, and weighting for both at once. However, care must still be taken as the weights to transform the minor into the major beam component will be large. The weights used for ν_μ and $\overline{\nu}_\mu$ are shown in figure 5.14. Again, these have been projected onto the energy axis, removing the radius squared dependence. The graphs show some of the trends of figure 5.6 reflecting the improvement in NUBEAM. The change in polarity is seen as a reduction in ν_μ and increase in $\overline{\nu}_\mu$ along with shifting the ν_μ peak to a lower energy than in the positive beam, and the $\overline{\nu}_\mu$ peak to a higher energy.

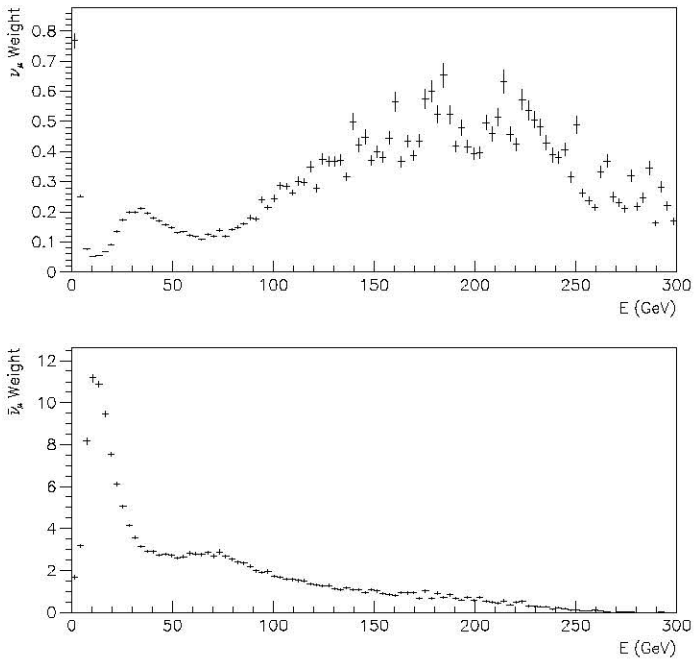

Figure 5.14: The weight functions used, without radial dependence, to bring ν_μ and $\overline{\nu}_\mu$ positive focusing event Monte Carlo to that from a negative focusing beam, including the update to NUBEAM 6.12 with FLUKA 98 and SPY C5.1.

A zero focusing beam is expected to have a factor of ten reduction in neutrino flux. Whilst this beam could provide a great deal of relevant information, including the effects of interactions in the beamdump, the low flux makes large data collection impractical. Thus only a few thousand events were collected, and the zero focusing data became useful for only the most basic checks of the beam simulation. Again the Monte Carlo must be adapted to the different beam conditions by a weight table, the ν_μ and $\overline{\nu}_\mu$ weights are plotted in figure 5.15, (note that no weights have yet been produced with C5.1 for a zero focusing beam).

5.6.2 Data Monte Carlo Comparisons

The most important check of the beam simulation is how it compares with NOMAD drift chamber data, the data that will eventually be used for the

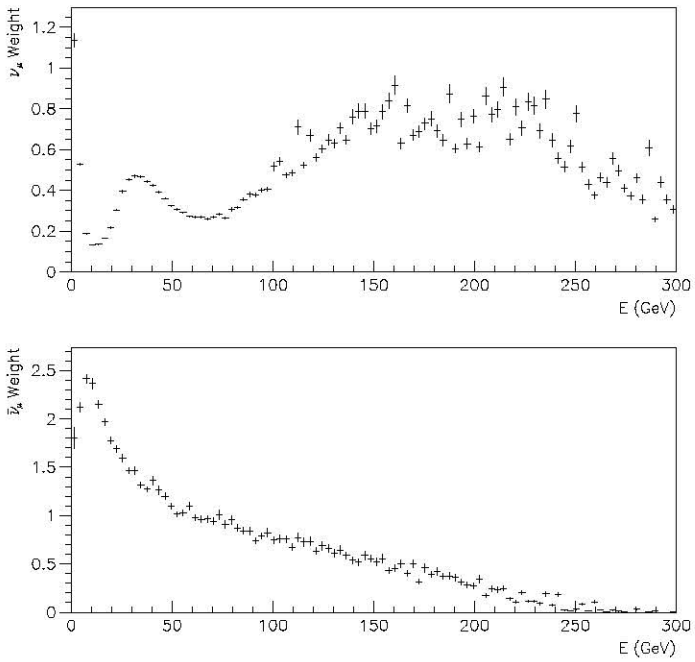

Figure 5.15: The weight functions used, without radial dependence, to bring ν_μ and $\overline{\nu}_\mu$ positive focusing event Monte Carlo to that from a zero focusing beam, including the update to NUBEAM 6.12 with FLUKA 98 and SPY C5.0.

$\nu_\mu \rightsquigarrow \nu_e$ oscillation search. Drift chamber events, from the three beam running conditions above, will now be contrasted with correctly weighted event Monte Carlo, (correctly weighted means to the latest simulation and the corresponding beam focusing). This study uses deep inelastic scattering (DIS) events. To achieve this, only events with ν greater than 5 GeV are used, that is to say the complement of the flux events used by the empirical parametrisation. This decision was made traditionally to remove complications arising from the inclusion of quasielastic (QE) and resonance (RES) events. Whilst now a method has been determined for their inclusion, see section 6.3.2, and furthermore as some QE and RES events will survive the ν cut and have to be accounted for, the comparison is still made with DIS, (or DIS like), events.

As section 5.3.3 details, the normalisations for the four neutrino types must be applied separately. For the positive and zero focusing beams, the

Monte Carlo is normalised to the data so that the number of ν_μ DIS events agree. The normalisation factor obtained, is then modified by the ratios in table 5.5, before being applied to the other neutrino types. In the negative beam, the Monte Carlo is normalised to the number of $\overline{\nu}_\mu$ data events.

	Positive	Negative	Zero
$\overline{\nu}_\mu$	0.0257	2.61	0.255
ν_e	0.0154	0.043	0.0272
$\overline{\nu}_e$	0.00153	0.0339	0.0079

Table 5.5: Ratios of charged current neutrino events expected in the beam according to NUBEAM 6.12 with FLUKA 98 and SPY C5.1, (C5.0 for the zero focusing beam). The number of ν_μ events are used as the denominator for all beam types. These ratios are used to normalise the event Monte Carlo between neutrino types.

The latest simulation and data spectra for ν_μ, $\overline{\nu}_\mu$, and $\overline{\nu}_e$ in the positive focusing beam are presented in figures 5.16, 5.17 and 5.18. The spectra show excellent agreement at all energies, the culmination of much work on the NUBEAM geometry, FLUKA physics model and the benefits of the SPY measurements. Note the lack of data events at low energy, seen in the efficiencies of section 4.4, is exacerbated by the ν greater than 5 GeV condition. The $\overline{\nu}_e$ plots required larger bin sizes due to lower statistics. Backgrounds to the $\overline{\nu}_\mu$ and $\overline{\nu}_e$ signals have been included from ν_μ NC and CC misidentified interactions, correctly normalised to the true number of data CC events, as per the prescription of section 6.3.4, and scaled according to the background scaling factors of table 6.4.

The results of the comparison are further illustrated in table 5.6. This table lists the average neutrino energies of the data and Monte Carlo spectra, and also the total number of neutrinos measured and expected. Recall that the number of ν_μ will agree exactly as the Monte Carlo is normalised to the data here. Further, the background to the ν_μ is assumed to be negligible. The average energies are in superb agreement, and there is good agreement between the number of neutrino events. This shows that not only are the energy distributions well reproduced by the Monte Carlo but the relative contributions of the $\overline{\nu}_\mu$, and $\overline{\nu}_e$ are now also reproduced correctly.

The results of the comparison with the negative focusing data are seen in figures 5.19 and 5.20, for the $\overline{\nu}_\mu$ and ν_μ respectively, (there are insufficient $\overline{\nu}_e$ statistics for a meaningful comparison). Recall that the Monte Carlo is normalised to the $\overline{\nu}_\mu$ data. Note that there is no appreciable background to the $\overline{\nu}_\mu$ as it is the major component of the negative beam. Furthermore, there

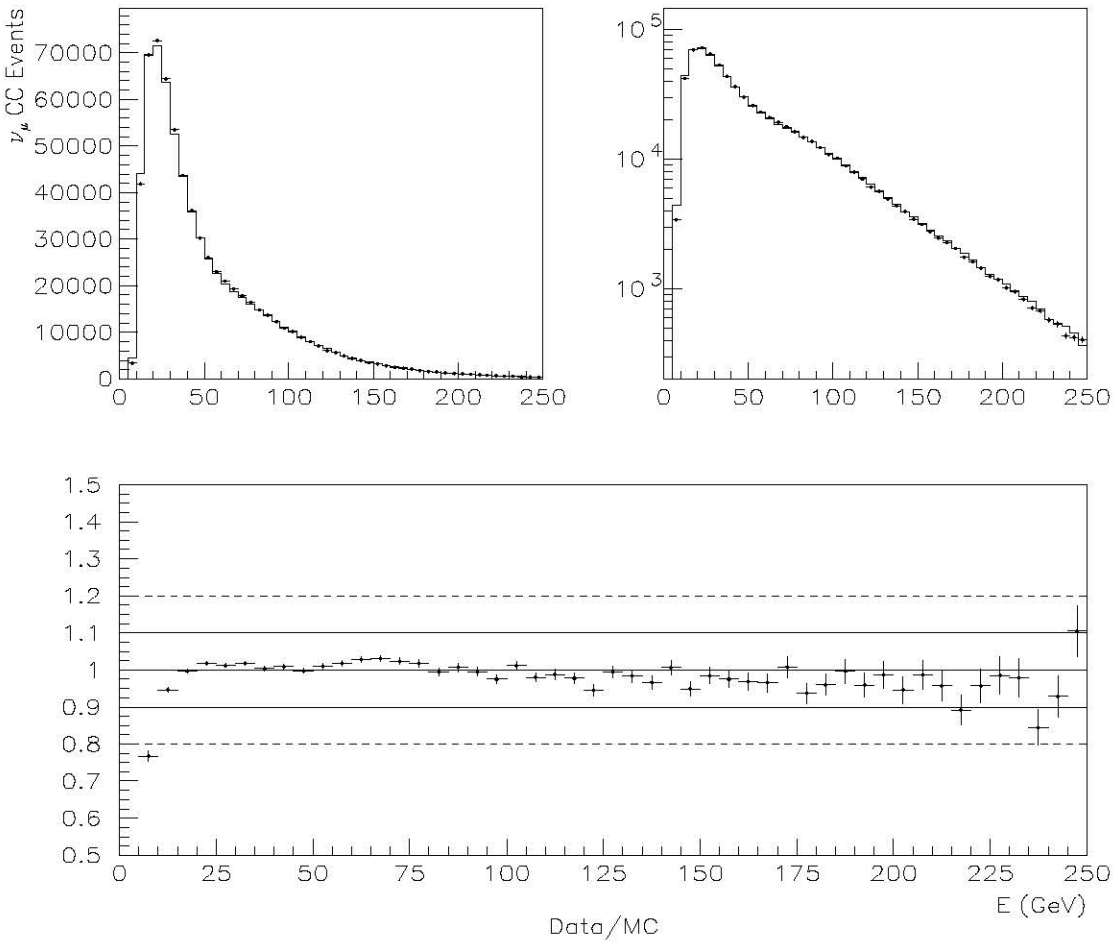

Figure 5.16: Comparison of positive focusing ν_μ DIS drift chamber data (points) to the predictions of NUBEAM 6.21 with FLUKA 98 and SPY C5.1. Linear and logarithmic scales are used, along with the ratio of data to prediction(MC).

is negligible background to the ν_μ signal due to the low flux of $\overline{\nu}_\mu$. Whilst the $\overline{\nu}_\mu$ spectrum is reproduced fairly well, the relative normalisation for the number of ν_μ is seen to be too low. This could be due to inaccuracies in the weighting tables from lack of statistics in their generation, normalising to too large an energy range or by fluctuations in the contributions of QE and RES events. Nevertheless, this discrepancy constitutes a significant improve-

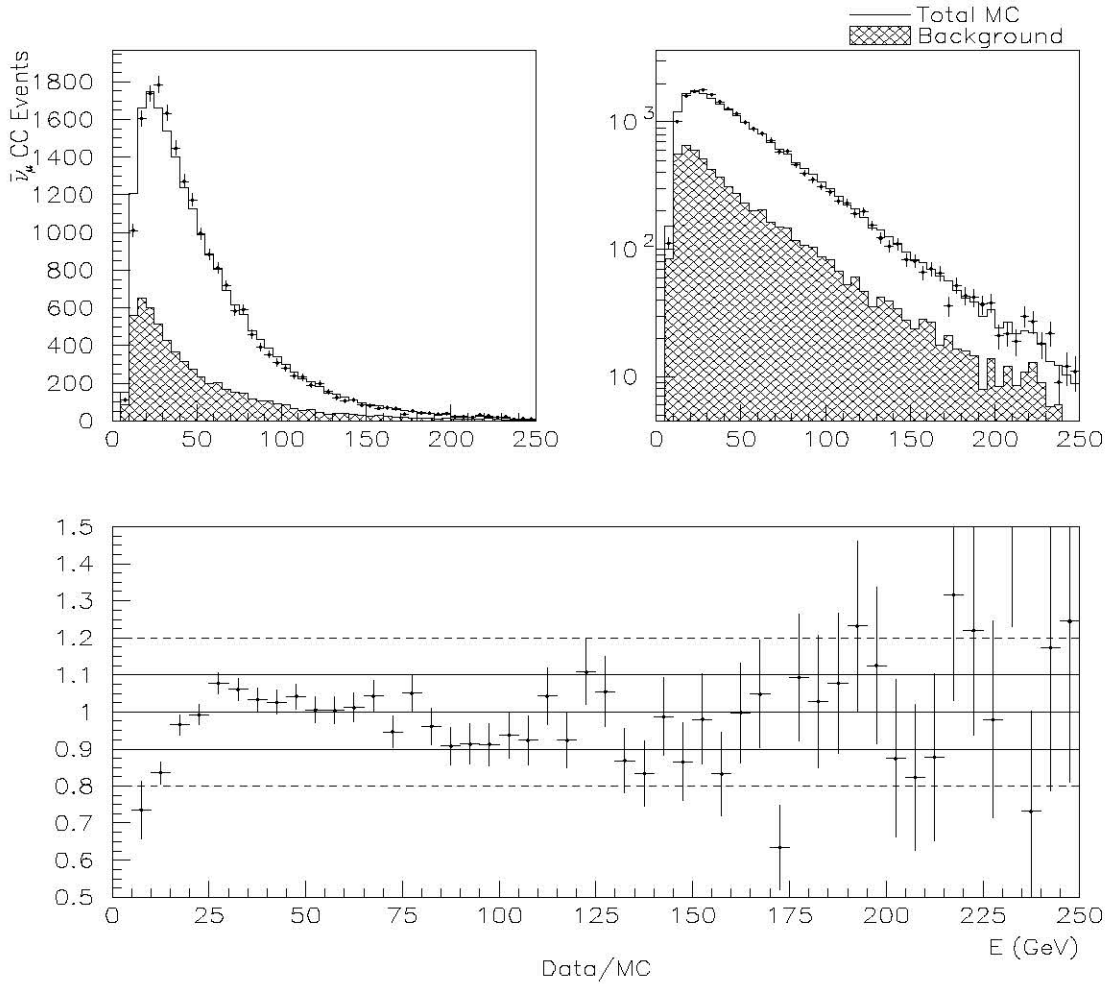

Figure 5.17: Comparison of positive focusing $\overline{\nu}_\mu$ DIS drift chamber data (points) to the predictions of NUBEAM 6.21 with FLUKA 98 and SPY C5.1. Linear and logarithmic scales are used, along with the ratio of data to prediction(MC). The background from misidentified ν_μ NC and CC events is also plotted, total MC is the sum of the $\overline{\nu}_\mu$ signal and background.

ment from the 30% difference produced by earlier versions of NUBEAM and FLUKA, Godley (1998). This is reiterated in table 5.7, as whilst the average energies agree well, there is 7.7% deficit in ν_μ Monte Carlo events.

The final comparison is with the zero focusing data. These are shown in

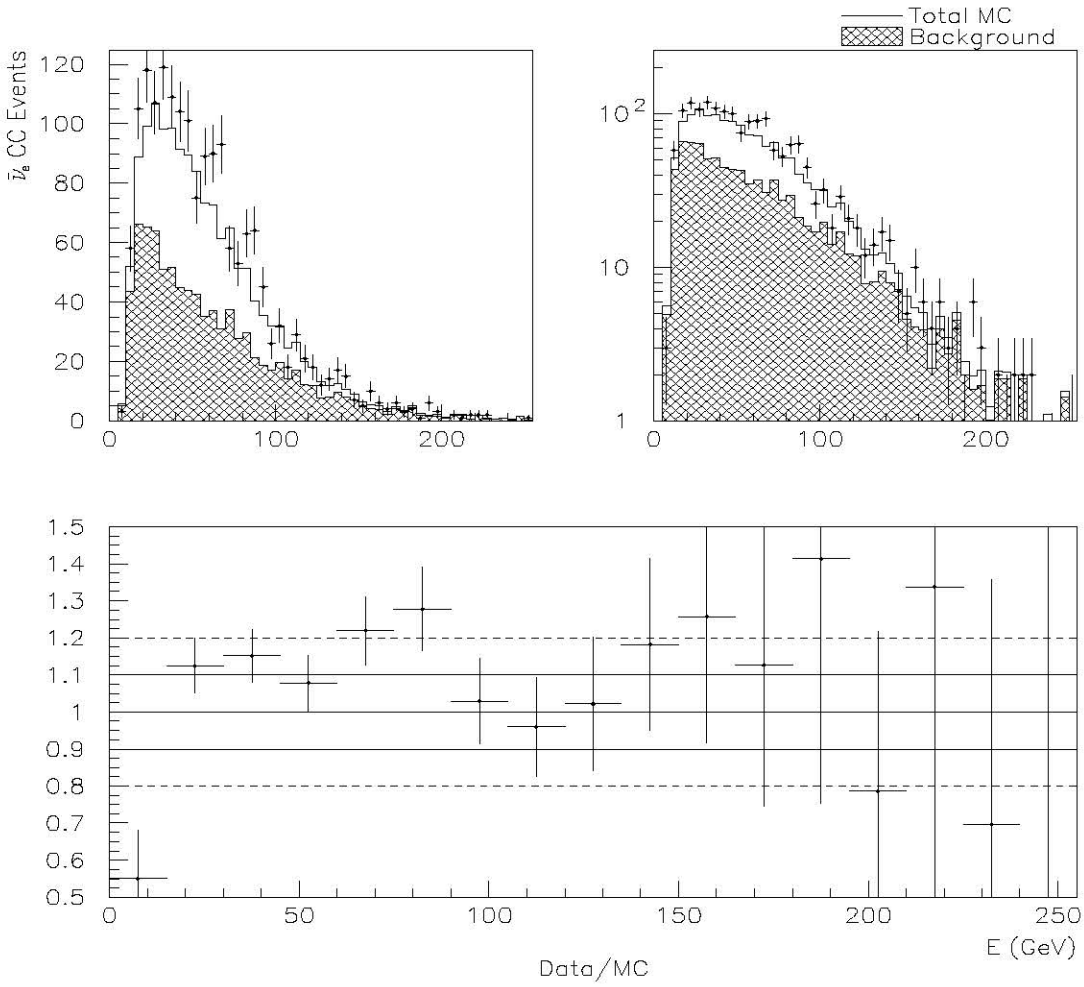

Figure 5.18: Comparison of positive focusing $\overline{\nu}_e$ DIS drift chamber data (points) to the predictions of NUBEAM 6.21 with FLUKA 98 and SPY C5.1. Linear and logarithmic scales are used, along with the ratio of data to prediction(MC). The backgrounds from misidentified ν_μ NC and CC events are also plotted, total MC is the sum of the $\overline{\nu}_e$ signal and backgrounds.

figures 5.21 and 5.22. The low statistics limit the relevance of any spectral shape comparison, however no glaring discrepancies were discovered.

Table 5.8, which displays the average energy and number of ν_μ and $\overline{\nu}_\mu$ events, is more elucidating. Again, the minor component, $\overline{\nu}_\mu$, is slightly too

	$\langle E \rangle$ GeV		Events			
	Data	MC	Data	MC+BKGD	MC	BKGD
ν_μ	54.6	55.0	681714	681713	681713	-
$\overline{\nu}_\mu$	55.6	55.1	20386	20488	14392	6096
$\overline{\nu}_e$	52.4	52.8	1725	1531	638	893

Table 5.6: The average DIS neutrino energy and number of events for positive focusing data and the predictions of NUBEAM 6.12 with FLUKA 98 and SPY C5.1.

	$\langle E \rangle$		Events	
	Data	MC	Data	MC
$\overline{\nu}_\mu$	46.3	45.8	13482	13482
ν_μ	70.4	72.6	7770	7145

Table 5.7: The average DIS neutrino energy and number of events for negative focusing data and the predictions of NUBEAM 6.12 with FLUKA 98 and SPY C5.1.

low in Monte Carlo, but this still represents the best prediction so far.

	$\langle E \rangle$		Events	
	Data	MC	Data	MC
ν_μ	65.6	67.4	1528	1528
$\overline{\nu}_\mu$	55.5	53.0	320	300

Table 5.8: The average DIS neutrino energy and number of events for zero focusing data and the predictions of NUBEAM 6.12 with FLUKA 98 and SPY C5.0.

5.6.3 Comparison with CHORUS Data and Simulation

CHORUS measures the same neutrino beam as NOMAD and as such provides yet another cross check of the beam simulation. CHORUS uses GBEAM, which as explained in section 5.1, has undergone development over the lifetime of CHORUS, with some developments being the result of direct comparison to NUBEAM. GBEAM also has the ability to use FLUKA stand-alone versions for its input. The average neutrino energy and flux is presented in table 5.9 as predicted by GBEAM 99 and NUBEAM 5.00, its equivalent

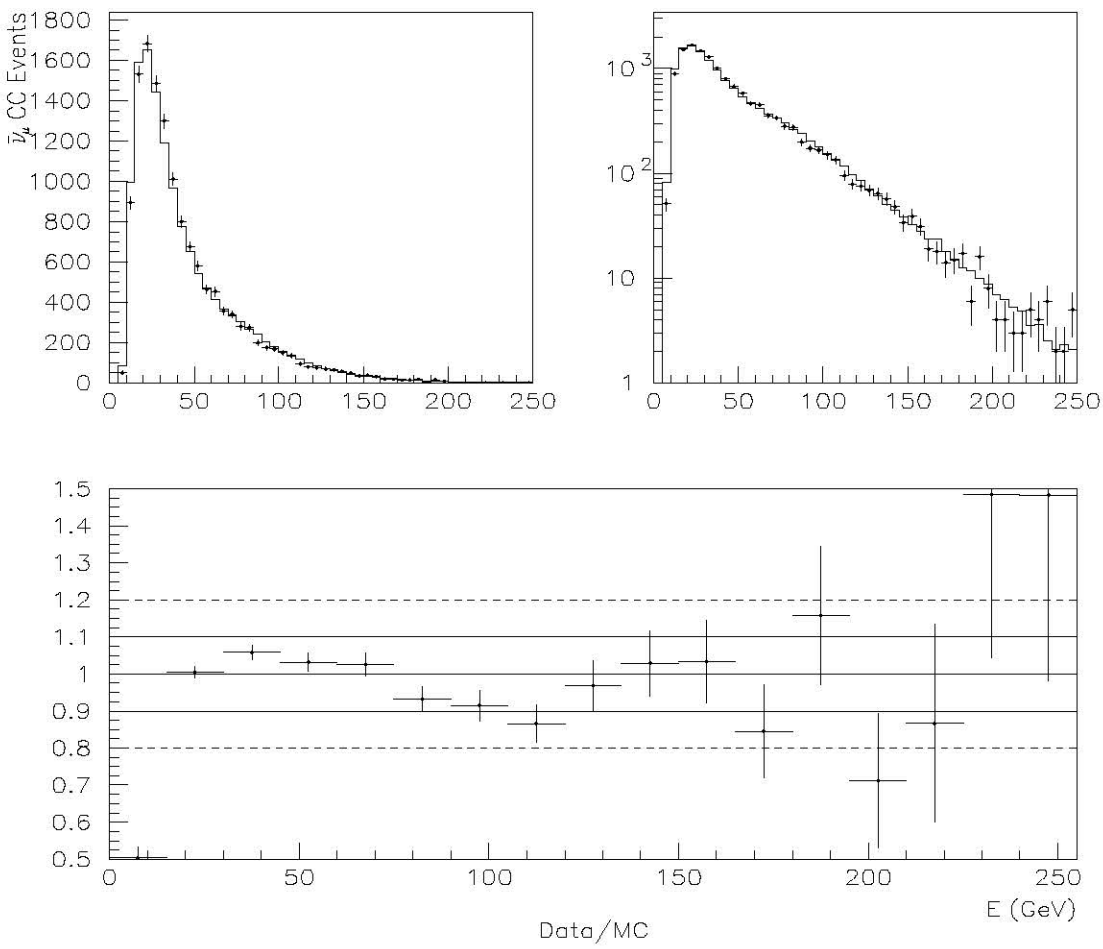

Figure 5.19: Comparison of negative focusing $\overline{\nu}_\mu$ DIS drift chamber data (points) to the predictions of NUBEAM 6.12 with FLUKA 98 and SPY C5.1. Linear and logarithmic scales are used, along with the ratio of data to prediction(MC).

NUBEAM version. Both used FLUKA 97.5. The comparison was made with the beam at NOMAD, over a 2.6 × 2.6 m^2 fiducial area. NUBEAM 6.12, with FLUKA 98 and SPY C3.0, is also included. NUBEAM and GBEAM are shown to agree very well at this stage, ensuring that the basis from which NUBEAM 6.00 was developed is sound.

CHORUS also produced neutrino flux studies, looking at distributions of

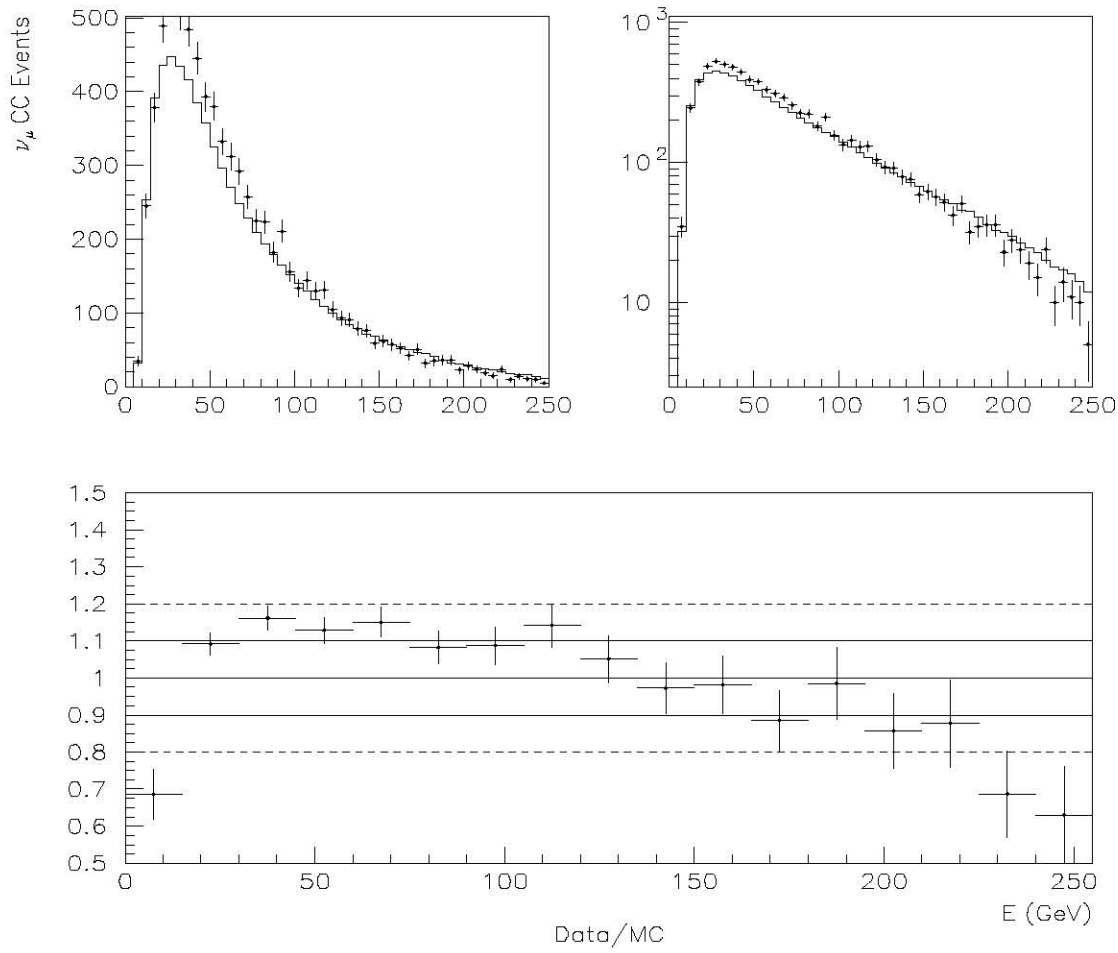

Figure 5.20: Comparison of negative focusing ν_μ DIS drift chamber data (points) to the predictions of NUBEAM 6.12 with FLUKA 98 and SPY C5.1. Linear and logarithmic scales are used, along with the ratio of data to prediction(MC).

neutrino interactions in their calorimeter, see Eskut et al. (1997). These studies were conducted with positive and negative focusing data. A comparison has been made to CHORUS deep inelastic scattering events. The important adjustment to make when comparing CHORUS and NOMAD data is that CHORUS has a smaller fiducial area, and so only samples the core of the beam. The average neutrino energy and neutrino/antineutrino ratio for

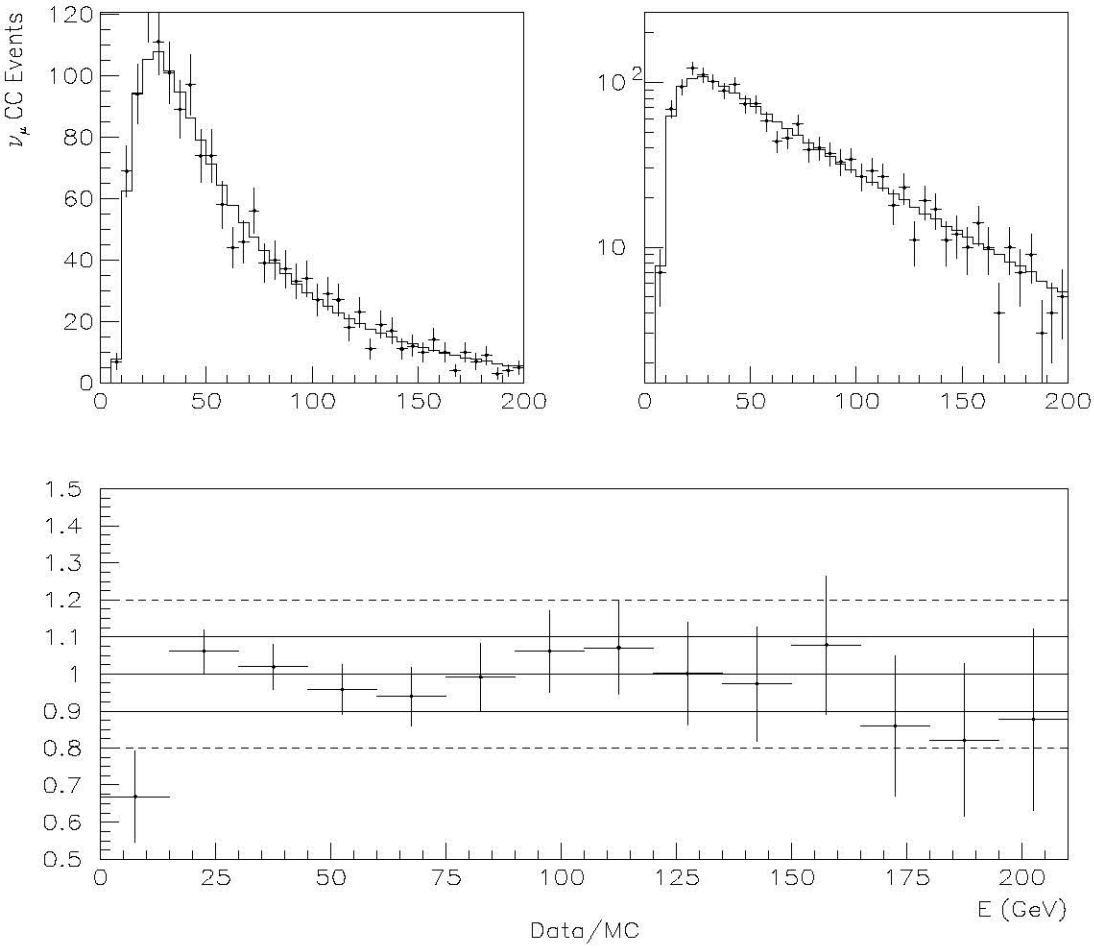

Figure 5.21: Comparison of zero focusing ν_μ DIS drift chamber data (points) to the predictions of NUBEAM 6.12 with FLUKA 98 and SPY C5.0. Linear and logarithmic scales are used, along with the ratio of data to prediction(MC).

NOMAD drift chamber and CHORUS calorimeter events is presented in table 5.10. It is heartening to note that there are no large differences in the values especially when considering different biases and inefficiencies in the detectors.

CHORUS has provided a completely independent confirmation that the NOMAD beam prediction is reproducing the WANF correctly, and further

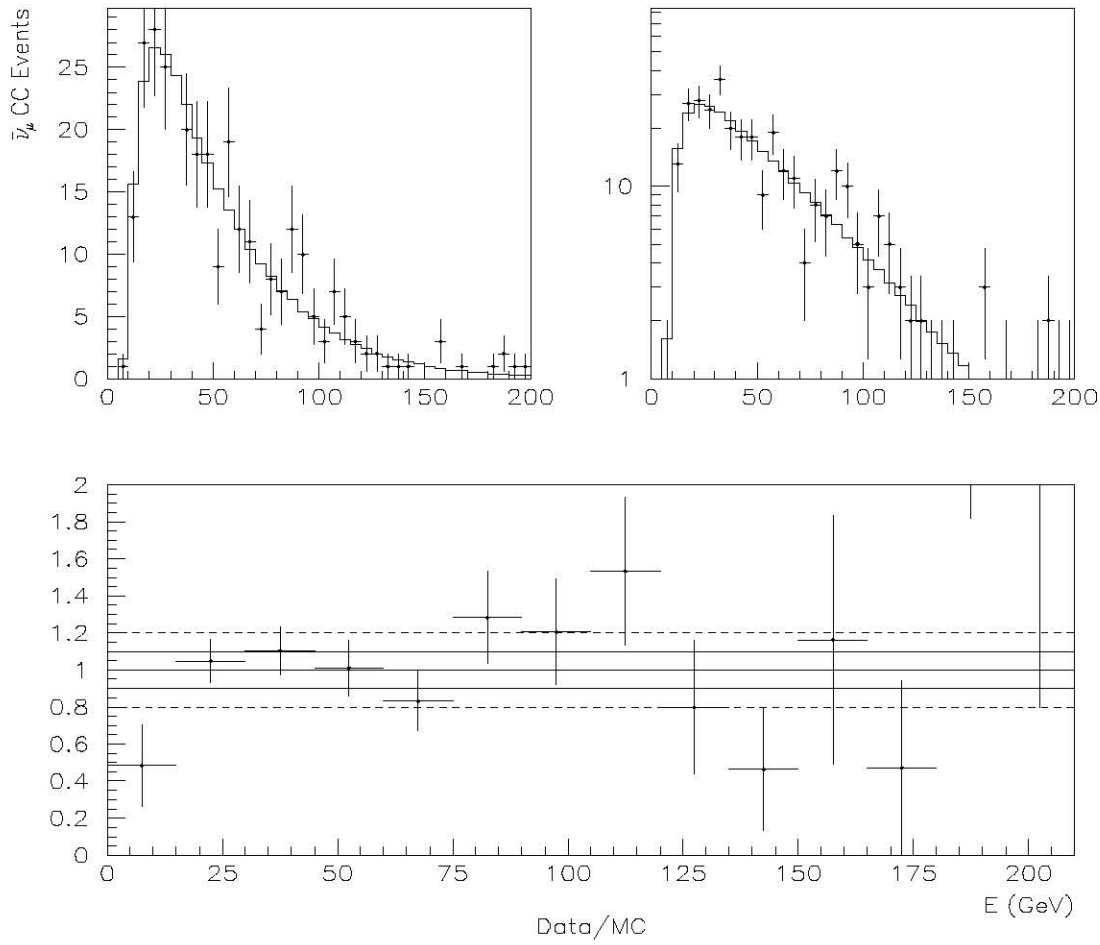

Figure 5.22: Comparison of zero focusing $\overline{\nu}_\mu$ DIS drift chamber data (points) to the predictions of NUBEAM 6.12 with FLUKA 98 and SPY C5.0. Linear and logarithmic scales are used, along with the ratio of data to prediction(MC).

confirms the analysis procedures.

5.7 Systematic Errors

The systematic error in the flux predicted by NUBEAM and FLUKA must now be estimated. Sources of error have been isolated from the recent al-

	$\langle E_{\nu_\mu} \rangle$ GeV	$\langle E_{\overline{\nu}_\mu} \rangle$ GeV	ν_μ Flux	$\overline{\nu}_\mu$ Flux
GBEAM	23.3	17.5	1.15	0.0745
NUBEAM 5.00	23.5	19.2	1.11	0.068
N6.12 F98 SPY C3.0	24.4	15.6	0.966	0.0784

Table 5.9: The predictions of GBEAM 99 with FLUKA 97.5 versus NUBEAM 5.00 with FLUKA 97.5. Also shown are the results from NUBEAM 6.12. All were sampled at the NOMAD plane in a 2.6×2.6 m^2 fiducial area. Fluxes are in neutrinos per 100 POT. (Adapted from Sorrention, 1998)

	Positive Focus			Negative Focus		
	$\langle E_{\nu_\mu} \rangle$	$\langle E_{\overline{\nu}_\mu} \rangle$	$\nu_\mu / \overline{\nu}_\mu$ CC	$\langle E_{\nu_\mu} \rangle$	$\langle E_{\overline{\nu}_\mu} \rangle$	$\overline{\nu}_\mu / \nu_\mu$ CC
CHORUS	48.8	48.4	0.027	68.9	37.2	0.328
NOMAD	46.0	45.4	0.021 ± 0.00015	60.4	35.9	0.289 ± 0.0065

Table 5.10: NOMAD drift chamber events in the reduced fiducial area 2.0×2.0 m^2, compared to CHORUS calorimeter events. (Adapted from Oldeman, 1998)

terations to NUBEAM, see section 5.1.4. The three main sources of error within NUBEAM are the magnetic field description in the focusing elements, missing material throughout the beamline, and the alignment of the focusing elements, target and collimators. It is proposed to run versions of NUBEAM, each changed in one of these areas by the estimated maximum difference the current standard NUBEAM could be from reality. These changes, and their values are itemised below.

- Revert to the old description of the horn, without magnetic field in the inner conductor.
- Reduce the horn current to 98% of its nominal value. A horn current any lower would trigger an alarm.
- Add 2 cm of aluminium 50 cm upstream of the horn.
- Add 1 cm of aluminium just upstream of the decay tunnel entrance.
- Add 2 cm of aluminium just upstream of the decay tunnel entrance.
- Shift the aluminium collimator by +3 mm in x and -3 mm in y.

- Shift the horn by 1 mm in x.

- Shift the horn by 1 mm in x and 1 mm in y.

The addition of more material comes from the fact that nearly all changes to NUBEAM have increased the amount of material in the beamline. It is hoped that with the number of comparisons between the NUBEAM geometry and technical drawings, along with physical inspections of the beamline, that any further missing material would be minimal. However to obtain the error on the flux caused by this, up to 2 cm of aluminium has been added at two points of the beamline.

The changes in the alignment reproduce the degree of movement undertaken in the WANF alignment, (Casagrande et al., 1996).

Due to the large amount of resources, both computing and time, the systematic error study reported in Valuev (2000) will be used, rather than repeating the multitude of NUBEAM productions. NUBEAM 6.12 was used in this study.

The effects of the above changes were first considered in the ν_μ and $\overline{\nu}_\mu$ spectra to ensure that they were reasonable. Then the effects on the ν_e/ν_μ contamination was determined. As was noted earlier, the ν_e are less sensitive to changes in NUBEAM than $\overline{\nu}_\mu$. The ratio of the altered NUBEAM ν_e/ν_μ to that of the standard NUBEAM will be used as the estimate of the systematic error. These ratios, in energy ranges, are tabulated below for magnetic field changes, table 5.11, additional material, table 5.12, and alignment, table 5.13. The errors on the ratios quoted in the table represent the statistics of the samples.

To crudely estimate the maximum systematic error from all the above sources, the errors from the 2 mm horn movement, collimator, 2 cm of aluminium up and downstream of the horn, inner conductor field at zero and horn current at 98% are combined in quadrature. These give errors ranging from 4.5-8% depending on the energy bin. Larger errors can be seen at high energies, but oscillations are expected below 40 GeV.

For FLUKA, the main systematic error is the proton profiles. FLUKA has been run with a decreased divergence of the proton profiles, from 0.075 mrad of FLUKA to 0.05 mrad from the SPS simulation of Gianluigi Arduing. This had no effect on the ν_e/ν_μ ratio. The proton profiles were also offset by $\pm$ 0.25 mm in x and y. This caused a 2% increase in ν_e/ν_μ.

Energy (GeV)	Horn Magnetic Field	
	Inner Conductor B=0	Current at 98%
3-6	1.02 ± 0.04	0.97 ± 0.04
6-12	1.01 ± 0.03	0.98 ± 0.03
12-18	1.02 ± 0.03	1.02 ± 0.03
18-24	1.00 ± 0.03	1.00 ± 0.03
24-32	0.96 ± 0.02	1.01 ± 0.02
32-40	0.98 ± 0.03	1.02 ± 0.03
40-50	1.00 ± 0.03	1.05 ± 0.03
50-65	1.02 ± 0.03	1.02 ± 0.03
65-80	1.04 ± 0.04	1.02 ± 0.04
80-100	0.99 ± 0.04	0.99 ± 0.04
100-140	1.09 ± 0.06	1.09 ± 0.06
140-200	1.08 ± 0.11	1.08 ± 0.11

Table 5.11: Ratios of ν_e/ν_μ in the modified field versions to the standard version, in the given energy ranges. These will be used as the systematic errors from NUBEAM. (Taken from Valuev, 2000)

5.8 Summary of Improvements

NUBEAM has been greatly developed over the duration of the NOMAD experiment, and is now very trustworthy, particularly as it has been shown to agree very well with neutrino beam data from a wide range of sources. The noteworthy improvements are the incorporation of the SPY measurements which help to ensure that the neutrino spectra of NUBEAM are produced from correct meson distributions at the target. Also, the description of the beamline components within NUBEAM is the best ever, with all available technical drawings and physical inspections being used to guarantee this. Finally, corrections in the models of physical processes in both FLUKA and NUBEAM have improved the agreement with data. The agreement shown by NUBEAM with the ν_μ, $\overline{\nu}_\mu$ and $\overline{\nu}_e$ data indicate it is now a reliable simulator for the $\nu_\mu \rightsquigarrow \nu_e$ oscillation search. It now remains to see if the empirical parametrisation of the following chapter can improve further on NUBEAM, and reduce its large systematic errors.

Energy (GeV)	Additional Material (Al)		
	2 cm upstream	2 cm downstream	1 cm downstream
3-6	1.01 ± 0.04	0.97 ± 0.04	0.97 ± 0.04
6-12	1.02 ± 0.03	1.02 ± 0.03	0.96 ± 0.03
12-18	1.04 ± 0.03	1.06 ± 0.03	0.99 ± 0.03
18-24	1.04 ± 0.03	1.04 ± 0.03	0.98 ± 0.03
24-32	1.00 ± 0.02	1.02 ± 0.02	1.00 ± 0.02
32-40	1.02 ± 0.03	1.03 ± 0.03	1.03 ± 0.03
40-50	1.03 ± 0.03	1.00 ± 0.03	1.02 ± 0.03
50-65	1.00 ± 0.03	1.00 ± 0.03	1.02 ± 0.03
65-80	1.05 ± 0.04	1.02 ± 0.04	1.02 ± 0.04
80-100	1.02 ± 0.04	1.02 ± 0.04	1.04 ± 0.04
100-140	1.10 ± 0.06	1.08 ± 0.06	1.07 ± 0.06
140-200	1.19 ± 0.12	1.10 ± 0.11	1.08 ± 0.11

Table 5.12: Ratios of ν_e/ν_μ in the modified material versions to the standard version, in the given energy ranges. These will be used as the systematic errors from NUBEAM. The additional material is placed upstream and downstream of the horn and reflector system. (Taken from Valuev, 2000)

Energy (GeV)	Alignment		
	Al Collimator 5 mm	Horn 1 mm	Horn 2 mm
3-6	0.99 ± 0.04	0.98 ± 0.04	0.97 ± 0.04
6-12	0.99 ± 0.03	0.96 ± 0.03	0.97 ± 0.03
12-18	0.99 ± 0.02	0.98 ± 0.03	0.99 ± 0.03
18-24	0.99 ± 0.03	0.98 ± 0.03	0.98 ± 0.03
24-32	1.00 ± 0.02	0.98 ± 0.02	0.99 ± 0.02
32-40	0.99 ± 0.03	0.97 ± 0.03	0.98 ± 0.03
40-50	0.98 ± 0.03	1.01 ± 0.03	1.00 ± 0.03
50-65	1.01 ± 0.03	1.00 ± 0.03	0.99 ± 0.03
65-80	1.03 ± 0.04	1.00 ± 0.04	1.02 ± 0.04
80-100	1.00 ± 0.04	0.97 ± 0.04	1.01 ± 0.04
100-140	1.06 ± 0.06	1.09 ± 0.06	1.08 ± 0.06
140-200	1.04 ± 0.11	1.09 ± 0.11	1.08 ± 0.11

Table 5.13: Ratios of ν_e/ν_μ in the modified alignment versions to the standard version, in the given energy ranges. These will be used as the systematic errors from NUBEAM. (Taken from Valuev, 2000)

Chapter 6

Empirical Parametrisation of the Neutrino Beam

6.1 Introduction and Motivation

The accurate prediction of the flux of ν_e at NOMAD is perhaps the most crucial element of the $\nu_\mu \rightsquigarrow \nu_e$ oscillation search. In truth, the absolute ν_e flux is not required, rather the ν_e flux relative to the ν_μ flux. It is this relative flux which will then be compared to data, to search for the $\nu_\mu \rightsquigarrow \nu_e$ oscillation signal. The goal of predicting the relative ν_e energy spectrum to within 3% error has been set in order to extract a signal as small as expected, from the comparison to data. The combination of NUBEAM, FLUKA and SPY have produced an excellent beam simulation, which was shown in the previous chapter to compare very well with data. Complementary to this, a flux prediction can be generated empirically from the NOMAD data. This new and novel approach should compare even more favourably to the data, and achieve the 3% error goal. The advantage of the empirical parametrisation is that it avoids both the ill defined production cross sections inherent in FLUKA, (which were in part fixed by fitting to the SPY data), and more importantly any uncertainty in the implementation of the geometry of the beamline within NUBEAM.

This is the first time that an empirical parametrisation has been used for the flux prediction of an oscillation search in NUBEAM.

Like NUBEAM, the empirical parametrisation will also be useful to the next generation of neutrino experiments, including long baseline experiments such as MINOS, (MINOS Collaboration, 1998). Here, a knowledge of the hadron production at the target garnered from the NOMAD data, will greatly aid the prediction of the number of neutrino interactions expected.

6.2 Theoretical Concept

The neutrino beam is a tertiary beam, generated largely from the decays of mesons produced in the initial proton on beryllium collisions. It is possible to differentiate neutrinos according to their parent, as illustrated in figure 6.1. The figure shows ν_μ are largely parented by π^+ at low energies and K^+ at high energies with a negligible contribution from charm mesons and K_L^0. This energy dependent behaviour arises from the difference between the pion and kaon masses. Due to energy and momentum conservation, less than 43% of the energy of the lighter pion is transfered to the neutrino, whilst the heavier kaon imparts up to 96%. The $\overline{\nu}_\mu$ situation is similar, with π^- and K^- dominating at low and high energies respectively, and a small component from charm mesons, K_L^0 and μ^+. ν_e arise primarily from K^+ decays, with appreciable contributions from μ^+, K_L^0 and charm. For the $\overline{\nu}_e$ the main parent is K_L^0, with a small number produced from K^-, charm mesons and μ^-.

The distributions of figure 6.1 are from Monte Carlo. However it is possible to obtain equivalent distributions from the NOMAD neutrino data. That is to say, the meson production at the target can be predicted from measured neutrino spectra. Further, by using the ν_μ, $\overline{\nu}_\mu$ and $\overline{\nu}_e$ alone, the production of the ν_e parents, (K^+, μ^+ and K_L^0), can be determined. This then allows for the prediction of the ν_e spectra at NOMAD, without examining the oscillation signal region, i.e. the ν_e data.

The following strategy is then enacted to determine the ν_e relative flux. The π^+ and K^+ production is obtained by fitting the separate π^+ and K^+ components of the neutrino spectra to the ν_μ data. Knowing the π^+ production constrains the μ^+ component of the $\overline{\nu}_\mu$, allowing the π^- and K^- to be determined with a similar fit. Now all the parents of the $\overline{\nu}_e$ are known except for K_L^0. After the K_L^0 production is extracted from the fits to $\overline{\nu}_e$ data, all the parents of the ν_e have been fixed, and it is then a trivial task to produce the ν_e flux. Charm production of neutrinos is treated as negligible for the ν_μ and $\overline{\nu}_\mu$ and is added to the $\overline{\nu}_e$ and ν_e according to known production rates, see section 6.3.3, (it would be difficult to determine charm production empirically from the NOMAD neutrino data due to the low number of neutrinos from charm meson decay expected).

The empirical parametrisation strategy is feasible because the ν_μ, $\overline{\nu}_\mu$ and $\overline{\nu}_e$ fluxes are not expected to be appreciably altered by the oscillation signal searched for, (at low mixing angles, as predicted by LSND, see figure 1.3).

The method developed for retrieving the meson production from the NOMAD data, culminating in the prediction of the ν_e flux, is now described.

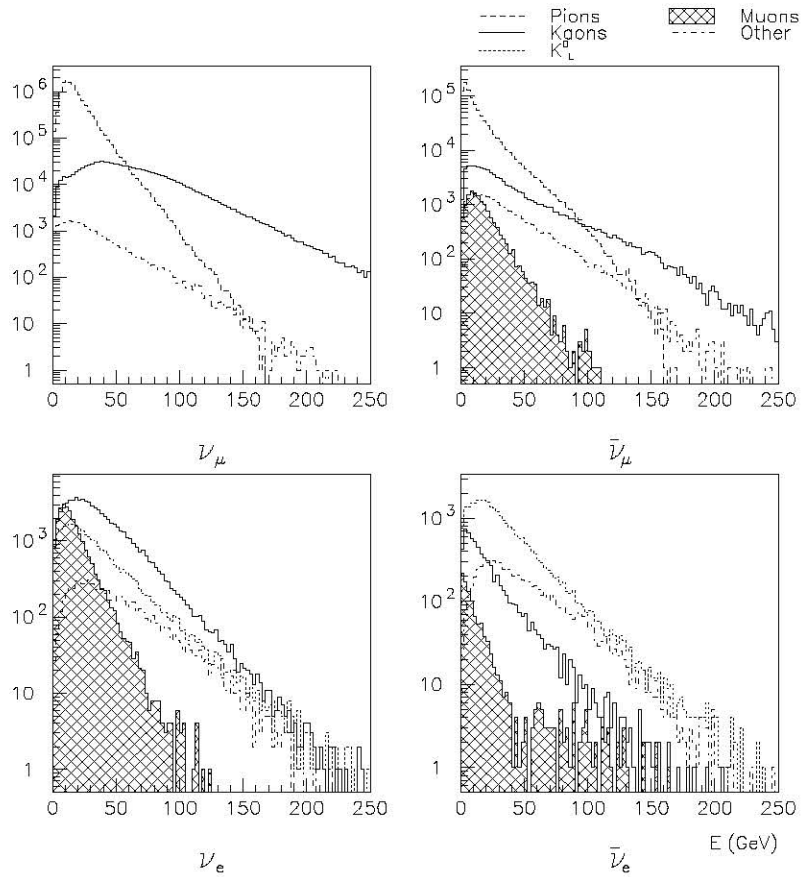

Figure 6.1: Neutrino spectra separated according to neutrino parent. See text for more detail on the parent types of each neutrino type. The spectra were generated with NUBEAM 6.10 using the empirical parametrisation of section 6.3.3, for meson production at the target.

6.3 Implementation

6.3.1 Data Sample

The neutrino events are selected, using the procedures outlined in chapter 4. All four years of NOMAD data are used, including the 4, 8 and 11 module data of 1995. As explained in section 5.5.2, the number of events with low exchange energy (ν) is proportional to the flux, which gives the best reflection of the true meson spectra. Thus, only low ν events are used. As there are fewer ν_μ events recorded in the drift chambers than in the FCAL, and as

the minor components of the beam are also required, the maximum value of ν has been set at 5 GeV. Table 6.1 presents a summary of neutrino events in data selected as per the criteria of chapter 4, and those also satisfying $\nu < 5$ GeV.

	Total	$\nu < 5$ GeV
ν_μ	1041950	357508
$\overline{\nu}_\mu$	34579	14073
ν_e	12277	2885
$\overline{\nu}_e$	3880	954

Table 6.1: Results of event selection, with and without the $\nu < 5$ GeV condition.

An important contribution to the number of low ν events are one track events, were only a single track is reconstructed in the drift chamber. These events are included in this study, with due care taken to remove the extra background from through-going muons, (which also almost always produce just one track). Further information on their selection is found in section 4.1.

Events are selected from the fiducial volume, defined in section 4.1.1. The events are separated into five radial bins. The bins are for $|x|$ and $|y|$ in the ranges 0-30, 30-60, 60-95, 95-120 and 120-130 cm, as shown in figure 6.2. The 120-130 cm bin is actually offset by 5 cm in y to match the shift in the fiducial volume. The actual area of the drift chamber is also displayed in the figure. The bins are defined in the NOMAD reference frame, section 2.5.

The radial distribution of the ν_e is much flatter than the ν_μ. This is because the ν_μ are mainly from pions which are almost always focused before they decay to the ν_μ. ν_e come from kaons, which often decay before they are focused, leading to a broader distribution. Thus, by using five radial bins, a better determination of the relative pion to kaon production can be obtained.

The data then is treated as a reflection of the true neutrino flux and is binned in 2.5 GeV energy bins, to produce neutrino spectra for each radial bin.

6.3.2 Target Monte Carlo Sample

To furnish selection efficiencies, smearing and background samples, (see section 6.3.4), Monte Carlo is used. The Monte Carlo is generated with NEGLIB and reconstructed after detector effects have been included, as described in section 2.7. NEGLIB does not include the beam slope and so its events must be rotated to the NOMAD frame with equation 2.9.

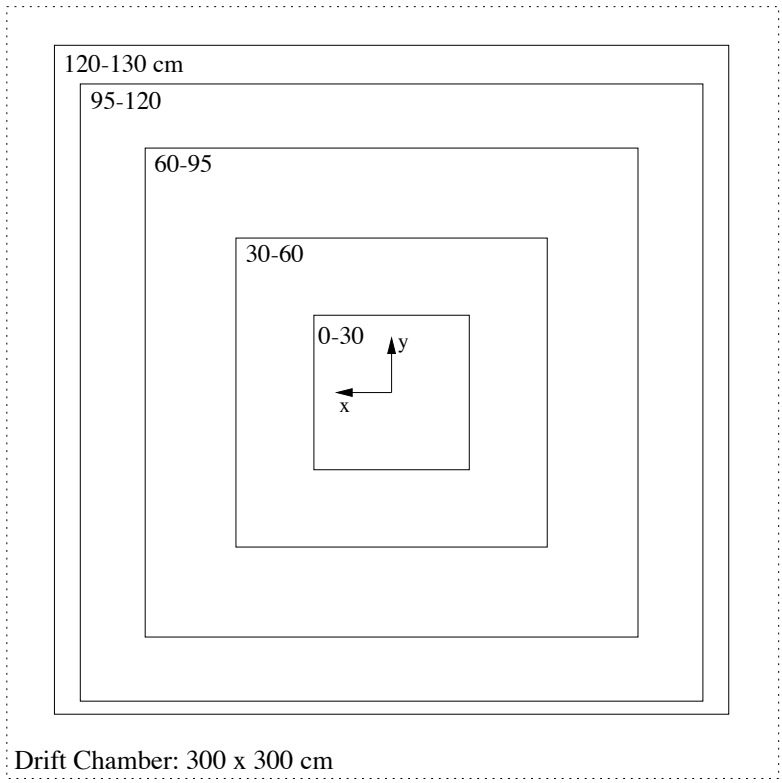

Figure 6.2: The five radial bins and the drift chamber.

At low ν, the neutrino events are a combination of quasielastic (QE) resonance (RES) and deep inelastic scattering (DIS) events. The Monte Carlo therefore must not only reproduce the individual interactions, but additionally, the mixture of the three event types. There exist special Monte Carlo programmes that reproduce QE and RES interactions, as well as a general one that reproduces all neutrino interactions, (dominated by DIS).

The QE event generator is based on calculations developed in LLewellyn-Smith (1972). The cross section for QE events on an isoscalar target in the NOMAD generator is 0.4455 $\times 10^{-38}$ cm^2.

There are three resonant processes relevant to NOMAD with cross sections in units of $\times 10^{-38}$ cm^2:

$$\nu_\mu + n \rightarrow \mu^- + p + \pi^0 \quad 0.537 \tag{6.1}$$
$$\nu_\mu + n \rightarrow \mu^- + n + \pi^+ \quad 0.276 \tag{6.2}$$
$$\nu_\mu + p \rightarrow \mu^- + p + \pi^+ \quad 0.330 \tag{6.3}$$

Three individual RES event generators were developed. These are based on Rein and Sehgal (1981). When the three are combined for an isoscalar target, the average cross section is 0.5715 $\times 10^{-38}$ cm^2. Improvements to the resonant event generator of NOMAD are given in Marchionni (1998).

The separate QE and RES Monte Carlo samples generated had to subsequently be normalised to the standard Monte Carlo according to the ratio of integral number of events. The QE and RES cross sections are assumed to be independent of neutrino energy, a good assumption above 1 to 2 GeV. The DIS cross section is 0.67 $\times 10^{-38}$ E cm^2 GeV^{-1}, Auchincloss et al. (1990). The ratios are:

$$\text{QE Norm} = \frac{\int 0.4455\phi(E)dE}{\int 0.67E\phi(E)dE} \tag{6.4}$$

$$\text{RES Norm} = \frac{\int 0.5715\phi(E)dE}{\int 0.67E\phi(E)dE} \tag{6.5}$$

where $\phi(E)$ is the neutrino flux. The normalisation becomes the ratio of the constant cross sections, with the ratio of the two integrals reducing to the inverse of the average energy, $\langle E \rangle$:

$$\text{QE Norm} = \frac{0.4455}{0.67}\frac{1}{\langle E \rangle}(GeV) \tag{6.6}$$

$$\text{RES Norm} = \frac{0.5715}{0.67}\frac{1}{\langle E \rangle}(GeV) \tag{6.7}$$

$\langle E \rangle$ is obtained from table 5.1. A similar procedure is repeated for $\overline{\nu}_\mu$, ν_e and $\overline{\nu}_e$. The normalisations thus obtained are listed in table 6.2. The RES, QE and DIS Monte Carlo samples are then combined using these factors, before the selection efficiencies and smearing are determined.

	ν_μ	$\overline{\nu}_\mu$	ν_e	$\overline{\nu}_e$
Deep Inelastic	1.0	1.0	1.0	1.0
Quasielastic	0.028	0.068	0.0177	0.042
Resonance	0.036	0.080	0.0227	0.049

Table 6.2: Normalisation factors for combining the resonance, quasielastic and deep inelastic Monte Carlo samples.

The standard Monte Carlo is in fact an extended DIS generator, which incorporates some RES and QE events. These must be removed to avoid QE and RES events being double counted. This is achieved with the condition (cut), of $W^2 > 1.4$ GeV^2, being imposed on DIS events, (where W^2 is the mass squared of the system recoiling against the lepton, low for QE and RES events). A cut at 1.4 instead of 2 GeV, where the standard generator implemented stops producing RES events, also allows for the inclusion of multi pion resonance events, which are produced in the standard generator but not the dedicated RES generator. The choice of this cut is reported in Autiero et al. (1998a). This cut is imposed prior to the determination of the selection efficiency. Its inclusion ensures a Monte Carlo sample more consistent with data.

Monte Carlo samples were generated for each of the four neutrino types. The sample sizes are given in tables 4.9 and 4.5.

6.3.3 Meson Production Parametrisation

The nucleus of the empirical method is the parametrisation, which models the secondary meson production at the target. An empirical formula for this was developed by Malensek (1981). That study attempted to fit a parametrised production formula to the data from Atherton et al. (1980). The Atherton experiment was very similar to the SPY experiment, (both are described in chapter 3). The formula developed by Malensek for the cross section was:

$$\frac{d^2N}{dpd\Omega} = Bx\frac{(1-x)^A(1+5e^{-Dx})}{(1+p_T^2/M^2)^4} \tag{6.8}$$

where A, B, D and M^2 are the parameters, x is x-Feynman, the ratio of secondary to primary momentum, and p_T is the transverse momentum.

Briefly, the explanation for the choice of parametrisation by Malensek is as follows. The cross section is factorised in the form $f(x)G(p_T)$, according to the scaling of Feynman (1969). $f(x)$ is taken as $(1-x)^A$ from Gunion (1979) and reduces the cross section to zero at high x. $G(p_T)$ is $(1+p_T^2/M^2)^{-4}$ as it is known that invariant cross sections exhibit a dependence on p_T^{-8}, (Antreasyan et al., 1977), and the parameter M^2 is included to account for the observed variation from p_T^{-8} at low p_T. To include nuclear cascades present in thick targets, the extra term $(1+5e^{-Dx})$ is added. This factor is small except at low x, and also helps reproduce the shape of the low energy peak in the neutrino spectrum, due to the focusing of the horn.

The SPY experiment took most of its data in a lower momentum range than the Atherton experiment, a range responsible for around 50% of the

neutrinos at NOMAD. It was shown that the Malensek parametrisation could not fit the SPY data, Guglielmi and Collazuol (1997). A new parametrisation was developed from the Malensek parametrisation in Das and Mishra (1997), to specifically model the meson production relevant to the lower energies of SPY and NOMAD.

$$\frac{d^2N}{dpd\Omega} = Bx^F e^{-Gp_T^2} \frac{(1-x)^A(1+Ce^{-Dx})}{(1+p_T^2/M^2)^R} \tag{6.9}$$

where C, F, G and R are the additional parameters. Parameters F and C allow increased flexibility in modeling the production in the low x domain. A further three parameters, S, T and U, were later required to describe kaon production after the inclusion of the SPY data to the fit, see section 6.3.8. The kaon parametrisation is then:

$$\frac{d^2N}{dpd\Omega} = Bx^F e^{-Gp_T^2} \frac{(1-x)^A(1+Ce^{-Dx})}{(1+p_T^2/M^2)^R} e^{-Sp_T}(1+T\log(x+.99))e^{Ux} \tag{6.10}$$

These particle production formulae must also be scaled according to the length of the target, L, as given in equation 3.6. This is particularly important as both SPY and the WANF use 100 mm targets, whilst the Malensek parametrisation was based on the 500 mm target data of the Atherton experiment.

The parametrisation of equation 6.9 was implemented in NUBEAM to replace GEANT-FLUKA for the production of all non charm mesons in the proton on beryllium target collision. Outside the beryllium target, interactions are again handled by GFLUKA.

The contributions of charm mesons, not implemented in GFLUKA, are handled separately. Charm meson production cross sections in 400 GeV proton on proton collisions were measured most precisely by Aguilar-Benitez et al. (1988):

$$\sigma(p+p \rightarrow D+X) = 30.2 \pm 3.3 \times 10^{-38}\ \mathrm{cm}^2 \tag{6.11}$$

where D refers to D^+, D^-, D^0 and $\overline{D}^0$. The production of charm mesons was parametrised as:

$$p_T(1-x)^B e^{-Ap_T^2} \tag{6.12}$$

by Kodama et al. (1991), where A and B are the parameters. The best fit obtained to their charm data provided the parameters $B = 6.9$ and $A = 0.84$ (GeV/c)$^{-2}$. As stated earlier, NOMAD does not have enough charm data to perform its own fit, so these values are used and not varied. The subsequent decays of charm mesons to leptons were implemented in accordance with:

$$D \rightarrow \nu_y + l_y + X \tag{6.13}$$

where ν_y and l_y are the neutrino and corresponding lepton and X represents a strange hadron. Further, X is assumed to have a mass of 0.65 GeV, (representative of strange hadrons), and the branching ratio for each lepton is taken as 10%. The spectra of neutrinos from charm, as determined by this method, were compared to beam dump neutrino production experiments, see for example Berge et al. (1992) as a check. Good agreement was found between the two, as reported in Das and Mishra (1997).

NUBEAM was run using the base parameters listed in table 6.3. This produced the spectra, and parent particle distributions, of figure 6.1.

Meson	A	B/ (sr GeV/c)	C	D	F	G/ (GeV/c)^2	M^2 (GeV/c)^2	R
π^+	4.457	183.75	5.3721	18.472	0.9316	0.0965	0.901	4.039
π^-	4.122	70.60	5.0000	11.29	1.0	0.0	0.893	4.0
K^+	3.115	14.45	5.4837	21.025	0.416	0.0854	1.227	4.068
K^-	6.107	12.33	5.0000	17.78	1.0	0.0	1.098	4.0
K_L^0	3.6133	2.7970	5.0000	10.671	1.0	0.0	0.769	4.0

Table 6.3: Base parameters entered in NUBEAM for meson production.

6.3.4 Corrections to the Estimate

The neutrino flux generated with NUBEAM as described above is not directly comparable to NOMAD data spectra. A number of corrections must first be made to the generated flux. These comprise the smearing of the true energy of the neutrino, due to detector resolution effects, folding in the energy dependent selection efficiency and adding an irreducible background to the minor components of the beam. These effects will be discussed in this section.

Selection Efficiency

The neutrino event selection criteria are those outlined in chapter 4. The efficiency and energy dependence of this selection must be determined. Two spectra of the true neutrino energy, E_ν, are produced, one with all the Monte Carlo events generated, and one with just those selected. The ratio of these two spectra provides the selection efficiency as a function of E_ν, figure 6.3. Overall the efficiency is high, and constant after the low energy turn on, see section 4.4. Two curves are plotted, both are from the same sets of events, but the solid curve has been averaged over an increasing number of bins, to remove the statistical fluctuations. Both curves were tried in the fitting procedure, without significantly altering the result.

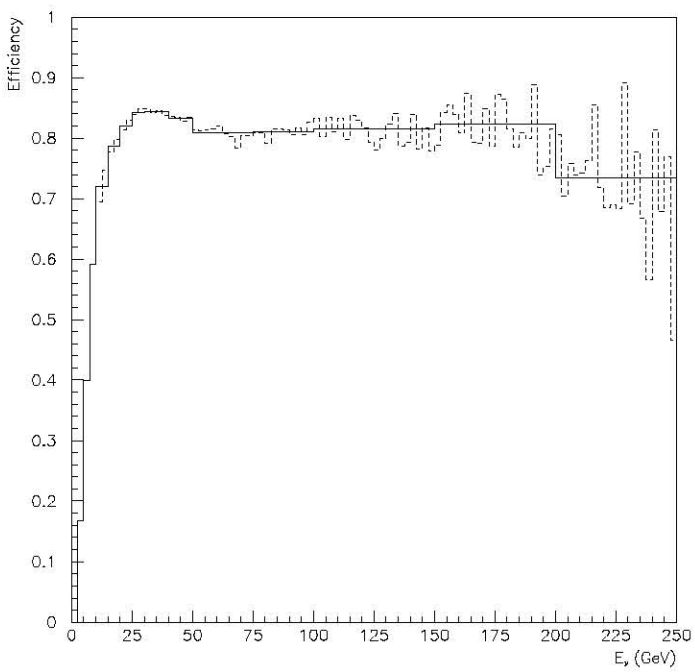

Figure 6.3: Selection efficiency for ν_μ as a function of true neutrino energy. Two curves are shown, the solid curve is the average of the dashed curve over an increasing bin range.

Correction for Finite ν Cut

As stated in section 6.3.1, only events with $\nu < 5$ GeV are used. This finite energy cutoff requires the use of a correction function. The function is described and given in section 5.5.2. The correction is applied to the Monte Carlo, as a function of generated neutrino energy.

Background Addition

To the $\overline{\nu}_\mu$, ν_e and $\overline{\nu}_e$ spectra, a background must be added. The main sources of background are from ν_μ charged current (CC) interactions where the leading muon is misidentified or lost, and neutral current (NC) interactions of all species. In both these cases, leptons from the hadron shower can be mistaken to be the leading lepton of the event. This is termed non-prompt background. Monte Carlo is used to produce a background estimate, by running the $\overline{\nu}_\mu$, ν_e and $\overline{\nu}_e$ selection algorithms on the ν_μ CC and ν_μ NC Monte Carlo. This estimate then needs to be normalised to the data. The procedure for normalising the background is now described, using $\overline{\nu}_\mu$ as an example.

Firstly, the true number of ν_μ CC interactions must be determined. This necessitates scaling the number found in data by the inverse of the selection efficiency from Monte Carlo, (the number selected over generated).

$$\mathrm{N}^{True}_{\nu_\mu CC} = \frac{\mathrm{N}^{Gen}_{CC}}{\mathrm{N}^{Sel}_{CC}} \mathrm{N}^{Data}_{CC} \tag{6.14}$$

The CC background is then scaled by the ratio of the true number of ν_μ CC events to the number of ν_μ CC Monte Carlo events generated on which the $\overline{\nu}_\mu$ selection was run:

$$\text{Corrected CC Background} = \text{CC Background} \frac{\mathrm{N}^{True}_{\nu_\mu CC}}{\mathrm{N}^{Gen}_{\nu_\mu CC}} \tag{6.15}$$

$$= \mathrm{N}^{\overline{\nu}_\mu Sel}_{\nu_\mu CC} \frac{\mathrm{N}^{True}_{\nu_\mu CC}}{\mathrm{N}^{Gen}_{\nu_\mu CC}} \tag{6.16}$$

A similar process is used to determine the NC background, where the true number of NC events in NOMAD, equals the true number of CC events multiplied by 0.40. This factor is determined from the ratio of ν_μ NC to CC cross sections, measured by Arroyo et al. (1994), adapted for NOMAD conditions to include charm production, the ν_μ equivalent of NC from $\overline{\nu}_\mu$, ν_e and $\overline{\nu}_e$ and the non-isoscalarity of the target, Mishra (1998).

$$\text{NC Background} = \mathrm{N}^{\overline{\nu}_\mu Sel}_{\nu_\mu NC} \frac{\mathrm{N}^{True}_{\nu_\mu NC}}{\mathrm{N}^{Gen}_{NC}} \tag{6.17}$$

The background distribution is obtained by applying this process to the number of events in each bin of the energy spectra in a given radial bin. Due to low statistics of the $\overline{\nu}_\mu$, ν_e and $\overline{\nu}_e$ selected samples, the scales are not determined individually for each radial bin.

A further check was performed to determine whether the Monte Carlo is a reliable estimator of the background. In general, simulated events are cleaner than data events, with fewer broken or missing tracks, or underestimated energies. Thus, an event is less likely to be misidentified than in data. Further the Monte Carlo is unable to well reproduce neutrino interactions in the plane transverse to the beam. Alone, it can no longer be relied upon to determine the rejection power of cuts, and must therefore be calibrated. The procedure to calibrate the background is as follows, again using the background to the $\overline{\nu}_\mu$ as an example.

All the events, data and Monte Carlo, are processed twice. The first production is just the $\overline{\nu}_\mu$ selection of chapter 4, giving N_1 events. The second production has the additional isolation cut of equation 4.6 to remove non-prompt background, and has N_2 events.

The difference between the two sets contains background events and true $\overline{\nu}_\mu$ events that fail the isolation cut. To calculate the background scale, the differences must be compared between Monte Carlo, (ν_μ NC and CC), and the data. Before making the comparison however, the true number of $\overline{\nu}_\mu$ events that fail the isolation cut must be removed from the data sample. This is taken as the N_1 N_2 difference in the $\overline{\nu}_\mu$ CC Monte Carlo.

$$\text{Background Scale} = \frac{(N_1 - N_2)_{Data} - (N_1 - N_2)_{\overline{\nu}_\mu CC}}{(N_1 - N_2)_{\nu_\mu CC} + (N_1 - N_2)_{\nu_\mu NC}} \tag{6.18}$$

The scales calculated are presented in table 6.4, for $\overline{\nu}_\mu$, ν_e, and $\overline{\nu}_e$. The background to the ν_μ signal is assumed to be negligible and so no scale is needed. The scales are determined for three ranges of ν, representing all data, the deep inelastic comparison of section 5.6 and the quasielastic-like data of interest here. The errors quoted are dominated by the poor statistics of the simulated background samples.

	All ν	$\nu > 5$ GeV	$\nu < 5$ GeV
$\overline{\nu}_\mu$	1.388 ± 0.029	1.282 ± 0.029	2.551 ± 0.21
ν_e	1.083 ± 0.037	1.054 ± 0.043	1.428 ± 0.14
$\overline{\nu}_e$	1.127 ± 0.038	1.124 ± 0.042	1.164 ± 0.10

Table 6.4: Scales to the backgrounds to the $\overline{\nu}_\mu$, ν_e, and $\overline{\nu}_e$ signals for different ranges of ν.

Additional Corrections

Smearing of the generated energy, described in section 4.4.1, must also be applied. However, due to the poor statistics of the generated Monte Carlo for $\overline{\nu}_\mu$ and $\overline{\nu}_e$, especially after division into radial bins, the smearing process cannot be used as the smearing distributions are not sufficiently smooth. Thus the smearing is included in the efficiency as mentioned in section 4.4.1. The final effect is the rotation and translation of the NUBEAM flux from the beam frame to the NOMAD reference frame. This is achieved via equation 5.1.

6.3.5 Normalisation of Pion and Kaon Spectra

The corrected NUBEAM output must be normalised to the data, (from which the background for $\overline{\nu}_\mu$ and $\overline{\nu}_e$ has been subtracted), before any comparison is made. Instead of a global normalisation to the spectrum, the neutrinos from pions and kaons are normalised separately. This separate normalisation is performed in each radial bin. This makes redundant B, the normalisation factor of the empirical parametrisation, and so it is no longer included in the fitting process.

To understand the normalisation process, consider the distributions of figure 6.4. It shows that there are two distinct regions in the ν_μ spectrum, a pion dominated region and a kaon dominated region. Thus an energy range can be selected in which the neutrinos from pions could be directly normalised to the data, ignoring the small contribution from kaons. This range is from $E_0 = 7.5$ GeV to E_{low}, which varies between 40 and 25 GeV, decreasing with radial bin. An energy range can also be found for kaons, $E_{high} = 75$ GeV to E_1, which is between 125 and 175 GeV, depending on the statistics of the radial bin.

To produce the pion and kaon normalisation factors, a two step process is used. Firstly, the pion normalisation is naïvely calculated ignoring the kaon contribution:

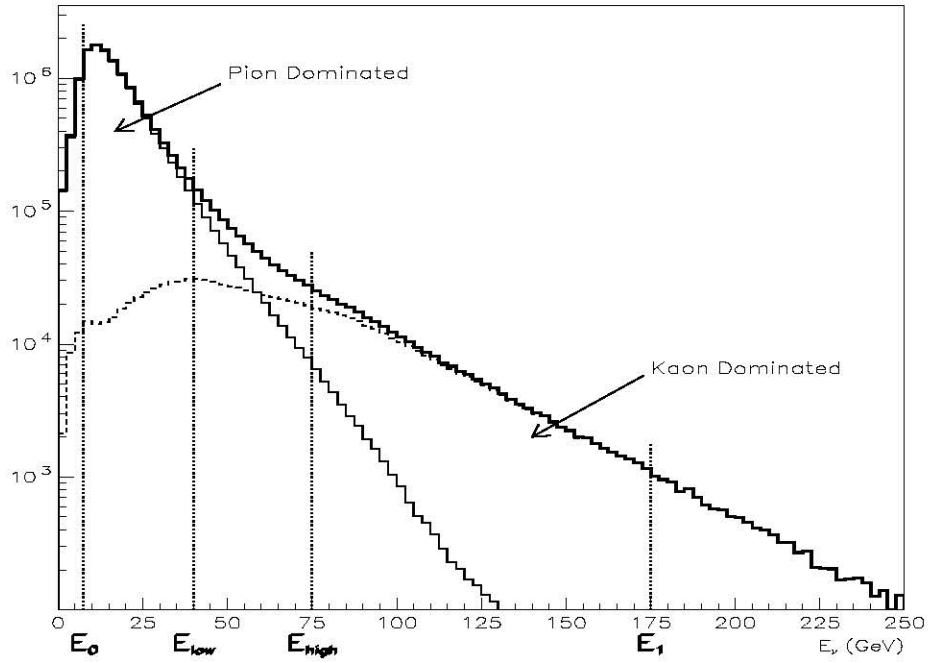

Figure 6.4: ν_μ spectrum showing the approximate energy ranges where pions and kaons dominate. This is the combined radial bin, individual bins have different E_{low} and E_{high}. Three spectra are shown, the ν_μ (bold), the π^+ component (thin) and the K^+ component (dashed).

$$NormaPi^{(0)} = \left[\frac{N_{Data}}{N_\pi}\right]_{E_0 - E_{low}} \tag{6.19}$$

i.e. it is given by the ratio of events within $E_0 < E < E_{low}$. This factor is then used to scale the number of pions in the kaon dominated energy range, before they are subtracted from the data, to allow the derivation of the kaon normalisation:

$$NormaK^{(0)} = \left[\frac{N_{Data} - NormaPi^{(0)} \times N_\pi}{N_K}\right]_{E_{high} - E_1} \tag{6.20}$$

The process can now be iterated, this time using the above kaon normalisation to remove the few kaons from the pion dominated energy range, before producing a new factor:

$$NormaPi^{(1)} = \left[\frac{N_{Data} - NormaK^{(0)} \times N_K}{N_\pi}\right]_{E_0 - E_{low}} \tag{6.21}$$

and similarly for the kaons:

$$NormaK^{(1)} = \left[\frac{N_{Data} - NormaPi^{(1)} \times N_\pi}{N_K}\right]_{E_{high} - E_1} \tag{6.22}$$

Table 6.5 lists the factors from the final ν_μ fit as an example. This method of normalisation is also applied in fitting the $\overline{\nu}_\mu$ spectrum, with different energy ranges.

	0-30	30-60	60-95	95-120	120-130	0-130
Pions	2.010	1.739	2.045	1.668	1.442	1.824
Kaons	2.255	2.115	2.544	2.182	2.311	2.281

Table 6.5: Pion and kaon normalisation factors, for each of the five radial bins and combined bin (cm).

6.3.6 Mechanism to Produce a Trial Flux Estimate

The NUBEAM flux from the base parameters of table 6.3, $PARAM^{(0)}$, is compared to the NOMAD neutrino data, after the above corrections have been applied. To obtain a quantitative measure of how well the data and NUBEAM spectra agree, a χ^2 is generated, defined as:

$$\chi^2 = \sum_{EBin,RBin} \frac{(Data - Fit)^2}{\sigma^2} \tag{6.23}$$

where σ^2 is given by the error on the data and on the NUBEAM flux, added in quadrature. The χ^2 excludes energy bins below 7.5 GeV and above 250 GeV. Recall that the energy bin size is 2.5 GeV.

In order to obtain a new estimate, NUBEAM is not rerun, but rather the base NUBEAM flux is reweighted for a new set of trial parameters,

$PARAM^{(1)}$. Each neutrino produced by NUBEAM is reweighted as follows, where f represents the function in equation 6.9.

$$w^{(1,0)} = \frac{f(x_F, p_T, PARAM^{(1)})}{f(x_F, p_T, PARAM^{(0)})} \tag{6.24}$$

For kaons the numerator f is actually equation 6.10. Neutrinos with weights too high, $w > 15$, are not included as they distort the spectra unreasonably. However, this is typically a tiny fraction of events.

To produce the new flux, p_T, x_F and the neutrino parent type are required. These variables depend on the manner in which the neutrino was produced. A number of decay/interaction chains exist that can produce ν_μ. For 83% of the neutrinos the chain is simply:

$$p \rightarrow \pi, K \rightarrow \nu \tag{6.25}$$

14% additionally have the meson interacting in the beamline to produce a second meson:

$$p \rightarrow \pi, K \rightarrow \pi, K \rightarrow \nu \tag{6.26}$$

The remaining 3% have more than two non proton parents in their decay chain.

The parent type is always taken as the one producing the neutrino. However, the parametrisation models the production of mesons from the proton beryllium interaction. As such, the p_T and x_F *should* be those of the first meson in the chain. So, if the grandparent is a proton, as in equation 6.25, the p_T and x_F are taken as those of the pion or kaon. If the grandparent is not a proton, then the p_T and x_F are taken as those of the grandparent, regardless of the great-grandparent. As only 3% of neutrinos have more than 2 mesonic parents, approximating the true p_T and x_F to that of the grandparent in these cases will not have an appreciable effect on the reweighted neutrino flux.

The empirical parametrisation also assumes that all neutrinos come from mesons produced at the target. This therefore does not include protons that interact downstream of the target to produce neutrinos at NOMAD. The 4% of neutrinos that arise in this manner are actually generated with GFLUKA in NUBEAM, but are still reweighted as if they were produced by equation 6.9. As a test, the parametrisation was used as a replacement for

GFLUKA in every proton interaction, with no discernible differences in the fits to the neutrino spectra. Also, whilst the contamination of antineutrinos is higher from protons interacting downstream of the target, the systematic tests of sections 6.4.1 and 6.4.2 show no evidence for the invalidity of this approximation.

A new spectrum is produced by summing the weights as a function of energy, with the errors being defined by:

$$\sigma_i = \sqrt{\sum_k w_{ik}^2} \tag{6.27}$$

where i refers to the energy bin and k to the number of neutrinos in said bin. After applying the corrections again, a new χ^2 is produced by comparing to the data. This process is then iterated to find the set of parameters that minimise the χ^2. The minimisation process implemented is now described.

6.3.7 Simplex Minimisation

The downhill simplex method is a multi dimensional minimisation method prescribed in Nelder and Mead (1965), where each dimension represents a variable of the function to be minimised. A simplex is the simplest non degenerate geometrical figure in N dimensions, with N+1 vertices or points. For example, in two dimensions the simplex would be a triangle, and a tetrahedron in three. Each vertex of the simplex, $\mathbf{P}_i$, is an input vector for the multi dimensional function to be minimised. The simplex vertices are created from an initial guess of the vector that minimises the function, $\mathbf{P}_0$, and N other points derived from $\mathbf{P}_0$ via:

$$\mathbf{P}_i = \mathbf{P}_0 + \lambda_i \mathbf{e}_i \tag{6.28}$$

where λ_i is the expected characteristic length scale of the problem in the ith dimension, and $\mathbf{e}_i$ is a unit vector. Thus each of the N generated vertices of the simplex differ in just one dimension from the initial vertex. The functional value must then be calculated for each of the N+1 vertices.

The method iterates, working each time with the vertex with the highest value for the function, $\mathbf{P}_h$. The vertex is reflected through the centroid $\overline{\mathbf{P}}$, or centre of mass, of all points in the simplex except $\mathbf{P}_h$, to create a new point $\mathbf{P}^*$.

$$\overline{\mathbf{P}} = \frac{1}{N}\left(\sum_{i=1}^{N+1} \mathbf{P}_i - \mathbf{P}_h\right) \tag{6.29}$$

There can then be three cases for $\mathbf{P}^*$, (where $\mathbf{P}_l$ is the vertex with the lowest functional value):

- $\mathbf{P}^* < \mathbf{P}_l$ In this case, the point is further expanded along the line between itself and $\overline{\mathbf{P}}$, to see if an even lower value can be obtained. If this second new point is still the lowest, it replaces $\mathbf{P}_h$. If not, $\mathbf{P}_h$ is replaced with $\mathbf{P}^*$.
- $\mathbf{P}_l < \mathbf{P}^* < \mathbf{P}_h$ Here, $\mathbf{P}_h$ is replaced with $\mathbf{P}^*$.
- $\mathbf{P}^* > \mathbf{P}_h$ A contraction along the line between $\mathbf{P}_h$ and $\overline{\mathbf{P}}$ is tried to produce a second new point. If this is no longer the highest point then it replaces $\mathbf{P}_h$, else the simplex contracts all points towards $\mathbf{P}_l$.

The method then begins anew with the next highest point, quickly minimising the function. There are no rigorous termination conditions. Generally, the method is terminated when the difference in the functional value between the highest and lowest point reaches some set tolerance, but this is not a true convergence criterion.

The benefits of the method are that it is fast, with few function evaluations and iterations, it takes large steps, allowing it to avoid local minima, and finally, it enables the minimisation with respect to all the variables of the function simultaneously.

In application to the empirical parametrisation, the function is the χ^2. There are 19 parameters for the ν_μ and $\overline{\nu}_\mu$ fits, (8 for the pions and 11 for the kaons), requiring a simplex with 20 points in 19 dimensional space. The $\overline{\nu}_e$ has just 8 parameters, describing the K_L^0 production. The simplex is initialised, using the base parameters for $\mathbf{P}_0$. The λ_i are selected accordingly to restrict the degree to which meson spectra can change in a given fit. The tolerances used were 1% for the initial fits and 0.05% for the final iteration.

The minimisation routine is taken from Press et al. (1986).

6.3.8 SPY Data Fit

At high energies, the kaon contribution is well constrained by the neutrino spectrum. However, the kaon distribution at low energies, where the pion contribution dominates, still has considerable freedom. The kaon distribution

can move by up to 50% in the region below 30 GeV without altering the χ^2 of the fit to the neutrino spectrum. That is to say, the neutrino data provides no handle on kaon production at low energies. If the LSND oscillation signal is correct, a distortion in the ν_e spectrum due to oscillations would appear at around 20 GeV. As the main source of ν_e is kaons, it is essential that the low energy kaon distribution be well determined, if this signal is to be observed.

The SPY experiment of chapter 3 measured the ratio of pion to kaon production at low energies. Its measurements can be included within the fitting procedure to help constrain the low energy kaons. The SPY data to be used are tabulated in tables 6.6, 6.7 and 6.8, according to the transverse momentum, p_T, and forward momentum of the secondary, p. Note that the errors on the particle ratios are considerably reduced, (now less than 3%), compared with the large, 5-10%, errors on the particle yields used in the FLUKA SPY weighting of section 5.2.2. This is because of the removal of common systematic errors, see chapter 3 and Ambrosini et al. (1999). Data from the Atherton experiment, referred to in chapter 3, has been used to augment the available SPY data at high momenta. Blank spaces in the tables indicate where no data exists, and asterisks denote data from the Atherton experiment. From here on, SPY is used in reference to the combined Atherton experiment and SPY data sets.

To compare to the SPY measurements, the K/π ratio is generated from the current empirical parameters using equations 6.9 and 6.10, for each p_T and momentum that SPY made a measurement. However, this reflects the ratio of pions and kaons as neutrino parents, and not target production. The two are not the same due to the different lifetimes between kaons and pions, the K/π ratio from the parameters needs to be normalised to the SPY data. Firstly however, the expected value of this normalisation is obtained as a check. The number of pion and kaon decayed is given by:

$$\text{Mesons decayed} = 1 - e^{\left(\frac{-Lm}{Ec\tau}\right)} \tag{6.30}$$

where L=41432 cm, the distance from the target to the end of the decay pipe, and m and τ are the mass and lifetime of the meson. Substituting in values for pions and kaons, the energy dependent ratio of kaon to pion decays is then:

$$\frac{Kaon}{Pion} = \frac{1 - e^{-55.1/E}}{1 - e^{-7.432/E}} \tag{6.31}$$

Additionally, the branching ratio for the kaon decay to ν_μ of 0.66 must also be included. For positives, the value of the normalisation is checked at 135 GeV,

a point that was measured in agreement by both the Atherton experiment and SPY. The observed normalisation of the K/π ratio determined from the neutrino data to that of SPY is 4.41, in reasonable agreement with the calculated value of 4.13. The *observed* normalisation is then applied to the K/π ratio from the neutrino data, taking into account its energy dependence. A similar process is undertaken for the negative mesons, except the normalisation is calculated at 67.5 GeV, a point again measured by both the Atherton experiment and SPY.

Comparing the measured and fitted ratios gives a χ^2, which is then included in the minimisation process. Therefore, a set of parameters must minimise the combined χ^2 from the neutrino spectrum and the SPY data fits. The values of K/π from the empirical parametrisation obtained in the next section are included in tables 6.6, 6.7 and 6.8, and are plotted with the SPY data in figures 6.5 and 6.6. It is important to note that mesons with secondary momentum less than 10 GeV/c contribute very little to the neutrino spectra at NOMAD. Further those with $p_T > 0.2$ GeV/c at 15 GeV/c and $p_T > 0.4$ GeV/c at 40 GeV/c are too greatly angled to create neutrinos that cross NOMAD. Considering this, SPY and the fits are in excellent agreement.

	K^+/π^+		K^-/π^-	
p (GeV/c)	SPY	Fit	SPY	Fit
7.0	0.0691 ± 0.0031	0.0570	0.0635 ± 0.0069	0.0717
10.0	0.0741 ± 0.0024	0.0710	0.0697 ± 0.0038	0.0746
15.0	0.0832 ± 0.0028	0.0853	0.0751 ± 0.0026	0.0749
20.0	0.0965 ± 0.0023	0.0942	-	-
30.0	0.1060 ± 0.0019	0.1043	-	-
40.0	0.1096 ± 0.0016	0.1088	0.868 ± 0.0019	0.0841
67.5	0.1057 ± 0.0018	0.1034	0.853 ± 0.0020	0.0838
135.0	0.0807 ± 0.0014	0.0806	0.0656 ± 0.0009*	0.0691
225.0	0.1190 ± 0.0015*	0.0957	0.0452 ± 0.0014*	0.0393
337.5	-	-	0.0105 ± 0.0002*	0.0106

Table 6.6: SPY K/π production, versus those obtained from the fit, displayed according to secondary momentum.

6.3.9 Producing the ν_e Estimate

The neutrino types are fitted in series, from the largest, ν_μ, to the smallest, $\overline{\nu}_e$, component of the beam. The individual neutrino fitting procedures are

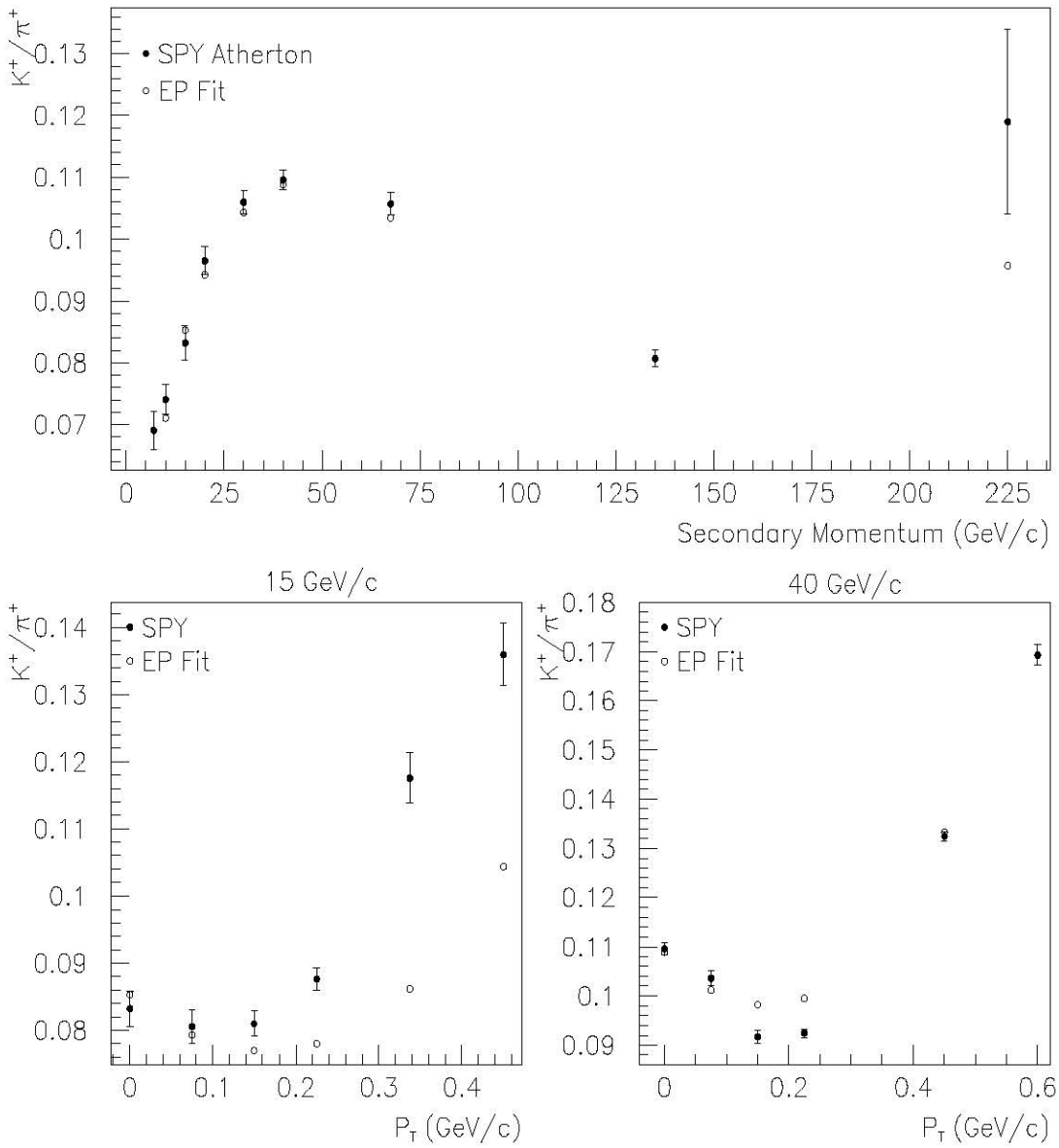

Figure 6.5: Fits to SPY K^+/π^+ data, as a function of secondary momentum in the forward direction (top plot), and of p_T at fixed secondary momenta of 15 GeV/c (bottom left), and 40 GeV/c (bottom right).

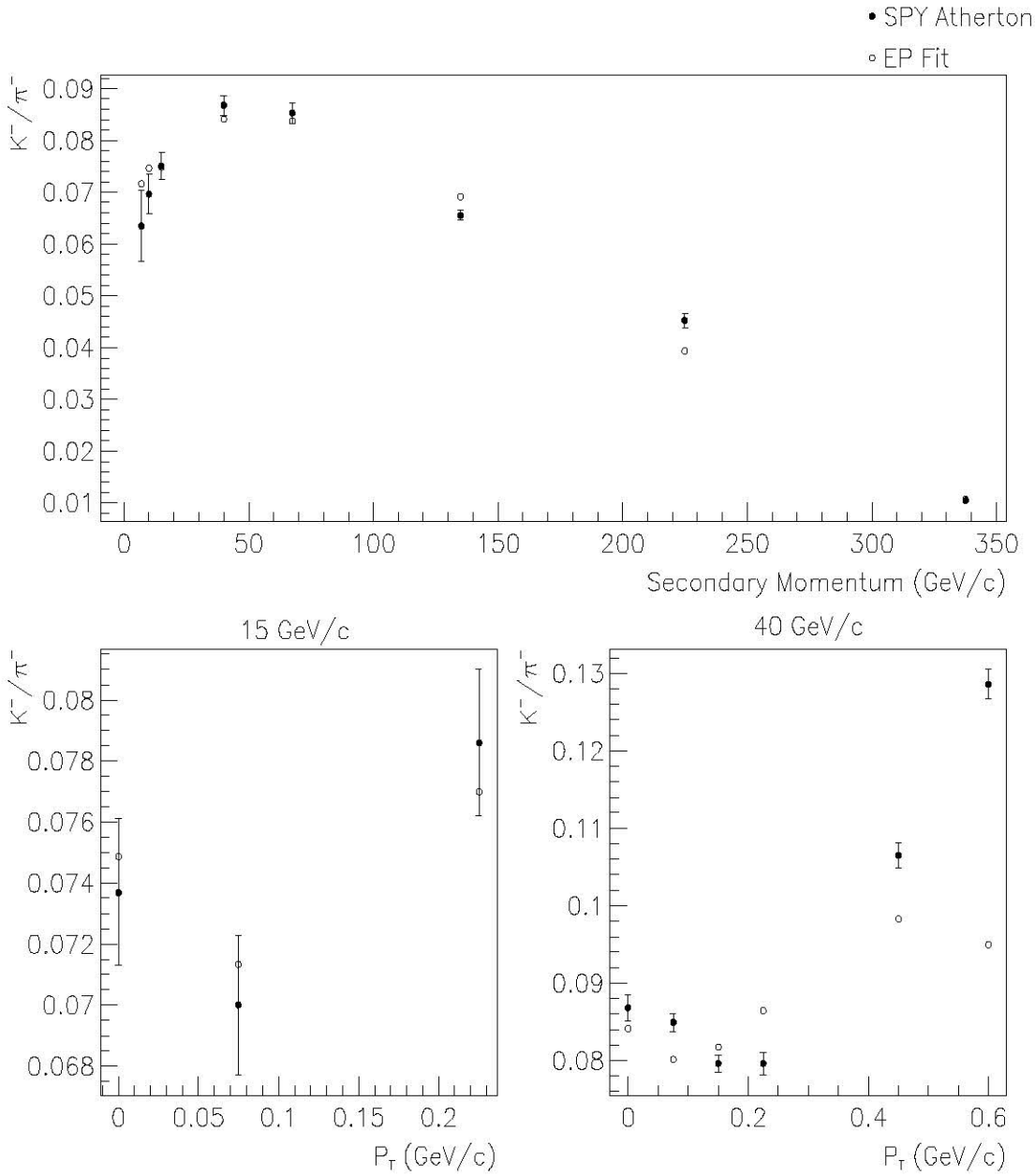

Figure 6.6: Fits to SPY K^-/π^- data, as a function of secondary momentum in the forward direction (top plot), and of p_T at fixed secondary momenta of 15 GeV/c (bottom left), and 40 GeV/c (bottom right).

p_T (GeV/c)	$p = 15.0$ (GeV/c)		$p = 40.0$ (GeV/c)	
	SPY	Fit	SPY	Fit
0.075	0.0805 ± 0.0025	0.0792	0.1036 ± 0.0015	0.1012
0.150	0.0810 ± 0.0019	0.0770	0.0917 ± 0.0013	0.0982
0.225	0.0876 ± 0.0017	0.0780	0.0924 ± 0.0009	0.0995
0.3375	0.1176 ± 0.0037	0.0861	-	-
0.450	0.1360 ± 0.0046	0.1044	0.1324 ± 0.0010	0.1332
0.600	-	-	0.1693 ± 0.0021	0.1983

Table 6.7: SPY K^+/π^+ production, versus those obtained from the fit, displayed according to p_T at the two given secondary momenta.

p_T (GeV/c)	$p = 15.0$ (GeV/c)		$p = 40.0$ (GeV/c)	
	SPY	Fit	SPY	Fit
0.075	0.0700 ± 0.0023	0.0713	0.0848 ± 0.0012	0.0802
0.150	-	-	0.0796 ± 0.0011	0.0817
0.225	0.0786 ± 0.0024	0.0770	0.0796 ± 0.0015	0.0865
0.450	-	-	0.1065 ± 0.0017	0.0983
0.600	-	-	0.1286 ± 0.0019	0.0949

Table 6.8: SPY K^-/π^- production, versus those obtained from the fit, displayed according to p_T at the two given secondary momenta.

as follows:

- ν_μ Only the π^+ and K^+ are included in the fit; muon, K_L^0 and charm production are neglected. The χ^2 is minimised without the inclusion of SPY. This fixes the (pion) peak. The SPY data is then introduced, in two stages. Firstly, the $p_T = 0$ data is included, then the angular scans. Before including the SPY data, the λ_i of the π^+ parameters are halved. This restricts the π^+ parameters movement, as they are better fixed by the neutrino data, than by the inclusion of the SPY data. The culmination of this procedure is a π^+ and K^+ distribution that agrees with both the measured ν_μ spectra, and the measured SPY K^+/π^+ ratio.

- $\overline{\nu}_\mu$ The procedure is equivalent to the ν_μ fit, except π^- and K^- are fitted, and also *fixed* muon contribution is included, obtained from the previously determined π^+ production.

- $\overline{\nu}_e$ The K^- and μ^- have already been obtained. The K^- comes directly from the fit to the $\overline{\nu}_\mu$ data and the μ^- are inferred from the π^- distribution, and also from the $\overline{\nu}_\mu$ fit. The charm contribution is fixed according to the parametrisation of section 6.3.3, normalised to protons on target. There is no SPY data directly relevant to the $\overline{\nu}_e$ parent distributions. The χ^2 from the spectrum is then minimised with respect to just the K^0_L parameters.

Whilst fitting to determine the parents of a neutrino, a new efficiency is sometimes required as the beam distribution which NEGLIB used, NUBEAM 4.00, is markedly different to that of the data, see chapter 5. Thus there may exist irreducible differences in the data and fitted spectra, due to an incorrect beam distribution being used to determine the selection efficiency. To solve this, a new neutrino beam distribution can be obtained from an initial fit to the data. This distribution can then be used to reweight NEGLIB, as outlined in section 5.3.3, and the fit repeated.

Once these three neutrino types have been fitted, all the parameters describing the meson production have been fixed. The ν_e flux can now be produced. This is achieved by weighting the ν_e spectra, as described for the fitting process in section 6.3.6. A fixed charm contributions is added, in the same manner as for the $\overline{\nu}_e$.

The final fit parameters determined are listed in table 6.9. The new parameters often bear little resemblance to the base parameters in table 6.3, and they need not. The addition of the S, T and U parameters, as well as normalising the kaons and pions separately in each radial bin can cause large alterations to the initial parameters. Furthermore, the base parameters were determined in a fit that did not include the SPY data. Note however that the K^0_L parameters required no change from the base parameters, the small number of $\overline{\nu}_e$ events implied that actually fitting the data would not be worth while. The fits to the data are presented in the next section.

Finally, this fit used fluxes generated with NUBEAM 6.10, which has now been superseded. The effect of using a new NUBEAM version on the prediction is covered in the systematic error study of section 7.1.4.

6.4 Results

6.4.1 ν_μ Fit

The results of the fit to the ν_μ data for the five radial bins are presented in figures 6.7 and 6.8. In all plots, data are represented by the points. Two views are given, a linear scale to highlight the comparison in the peak of

	A	B/ (sr GeV/c)	C	D	F	G/ $(GeV/c)^2$	M^2 $(GeV/c)^2$	R	S/ (GeV/c)	T	U
π^+	2.70	3.68	2.32	2.86	0.337	2.36	5.05	4.40	0.0	0.0	0.0
π^-	5.23	70.6	1.39	0.581	1.03	0.0	0.0172	4.66	0.0	0.0	0.0
K^+	2.15	12.2	22.1	11.7	1.76	-0.245	1.01	-0.390	1.26	0.0002	-2.37
K	7.05	12.3	54.9	2.80	1.81	0.0006	0.261	5.09	1.19	-0.156	1.03
K_L^0	3.61	2.80	5.00	10.7	1.00	0.0	0.769	4.00	0.0	0.0	0.0

Table 6.9: Final meson production parameters after completion of the fitting process.

the distribution and a logarithmic scale for the tail. The radial bin plots are meant only to show the broad characteristics in each bin, the third and fourth bins have larger plots as they are the most important, i.e. they contain the highest number of events. The plots do show good agreement between the fit and the data, except in the first radial bin. Here a problem in the simulation of the focusing elements causes a discrepancy at low energies, (now fixed in NUBEAM 6.21). However, the first radial bin represents a small portion of the fitted data, and so this can be neglected.

The combined comparison of all the radial bins is presented in figure 6.9. This figure also shows the separate contributions from π^+, dashed line, and K^+, dotted line. The ratio plot shows excellent agreement up to 140 GeV/c, well beyond the expected ν_e signal region. The χ^2 of the fits, in each radial bin and combined, are given in table 6.10. Overall, they are quite acceptable.

	0-30	30-60	60-95	95-120	120-130	0-130
χ^2	182.0	95.8	75.1	101.9	77.1	129.5

Table 6.10: χ^2 of the fitted flux to the ν_μ data, in the five radial bins and combined radial bin (cm).

NOMAD also ran with negative currents in the horn and reflector. See section 5.6.1 for details of this setup. As stated therein, the main use of this negative focusing data is in systematics studies, particularly in regards to protons interacting downstream of the target. The negative focusing data provides an independent check of the parametrisation obtained. Entering the parameters into NUBEAM with a negative horn and reflector current produce new beam distributions, which after corrections can be compared to the ν_μ data from the negative focus running, (note, a new selection efficiency must also be obtained for this negative focusing beam). The comparison is shown in figure 6.10 for the combined radial bin. There is too little negative

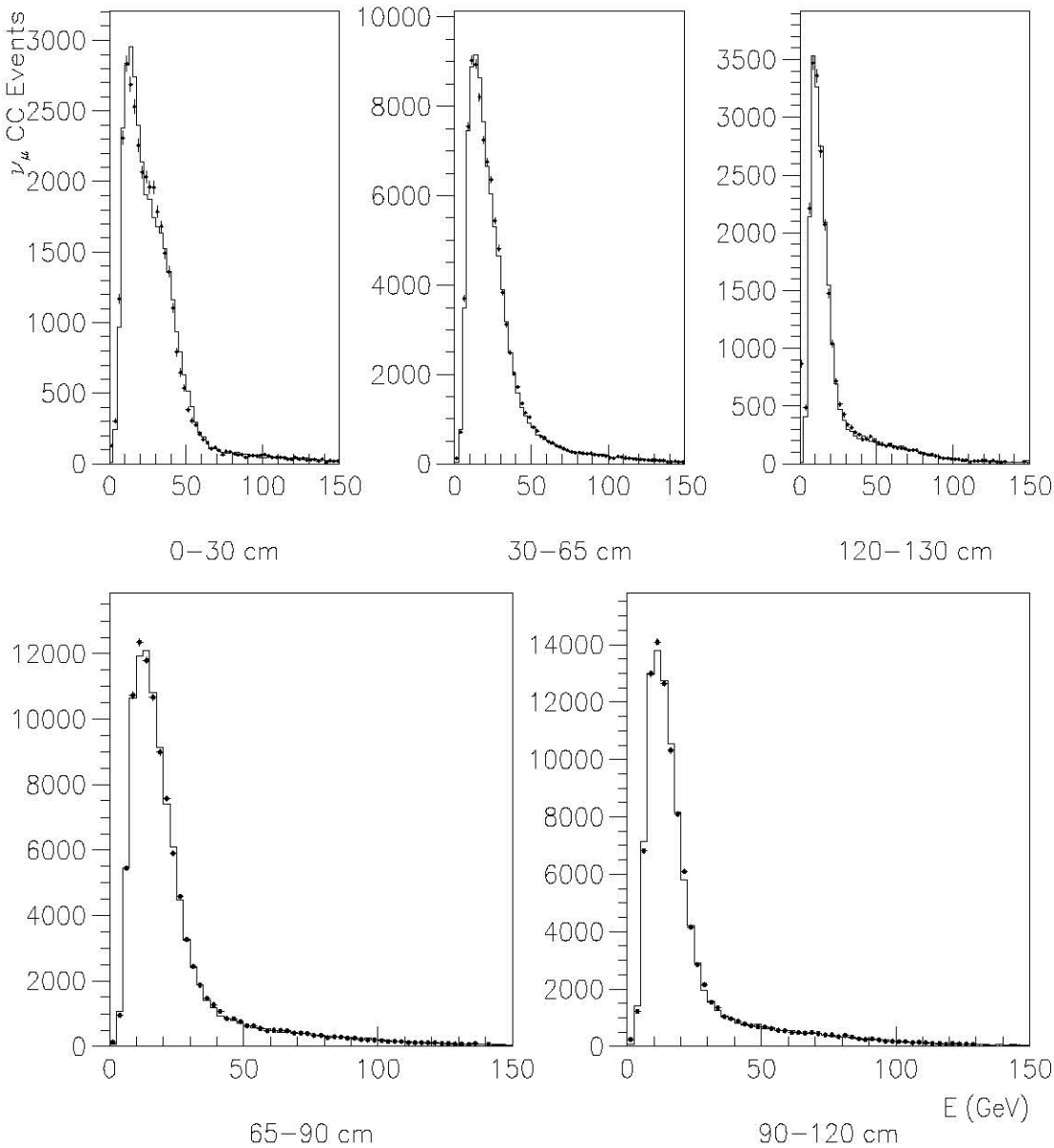

Figure 6.7: Comparison of the NOMAD data to the empirical parametrisation for ν_μ in the five radial bins, on a linear axis.

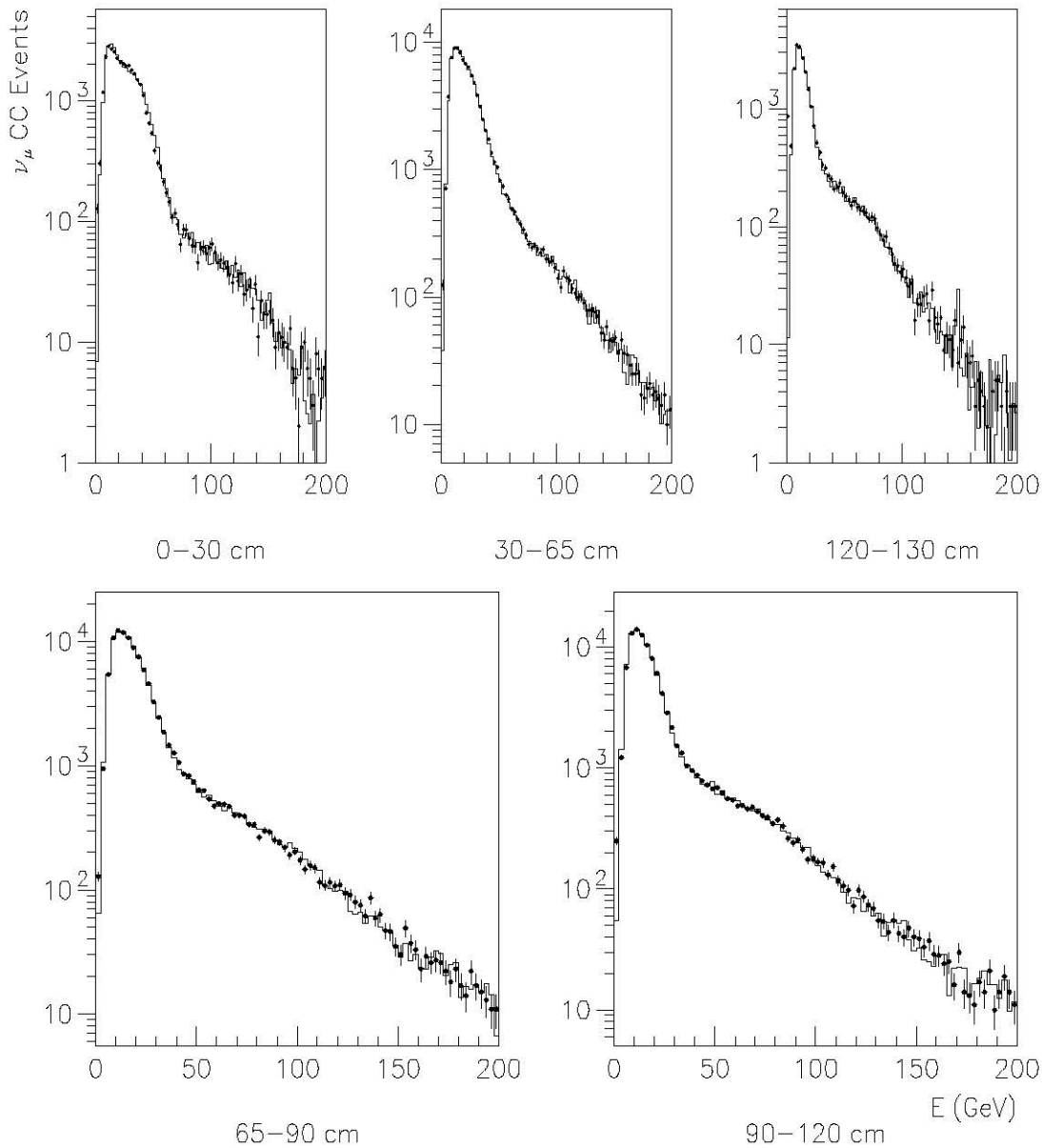

Figure 6.8: Comparison of the NOMAD data to the empirical parametrisation for ν_μ in the five radial bins, on a logarithmic axis.

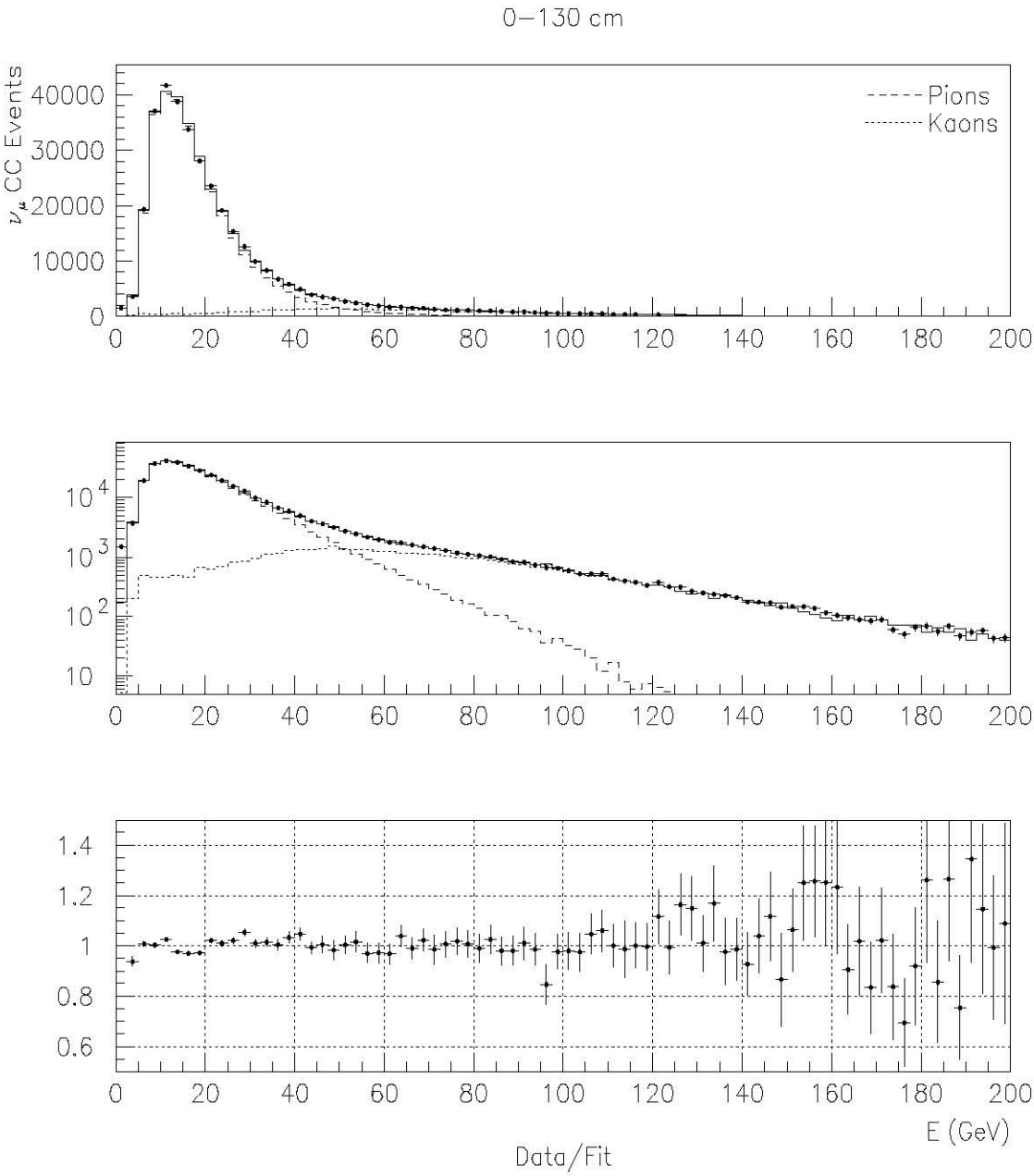

Figure 6.9: Comparison of the NOMAD data to the empirical parametrisation for ν_μ with the five radial bins combined. The plots, from top to bottom, are a linear, and logarithmic view of the spectra, and a ratio of the data over the fitted spectrum.

focusing ν_μ data to allow meaningful comparisons in the individual radial bins, and further, the combined radial bin required the energy bin size to be tripled. The agreement here is acceptable, showing that the empirical parametrisation method does not suffer from large systematic effects relating to the focusing or defocusing of the parent mesons.

6.4.2 $\overline{\nu}_\mu$ Fit

The results of the fit to the NOMAD $\overline{\nu}_\mu$ data in the five radial bins are presented in figures 6.11 and 6.12 with linear and logarithmic scales respectively. The normalised and scaled background is represented by the histogram filled with negative gradient lines, and the contribution from muon parented neutrinos by the positive gradient lines, (the muon histograms mostly looked hatched due to overlapping with the background histograms). All the figures in this section follow this convention. The fit is in quite good agreement with the data in all radial bins.

The comparison in the combined radial bin is presented in figure 6.13. This figure also shows the separate contributions from π^- (dashed line) and K^- (dotted line). The ratio plot shows few discrepancies between the fit and the data. The χ^2 of the fits, in each radial bin and combined, are given in table 6.11.

	0-30	30-60	60-95	95-120	120-130	0-130
χ^2	114.4	181.1	131.1	164.7	151.1	148.6

Table 6.11: χ^2 of the fitted flux to the $\overline{\nu}_\mu$ data, in the five radial bins and combined radial bin (cm).

As with the ν_μ fit, it is worthwhile comparing the fit to the negative focusing $\overline{\nu}_\mu$ data. As the $\overline{\nu}_\mu$ was the main component of the beam, enough data was recorded to allow the inclusion of the radial bins. The results are plotted with a linear and logarithmic scale in figures 6.14 and 6.15 respectively. The comparison to the combined radial bin data is given in figure 6.16. Again this plot includes the contributions from π^- (dashed line) and K^- (dotted line). Whilst agreement is not good in the individual radial bins, perhaps due to the radically different radial distributions of the $\overline{\nu}_\mu$ expected in the positive and negative focusing beams, the combined plots show few differences.

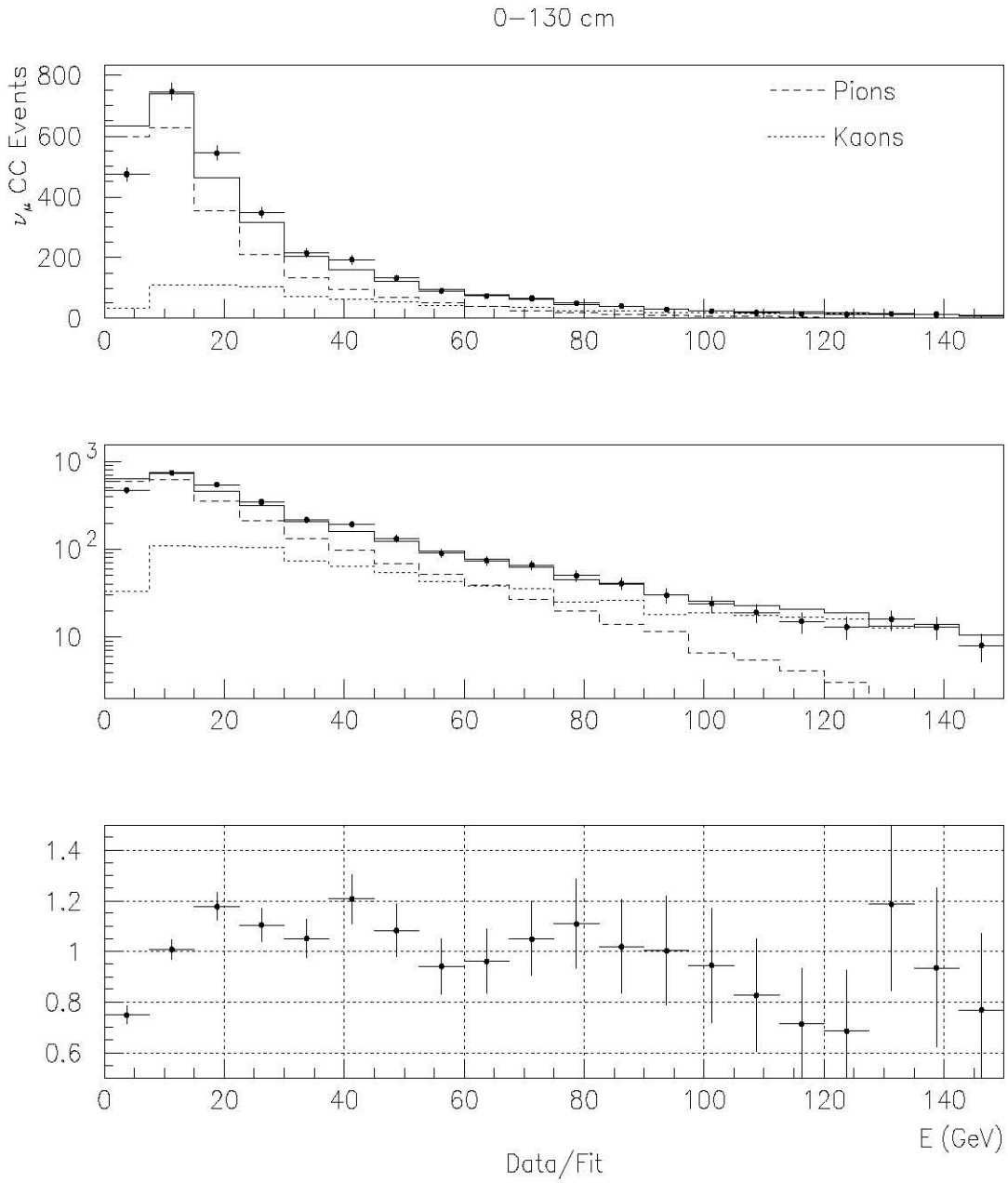

Figure 6.10: Comparison of the negative focusing ν_μ data in the combined radial bin, to the empirical parametrisation. The plots, from top to bottom, feature a linear, and then a logarithmic scale, and finally a ratio of the data to the fit.

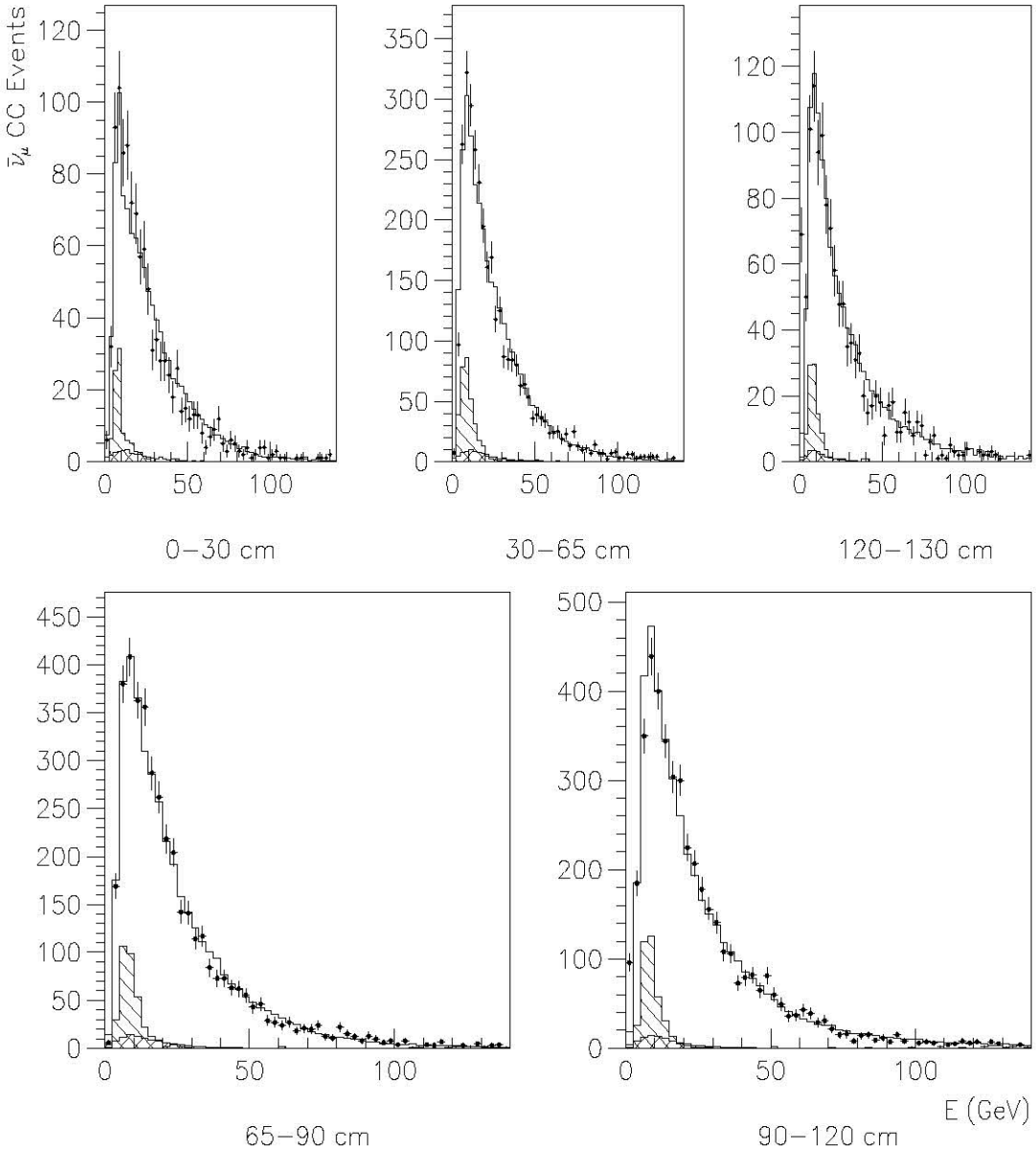

Figure 6.11: Comparison of the NOMAD $\overline{\nu}_\mu$ data to the empirical parametrisation in the five radial bins, on a linear scale.

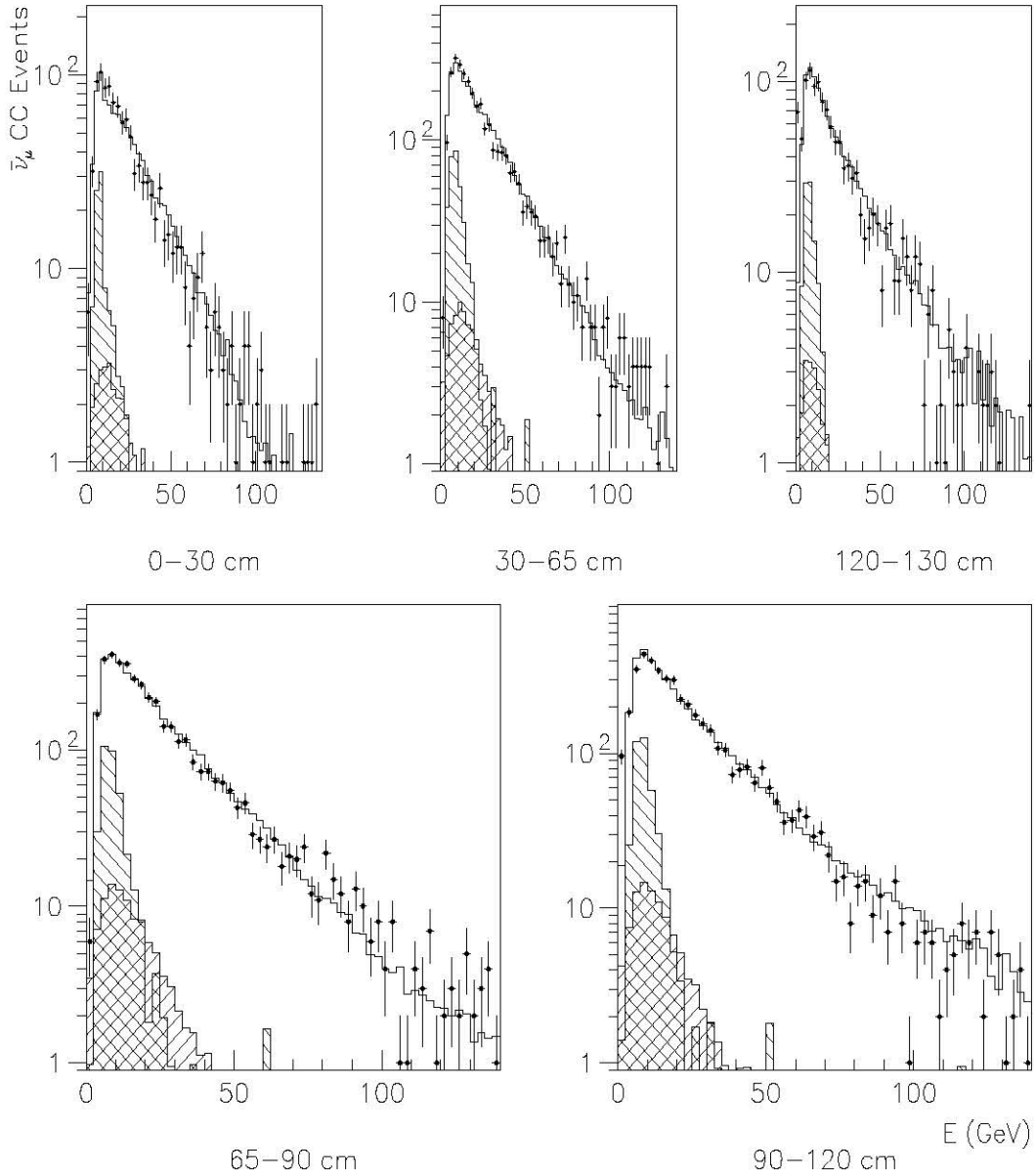

Figure 6.12: Comparison of the NOMAD $\overline{\nu}_\mu$ data to the empirical parametrisation in the five radial bins, on a logarithmic scale.

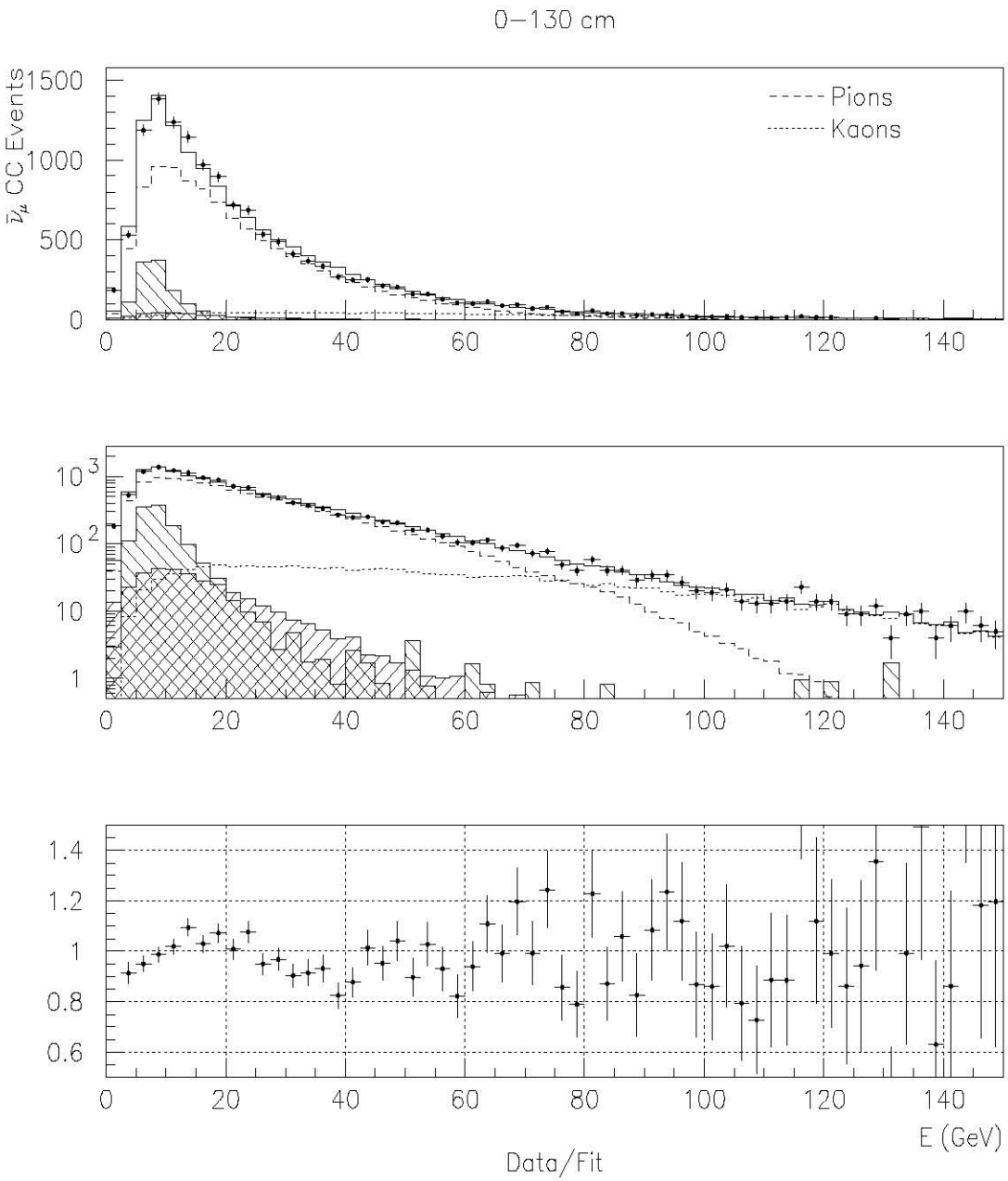

Figure 6.13: Comparison of the NOMAD $\overline{\nu}_\mu$ data in the combined radial bin, to the empirical parametrisation. The plots, from top to bottom, feature a linear, and then a logarithmic scale, and finally a ratio of the data to the fit.

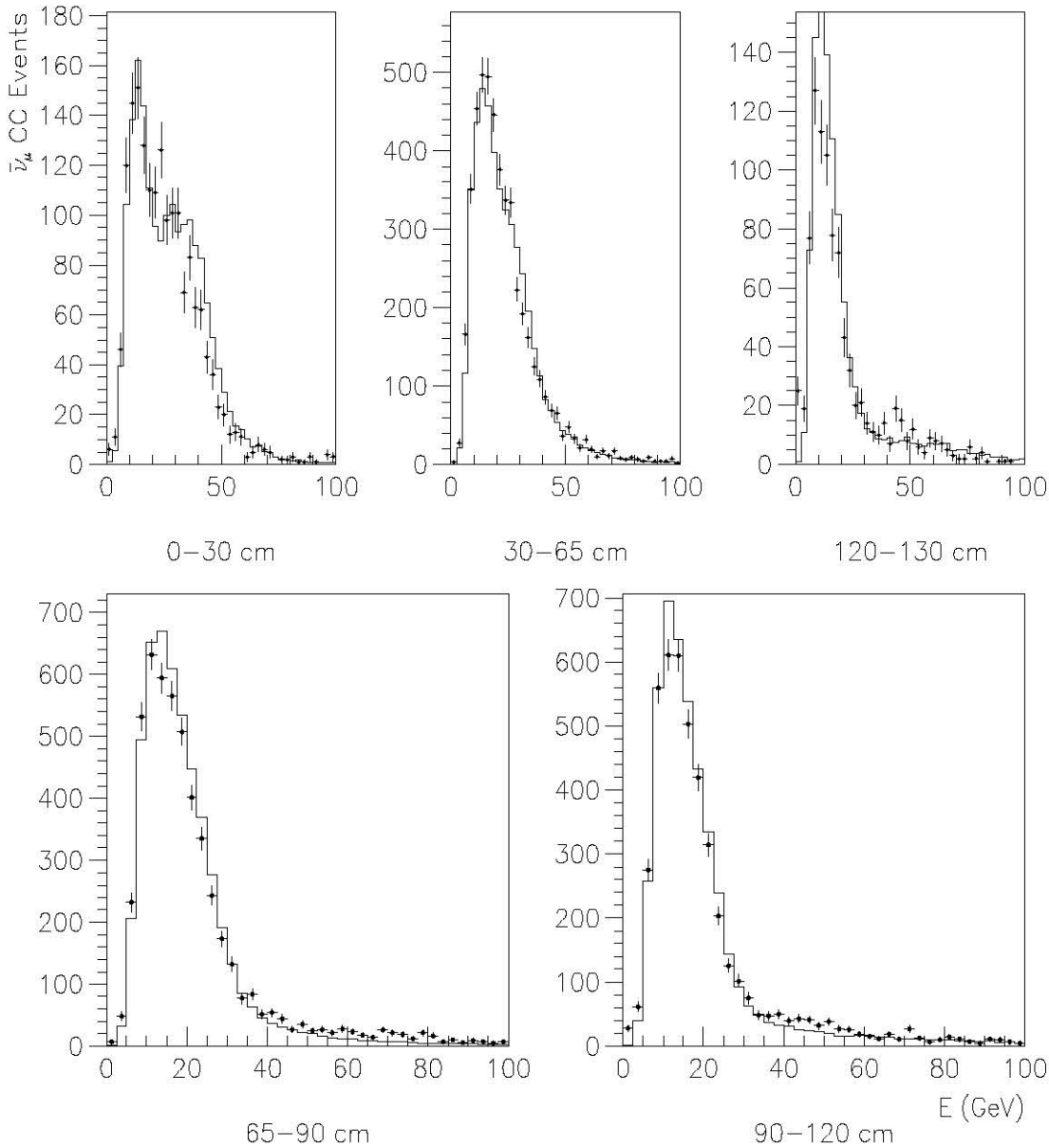

Figure 6.14: Comparison of the negative focusing $\overline{\nu}_\mu$ data to the empirical parametrisation in the five radial bins, on a linear scale.

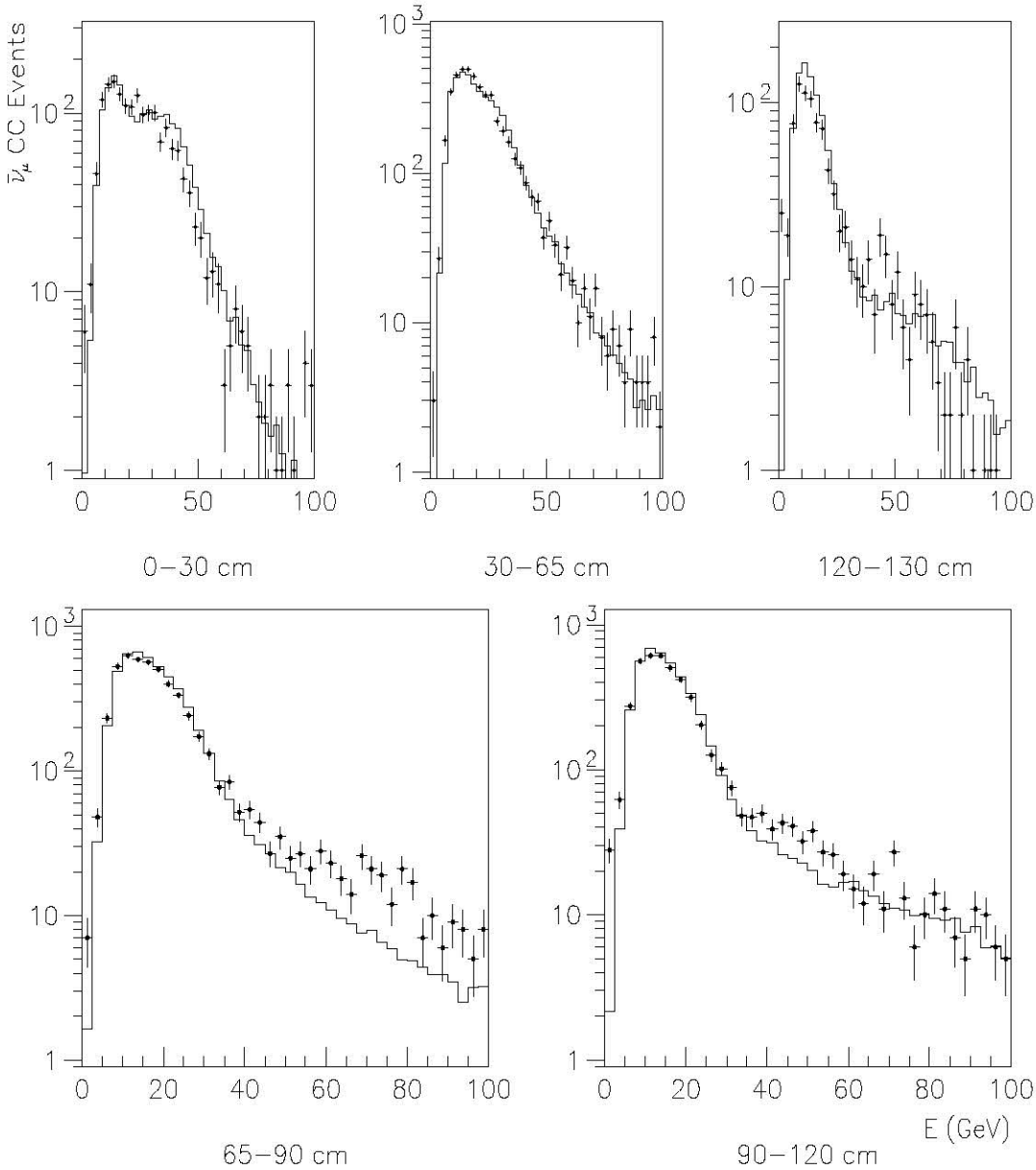

Figure 6.15: Comparison of the negative focusing $\overline{\nu}_\mu$ data to the empirical parametrisation in the five radial bins, on a logarithmic scale.

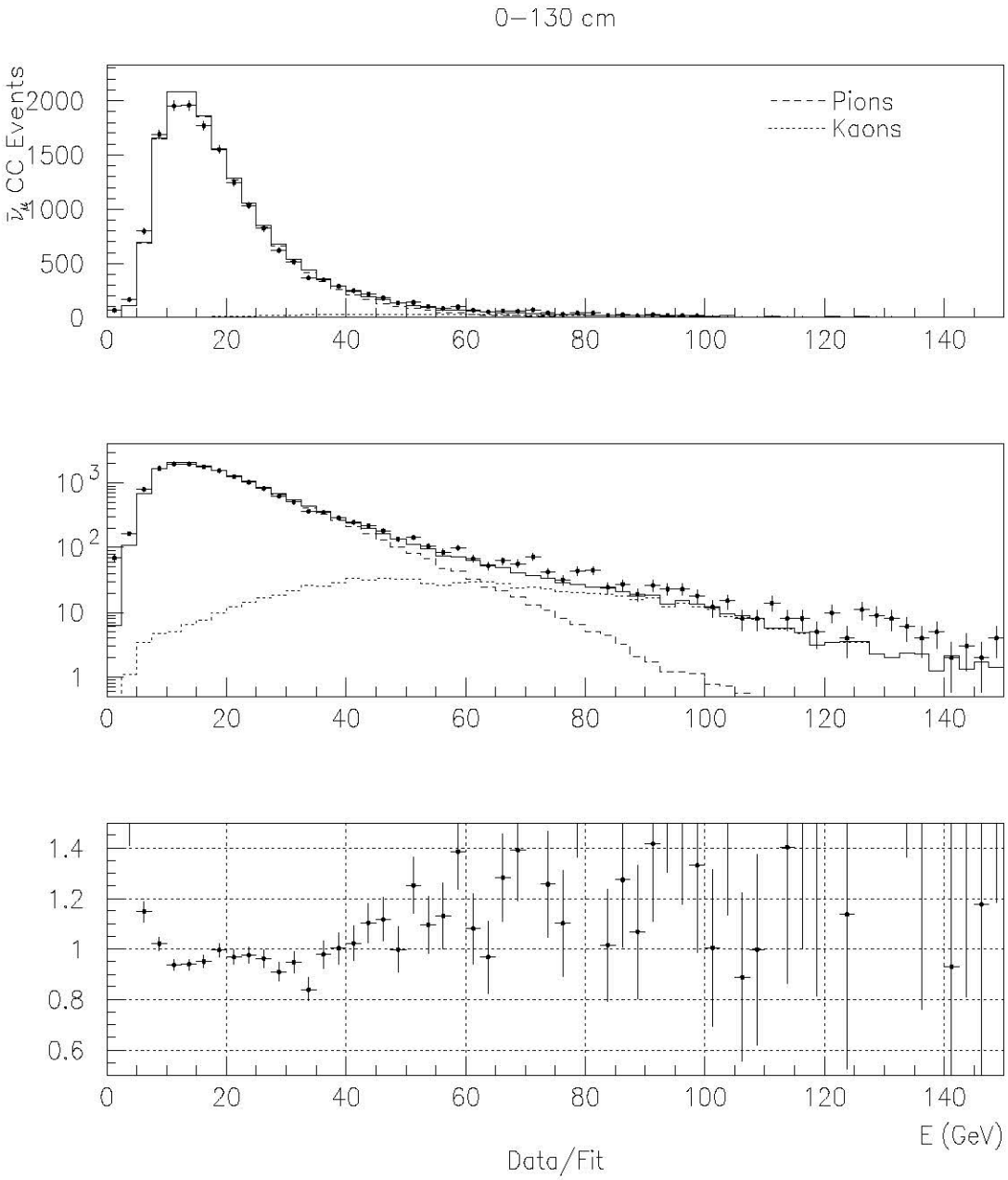

Figure 6.16: Comparison of the negative focusing $\overline{\nu}_\mu$ data in the combined radial bin, to the empirical parametrisation. The plots, from top to bottom, feature a linear, and then a logarithmic scale, and finally a ratio of the data to the fit.

6.4.3 $\overline{\nu}_e$ Fit

Unlike the previous fits, the fit to the $\overline{\nu}_e$ data is not carried out in radial bins, due to the lack of $\overline{\nu}_e$ data. Also, as mentioned earlier, after fixing the K^-, charm mesons and muons, adjusting the starting K_L^0 production is not necessary. The $\overline{\nu}_e$ spectrum from the empirical parametrisation is then plotted in figures 6.17 and 6.18, on linear and logarithmic scales respectively. Also included are the $\overline{\nu}_e$ data points and the complete breakdown of the $\overline{\nu}_e$ parents, as given by the key of figure 6.17. Due to the low statistics, it is simple to obtain good agreement, but it is still encouraging to see that there are no problems between the fit and data.

6.4.4 ν_e Prediction

The prediction of the ν_e spectrum at NOMAD is the culmination of the work of this chapter. Using the normalisations and parameters obtained in the fits above, the NUBEAM ν_e spectrum can be reweighted. The new spectrum is plotted in figures 6.19 and 6.20, again on a linear and logarithmic scale. This prediction will be compared with that from NUBEAM with FLUKA and SPY, and that of a separate parametrisation in the next chapter to decide which will be used in the oscillation analysis.

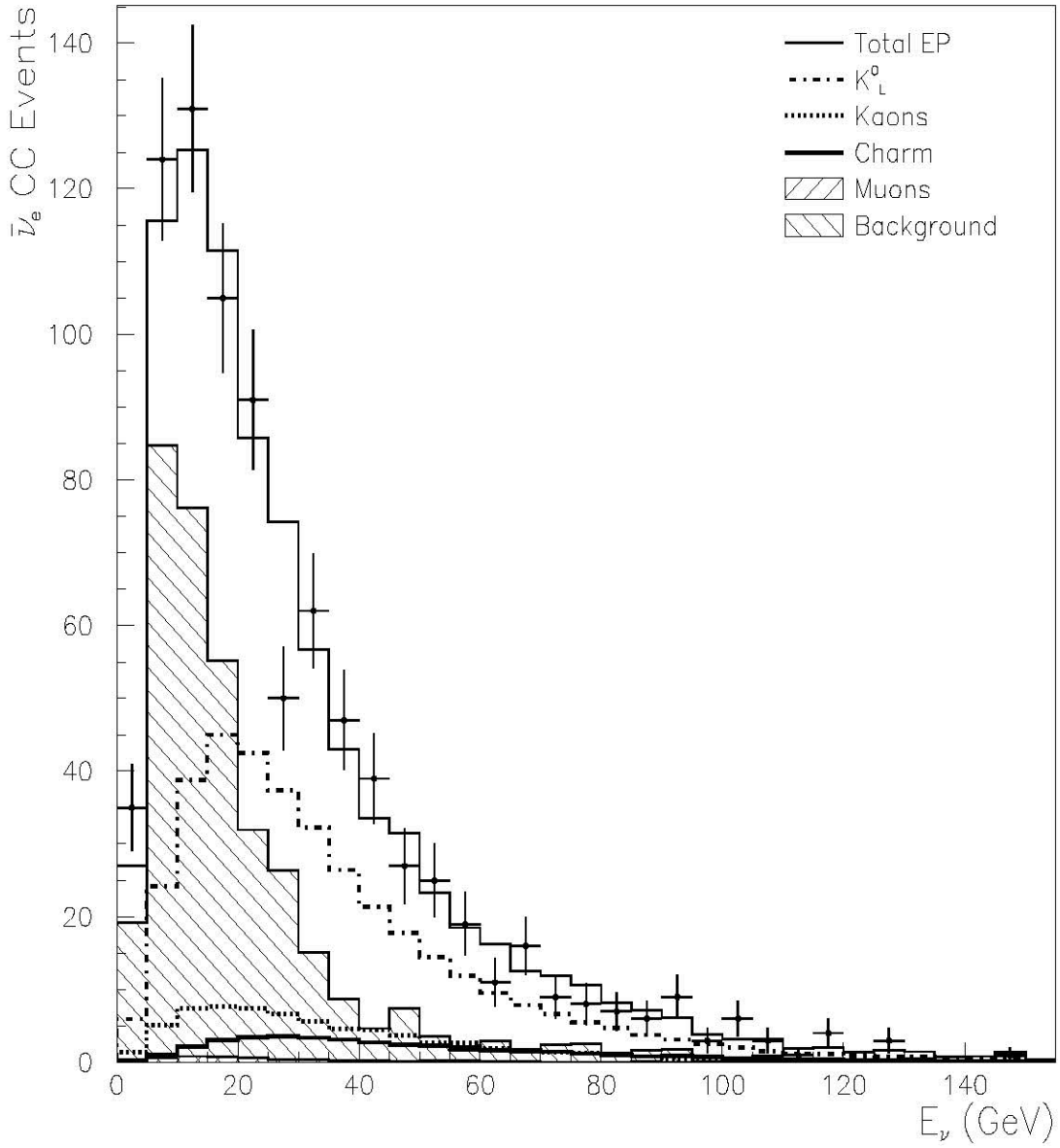

Figure 6.17: Comparison of the NOMAD $\overline{\nu}_e$ data in the combined radial bin, to the empirical parametrisation, on a linear scale.

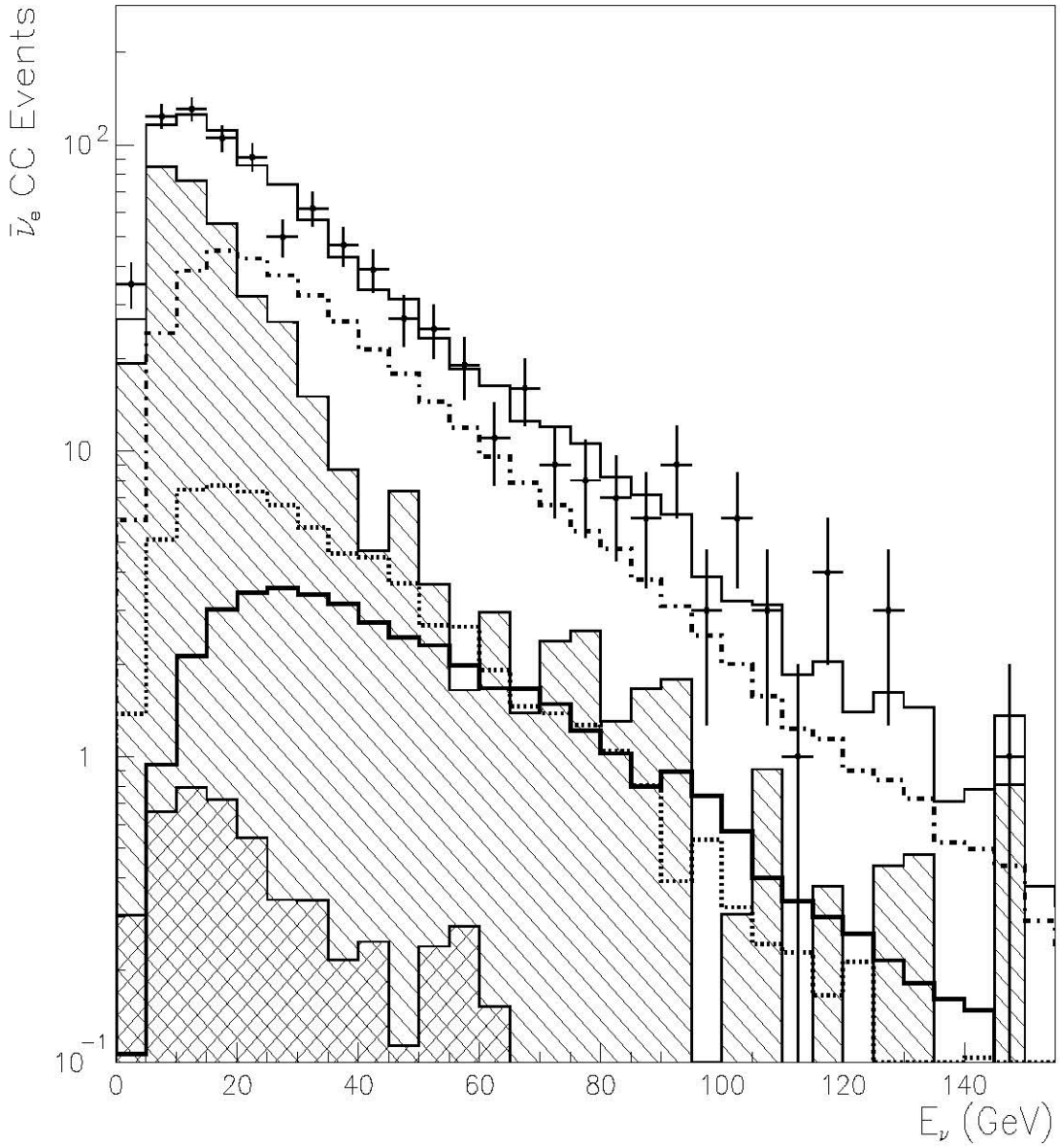

Figure 6.18: Comparison of the NOMAD $\overline{\nu}_e$ data in the combined radial bin, to the empirical parametrisation, on a logarithmic scale.

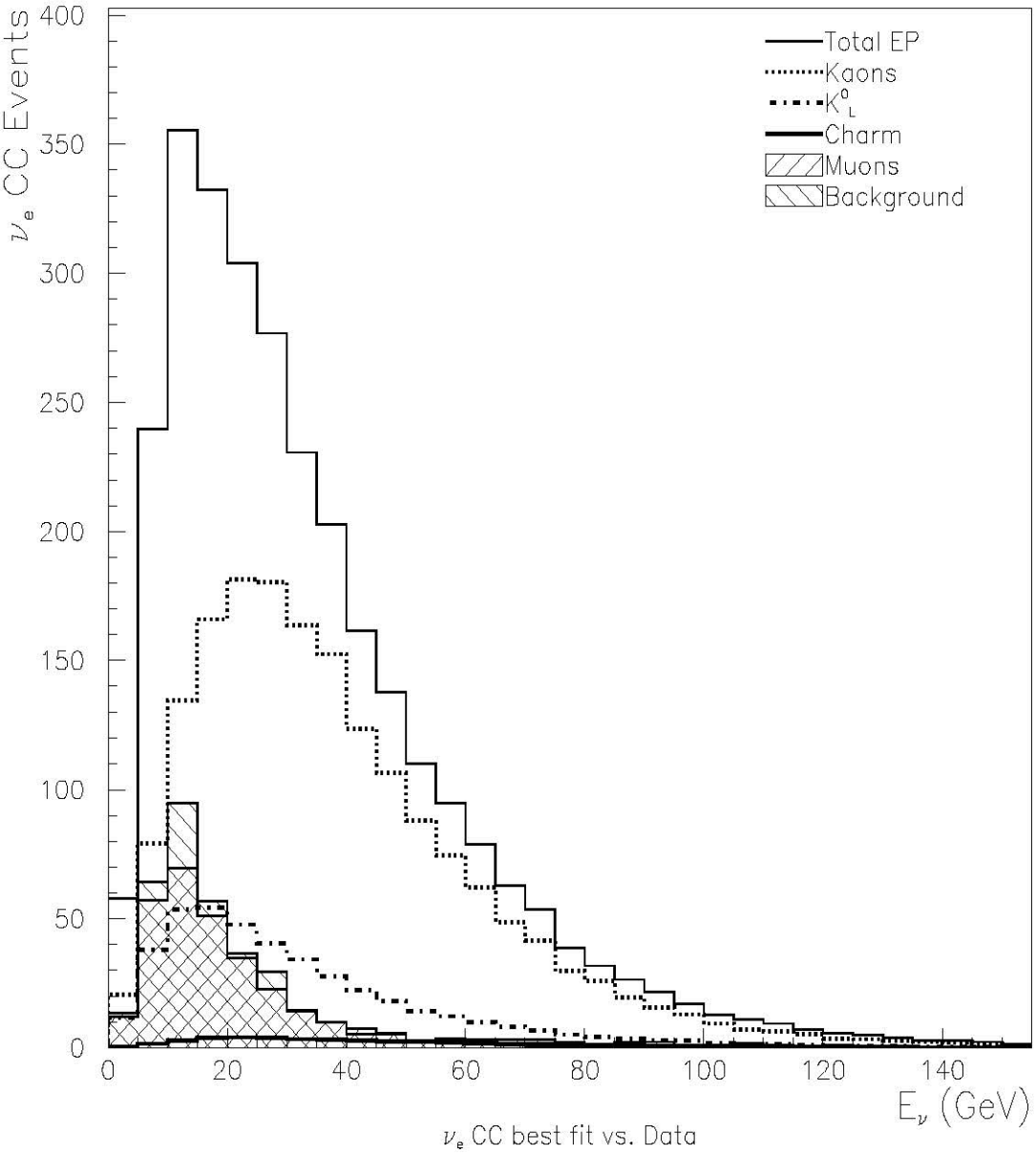

Figure 6.19: The empirical parametrisation prediction of ν_e also displaying the neutrino parents, on a linear scale.

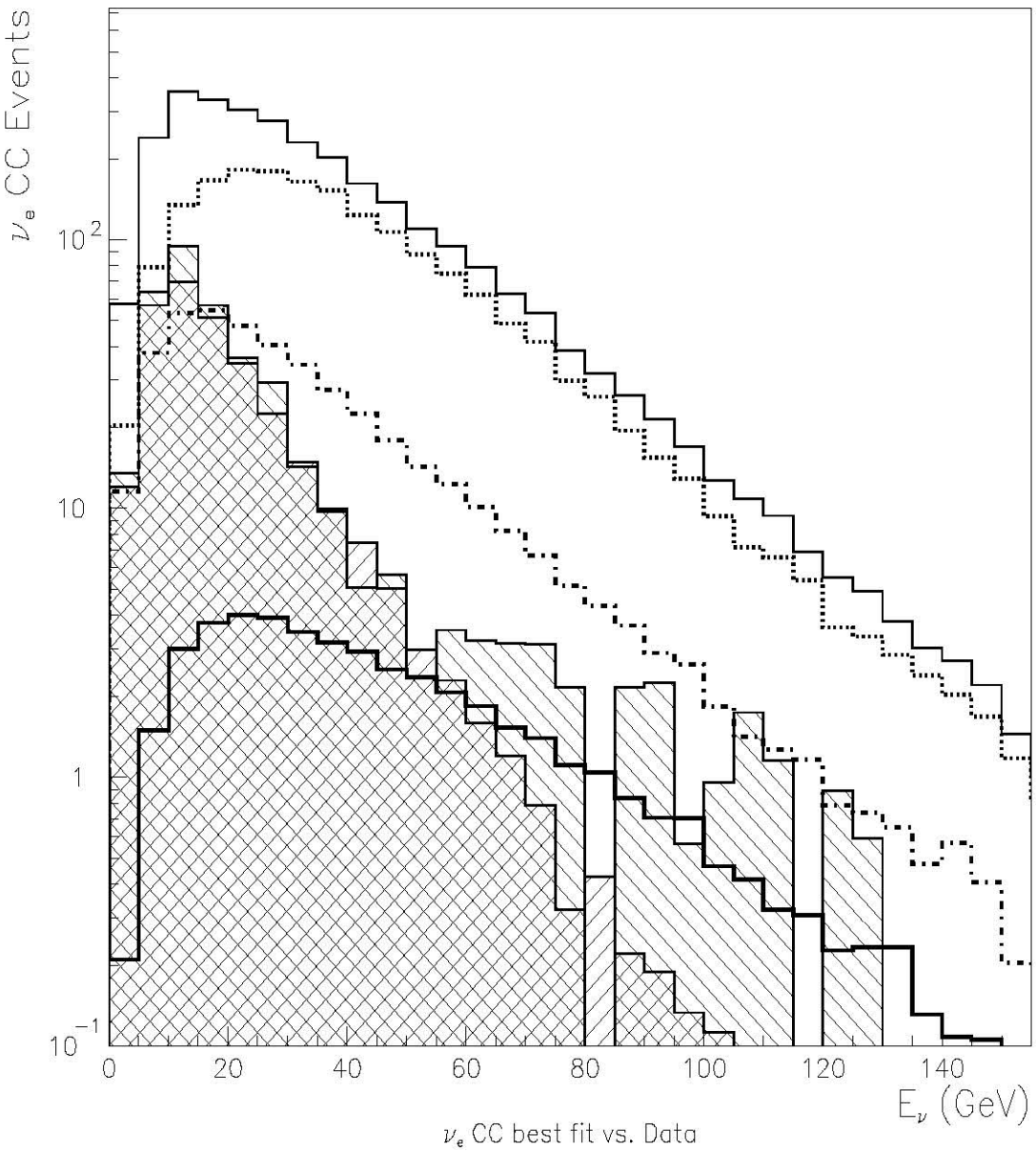

Figure 6.20: The empirical parametrisation prediction of ν_e also displaying the neutrino parents, on a logarithmic scale.

Chapter 7

Oscillation Search

The analysis of the event selection, the improvements to the standard beam simulation, and the generation of an empirical parametrisation of the beam are now combined into the search for an oscillation signal. Firstly though, the selection of the beam simulation and the estimation of the systematic errors of the beam simulator and the event selection must be completed. Then the statistical approach used for the oscillation search is described before the presentation of the final result of the oscillation signal obtained from the NOMAD data.

7.1 Discussion of Beam Simulators

The choice of beam simulator must be made *before* commencing the oscillation search. The decision is drawn from how well, and with what errors, NUBEAM with FLUKA and SPY weighting, (referred to just as NUBEAM below), and the empirical parametrisation predict the ν_μ, $\overline{\nu}_\mu$ and $\overline{\nu}_e$ data. As will be made clear when discussing the features of a blind analysis in section 7.2.1, the ν_e data cannot be used in deciding which simulation to use, since this might cause a bias in the results of the oscillation search, according to the prior beliefs of the experimenter. Moreover, the oscillation signal cannot be generated twice, with NUBEAM, and the parametrisation, as then the choice of which to accept would be biased by knowing the final result. The comparisons of the beam simulators and the allowed data is now presented.

7.1.1 Empirical Parametrisations

The empirical parametrisation developed in chapter 6, (henceforth referred to as the independent parametrisation), was initially proposed as a cross check of a much more detailed study already being conducted by S.R. Mishra. Whilst the independent parametrisation was taken to fruition, with good fits to the neutrino and SPY data, and predicting a ν_e flux, the parametrisation from the more rigorous study of S.R. Mishra, (henceforth referred to as the official parametrisation), is favoured for this analysis due to the following reasons:

- It is the product of many passes of the minimising processes described in section 6.3.9.
- It has better fits to the SPY data and the high energy neutrino tail.
- It has had more cross checks made of it, to all available neutrino data, relevant theory and other beam simulators.
- A study has been made of its systematic errors, as will be expanded on in section 7.1.4.

As the independent parametrisation is determined from a fit to the data of this analysis, the comparisons of it to the data will be superior to those of the official parametrisation. The official parametrisation is based on fits to data obtained in the analysis of S.R. Mishra, however these data samples are quite similar to those of this analysis. Having slightly worse fits is however outweighed by the above reasons. It is still very important though to compare the predictions of the two parametrisations. Figure 7.1 plots their predictions of the number of low ν, ($\nu < 5$ GeV, see section 5.5.2) ν_μ CC events. In the ratio plot, the variable binning of the oscillation analysis, section 7.2.2, is used. The two agree well. At high energies, the two start to slightly diverge. This is suspected to be due to a small difference in the hadronic energy scales being used by the separate analyses, see section 4.5. However, one of the purposes of this thesis is to investigate the LSND result, and if the LSND oscillation parameters are correct, section 1.5.3, then the oscillation signal will appear in the low energy part of the spectrum, so disagreement at high energies would not be important. The graph shows the reproducibility of the ν_μ fitting process and the empirical parametrisation ideology.

Figure 7.2 shows the predicted ratio of ν_e/ν_μ events as determined by the independent parametrisation divided by the official parametrisation. The plot shows the excellent agreement between the two parametrisations in predicting ν_e/ν_μ, which as explained below, is the value compared to data to

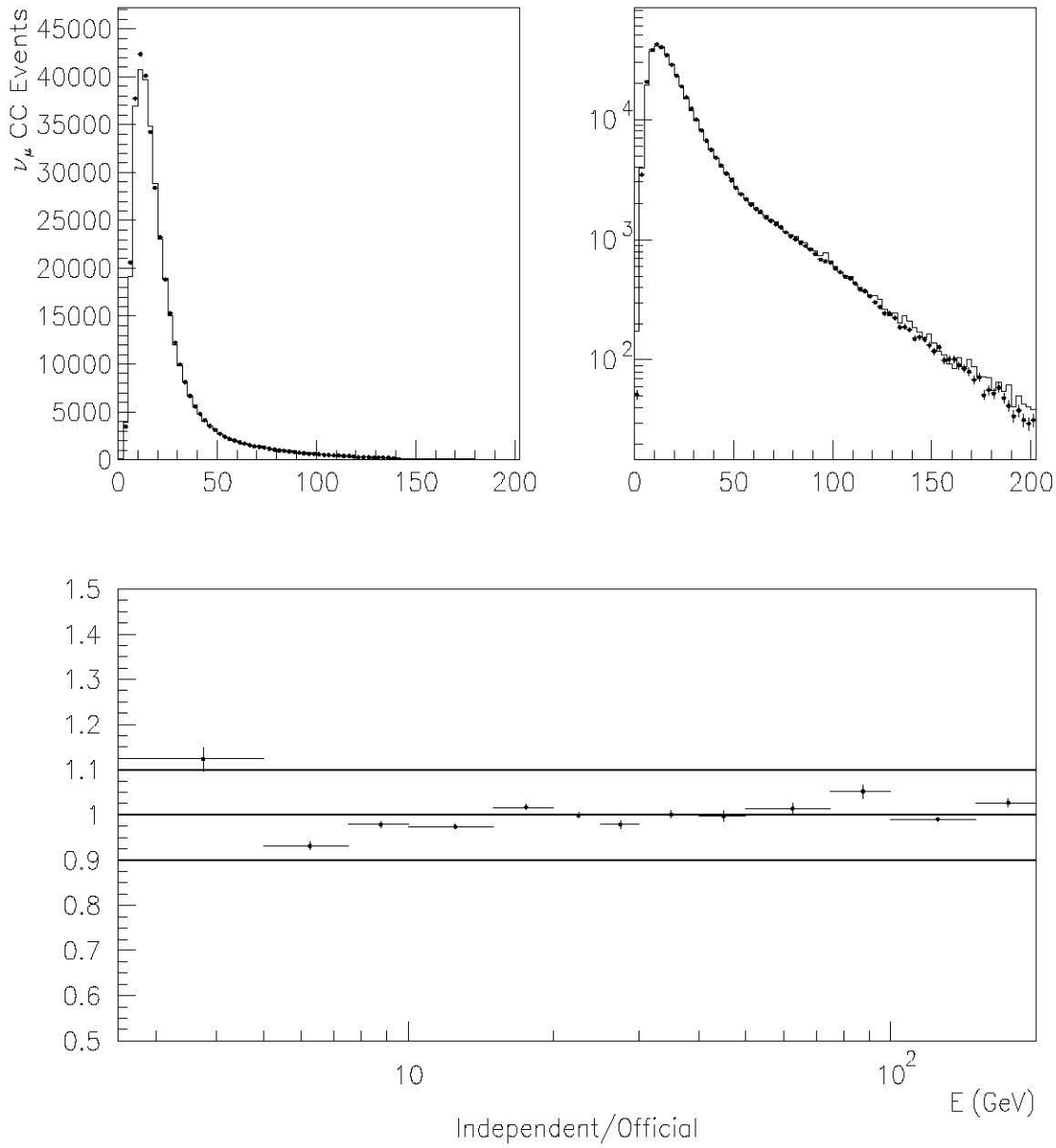

Figure 7.1: Predictions of the number of ν_μ CC low ν events in data from the independent (histogram) and official (points) parametrisation. Linear and logarithmic scales are used, along with the ratio of the independent over the official parametrisation.

extract the oscillation signal. Recall that the ν_e/ν_μ prediction is determined from target production distributions garnered from fits to the ν_μ, $\overline{\nu}_\mu$ and $\overline{\nu}_e$ data. There are potentially many sources of divergence yet the two separate parametrisations agree to within 1 to 2%, a considerable achievement.

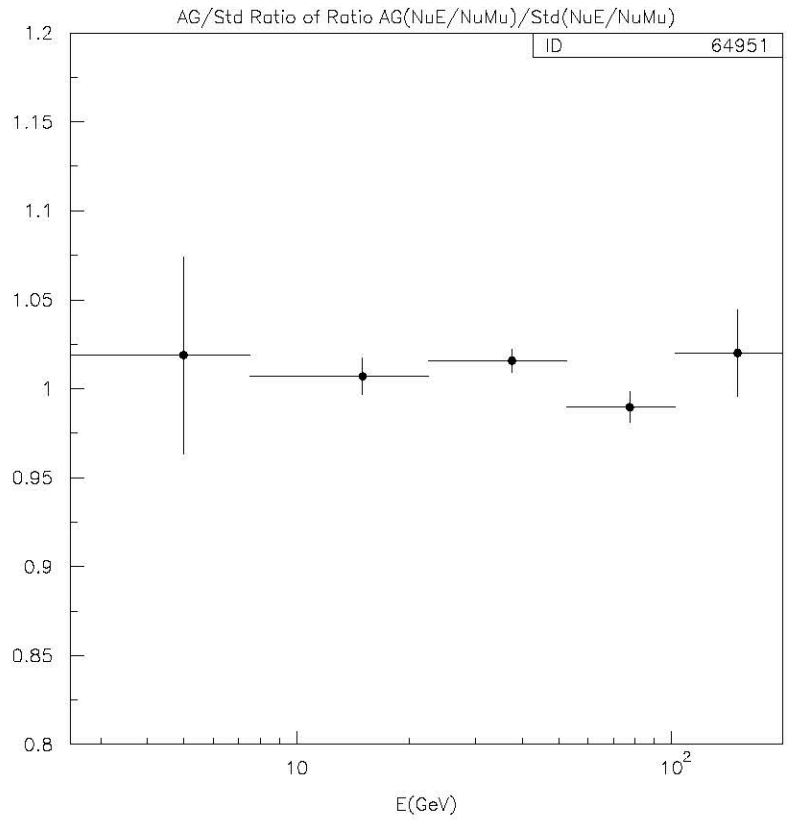

Figure 7.2: Ratio of independent over official parametrisation prediction of the ν_e/ν_μ ratio at low ν. The figure was produced by S.R Mishra.

It is also worth comparing the contributions to the four neutrino spectra from the fitted parents. These can illustrate if the neutrino spectra shown in the figures are in agreement because the correct parent distributions are produced by both parametrisations. The comparison of these contributions is especially important for the ν_e as its prediction can not be checked against data. The breakdown of the neutrino parents is given in table 7.1. The ν_μ and $\overline{\nu}_\mu$ kaon and pion parents are in fair agreement, the minor parents being of only secondary importance. For the ν_e and $\overline{\nu}_e$ all the parents to agree fairly well between the two parametrisations.

	ν_μ	$\overline{\nu}_\mu$	$\overline{\nu}_e$	ν_e
Pions: Independent	87.4	84.9	-	-
Official	87.2	80.4	-	-
Kaons: Independent	12.5	12.3	14.2	69.8
Official	12.7	14.5	18.4	68.1
Muons: Independent	NI	2.73	1.15	11.5
Official	0.001	1.60	1.83	12.3
K_L^0: Independent	NI	NI	76.1	16.8
Official	0.1	2.89	71.9	17.6
Charm: Independent	NI	NI	8.53	1.76
Official	0.002	0.55	8.43	1.9

Table 7.1: The breakdown of the neutrinos in terms of their parents. The number quoted is the percentage contribution of the parent. Where parents have not been included in the fitting procedure of an analysis, NI is placed.

The similarities in the comparisons of parent contributions and the excellent agreement of the ν_μ and ν_e spectra add much weight to the case for using an empirical parametrisation. The official parametrisation has been shown to agree with the independent parametrisation, and as it is fully developed, in terms of iterations and systematic studies, it shall be adopted over the independent parametrisation for this analysis. The official parametrisation will now be compared to the neutrino data.

7.1.2 Official Parametrisation Compared to Data

In the previous section, the official parametrisation was shown to compare well to the independent parametrisation. As this is known to agree well with the low ν data, see section 6.4, the official parametrisation now need only be compared to high ν ($\nu > 5$ GeV) data. The comparison will be made graphically in this section, integral numbers from the prediction are presented in table 7.2 of the following section, along with those of data and NUBEAM.

The ν_μ data and prediction are given in figure 7.3. The figure shows the data is well predicted by the official parametrisation in spite of it being fitted to low ν data. The agreement is particularly good below 200 GeV, although it begins to diverge at higher energies, which recall are not relevant to the oscillation search.

The predicted and measured $\overline{\nu}_\mu$ spectra are given in figure 7.4. This

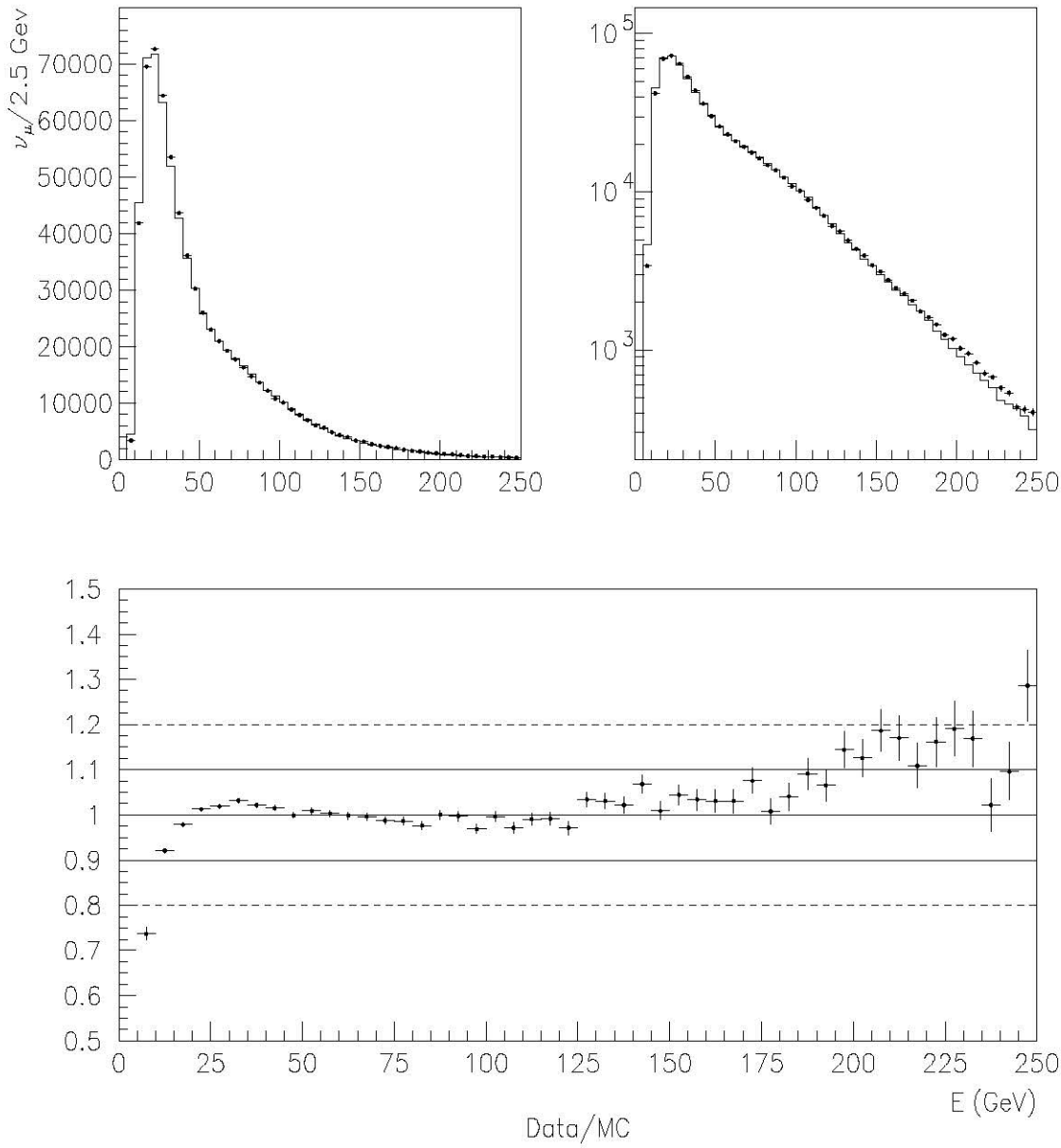

Figure 7.3: The ν_μ energy spectra obtained from high ν data (points) and the prediction (histogram) of the official parametrisation. Linear and logarithmic scales are used, and a plot of the ratio of data to prediction is included.

graphs shows some scatter, but the overall level of predicted $\overline{\nu}_\mu$ agrees with the data.

Figure 7.5 plots the $\overline{\nu}_e$ prediction against data. The prediction agrees reasonably well with the data, certainly better than the prediction of NUBEAM presented in figure 5.18.

Overall, the official parametrisation well reproduces the high ν neutrino data even though it was produced from a fit to the low ν data. Whilst the prediction of the $\overline{\nu}_\mu$ is slightly worse than that obtained with NUBEAM, the $\overline{\nu}_e$ prediction is much better. Combined with the agreement vicariously shown to the low ν data in the preceding section, the official parametrisation is placed as the preferred beam simulator. It is however useful to compare the official parametrisation to NUBEAM to ensure that there are no drastic discrepancies that might point to a fault in either of the two.

7.1.3 Official Parametrisation Compared to NUBEAM

Although it is not necessary for the official parametrisation to agree with NUBEAM as much as data, it is important that there are no regions of large disagreement. Whilst the empirical parametrisation can still fit the data despite misrepresentations of the beamline geometry in NUBEAM, most of these have been removed so the two should now be in good agreement, unless there are further problems with NUBEAM, or the parametrisation. Figure 7.6 displays the distribution of ν_μ CC high ν events predicted by NUBEAM with FLUKA 98 and SPY C5.1, and by the official parametrisation. The ratio shows differences below 5% until 130 GeV, indicating that the two beam simulators have converged quite well.

The comparison of predicted $\overline{\nu}_\mu$ spectra appears in figure 7.7. The background plotted is that weighted by the official parametrisation, however the background determined by NUBEAM is included in its $\overline{\nu}_\mu$ prediction. There are no significant differences between the background samples weighted by the official parametrisation and NUBEAM. This also applies to the ν_e and $\overline{\nu}_e$ background. As expected from figure 7.8, showing the ratio of the parametrisation and the data, NUBEAM and the parametrisation do not agree as well as they do in ν_μ.

The NUBEAM prediction of the $\overline{\nu}_e$ spectrum is systematically lower than that from the parametrisation, figure 7.8. This is to be expected as NUBEAM was earlier shown to underestimate the data, figure 5.18, whilst figure 7.5 shows the parametrisation to be in fair agreement with the data. However the shape of the $\overline{\nu}_e$ spectrum from the two simulators is quite similar.

These results are summarised numerically in table 7.2, which displays the integral number of predicted and measured ν_μ, $\overline{\nu}_\mu$ and $\overline{\nu}_e$ CC high ν events.

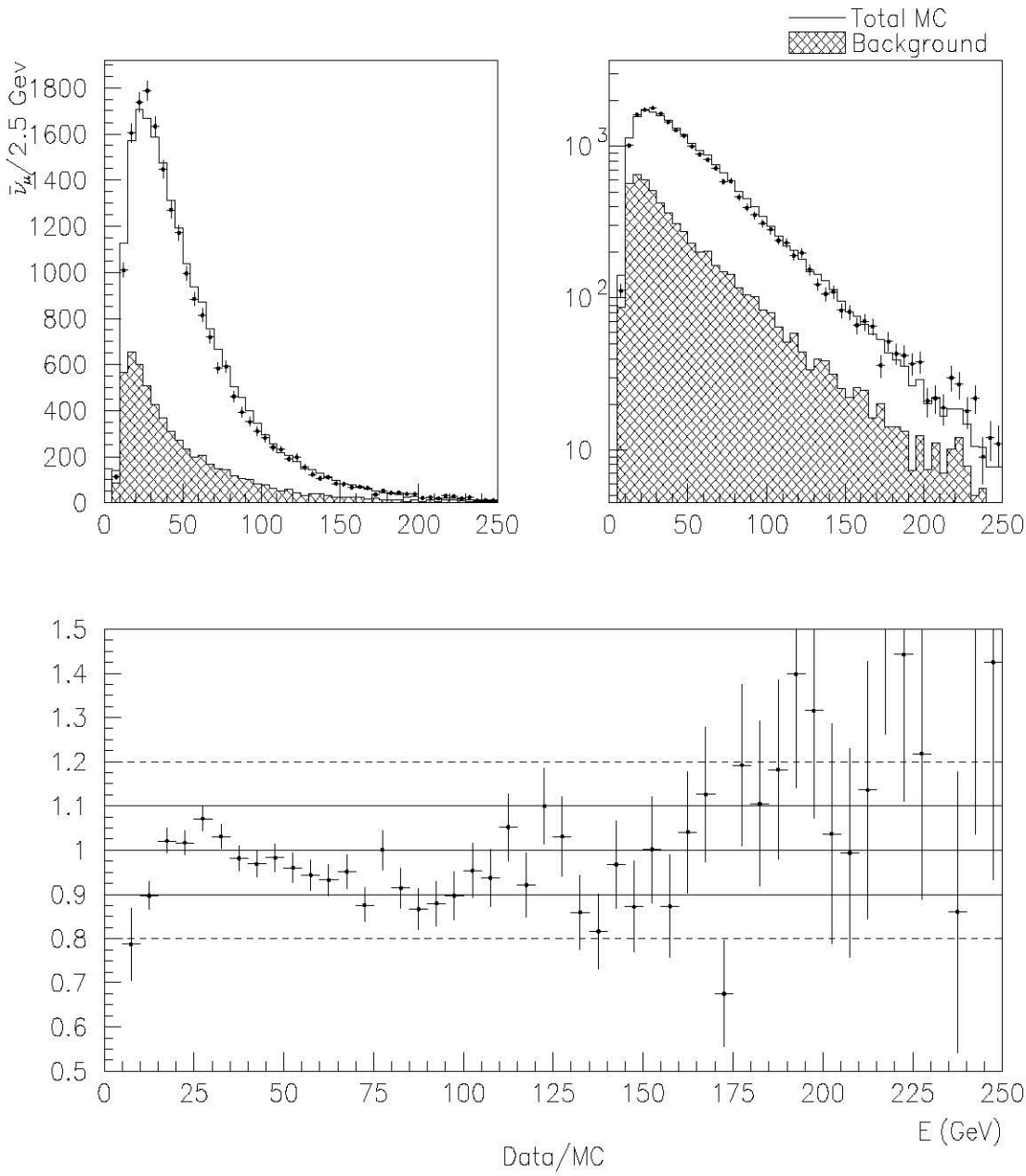

Figure 7.4: The $\overline{\nu}_\mu$ energy spectra obtained from high ν data (points) and the prediction (histogram) of the official parametrisation. Linear and logarithmic scales are used, and a plot of the ratio of data to prediction is included. The prediction includes the background from ν_μ NC and CC, which is also plotted separately (hatched).

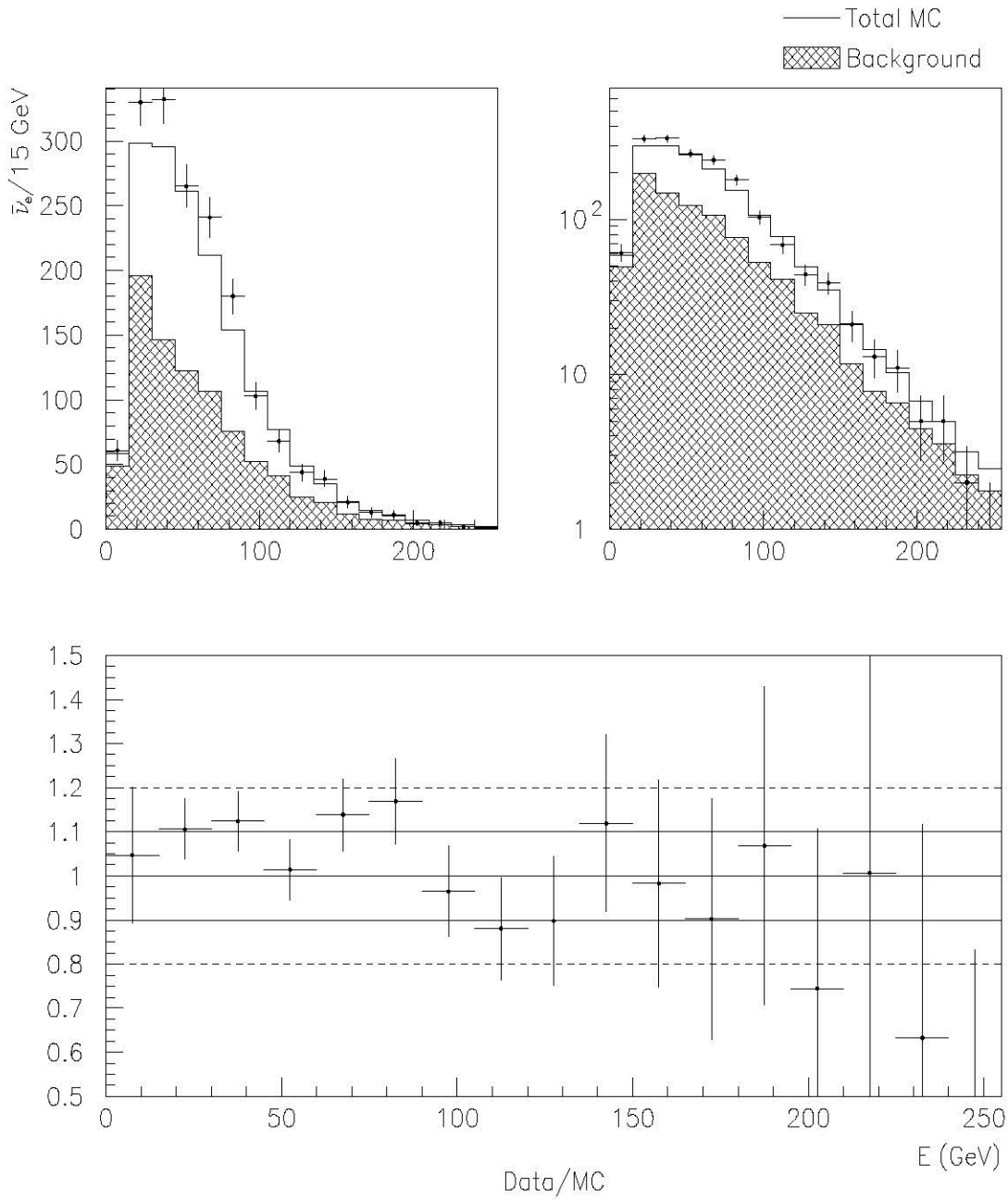

Figure 7.5: The $\overline{\nu}_e$ energy spectra obtained from high ν data (points) and the prediction (histogram) of the official parametrisation. Linear and logarithmic scales are used, and a plot of the ratio of data to prediction is included. The prediction includes the background from ν_μ NC and CC, which is also plotted separately (hatched).

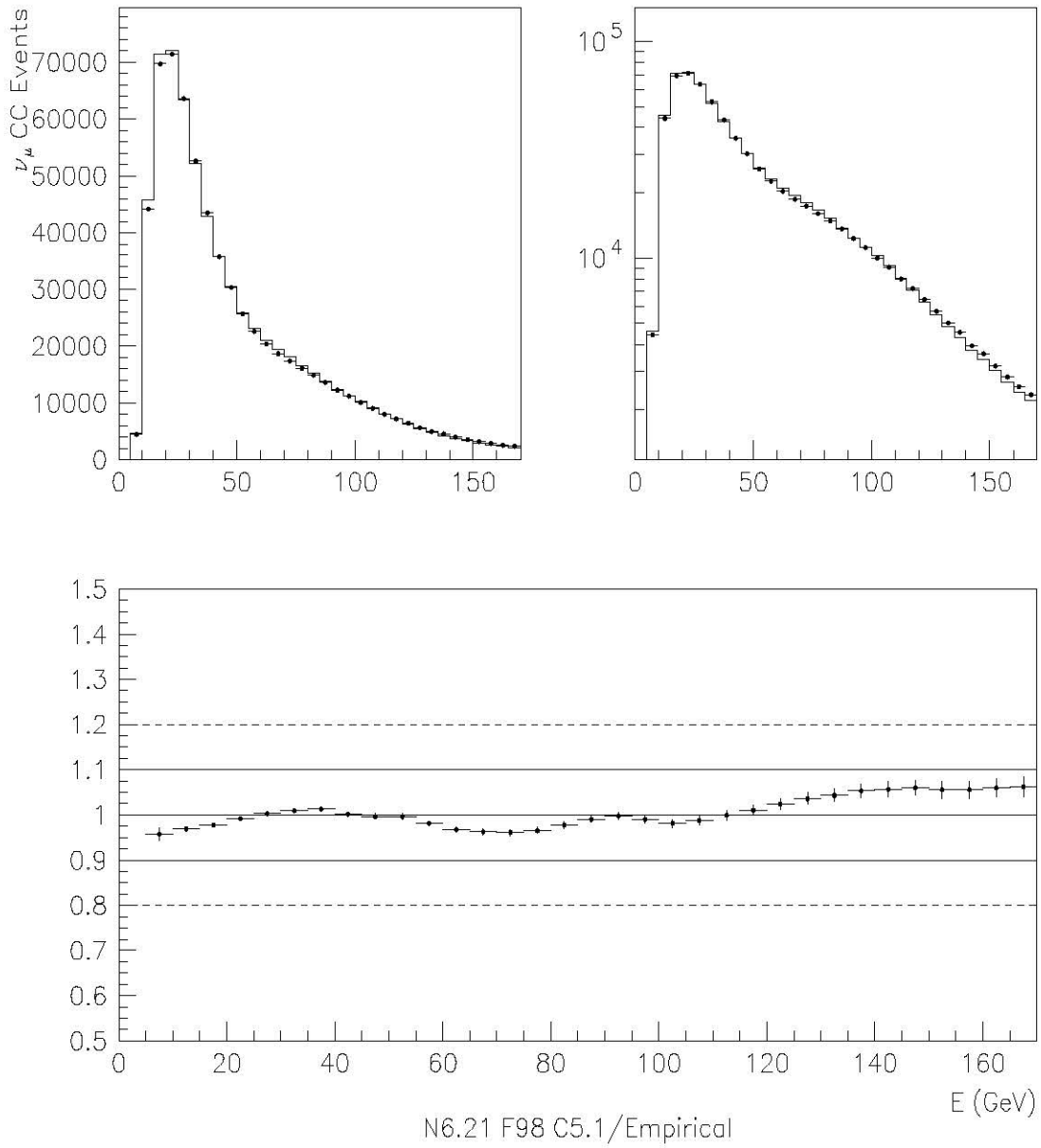

Figure 7.6: Predictions of the number of ν_μ CC events in high ν data from NUBEAM (points) and the official parametrisation (histogram). Linear and logarithmic scales are used, along with the ratio of NUBEAM over the official parametrisation.

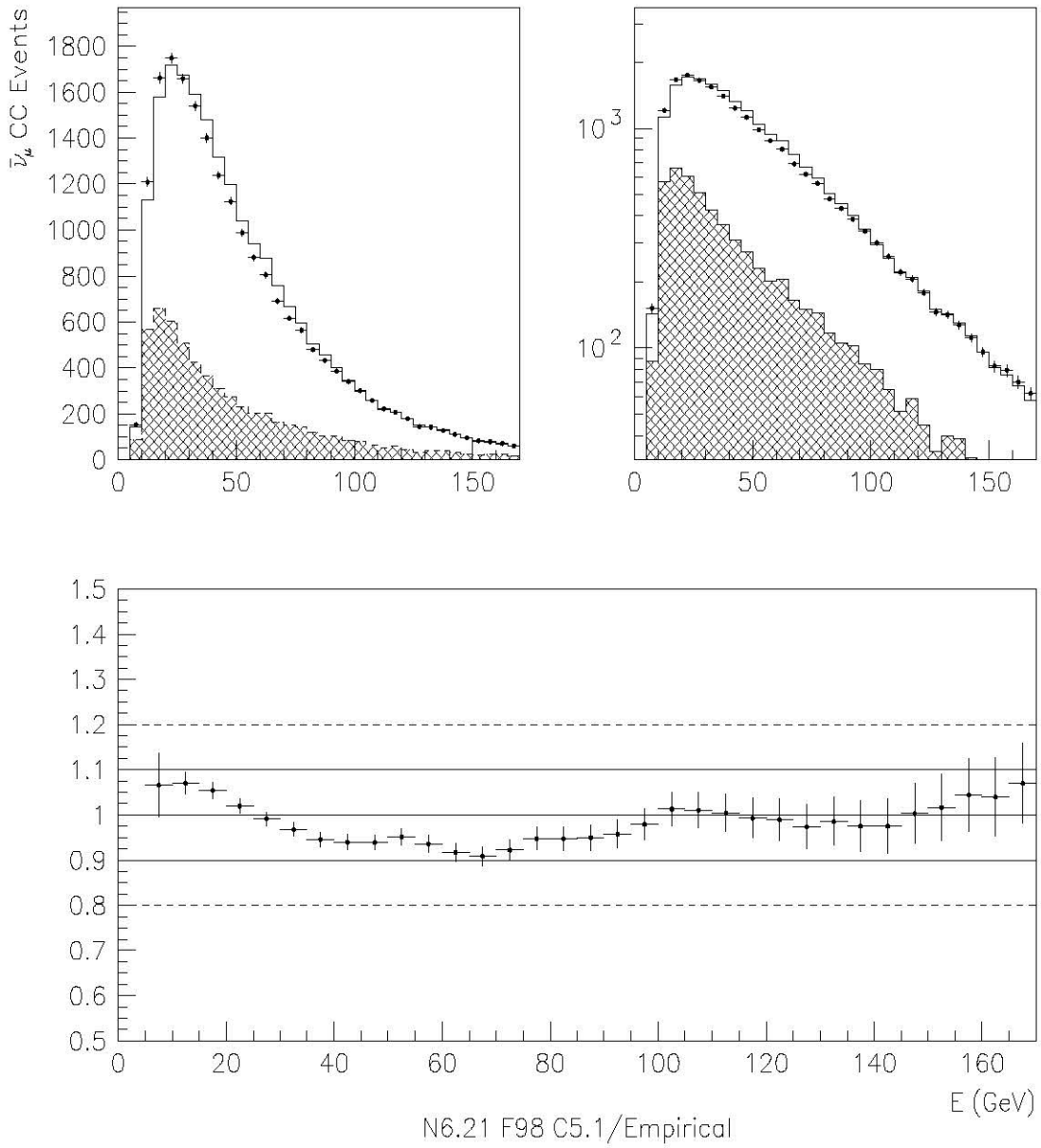

Figure 7.7: Predictions of the number of $\overline{\nu}_\mu$ CC events in high ν data from NUBEAM (points) and the official parametrisation (histogram). Linear and logarithmic scales are used, along with the ratio of NUBEAM over the official parametrisation. The background (hatched) from ν_μ NC and CC is plotted.

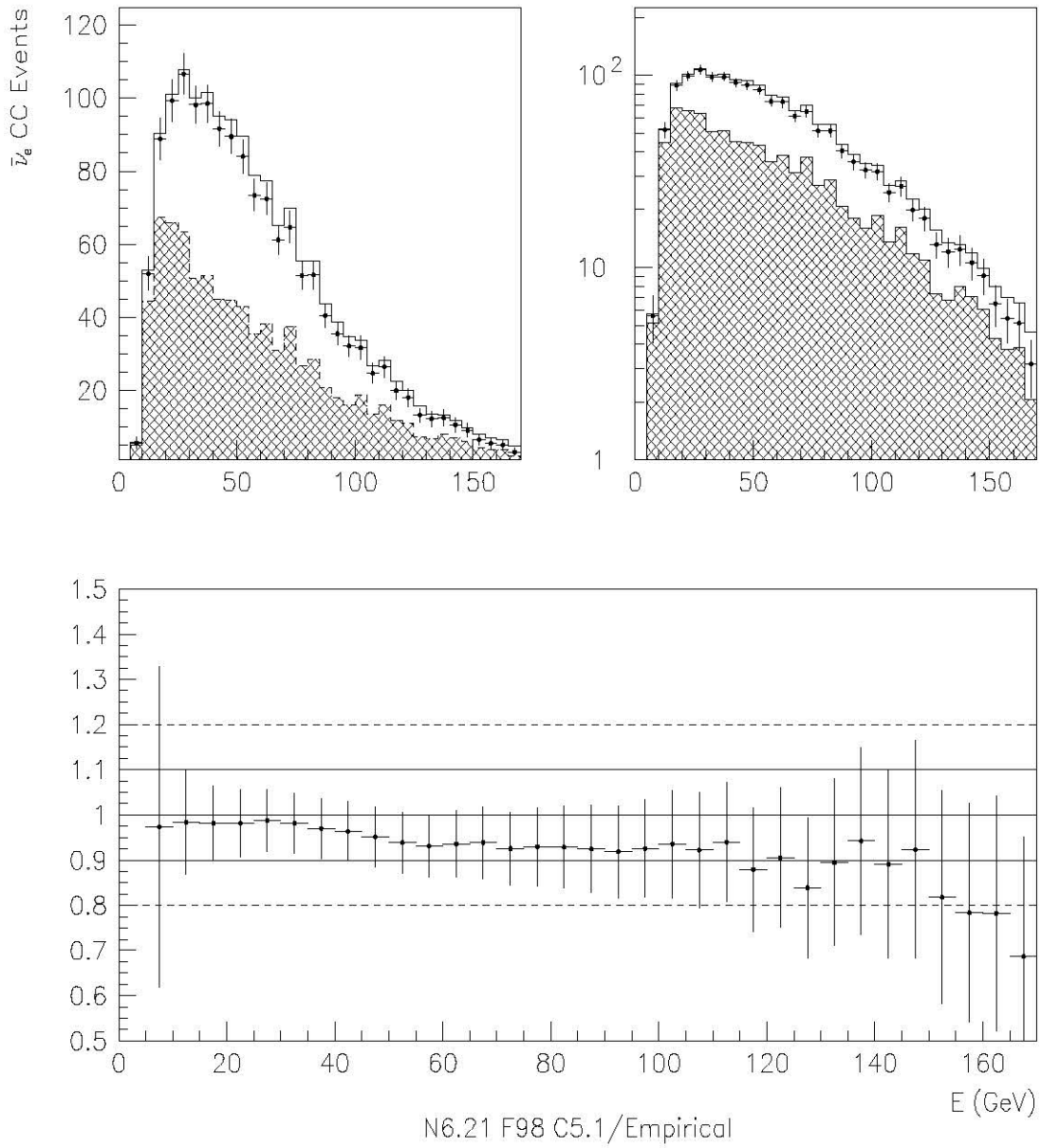

Figure 7.8: Predictions of the number of $\overline{\nu}_e$ CC events in high ν data from NUBEAM (points) and the official parametrisation (histogram). Linear and logarithmic scales are used, along with the ratio of NUBEAM over the official parametrisation. The background (hatched) from ν_μ NC and CC is plotted.

Recall that the data and Monte Carlo are normalised to the integral number of ν_μ. For NUBEAM, the other neutrino types are normalised according to table 5.5. The official parametrisation normalises $\overline{\nu}_\mu/\nu_\mu$ at 0.025, ν_e/ν_μ at 0.0152 and $\overline{\nu}_e/\nu_\mu$ at 0.001699, with similarly small statistical errors as NUBEAM. The number of $\overline{\nu}_\mu$ events agrees well between data and the two simulators, including the background level, as mentioned earlier. However as was apparent in the graphs, the $\overline{\nu}_e$ is underestimated by NUBEAM, far more than by the parametrisation.

		NUBEAM			Official Parametrisation		
	Data	MC+BKGD	MC	BKGD	MC+BKGD	MC	BKGD
ν_μ	681714	681713	681713	-	681713	681713	-
$\overline{\nu}_\mu$	20386	20488	14392	6096	20838	14810	6028
$\overline{\nu}_e$	1725	1531	638	893	1613	737	876

Table 7.2: Comparison of the number of high ν CC events in data with the predictions of NUBEAM and the official parametrisation.

The comparisons between the ν_e prediction of NUBEAM and the parametrisation is again of greatest interest as a further cross check to recover from not being allowed to compare to the ν_e data. This is presented in figure 7.9 which shows little difference between the two predictions, adding a great deal of weight to the reliability of both simulators. Also shown is the predicted ratio of ν_e/ν_μ of the two simulators, figure 7.10. Again this plot is in the energy binning that will be used to analyse the data for the oscillation signal, section 7.2. The agreement is within the errors of the ν_e statistics.

The agreement here means that the simulation of the NOMAD neutrino beam has converged sufficiently. Reliable and reproducible predictions of the ν_e spectrum relative to ν_μ are being produced. Thus it is now possible to begin the oscillation analysis.

7.1.4 Official Parametrisation Systematics

Before the official parametrisation can be included in any analysis, its systematic errors must be understood. To estimate the size of the systematics in the empirical parametrisation process a number of complete parametrisation processes were run to produce new ν_e/ν_μ spectra to be compared. These investigations were presented in Mishra (2000b), and feature adjustments made to the *official* parametrisation, (the independent parametrisation actually forms part of these systematic error calculations).

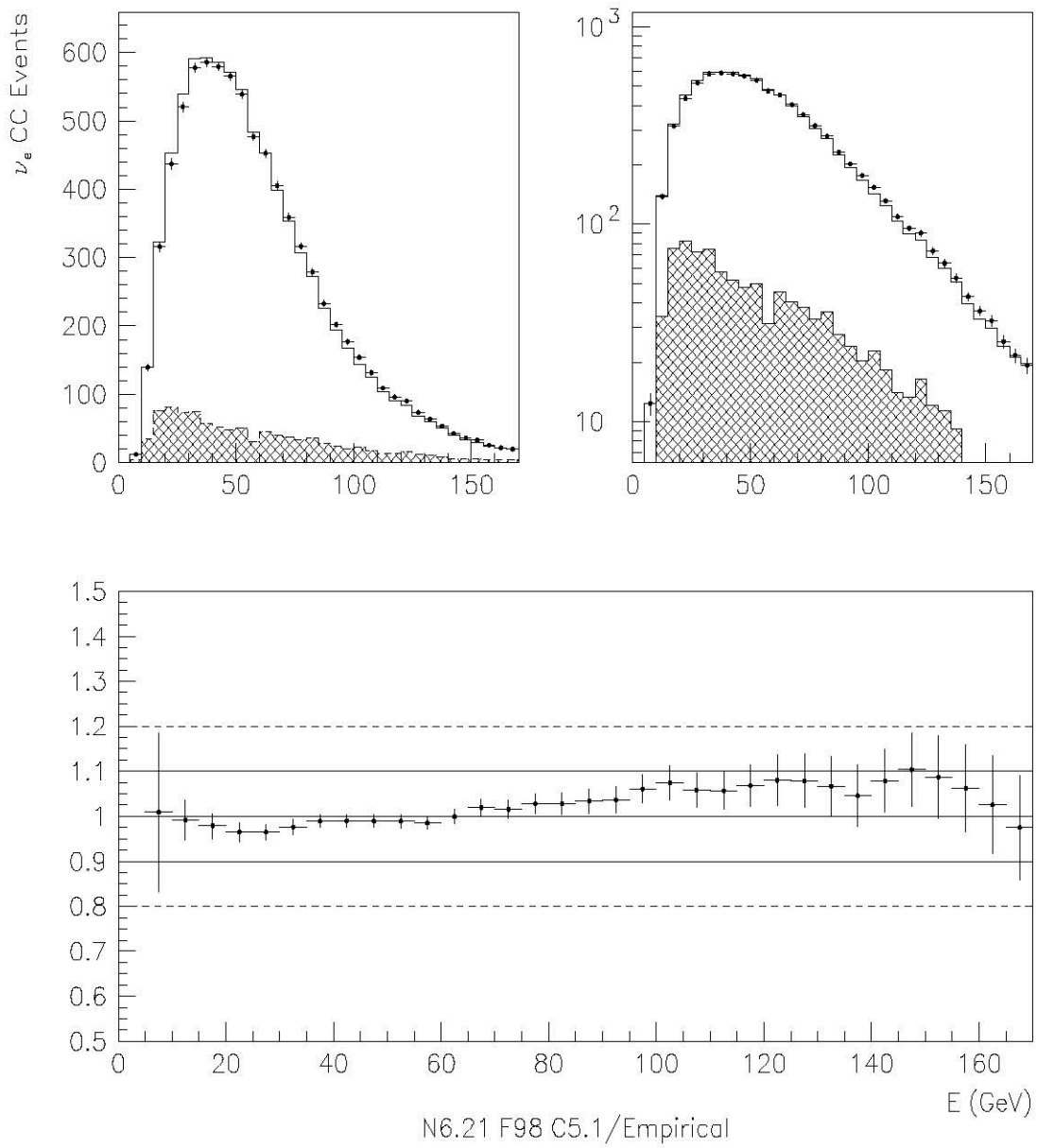

Figure 7.9: Predictions of the number of ν_e CC high ν events in data from NUBEAM (points) and the official parametrisation (histogram). Linear and logarithmic scales are used, along with the ratio of NUBEAM over the official parametrisation. The background (hatched) from ν_μ NC and CC is plotted.

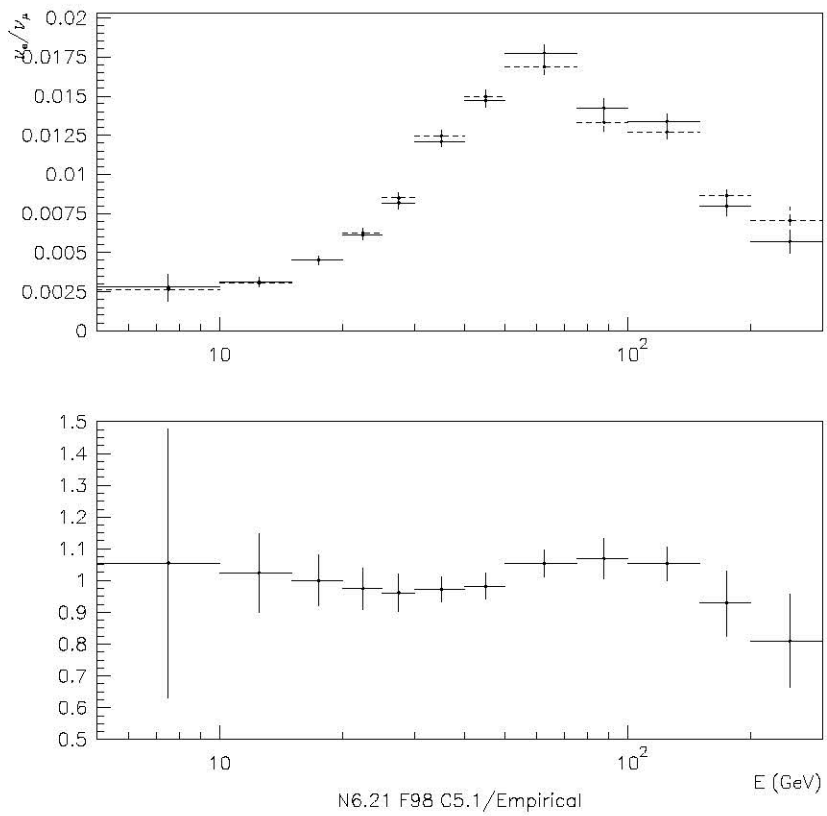

Figure 7.10: Comparison of the ν_e/ν_μ ratio as predicted by NUBEAM (solid) and the official parametrisation (dotted). Also shown is the ratio of the two.

The first set of additional parametrisations were based on fits from altered NUBEAM geometries, similar to those used in the NUBEAM systematic study of section 5.7. The empirical parametrisation is still able to fit to the data, despite the effects on the neutrino spectra brought about by the changes in the NUBEAM geometry. As such, the difference between these parametrisations and the standard parametrisation was less than 1%, a remarkable improvement on the systematic errors of NUBEAM which were of the order of 4.5-8%. These studies also included repeating the parametrisation, originally performed with NUBEAM 6.10, with version 6.21, (the differences in these versions are described in chapter 5). Again the empirical parametrisation showed negligible variation.

Whilst insensitive to any errors in the NUBEAM geometry, the empirical parametrisation potentially introduces systematic effects of its own. These include those from the functional form of the parametrisation, the use of the SPY data and the reproducibility of the method. The first two points were addressed by more sets of parametrisations, covered below. The most important point however is the last one, and this was the task of the independent parametrisation of this thesis. Figure 7.2 clearly showed that the two separate parametrisations, that were fitted to roughly similar data sets but with their own unique programmes, agree very well. As was already stated, this is a remarkable achievement considering the degree of isolation in the generation of the two parametrisations. The independent parametrisation of the last chapter has been an extremely critical check on the empirical parametrisation method and its use in the oscillation analysis.

To answer any concerns over the inclusion of the SPY data, the fit was reperformed without SPY, with the SPY K/π values inflated by 5% and with the SPY 20, 30 and 40 GeV points being removed.

The functional form of the parametrisation was also changed. One parametrisation was no longer factorisable into x_F and p_T terms and another parametrisation was different again, and had just 8 parameters for the kaons. Not every form imaginable can fit the neutrino and SPY data, other forms were tried for the systematic studies, but the fits did not converge, showing there is physics understanding necessary in selecting a functional form.

The differences in the ν_e/ν_μ spectrum observed between the standard parametrisation and these sets of alternative parametrisations, including the independent parametrisation, showed a level of change less than 1.5%. This is used as the overall normalising error of the official parametrisation. A systematic error must also be included on the ν_e flux prediction from each of its parents. The errors on K^+ and μ^+ are found by looking at their variation in the different parametrisations. These variations are less than 2.5%. As 80% of the ν_e are from K^+ and μ^+, table 7.1, the contribution to the ν_e flux error is 2%. Charm is not fitted by the parametrisations, as explained in chapter 6, and its contribution to the ν_e flux error arises from uncertainties in cross sections and its normalisation. This error has been estimated at 15%, to be scaled by 2.93%, the fraction of ν_e from charm meson decays. Finally there is an error from the K_L^0, which are normalised with the $\overline{\nu}_e$ data and use the data of Skubic et al. (1978) to determine the shape of the spectrum. Considering the data of Skubic et al. and the variations in normalisations with the parametrisations, the K_L^0 are estimated to have a 15% error. They additionally contribute to the error on the ν_e/ν_μ spectrum, at an estimated 5%. Both these errors are scaled by 16.8%, the K_L^0 contribution to total ν_e flux.

Both the errors on the ν_e/ν_μ spectrum, and the ν_e flux from the different sources are combined in quadrature. This gives the error on ν_e/ν_μ as 1.72%, and the error on ν_e as 3.25%.

7.1.5 Benefits of the Empirical Parametrisation

The empirical parametrisation has been put through a large number of cross checks in this section and passed. It has been compared to data, to the independent parametrisation of the previous chapter and to NUBEAM. The agreement found has strengthened the reliability of its predictions. The empirical parametrisation, through the systematic error study of Mishra (2000b) is also seen to be a stable prediction, not affected by changes in the NUBEAM geometry or alterations of the functional form of the parametrisation. These key traits indicate that the empirical parametrisation is the preferred prediction to be used in the oscillation analysis.

7.2 Theory of Small Signal Searches

The NOMAD $\nu_\mu \rightsquigarrow \nu_e$ search *is* a small signal search as it is trying to ascertain the number of ν_e oscillated from ν_μ. This is achieved using the double ratio of expected to measured ν_e over ν_μ energy spectra. Care must obviously be taken when searching for a small signal. The systematics of the experiment must be well understood and a sound method for extracting the signal must also be put in place. It is hard to trust results with only small deviations from expectation. Two or three sigma effects are often not considered exciting. To combat this a blind analysis can be used to instil faith in the result. Further, a new statistical approach to setting limits and confidence regions on small signals has been developed to ensure the result quoted better represents the measurement made. These techniques will now be described in application to NOMAD.

7.2.1 Blind Analysis and Consequences

The essence of a blind analysis is that the signal region is not "opened" until the rest of the analysis has been completed. Then information from the signal region is included and the final result generated, "opening the box". This result then stands, and no adjustments can be made to it. The strength of this analysis technique is that it removes any bias the experimenter may have towards the outcome of the measurement. If the result of the experiment is

unknown until the analysis is complete, then the experimenter cannot change the analysis to obtain an answer closer to prior expectations.

It is the policy of NOMAD to be blind in all its oscillation analyses. In the $\nu_\mu \rightsquigarrow \nu_e$ search, the signal region is the ν_e data. Thus no ν_e data versus Monte Carlo energy spectra can be plotted as referred to earlier. All the other data is open for analysis though, and as such, these have been used in the previous chapter to understand the beam. Agreement has been reached between the beam prediction and the ν_μ, $\overline{\nu}_\mu$ and $\overline{\nu}_e$ data. Further, the systematic study above has showed the resilience to changes in these predictions.

The consequence of the NOMAD policy is that no-one can present an analysis without permission. There has yet to be an official NOMAD presentation for the $\nu_\mu \rightsquigarrow \nu_e$ search on the entire 1995 to 1998 data. Therefore, in accordance with NOMAD protocol, this analysis will only include the 1995 data, which was previously used in the presentation of DeSanto (1997). The NOMAD analysis is being completed now but there is yet no date set for a box opening of the rest of the data. The finalising of the NOMAD analysis is out of the author's control. Currently, the collaboration is waiting on the refinement of systematic errors of NUBEAM for the latest version. These are not needed for this analysis as it will use the empirical parametrisation as the beam prediction, (one of the goals of this thesis is to show how well the empirical parametrisation can predict the data). Further, the use of the empirical parametrisation is a major difference between this work and the analysis of DeSanto (1997).

There is no additional work required to expand the results of this thesis with the 1995 data to include the rest of the data. More importantly, the work conducted as part of this thesis, both in checking NUBEAM and developing an independent parametrisation, forms part of the NOMAD official analysis. This might be voided however if the full data set is opened, and also prevent the author from working further in the NOMAD $\nu_\mu \rightsquigarrow \nu_e$ analysis.

7.2.2 Double Ratio and Analysis Binning

It is difficult to predict the ν_e flux absolutely as this would involve normalising all results to some external number like protons on target, which is itself an uncertain number. Thus it is determined relative to ν_μ. Also, use of the ratio of ν_e/ν_μ in the data reduces systematics common to electron and muon identification. Thus $R_{e\mu}$ is used in the oscillation search:

$$R_{e\mu} = \frac{N_{\nu_e}}{N_{\nu_\mu}} \tag{7.1}$$

$R_{e\mu}$ as measured in data is compared to the predicted $R_{e\mu}$ and hence the double ratio. The comparison is made in the variable energy bins defined in table 7.3. The data and prediction are further split into the radial bins defined in section 6.3.1, and two ν bins, with ν greater or less than 5 GeV, (recall that in data ν is taken as the hadronic energy). How the oscillation signal is determined from these comparisons is now explained.

Bin	1	2	3	4	5	6	7	8	9	10	11	12	13	14	15
Min	0.0	2.5	5.0	7.5	10	15	20	25	30	40	50	75	100	150	200
Max	2.5	5.0	7.5	10	15	20	25	30	40	50	75	100	150	200	300

Table 7.3: Energy binning for $R_{e\mu}$, (GeV).

7.2.3 Statistical Approach

The statistical approach will be the unified classical approach proposed in Feldman and Cousins (1998). This approach avoids difficulties suffered by previously used raster and global scan techniques in setting confidence regions and limits on small signals from a Poisson process with a background, (the situation in NOMAD). In particular the approach reduces any over coverage of the set limit, caused by proximity of the measurement to an unphysical region, (in NOMAD, this would be *fewer* events observed than expected).

The approach also recommends the citing of the sensitivity of the experiment. This is equivalent to the result obtained from an ensemble of identical experiments. The sensitivity can also be defined as the limit obtained if the measurement equals exactly the expected background. The sensitivity compared to the limit, then supplies a measure of the reliability of the results of an experiment.

A programme has been set up within NOMAD by G. Feldman and Y. Nefedov, with additional functions specific to the $\nu_\mu \rightsquigarrow \nu_e$ search programmed by D. Shih. It calculates the confidence region or limit, as well as the sensitivity of the analysis according to the approach of Feldman and Cousins (1998). Its routines are also used by a number of other neutrino oscillation experiments to determine senstivities and limits. It requires the following inputs, distributed in the above binning:

- Data: $R_{e\mu}$ from data.
- Errors: Energy dependent statistical and systematic errors on $R_{e\mu}$.

- Background: Predicted $R_{e\mu}$, (predicted ν_e and background divided by predicted ν_μ).
- Oscillation contribution to $R_{e\mu}$, section 7.2.4 below.

A limit is determined by comparing the signal in the data, to that from various simulations using a range of oscillation parameters, ($sin^2(2\theta)$ and Δm^2 as defined in section 1.4). These are given by the combination of the background, (prediction of $R_{e\mu}$ assuming no oscillations), and the oscillation contribution, defined below. Thus a set of oscillation parameters can be found that best fit the data, excluding parameters in unphysical regions, i.e. negative $sin^2(2\theta)$. A range of parameters can then be used to set the 90% confidence region around the best fit in accordance with the ordering system set out in in Feldman and Cousins (1998).

7.2.4 Oscillation Contribution

The contribution of oscillations to $R_{e\mu}$ is determined from the oscillation probability $P_{\nu_\mu \to \nu_e}$ as given in equation 1.25. Firstly though, the dependence of this probability on the distance L that the neutrino travels from creation to interaction must be integrated out:

$$P_{\nu_\mu \to \nu_e}(E_\nu, \Delta m^2, sin^2 2\Theta) = \frac{\int_{L_{min}}^{L_{max}} P_{\nu_\mu \to \nu_e} dL}{L_{max} - L_{min}} \tag{7.2}$$

where $L_{min} = 421$ m, the distance to NOMAD from the end of the decay tunnel, (the most upstream a neutrino can be produced), and $L_{max} = 831$ m, the distance from the target. After integration, the oscillation probability can be determined for any given set of (Δm^2, $sin^2(2\theta)$).

The oscillation contribution represents the number of ν_e expected from oscillations, given a probability and knowing the true number of ν_μ available to oscillate. The true number of ν_μ is simply the data sample, unfolded with the ν_μ selection efficiency. After applying the probability to the true number of ν_μ the selection efficiency of the ν_e must be applied, to ascertain the final number of ν_e expected in the data, given the oscillation parameters. Note that the correction to the ν_μ from those that oscillate is negligible. This procedure is summarised by:

$$\text{Oscillation contribution} = \frac{N_{\nu_\mu}^{data}}{\epsilon_\nu} \times P_{\nu_\mu \to \nu_e} \times \epsilon_{\nu_e} \tag{7.3}$$

The data, background (no oscillations) and oscillation contribution to $R_{e\mu}$ have all been fixed. It now remains to calculate the errors on $R_{e\mu}$ in order that the signal can be extracted.

7.3 Statistical Errors

NOMAD has collected large samples of neutrino data on which to base its oscillation searches. Further, as was seen in chapter 4, a large amount of Monte Carlo has been generated. As such, the $\nu_\mu \rightsquigarrow \nu_e$ search should not be statistically limited, even if just the 1995 data is used. Table 7.4 lists the approximate statistical error in the energy bins for each of the data and Monte Carlo samples used in the search. These values come from the combined radial bin, with both high and low ν. The table confirms that the statistics of the samples are good, however, there is a substantial error on the ν_e data and the ν_e background prediction which must be included as an error on $R_{e\mu}$.

Sample	Error (%)	Included
ν_μ Data	0.8	Yes
ν_μ Monte Carlo	0.2	No
ν_e Data	10.0	Yes
ν_e Monte Carlo	0.4	No
ν_e Background	5.0	Yes

Table 7.4: Percentage statistical errors for the data and Monte Carlo samples used in the oscillation search. Also tabulated is whether they are included or are negligible.

7.4 Systematic Errors

Recall that $R_{e\mu}$ is being used, rather than comparing the ν_e alone between the data and prediction, to reduce systematics. The effects that remain are discussed below. The systematics, including those of the official parametrisation are then summarised and combined.

7.4.1 Event Classification

The size of the systematic errors associated with the event classification of chapter 4 must be estimated. This is achieved by observing the variations

in the $R_{e\mu}$ when the event selection criteria (cuts) are changed. Specifically two new sets of cuts are formulated, with tighter and with looser restrictions on event selection than the standard set detailed in chapter 4.

The variations in the cuts are given in table 7.5. The definition and purpose of these cuts can be found in chapter 4. These cuts were chosen as they either had a large effect on the signal or the background, see table 4.7, could be affected by reconstruction effects, or as the value of the cut was chosen only from studies of Monte Carlo samples.

	Loose	Standard	Tight
TRDPiCon	0.006	0.005	0.004
$y_{Bj} <$	0.935	0.850	0.765
$\hat{\nu} >$	-0.825	-0.750	-0.675
Min Mass (GeV/c)	0.09	0.10	0.11
$\Delta Z <$ (cm)	10	15	30

Table 7.5: Cuts and their variations used in the systematic error studies.

When $R_{e\mu}$ is compared here, the number of events used is actually the unfolded number i.e. the number of events observed in the data, with background appropriately subtracted for the ν_e, scaled up by the selection efficiency. The observed and background samples from the three selection regimes are presented in table 7.6 for ν_μ and ν_e, together with the efficiencies. The ν_μ selection is shown to be very robust with respect to the above changes to the selection cuts. This is to be expected as the cuts are related more to the ν_e selection. The tight and loose cuts reduce and increase the ν_e signal and background as expected.

	ν_μ		ν_e		
	Observed	Efficiency	Observed	Background	Efficiency
Loose	1042682	0.793	13599	3415	0.539
Standard	1041950	0.793	12277	2678	0.518
Tight	1040878	0.793	10985	2110	0.471

Table 7.6: Event numbers and efficiencies used to calculate the unfolded number of ν_μ and ν_e events.

The unfolded number of events should remain unchanged given reasonable alterations to the selection criteria. The unfolded number of ν_μ and ν_e events in data, along with their ratio, are presented in table 7.7. The table also lists

the ratios between the tight and loose selected samples with the standard selection. The unfolded number of ν_μ is not affected by the changes in cuts, as expected from the numbers in the previous table. The ν_e samples are different to the order of 2%.

	ν_μ	ν_e	$R_{e\mu}$
Loose	1314645	18889	0.01437
Standard	1314065	18520	0.01409
Tight	1313154	18848	0.01435
Loose/Standard	1.000	1.020	1.020
Tight/Standard	0.999	1.018	1.018

Table 7.7: The unfolded number and ratio of ν_μ and ν_e events identified in the data, using three different sets of cuts, as described in the text. Also tabulated are the ratios of the loose and tight event numbers to those from the standard cuts.

The variation in the $R_{e\mu}$ is used to estimate the systematic errors. The loose and tight cuts cause a 2% and 1.8% increase. These show that alterations in either direction to the standard cuts have a similar effect on $R_{e\mu}$ and as such, a 2% systematic error is appointed to the event classification process, the larger of the above two differences.

7.4.2 Background

The background scale, determined in section 6.3.4, will be used in the oscillation analysis. The benefit of the scale is that it accounts for most of the differences between the data and simulation. Any systematic error from the level or shape of the background should not be greater than the scale itself, see table 6.4. The scale for all ν is used in the search, and so an error of 8.3% is ascribed to the background in the ν_e signal.

7.4.3 Electron Selection

Due to differences between the simulated and real NOMAD data, the efficiency determined from Monte Carlo for the electron identification may be incorrect, and so it must carry a systematic error. This error is determined by comparing the efficiency of identification of Monte Carlo and data electrons. A sample of electrons coming from muon induced δ-ray events in the muon flat top is used. These are collected from the electromagnetic calorimeter trigger, (the flat top and trigger are both described in chapter 2). The

sample of δ-ray events is then inspected to see how often the electrons are identified. This is a measure of the electron identification efficiency in data. Monte Carlo δ-ray events are then generated, and a second efficiency was determined. The two efficiencies were then compared, the difference being used as an estimate of the systematic error. This work is reported in Flaminio et al. (1998), and a second independent study of δ-ray events is reported in Krasnoperov et al. (1999). Considering these two reports, a 2% systematic error is placed to the electron identification efficiency.

Related to this is the electron reconstruction efficiency. This was studied in Weber and Hurst (1998). The efficiency was determined by producing electron tracks from tracks in the transition radiation detector matched to clusters in the preshower and electromagnetic calorimeter. The number of these electrons that the reconstruction programme matched with drift chamber tracks implies the efficiency. Again, the efficiency from simulation and data are compared to estimate the systematic error. The study reports an error less than 1.7%.

A recent and more rigorous combined analysis of both electron identification and reconstruction was reported in Mishra (2000a). This work claims an error as small as 0.4% for the two effects. To reflect this newer work, and the previous two studies, a systematic error of 2.5% on $R_{e\mu}$ will be included. A smaller error could be used if the Monte Carlo efficiency was scaled according to the differences found in Weber and Hurst and Krasnoperov et al..

7.4.4 Energy Reconstruction

If the energy reconstruction of the real data is not well reproduced by the Monte Carlo, the ability to search for the oscillation signal in the $R_{e\mu}$ spectra will be impeded. Fortunately, the hadronic energy scale of section 4.5 has dealt with most of these inequalities. To account for any further discrepancies, an error can be estimated. To obtain this, the data was reprocessed with an energy scale 10% and 20% lower than the standard scale determined in section 4.5. $R_{e\mu}$ was then plotted to ascertain the magnitude of any changes. Figure 7.11 shows the comparison of the standard scale to the scale 10% lower. The differences are very small, especially in the low bins where the oscillation signal is expected. Using the 20% lower scale does not increase these differences. Summing the bin contents of $R_{e\mu}$ from 0 to 50 GeV gives an overall difference of 1.5%, which will be used conservatively as the systematic error on the energy reconstruction.

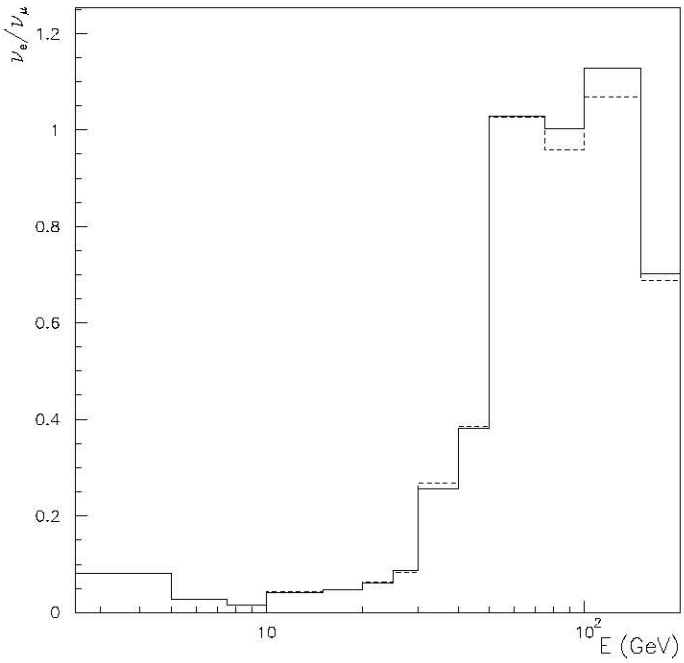

Figure 7.11: $R_{e\mu}$ determined with the standard energy scale (solid) and a 10% lower scale (dashed).

7.4.5 Summary of all Systematic Errors

The global (energy independent) errors on $R_{e\mu}$ are listed in table 7.8. This table also includes the total error, the combination of the individual errors in quadrature. The errors on the background and ν_e flux, as well as the statistical errors are included bin by bin.

7.5 Results

All the prerequisites of the analysis have now been met. A reliable beam simulator has been developed, a stable data sample has been classified, and the errors on these two are well understood and accounted for. It now remains to open the box, and compare the data and predicted $R_{e\mu}$.

Recall that the comparison will be made bin by bin. This includes separating the data into radial bins. The first four radial bins, defined in section 6.3.1 are used, there are insufficient statistics in just the 1995 data to

Source	Error (%)
Event Classification	2.0
Electron Selection	2.5
Energy Reconstruction	1.5
Empirical Parametrisation	1.72
Total	3.93

Table 7.8: The contributions to the systematic error on $R_{e\mu}$.

be able to use the fifth radial bin. The data is also split into two ν bins. The comparison of $R_{e\mu}$ from the 1995 high ν data and the official parametrisation is given in figure 7.12. The data and prediction coincide within the statistical errors plotted.

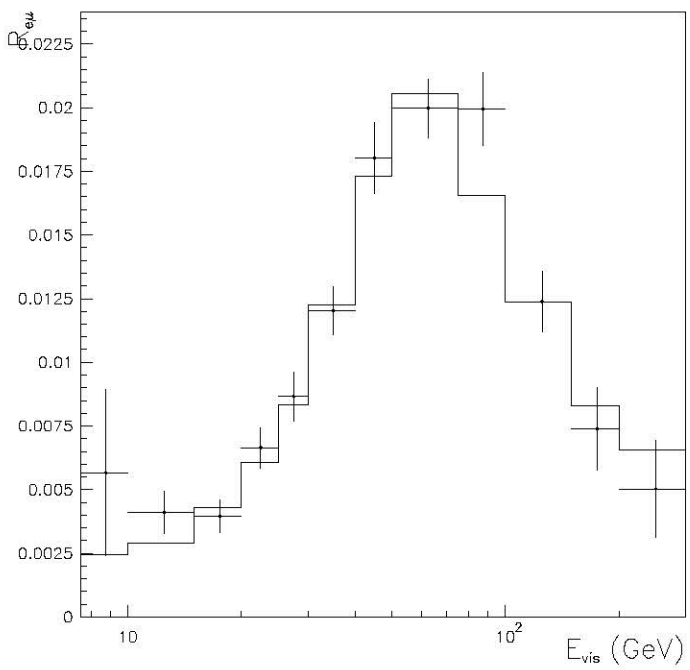

Figure 7.12: $R_{e\mu}$ from the 1995 high ν data (points) and as predicted by the official parametrisation (histogram). Only statistical errors are included.

The comparison with the low ν data is plotted in figure 7.13. Again

the differences between the data and prediction are within the statistical fluctuations inferred by the error bars.

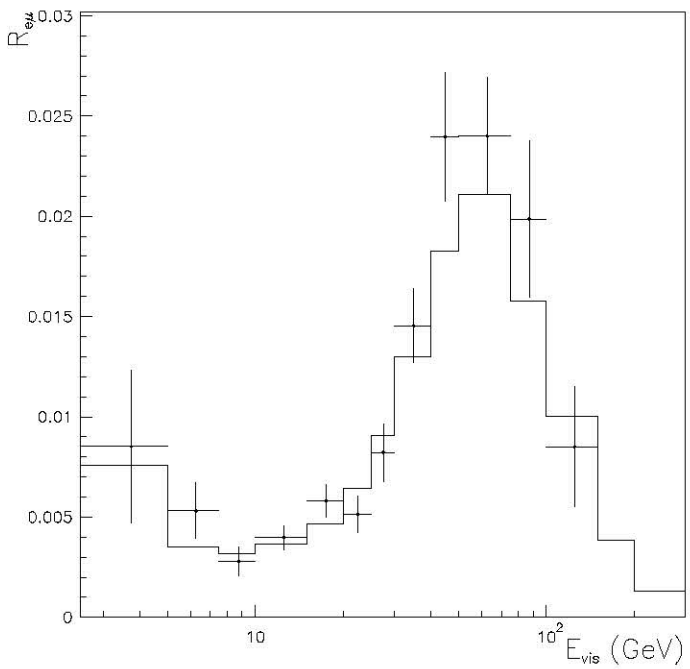

Figure 7.13: $R_{e\mu}$ from the 1995 low ν data (points) and as predicted by the official parametrisation (histogram). Only statistical errors are included.

7.5.1 Measured Oscillation Signal

To extract the oscillation signal from the above distributions, the data is compared to the results expected from an array of oscillation parameters, as described in section 7.2.3. Following the procedures of this section, (and using the programmes of Feldman, Nefedov, and Shih), the data is found to contain no evidence for muon neutrino to electron neutrino oscillations. A limit on $\nu_\mu \rightsquigarrow \nu_e$ oscillations can be set instead. This limit is presented in Δm^2 versus $sin^2(2\theta)$ phase space, figure 7.14. This is the 90% confidence limit, from the 1995 data only. The 90% confidence level sensitivity is also plotted.

The limit on mixing angle for large Δm^2 (greater than 1000 eV^2) is:

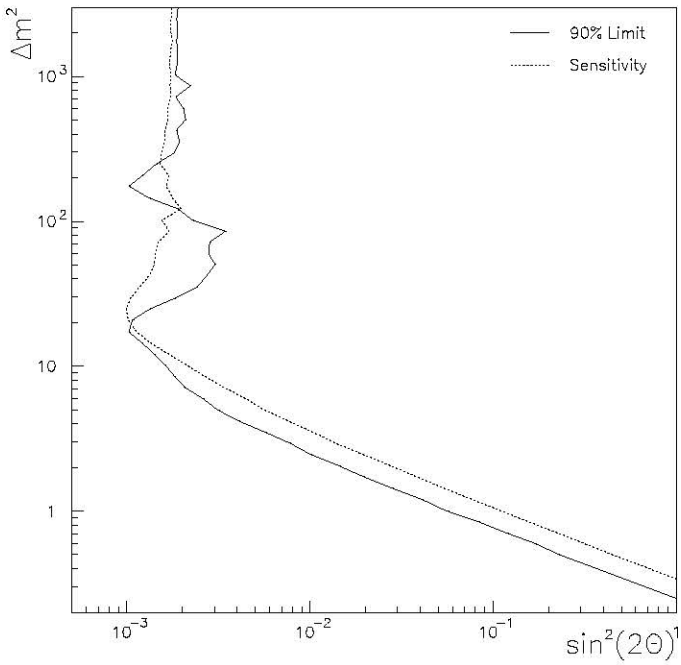

Figure 7.14: The 90% confidence limit obtained for $\nu_\mu \rightsquigarrow \nu_e$ oscillations from the 1995 NOMAD data. The phase space to the right of the limit contour is ruled out for these oscillations. The sensitivity is also included.

$$sin^2(2\theta) < 1.9 \times 10^{-3}(90\% \text{ CL}) \tag{7.4}$$

The corresponding sensitivity at large Δm^2 is:

$$sin^2(2\theta) < 1.7 \times 10^{-3}(90\% \text{ CL}) \tag{7.5}$$

Recall that the sensitivity is the average limit obtained by an ensemble of identical NOMAD experiments. The limit does not have to equal the sensitivity, and can be higher or lower than it. This limit is comparable to the limit of $sin^2(2\theta) < 1.8 \times 10^{-3}$ obtained in DeSanto (1997) with the 1995 data, given the differences in statistical method used.

7.5.2 Significance

It is of interest to see how this limit and corresponding exclusion region compares to the allowed region for $\overline{\nu}_\mu \rightsquigarrow \overline{\nu}_e$ oscillations defined by LSND. Recall, that due to unitarity arguments, there should be no difference in parameters describing $\overline{\nu}_\mu \rightsquigarrow \overline{\nu}_e$ and $\nu_\mu \rightsquigarrow \nu_e$ oscillations. The two regions are plotted in figure 7.15. This analysis rules out most of the high Δm^2 LSND region at 90% confidence.

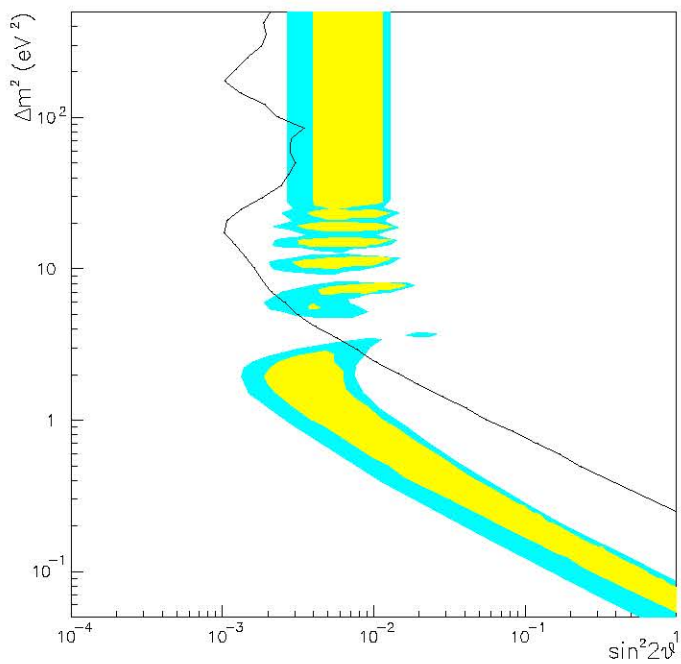

Figure 7.15: The LSND allowed region for $\overline{\nu}_\mu \rightsquigarrow \overline{\nu}_e$ oscillations (90% confidence region shaded light, 99% dark) taken from Athanassopoulos et al. (1996), plotted with the exclusion region of this analysis.

LSND have revised their analysis, and included a stricter energy cut on electrons to remove more background events, see Yellin (1999). These results should also be compared to the limit of this thesis, figure 7.16. The reanalysis by LSND has shifted the allowed region to lower mixing angles, and so this work is no longer capable of ruling out the high Δm^2 region. This will be the goal of the continuing NOMAD $\nu_\mu \rightsquigarrow \nu_e$ analysis.

7.5.3 Future Work

Determining the sensitivity does not require opening the box on the ν_e data and so can be presented without violating NOMAD policy. The sensitivity of this analysis, using the entire NOMAD data set, from 1995 to 1998, was calculated. The 90% confidence level sensitivity is presented in figure 7.17.

The sensitivity at high Δm^2 is:

$$sin^2(2\theta) < 9.7 \times 10^{-4} (90\% \text{ CL}) \tag{7.6}$$

This is almost a factor of two improvement. It could yet be improved further. In light of the of the results in the previous section, it is also interesting to see how the inclusion of the rest of the data will effect the ability of the analysis to verify the LSND result. The revised LSND allowed region and the sensitivity from the entire data set is given in figure 7.18. The figure shows that there is an excellent chance of being able to observe the LSND signal if it is in the high Δm^2 region, when all the NOMAD data is included.

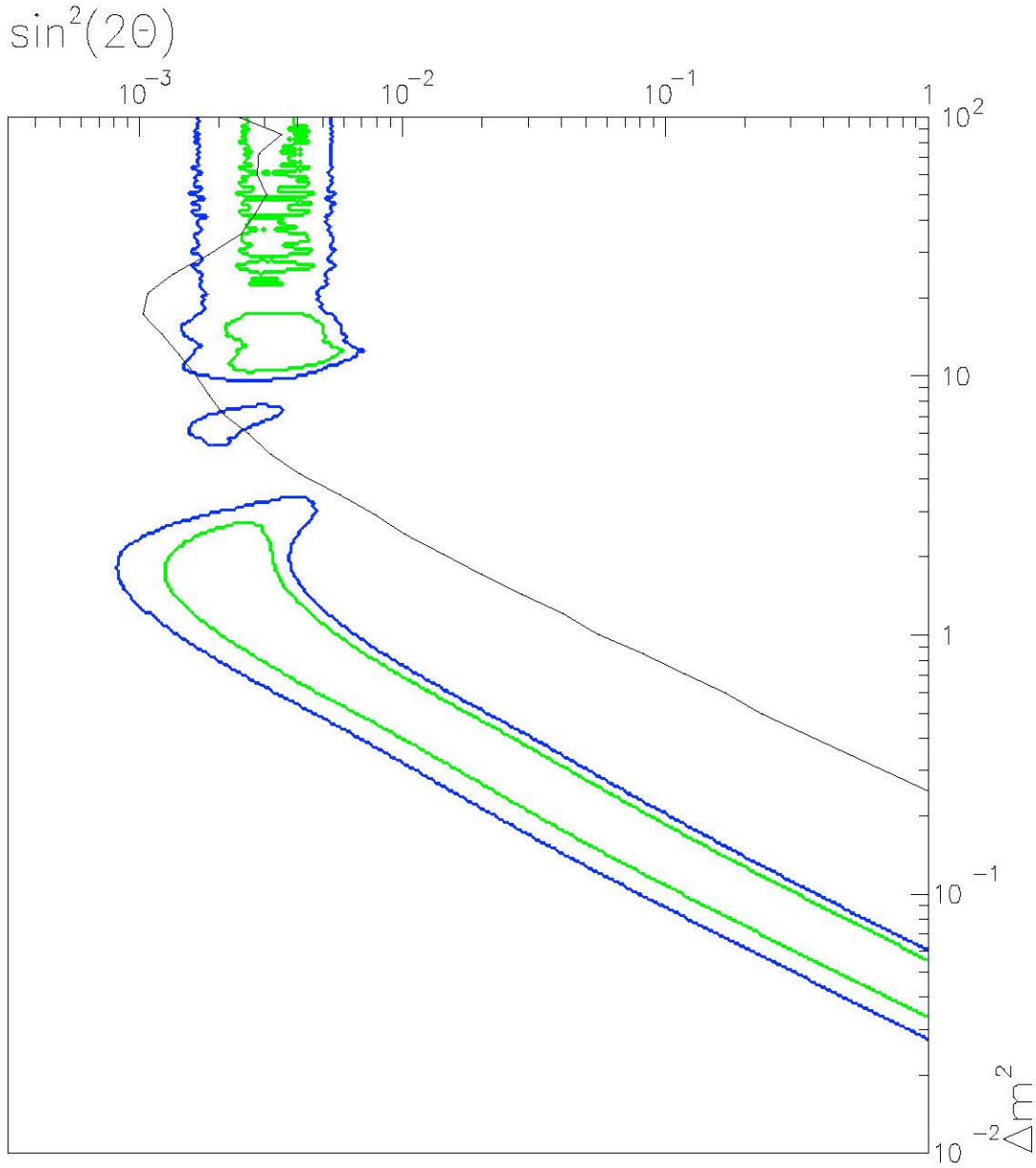

Figure 7.16: The LSND allowed region for $\overline{\nu}_\mu \rightsquigarrow \overline{\nu}_e$ oscillations, (90% and 99% confidence regions are inner and outer contours), taken from Yellin (1999), plotted with the exclusion region of this analysis.

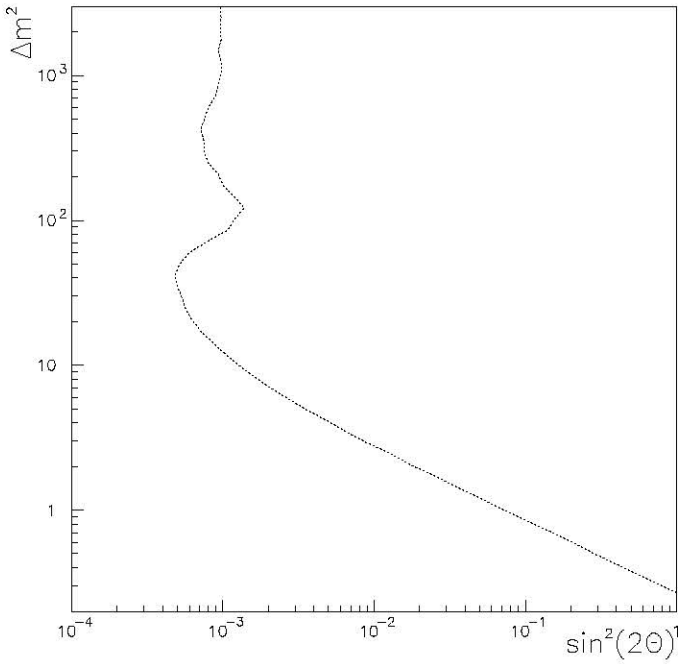

Figure 7.17: The 90% confidence level sensitivity expected from this analysis, using the entire NOMAD data set.

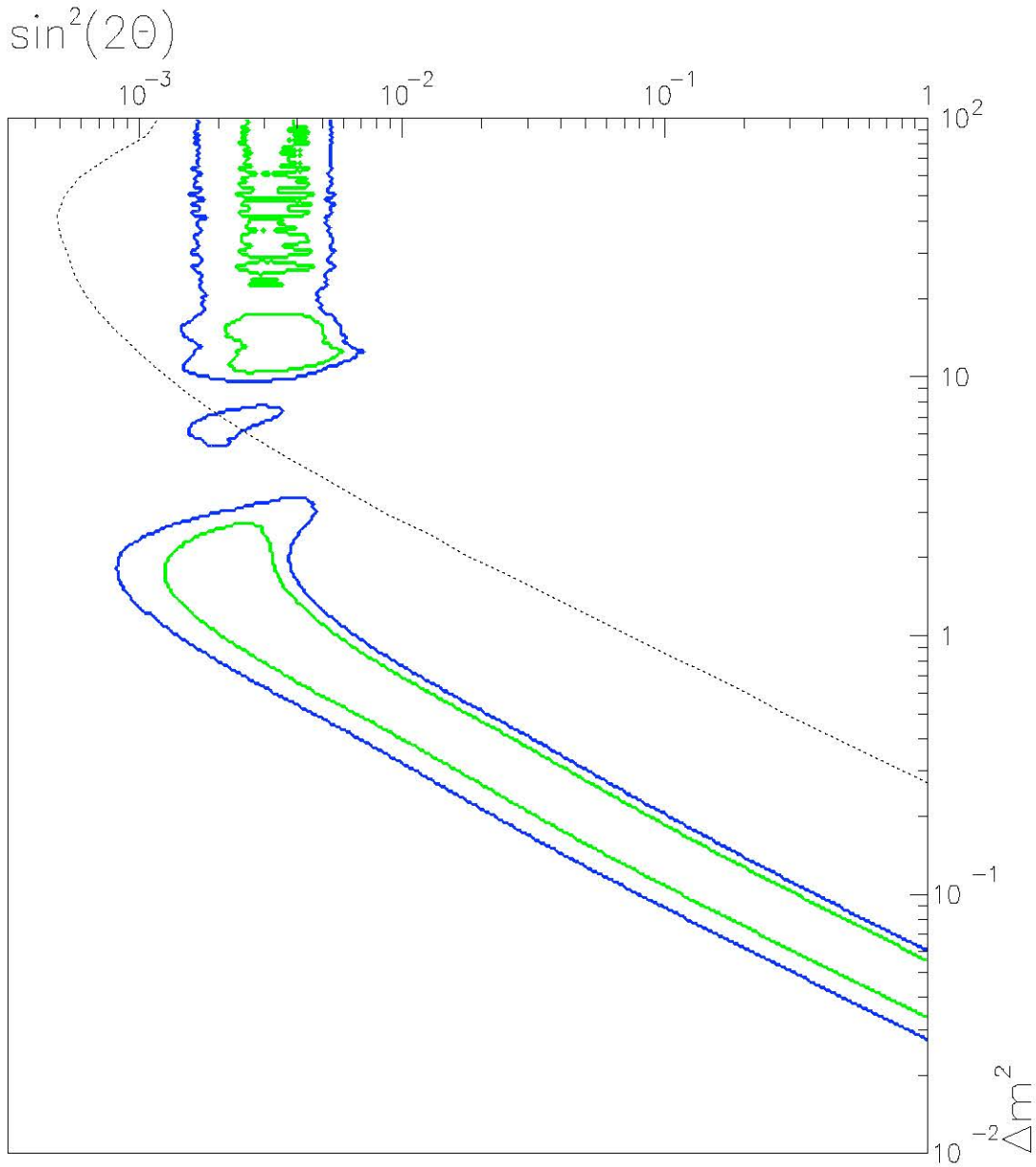

Figure 7.18: The revised allowed region of LSND compared to the sensitivity expected from this analysis, including the entire NOMAD data set.

Conclusion

This project aimed to study $\nu_\mu \rightsquigarrow \nu_e$ oscillations requiring the improvement of the original beam simulation technique. Also, a new and novel technique for predicting the ν_e spectrum was implemented. The prediction obtained with this technique in this thesis is an important cross check in the continuing NOMAD $\nu_\mu \rightsquigarrow \nu_e$ analysis. This new technique allowed a significant reduction in the systematic errors of the oscillation search analysis due to the beam prediction.

The search for $\nu_\mu \rightsquigarrow \nu_e$ oscillations in the 1995 NOMAD neutrino data has shown no evidence for neutrino oscillations in the high Δm^2 region searched. A limit has therefore been set. The 90% confidence limit on the mixing angle, at high Δm^2 is:

$$sin^2(2\theta) < 1.9 \times 10^{-3}(90\% \text{ CL}) \tag{7.7}$$

The sensitivity of the analysis is:

$$sin^2(2\theta) < 1.7 \times 10^{-3}(90\% \text{ CL}) \tag{7.8}$$

slightly better than the limit set. Whilst this limit rules out the existence of $\nu_\mu \rightsquigarrow \nu_e$ oscillations in the original LSND high Δm^2 allowed region, the revised LSND region cannot be excluded. This is the task of the ongoing NOMAD $\nu_\mu \rightsquigarrow \nu_e$ oscillation search, of which this analysis forms a part. The expected sensitivity of this analysis, using the entire NOMAD data set from 1995 to 1998 is:

$$sin^2(2\theta) < 9.7 \times 10^{-4}(90\% \text{ CL}) \tag{7.9}$$

This sensitivity covers the revised LSND high Δm^2 allowed region. and so with the inclusion of the rest of the NOMAD data this analysis will be able to observe the $\nu_\mu \rightsquigarrow \nu_e$ signal observed by LSND if it is there.

Bibliography

J.N. Abdurashitov. Results from SAGE (the Russian-American gallium solar neutrino experiment). *Physics Letters B*, 328:234 248, 1994.

I. Abt and B. Jongejans. An absolute calibration of the solid state detectors in the narrow band neutrino beam at CERN. *Nucl. Instr. and Meth. in Phys. Res. A*, 235:85–90, 1985.

G. Acquistapace et al. The West Area Neutrino Facility for CHORUS and NOMAD experiments (94-97) operation. Technical Report CERN-ECP/95-14, CERN, 1995.

G. Acquistapace et al. The CERN neutrino beam to Gran Sasso (NGS). Technical Report CERN 98-02, CERN, 1998.

M. Aguilar-Benitez et al. Charm in 400 GeV p-collisions. *Zeitschrift für Physik C Particles and Fields*, 40:321, 1988.

ALEPH Collaboration. Measurement of the Z resonance parameters at LEP. Technical Report CERN-EP/99-104, CERN, 1999. Submitted to EPJ C.

J. Altegoer et al. *NOMAD GEANT Offline Manual.* CERN, 5.11 edition, 1996.

J. Altegoer et al. The NOMAD experiment at the CERN SPS. *Nucl. Instr. and Meth. in Phys. Res. A*, 404:96 128, 1998a.

J. Altegoer et al. A search for $\nu_\mu \rightarrow \nu_\tau$ oscillations using the NOMAD detector. *Physics Letters B*, 431:219 236, 1998b.

J. Altegoer et al. The trigger system of the NOMAD experiment. *Nucl. Instr. and Meth. in Phys. Res. A*, 428:299–316, 1999.

G. Ambrosini et al. Proposal - measurement of pion and kaon fluxes below 60 GeV/c produced by 450 GeV/c protons on a beryllium target. Technical Report CERN-SPSLC/96-01, CERN, 1996.

G. Ambrosini et al. Measurement of charged particle production from 450 GeV/c protons on beryllium. *The European Physical Journal C*, 10:605–627, 1999.

M. Anfreville et al. The drift chambers of the NOMAD detector. To be submitted to Nucl. Instr. and Meth. in Phys. Res., 1997.

D. Antreasyan et al. *Physical Review Letters*, 38:112, 1977.

M. Apollonio et al. Limits on neutrino oscillations from the CHOOZ experiment. Preprint hep-ex/9907037, 1999.

H. Arason et al. A standard model extension with neutrino masses and an invisible axion. Technical Report UFIFT-HEP-90-26, 1990.

C.G. Arroyo et al. Precise measurement of the weak mixing angle in neutrino-nucleon scattering. *Physical Review Letters*, 72(22):3453–3455, 1994.

R. Arsenescu et al. New results on particle production in Pb-Pb collisions at 158 A GeV/c at CERN-SPS. *J.Phys.G: Nucl.Part.Phys*, 25:225–233, 1999.

K. Assamagan et al. Upper limit of the muon-neutrino mass and charged-pion mass from momentum analysis of a surface muon beam. *Physical Review D*, 53(11):6065–6077, 1996.

P. Astier et al. Proposal – Search for the oscillation $\nu_\mu \to \nu_\tau$. Technical Report CERN–SPSLC/91–21, CERN, 1991.

P. Astier et al. A more sensitive search for $\nu_\mu \to \nu_\tau$ oscillations in NOMAD. *Physics Letters B*, 453:169, 1999.

P. Astier et al. Limit on $\nu_e \rightsquigarrow \nu_\tau$ oscillations from the NOMAD experiment. *Physics Letters B*, 471:406–410, 2000.

C. Athanassopoulos et al. Evidence for $\overline{\nu}_\mu \rightsquigarrow \overline{\nu}_e$ oscillations from the LSND experiment at the Los Alamos Meson Physics Facility. *Physical Review Letters*, 77(15):3082–3085, 1996.

H.W. Atherton et al. Precise measurements of particle production by 400 GeV/c protons on beryllium targets. Technical Report CERN 80-07, CERN, 1980.

P.S. Auchincloss et al. Measurement of the inclusive charged-current cross section for neutrino and antineutrino scattering on isoscalar nucleons. *Zeitschrift für Physik C – Particles and Fields*, 28:411–431, 1990.

E. Auge. Present status of the NA31 experiment. In *Electroweak interactions and unified theories*, 1989.

D. Autiero et al. The electromagnetic calorimeter of the NOMAD experiment. *Nucl. Instr. and Meth. in Phys. Res. A*, 373:358 373, 1996a.

D. Autiero et al. A high stability light emitting diode system for monitoring lead glass electromagnetic calorimeters. *Nucl. Instr. and Meth. in Phys. Res. A*, 372:556 561, 1996b.

D. Autiero et al. Test beam performance of the electromagnetic calorimeter of the NOMAD experiment. *Nucl. Instr. and Meth. in Phys. Res. A*, 387: 352–364, 1997.

D. Autiero et al. Status of PAMM $\tau \to e$ QE analysis. Presented at the NOMAD Collaboration Meeting, July, 1998a.

D. Autiero et al. A study of the transverse fluctuations of hadronic showers in the NOMAD electromagnetic calorimeter. *Nucl. Instr. and Meth. in Phys. Res. A*, 411:285–303, 1998b.

D. Autiero et al. Parametrization of e and γ initiated showers in the NOMAD lead-glass calorimeter. *Nucl. Instr. and Meth. in Phys. Res. A*, 425:188 209, 1999a.

D. Autiero et al. Phase II "howtos". Taken from the NOMAD Web Pages, 1999b.

J.N. Bahcall and R.K. Ulrich. *Reviews of Modern Physics*, 60:297, 1988.

L. Bandis et al. Limits on the majorana neutrino mass in the 0.1 eV range. *Physical Review Letters*, 83:41, 1999.

G. Barichello et al. A B_4C silicon target for the detection of neutrino interactions. *Nucl. Instr. and Meth. in Phys. Res. A*, 419:1–15, 1998.

G.D. Barr et al. Proposal for a precision measurement of ϵ'/ϵ in CP violating $k^0 \to 2\pi$ decays. Technical Report SPSC/90-22, CERN, 1990.

M. Barranco Luque et al. The construction of the central detector for an experiment at the CERN $\overline{p} - p$ collider. *Nucl. Instr. and Meth. in Phys. Res.*, 176:175–180, 1980.

D.S. Barton et al. *Physical Review D*, 27:2580, 1983.

G. Bassompierre et al. A large area transition radiation detector for the NOMAD experiment. *Nucl. Instr. and Meth. in Phys. Res. A*, 403:363–382, 1998a.

G. Bassompierre et al. Performance of the NOMAD transition radiation detector. *Nucl. Instr. and Meth. in Phys. Res. A*, 411:63–74, 1998b.

P. Berge et al. Neutrino beam dump experiment. *Zeitschrift für Physik C – Particles and Fields*, 56:175, 1992.

R.M. Bionta et al. Observation of a neutrino burst in coincidence with supernova 1987a. *Physical Review Letters*, 58:1494 1496, 1987.

I.G. Bird. NOMAD reconstruction program. NOMAD Internal Note No. 37, 1993.

I.G. Bird. CAMEL: A general purpose NOMAD program. NOMAD Memo 51, 1994.

M. Bonesini. Monte carlo studies for particle identification - 1. SPY Memo 96-02, 1996.

M. Bonesini. A preliminary analysis of the NA56/SPY data. SPY Memo 97-01, 1997a.

M. Bonesini. Strange particle decays $K_s^0 \to \pi^+\pi^-$. Presented at the SPY collaboration meeting, Milan, 18th of June 1997, 1997b.

M. Bonesini. Extrapolating NA56/SPY data from beryllium to carbon targets. SPY Memo 98-01, 1998.

M. Bonesini et al. *Nucl. Instr. and Meth. in Phys. Res.*, 378:349, 1996.

S.B. Boyd. *Neutrino production of opposite sign dimuons in the NOMAD experiment.* PhD thesis, University of Sydney, 1998.

C. Bozza et al. Measurement of the muon flux in the CERN SPS wide band neutrino beam line. CHORUS Internal Note 97030, 1998.

K.L. Brown and Ch. Iselin. *Decay Turtle.* CERN, 1974.

J. Bunn et al. *HBOOK Reference Manual.* CERN, 4.23 edition, 1995.

A. Capella et al. *Physics Reports*, 236:225, 1994.

L. Casagrande et al. The alignment of the CERN West Area neutrino facility. Technical Report CERN Yellow Report 96-06, CERN, 1996.

A. Cavestro et al. An analog mean-timer for long scintillation counters. *Nucl. Instr. and Meth. in Phys. Res. A*, 305:488 491, 1991.

F. Cerutti. Determination of the upperlimit on m_{ν_τ} from LEP. Technical Report CERN EP/99-03, CERN, 1999. Submitted to DPF99 conference.

A. Cervera et al. A calisto user's guide. Programme documentation, 1998.

CHARM II Collaboration. *Physics Letters B*, 302:351, 1993.

G. Chazelle. Electroweak physics at LEP2. Technical Report CERN/EP 99-011, CERN, 1999. Submitted to PANIC99.

H.H. Chen. *Physical Review Letters*, 55:1534, 1985.

E. Church et al. A proposal for an experiment to measure $\nu_\mu \rightsquigarrow \nu_e$ oscillations and ν_μ disappearance at the fermilab booster: BOONE. 1997.

G. Collazuol and A. Guglielmi. Monte carlo simulation of the neutrino flux in NOMAD - I. NOMAD Memo 98-32, 1998.

G.M. Collazuol. PhD thesis, Padova, Italy, 1997. Laurea Thesis.

G.M. Collazuol and A. Guglielmi. Particle identification studies - 1. SPY Memo 96-06, 1996a.

G.M. Collazuol and A. Guglielmi. Particle identification studies - 2. SPY Memo 96-015, 1996b.

R. Das and S.R. Mishra. Measurement of neutrino flux in NOMAD. NOMAD Memo 97-038, 1997.

Y. Declais et al. *Nuclear Physics B*, 434:503, 1995.

A DeSanto. First results from the $\nu_\mu \rightsquigarrow \nu_e$ oscillations search in the NOMAD experiment. In *Rencontres de Moriond*, 1997.

A. DeSanto, 1998. Private Communication.

A. DeSanto and S.R. Mishra. Private Communication, 1999.

L. DiLella. Accelerator and reactor neutrino experiments. In *19th International Symposium on Lepton and Photon Interactions at High Energie*. Stanford, International Journal of Modern Physics A, 1999.

E531 Collaboration. *Physical Review Letters*, 57:2897, 1986.

W.T. Eadie et al. *Statistical Methods in Experimental Physics.* North Holland, 1971. Pages 269-270.

K. Eggert et al. Large area drift tube chambers for a muon detector at the $\overline{p}p$-collider. *Nucl. Instr. and Meth. in Phys. Res.*, 176:217 222, 1980.

K. Elsener and T. Tabarelli de Fatis. Considerations on SPY-C. SPY Memo 97-016, 1997.

E. Eskut et al. The CHORUS experiment to search for $\nu_\mu \to \nu_\tau$ oscillation. *Nucl. Instr. and Meth. in Phys. Res. A*, 401:7 44, 1997.

V. Falaleev et al. Absolute muon flux measurement in the SPS neutrino beam. NOMAD Memo 97-016, 1997.

A. Fasso et al. FLUKA 92. In *Workshop on Simulating Accelerator Radiation*, pages 134–144. Los Alamos Report LA-12835-C, 1993.

G. Feldman. Calometric contributions to the p_t measurements. Talk presented at the Missing p_T Group Meeting, 1995.

G. Feldman and R.D. Cousins. Unified approach to the classical statistical analysis of small signals. *Physical Review D*, 57(7):3873–3889, 1998.

A. Ferrari et al. An improved multiple scattering model for charged particle transport. *Nucl. Instr. and Meth. in Phys. Res.*, B71:412–426, 1992. Presented at the Int. Conf. on Radiation Physics, Dubrovnik, 1991.

A. Ferrari and P.R. Sala. A new model for hadronic interactions at intermediate energies for the fluka code. In M. Burbank P. Dragovitsch, S.L. Linn, editor, *Proc. of the MC93 International Conference on Monte Carlo Simulation in High Energy and Nuclear Physics*, pages 277–288. World Scientific, Singapore, 1993.

A. Ferrari and P.R. Sala. The physics of high energy reactions. In A. Gandini and G. Reffo, editors, *Workshop on Nuclear Reaction Data and Nuclear Reactors Physics.* World Scientific, 1996.

H. Fesefeldt. GHEISHA - The simulation of hadronic showers. Technical Report PITHA 85/02, RWTH Aachen, Germany, 1985.

R.P. Feynman. *Physical Review Letters*, 23:1415, 1969.

V. Flaminio et al. Electron identification efficiency from delta rays. NOMAD Memo 98-014, 1998.

Y. Fukuda et al. Atmospheric ν_μ/ν_e ratio in the multi-GeV range. *Physics Letters B*, 335:237–245, 1994.

Y. Fukuda et al. Solar neutrino data covering solar cycle 22. 77(9):1683–1686, 1996.

Y. Fukuda et al. Evidence for oscillation of atmospheric neutrinos. *Physical Review Letters*, 81:1562–1667, 1998a.

Y. Fukuda et al. Measurement of the solar neutrino flux from Super-Kamiokande's first 300 days. 81:1158–1162, 1998b.

G.M. Garibian. Contribution to the theory of transition radiation. *JETP*, 6 (6):1079–1085, 1958.

G.M. Garibian. Radiation from a charged particle traversing a layered medium. *JETP*, 8(6):1003–1006, 1959.

G.M. Garibian. Transition radiation effects in particle energy losses. *JETP*, 10(2):372–376, 1960a.

G.M. Garibian. Transition radiation for a charged particle at oblique incidence. *JETP*, 11(6):1306–1307, 1960b.

G.M. Garibian, L.A. Gevorgian, and C. Yang. The calculation of x-ray transition radiation generated in regular- and irregular-layered media. *Nucl. Instr. and Meth. in Phys. Res.*, 125:133 137, 1975.

A. Godley. Flux normalisation studies, 1998. Talk presented at NOMAD $\nu_\mu \rightsquigarrow \nu_e$ Analysis Meeting, 26th November.

M. Goodman. The neutrino oscillation industry. `http://www.hep.anl.gov/ndk/hypertext/nuindustry.html`, 2000.

M. Goossens et al. *GEANT Detector description and simulation tool.* CERN, 1994.

V.N. Gribov. *JETP*, 29:483, 1969.

V.N. Gribov. *JETP*, 30:709, 1970.

A. Guglielmi and G. Collazuol. Status of SPY, NUBEAM and FLUKA. Talks presented to the Neutrino Beam Working Group, 1997.

A. Guglielmi and G. Collazuol. Status of nubeam fluka. Talks presented at NOMAD analysis meetings, 1997-2000.

J.F. Gunion. *Physics Letters B*, 88:150, 1979.

W. Hampel et al. Final results of the ^{51}Cr neutrino source experiments in GALLEX. *Physics Letters B*, 420:114–126, 1998.

E.H.M. Heijne. Muon flux measurement with silicon detectors in the CERN neutrino beams. Technical Report 83-06, CERN, 1983.

K. Hirata et al. Observation of a neutrino burst from the supernova SN1987A. *Physical Review Letters*, 58(1490-1493), 1987.

G. Ingelman. LEPTO version 6.1 — the Lund Monte Carlo for deep inelastic lepton-nucleon scattering. In W. Buchmüller and G. Ingelman, editors, *Physics at HERA*, pages 1366–1394, Hamburg, 1992. DESY.

KARMEN Collaboration. The KARMEN limit on $\overline{\nu}_\mu \rightsquigarrow \overline{\nu}_e$ oscillations and its implication for the LSND result. In *Proceedings of the Sixth Topical Seminar on Neutrino and Astroparticle Physics*, 1999.

C.W. Kim and A. Pevsner. *Neutrinos in physics and astrophysics*. Harwood, 1993.

R. Kitano and K. Oda. Neutrino masses in the supersymmetric standard model with right-handed neutrinos and spontaneous r-parity violation. Technical Report KEK-TH-661, KEK, 1999.

K. Kodama et al. Charm meson production in 800 GeV/c proton-emulsion interactions. *Physics Letters B*, 263:573, 1991.

E.W. Kolb and M.S. Turner. *The Early Universe*. Addison-Wesley, 1990.

A. Krasnoperov et al. Study of electron identification efficiency in NOMAD. NOMAD Memo 99-007, 1999.

G. Lehmann. Collimator scans. Presented at the SPY collaboration meeting, Milan, 18th of June 1997, 1997.

C. LLewellyn-Smith. Neutrino reactions at accelerator energies. *Physics Reports*, 3, 1972.

P. Ramond M. Gell-Mann and S. Slansky. *Supergravity*. North Holland, 1979.

E. Majorana. Symmetrical theory of electrons and positrons. *INC*, 14:171, 1937.

A.J. Malensek. Empirical formula for thick target particle production. Technical Report FERMILAB-FN-341, FERMILAB, 1981.

J. Maneira. Borexino: a new calorimeter for low energy solar neutrinos. In *VIIIth International Conference on Calorimetry in High Energy Physics*, 1999.

A. Marchionni. Calibration of the secondary emission monitors for primary proton beam intensity measurements in SPY. SPY Memo 96-09, 1996.

A. Marchionni. Status report on QE and resonance channels. Presented at NOMAD Collaboration meeting, April, 1998.

J.P. Meyer and A. Rubbia. *NOMAD event generator offline manual*. CERN, 5.00 edition, 1994.

S.P. Mikheyev and A.Y. Smirnov. Resonance enhancement of oscillations in matter and solar neutrino spectroscopy. *Soviet Journal of Nuclear Physics*, 42:913 917, 1985.

MINOS Collaboration. The MINOS detectors technical design report. Technical Report NuMI-L-337, FermiLab, 1998.

S.R. Mishra, 1998. Private communication.

S.R. Mishra. Empricial parametrisation neutrino weights. Private communication, 1999.

S.R. Mishra. Electron identification study, 2000a. Private communication.

S.R. Mishra. Empirical parametrization, 2000b. Talks presented at NOMAD Meetings between April and August.

L. Moffitt. Calculation of the SPY spectrometer acceptance. Master's thesis, University of Melbourne, 1997.

J.A. Nelder and R. Mead. *Computer Journal*, 7:308–313, 1965.

NIC National Instruments Corporation, Austin, TX. *LabVIEW User Manual for Sun*, 1994 edition, 1994.

K. Nishikawa. A possible long base line neutrino oscillation experiment using KEK PS and super kamiokande. *J. Phys. Soc. Jpn.*, 1992.

R. Oldeman. Deep inelastic events in the CHORUS calorimeter. Presented at the joint CHORUS NOMAD beam meeting, 1st December, 1998.

K.A. Olive et al. Primordial nucleosynthesis : Theory and observations. Preprint astro-ph/9905320, 1999.

I. Papadopoulos, 1997. Private Communication.

Y. Perrin et al. CASCADE: a toolkit for the construction of distributed, real-time, data-acquisition systemms. Technical Report CERN-ECP/93-13, CERN, 1993.

W.H. Press et al. *Numerical Recipes in Fortran 77.* Cambridge University Press, 1986.

J.R. Primack et al. Cold + hot dark matter cosmology with $m(\nu_\mu) \approx m(\nu_\tau) \approx$ 2.4 eV. *Physical Review Letters*, 74(12):2160–2163, 1995.

D. Rein and L. Sehgal. Coherent production of photons by neutrinos. *Annals of Physics*, 133:79–153, 1981.

F. Reines et al. *Science*, 124:103, 1956.

B. Ricci et al. Helioseismology and beryllium neutrinos. *Physics Letters B*, 456:214–219, 1999.

W.K. Sakumoto et al. *Nucl. Instr. and Meth. in Phys. Res.*, A294:179, 1990.

B. Schmidt. *Study of ν_μ-Charged-Current Interactions and Search for $\nu_\mu \leftrightarrow \nu_\tau$ Oscillations in the Channel $\tau^- \to \mu^-\overline{\nu}_\mu\nu_\tau$ with the NOMAD Detector at the CERN Wideband Neutrino Beam.* PhD thesis, Universität Dortmund, 1997.

Torbjörn Sjöstrand. PYTHIA 5.7 and JETSET 7.4: Physics and manual. Technical Report CERN-TH.7112/93, CERN, 1994.

P. Skubic et al. *Physical Review D*, 18:3115, 1978.

F.J.P. Soler. Summary of NOMAD 1995-1998. Presented at the NOMAD Collaboration Meeting, 1998.

F.J.P. Soler. Beam description improvements. Presented at NOMAD Collaboration meeting, July 29, 1999a.

F.J.P. Soler. NUBEAM status reports. Talks presented at NOMAD analysis meetings between July and December, 1999b.

S. Sorrention. GBEAM: status and comparisons with NUBEAM. Presented at the joint CHORUS NOMAD beam meeting, 1st December, 1998.

A. Suzuki. *Nuclear Physics B (Proc. Suppl.)*, 335:237, 1994.

S. Suzuki et al. New mesh PMTs for high magnetic environments. Technical report, Hamamatsu Photonics K.K., Ichino-cho, Japan, 1987.

T. Tabarelli de Fatis. Acceptance studies. Presented at the SPY collaboration meetings, 18th of April and 22nd of May, 1997, 1997a.

T. Tabarelli de Fatis. Meglio tardi che mai. SPY Memo 97-010, 1997b.

F. Takasaki et al. *Nucl. Instr. and Meth. in Phys. Res.*, 228:369, 1985.

S. Tovey et al. The neutrino flux at NOMAD. NOMAD Memo 95-030, 1995.

E. Tsesmelis. Neutrino Beam Study Group meetings, 1994-96. Available from `http://rsch02.cern.ch/palladin`.

T.S. Tu and P.Y. Xue. Determination of GUT scale and a class of no scale SUSY GUTs. Technical Report BIHEP TH 84-30, 1984.

V. Valuev. NUBEAM update. Talks presented at NOMAD Collaboration meetings from September to December, 1999.

V. Valuev. Study of systematic errors in the beam transport. Presented at the NOMAD Collaboration meeting, May, 2000.

Kevin Varvell. NOMAD DST package - version v7r2. NOMAD Memo 97-034. The v7r3 version of the documentation, and other relevant information, is available from the URL `http://pauli.physics.usyd.edu.au/Public/dst/dst.html`, 1997.

Y. Wang. Recent results from palo verde and future prospects. In *34th Rencontres de Moriond on Electroweak Interactions and Unified Theories*, 1999.

F. Weber et al. Status of the empirical parameterization study. Presented at the NOMAD Collaboration Meeting, 1998.

F. Weber and P. Hurst. A study of absolute $e^{\pm}$ reconstruction efficiency using TRD tracks. NOMAD Memo 98-031, 1998.

Ch. Weinheimer et al. High precision measurement of the tritium beta spectrum near its endpoint and upper limit on the neutrino mass. *Physics Letters B*, 460:219 226, 1999.

T. Weiße. *Comparison of Muonic and Electronic Final States in the NOMAD Experiment at the CERN Wide-band Neutrino Beam.* PhD thesis, Universität Dortmund, 1997.

D.A. White and A.C. Fabian. Einstein Observatory evidence for the widespread baryon overdensity in clusters of galaxies. *MNRAS*, 273:72 84, 1995.

L. Wolfenstein. Neutrino oscillations in matter. *Physical Review D*, 17:2369–2374, 1978.

B.D. Yabsley. *A search for $\nu_\mu(\nu_e) \rightsquigarrow \nu_\tau$ oscillations using the three-prong tau decay signature in the NOMAD experiment.* PhD thesis, University of Sydney, 1999.

S. Yellin. A comparison of the LSND and KARMEN $\overline{\nu}$ oscillation experiments. Preprint hep-ex/990212, 1999.